Multiphysics pore network simulation of electrochemical devices as a design tool

by

Niloo Misaghian

A thesis

presented to the University of Waterloo

in fulfilment of the

thesis requirement for the degree of

Doctor of Philosophy

in

Chemical Engineering

Waterloo, Ontario, Canada, 2022

Examining Committee Membership

The following served on the Examining Committee for this thesis. The decision of the Examining Committee is by majority vote.

External Examiner	Prof. Jason Hattrick-Simpers Department of Materials Engineering, University of Toronto
Supervisor	Prof. Jeff Gostick Department of Chemical Engineering, University of Waterloo
Supervisor	Prof. Edward (Ted) Roberts Department of Chemical & Petroleum Engineering, University of Calgary
Internal Member	Prof. Marios Ioannidis Department of Chemical Engineering, University of Waterloo
Internal Member	Prof. Luis Ricardez-Sandoval Department of Chemical Engineering, University of Waterloo
Internal-external Member	Prof. Paul Fieguth Department of Systems Design Engineering, University of Waterloo

Author's declaration

This thesis consists of material all of which I authored or co-authored: see Statement of Contributions included in the thesis. This is a true copy of the thesis, including any required final revisions, as accepted by my examiners.

I understand that my thesis may be made electronically available to the public.

Statement of Contributions

Niloo Misaghian was the main author for Chapters 1, 2, and 6 which were written under the supervision of Prof. Jeff Gostick and Prof. Edward Roberts and were not written for publication.

This thesis is based on manuscripts and chapters 3, 4, and 5 are adapted from the following publications or manuscript:

Chapter 3 is based on the following publication:

Investigating the Role of the Triple-Phase Boundary in Zinc-Air Cathodes Using Pore Network Modeling, Misaghian, N., Sadeghi, M.A., Roberts, E., Gostick, J., *Journal of The Electrochemical Society*, (2022) 169, 100549.

Contributions:

Niloo Misaghian: Developed and implemented the PNM framework, visualizations, drafted the manuscript. Amin Sadeghi: Assisted with numerical method and Software development. Edward Roberts: Designed the study, aided analysis of data, interpretation of results, editing. Jeff Gostick: Designed the study, aided analysis of data, interpretation of results, editing.

Chapter 4 is based on the following manuscript in preparation:

Utilizing pore network modeling to analyze the performance of multi-layer electrode microstructures in vanadium redox flow batteries. Misaghian, N., Sadeghi, M.A., Roberts, E., Gostick, J.

Contributions: Niloo Misaghian: Developed and implemented the image generation and PNM framework, visualizations, drafted the manuscript. Amin Sadeghi: Assisted with numerical method and Software development. Edward Roberts: Designed the study, aided analysis of data, interpretation of results, editing. Jeff Gostick: Designed the study, aided analysis of data, interpretation of results, editing.

Chapter 5 is based on the following publication:

Prediction of diffusional conductance in extracted pore network models using convolutional neural networks. Misaghian, N., Agnaou, M., Sadeghi, M.A., Fathiannasab, H., Hadji, I., Roberts, E., Gostick, J. *Computers and Geosciences*, (2022) 162, 105086.

Contributions: Niloo Misaghian: Developed 3D deep learning framework, trained and tested the deep learning model, created modules in PoreSpy, drafted the manuscript, Mehrez Agnaou: Developed 3D deep learning framework, trained and tested the deep learning model, Amin Sadeghi: Aided direct numerical simulation, Hamed Fathiannasab: Aided data analysis, manuscript revisions, Isma Hadji: Aided development of 3D Resnet deep learning model, Edward Roberts: Designed the study, and aided interpretation of results, Jeff Gostick: Designed the study, and aided interpretation of results.

Abstract

Redox flow batteries including the vanadium redox flow battery (VRFB) and Zn-air batteries have attracted attentions in energy storage projects due to their scalability and high energy density. Performance of these devices is particularly dependent on the transport processes occurring in their porous electrodes which are in turn dependent on their microstructure. As a result, researchers have been focused on designing electrode structures that enhances the performance of the energy storage devices and reduces their operational cost. For this purpose, pore-scale modeling of reactive transport phenomena in porous electrodes is of strong interest to help unravel the structure performance relationship of porous electrodes. Two main approaches in pore-scale modeling are direct numerical simulations (DNS), and pore network modeling (PNM). DNS methods are computationally expensive especially in large samples and multiphysics and/or multiphase problems. PNM has been successfully used in porous electrode studies such as fuel cells due to its lower computational cost. However, PNM for structural design and studies of redox flow batteries including Zn-air and vanadium redox flow batteries (VRFB) requires improvements due to the more complicated multiphysics occurring. This thesis aims towards utilizing and improving pore network modeling framework for these two types of batteries by developing a rigorous framework that can be used for structural-performance and design studies of porous electrodes.

The development of a rigorous PNM framework for studying the microstructures in VRFB and Zn-air electrodes requires enhancements in the PNM. For example, in VRFB the effect of both mass transfer coefficients and migration are required to be captured. Moreover, to study the impact of various structures, a workflow is required for in-silico generation of materials with realistic properties to which PNMs can be applied to simulate performance. To resolve these issues, modifications on the PNM topology and formulations were applied to accommodate mass transfer coefficients. A framework was developed to generate fibrous materials with novel multi-layer structures and analyze their microstructure and performance relationship. It was found that in an interdigitated flow field placing a higher permeability layer near the membrane provided higher current density in contrast to the opposite order of the layers. The higher current density was due to higher flow rates in the regions closer to the membrane that were otherwise exhausted. However, it was shown that selecting the optimum design solely based on current density was ambiguous, as additional operational conditions such as pumping cost must be included in the selection process.

Another essential improvement on PNM framework is to properly capture complex multiphase transport in porous electrodes, such as air electrodes in Zn-air flow batteries. This improvement is essential, as air

electrodes operate with triple phase boundary regions where oxygen reduction reaction takes place within the pore-scale microstructure. A framework was developed to include the dissolution of oxygen in multiphase transport formulations and study the relationship between electrolyte invasion configuration, liquid-gas interface and performance of the air electrodes. It was found that invasion of electrolyte from low to intermediate saturation provides additional liquid-gas interface and higher power density while the optimum saturation depends on the structure, which was further investigated in terms of the pore size distribution.

Finally, a key step in PNM of porous electrodes is to properly represent the porous structure in the model, both topology and geometry. Much effort has been focused on improvements on extracting the network and properly estimating its mass transport properties, such as diffusive conductance. In extracted networks from volumetric images, this value is found by analyzing the geometrical properties of the pore-to-pore image or direct numerical simulation methods. DNS methods provide a more accurate estimation; however, they are computationally expensive. To resolve this issue, an image-based deep learning framework was developed to estimate diffusive conductance of PNM elements. It was shown that the deep learning framework can speed up the estimation of conductance values by 500x in contrast to DNS methods while providing a more accurate estimation in contrast to classic analytical solutions and geometry-based methods. The developed framework can be applied to migrative transport of species and dispersion, as they include the same parameter, thereby useful in modeling porous electrodes.

The presented work in this thesis was focused on improving PNM framework to include mass transport processes more effectively in multiphase and multiphysics problems with emphasis on electrochemical modeling of porous electrodes. The developed frameworks have enabled the study of microstructure and performance relationship in redox flow batteries including metal-air and vanadium redox flow battery. The developed in-silico generation of microstructures and performance analysis using PNM can be used as a computationally efficient tool to design high performing porous electrodes.

Acknowledgements

I would like to thank my supervisor Prof. Jeff Gostick for his continuous supports during my PhD study and research. His supports, training and guidance helped me in my research and shaped my research, programming, and professional skills. His mentorship and continuous feedback helped me become a better researcher. I am very grateful and indebted for all his supports and help. I would like to thank Prof. Edward Roberts for accepting to serve as my co-supervisor and for his supports and guidance during my PhD study. His ideas and constructive reviews helped me in my research and his supports through CREATE ME2 trainings helped me in my professional skills development. I would also like to thank all the examining committee members for their time and valuable comments.

I would like to thank Dr. Mehrez Agnaou for all his supports and guidance during my PhD research and his mentorship and patience during our collaboration. I would like to thank Dr. Amin Sadeghi for his supports during my PhD research and our collaborations. His ideas and supports in software development projects helped me improve my problem-solving skills and become a better researcher. I would also like to thank all co-authors of my research publications for their supports and contributions during our collaborations. Next, I would like to thank all other members of PMEAL group who were welcoming, supportive, and kind during my PhD study.

I would like to thank CREATE ME2 program for their financial and training supports during my PhD study and their program coordinator Dr. Aber Abulhassn for her supports during my trainings, collaboration in HQP association and attending the program's conference. I would also like to thank CANARIE and University of Waterloo for their financial supports during my PhD study.

Last but not least, I would like to thank my family, friends and loved ones for their continuous supports at each stage of my life. Their support, kindness, and belief in me helped me move forward and become more passionate. I am always grateful and indebted for their supports and love.

Table of contents

List of figures

List of tables

Chapter 1: Introduction

1.1. General research territory

In the past three decades, increasing demand for energy along with the associated environmental impacts and shortage of fossil fuels have increased the demand for renewable energy resources, such as wind and solar [1], [2]. However, renewable energy resources are intermittently available resulting in the lack of supply for the periods when the electricity demand is high. To stabilize the supply-demand market, large-scale energy storage devices are required. Amongst different energy storage technologies, redox flow batteries (RFB) including the vanadium redox flow battery (VRFB) and metal-air flow batteries have attracted attentions due to their high energy efficiency, scalability, and flexibility in terms of controlling power and energy separately [3], [4]. Metal-air flow batteries such as Zinc-air flow batteries have an additional advantage of having a high energy density while being cost-effective, as they use oxygen in the air as the oxidant. Despite the advances in VRFBs and Zinc-air flow batteries technology, they still need to be optimized to provide a high performance and long life cycle product [5]–[8]. Since United Nations' global call for actions for protecting the planet in 2015 [9], development of high performance RFBs have been more crucial due to decarbonization roadmaps, such as Canada's 2030 agenda for sustainable development that includes access to clean energy in remote communities. Increasing the performance of these electrochemical devices and their life cycle will then have a substantial economic and operational impact on the development of energy storage projects. VRFBs and Zinc-air flow batteries operate with porous electrodes and the structure of the electrodes affect the performance of these batteries, because key transport phenomena and electrochemical reactions take place within their microstructure [10], [11]. To design an optimum electrode structure that improves the performance of the batteries it is necessary to unravel the structure-performance relationship in porous electrodes [2]. Such studies require a proper tool to capture and analyze the physics and transport mechanisms occurring within the porous electrodes. Although experimental tools can provide insights on the structural-performance of the electrodes [8], [12], to study varieties of structures and details of transport at pore-scale a proper numerical modeling provides a cost-effective tool. Numerical modeling frameworks have been the focus of researchers in porous electrode studies, since advances in image acquisition techniques can now provide the 3D high-resolution images of these porous structures [13], [14]. The primary motivation of this work is to utilize and improve a pore-scale numerical modeling framework, known as pore network modeling to efficiently capture the microstructure and transport in porous electrodes and develop a rigorous framework that can be used for structural-performance studies.

1.2. Gaps in the existing research

Macroscopic modeling techniques are commonly used to model batteries, from full cells down to single electrodes [15], [16]. Macroscopic models assume the electrode is a homogeneous continuum domain while the structural properties are estimated using correlations at macroscopic scale, such as tortuosity and permeability. Although these models can be used to design overall cell configurations and provide information on the effect of changing macroscopic structural parameters, they do not resolve the conditions at the pore-scale. Capturing the effects of real geometry at the pore-scale is essential for several reasons:

- Macroscopic modeling uses effective properties such as tortuosity and effective diffusivity, which are estimated using developed correlations. However, those correlations can be erroneous outside the range of their applications [17], [18]. As a result, the macroscopic modeling results including the performance of the electrode can be erroneous.
- Even though a macroscopic model can provide information on the general structure such as permeability, its information is not enough for creating the porous structure and experimental studies. For example, the same value of permeability can be found in two different structures of foam and fibrous materials while having different performance. Therefore, microstructure information is essential for practical design and experimental studies. To tackle this limitation, some researchers have used effective properties correlations that include more structural information such as fiber diameter [19]. However, other structural information including anisotropy and fiber orientations that are necessary for design could not be captured.
- Capturing pore-scale information are even more essential in multiphase transport applications, such as air electrodes. The distribution of electrolyte within air electrodes are based on percolation theory and the reaction at air electrodes takes place at the interface of air-electrolyte, the location and extent of which is highly affected by the pore-scale morphology. These pore-scale phenomena are impossible to measure in macroscopic models.

Pore-scale modeling techniques can be categorized into two main approaches of direct numerical simulation (DNS) and pore network modeling (PNM). DNS methods capture the pore-scale information by discretizing the porous domain into computational meshes. DNS methods have been used to study the structural properties of porous electrodes, such as pore size distribution at pore-scale [10], [20]. While DNS methods provide pore-scale information in contrast to macroscopic modeling, they are computationally expensive especially in complex multiphysics problems and large domains [3]. As an alternative approach, pore network modeling (PNM) is a cost-effective pore-scale modeling technique that models the porous domain as a connected network of pores (nodes) and throats (edges) with simple geometries [2], [21]–[23]. This

approximation of the geometry and topology of the material reduces the number of variables in transport equations and makes the method computationally efficient and suitable to study large domains and multiphase multiphysics problems [24], [25].

Due to the computational efficiency of PNM and other benefits, this technique has been used successfully in various applications in energy storage devices, such as fuel cells [22], [23], [26], Li-ion batteries [27], and RFBs [2], [28], [29]. However, PNMs are not traditionally applied to electrochemical devices, and no established commercial software is available. Therefore, using PNM to rigorously study porous electrodes in VRFB and Zn-air flow batteries requires additional improvements on the modeling framework to capture multiphase multiphysics transport properly. For instance, previous PNM studies on VRFB electrodes did not include a mass transfer coefficient between the flow fluid and solid electrode [28], or they did not include migration effects on ion transport [29]. Such improvements on PNM framework would be a steppingstone for the ultimate goal of in-silico design of electrode structures and using PNM within an optimization framework to select high performing structures. A main gap in the structural-performance of VRFB research is that previous PNM studies on structure-performance relationship of RFBs were based on simple lattice networks [2] or existing commercial materials [29], [30]. For structural performance analysis it is necessary to develop a framework to generate varieties of novel structures and rapidly analyze their performance using electrochemical modeling in PNM.

Another area were PNMs can be of benefit is understanding the impact of multiphase transport, which adds another layer of complexity on top of the structural effects. Multiphase conditions are found in Zn-air cathodes (discussed herein) as well as PEM fuel cells and electrolzyers. An issue in multiphase transport in air electrodes is to capture the impact of multiphase mechanisms at reactive regions where solid-liquid-gas meet, the so-called triple phase boundary (TPB) region [31], [32]. The role of TPB in Zn-air electrodes and the impact that electrode microstructure has on the phase distributions have not been thoroughly studied [32]. For instance, the only PNM study of the Zn-air electrode was limited to a 2D pore network model, and the focus was on qualitative analysis of triple phase boundary so no performance calculations where made [33]. Proper modeling in the air electrode using PNM requires development of a framework that can capture TPB region and underlying transport phenomena including dissolution of gas in a multiphase scheme, transport of species and charge. Such framework can then be used for further studies on optimum structural and operational parameters in Zinc-air flow batteries.

The above goals all depend on a faithful representation of the structure by the pore network. A lot of effort has been directed toward extraction of topologically accurate networks and extracting suitable geometric properties to define the transport conductance of the network conduits. For instance, accurate estimation of

diffusive conductance is not only useful to describe diffusive mass transport, but also the migrative transport of species and dispersion, as the same parameter exists in both transport phenomena. Classic methods to estimate conductance are based on analytical solutions that assume simple pore geometries in place of irregular-shaped ones which are found in real porous media [34]. An alternative means of finding conductance is to use direct numerical simulation (DNS) on a pore-by-pore basis [35], [36]. However, it is computationally expensive to implement DNS on every tomogram from which a network is extracted. Therefore, there is a gap in research to accurately estimate diffusive conductance of PNM elements while being computationally feasible.

A common concept in the abovementioned gaps is to improve or properly capture mass transport parameters in PNM framework for electrochemical modeling of porous electrodes. Addressing those gaps results in a more rigorous PNM for studying VRFBs and Zn-air flow batteries and designing optimum electrode structures.

1.3. Filling the gaps

The objective of this thesis is to address the gaps in the PNM framework with a specific focus on properly defining mass transport processes in VRFBs and Zn-air electrodes. Occupying these gaps will result in a more rigorous PNM framework for design studies of porous electrodes and understanding their structure-performance relationship. In this regard, the objectives of this work was break down into three studies as follows:

Objective 1: Defining the dissolution of gaseous species and multiphase transport in PNM for the ultimate goal of **studying the role of TPB and structure-performance relationship in Zn-air electrodes**. The focus of this objective was to capture the multiphase transport in PNM including invasion of electrolyte into the catalyst layer and underlying transport phenomena, such as dissolution of oxygen at electrolyte-gas interface, diffusion and reaction of oxygen and mass transport of ionic species along with charge transport within the electrolyte. The developed framework was then used for structural-performance analysis in Zn-air electrodes with the impact of pore size distribution studied as a parameter which could ultimately be experimentally targeted. To focus on the complex multiphase behaviour and capture transport phenomena occurring in the developed PNM framework, a simple cubic lattice network geometry was used.

Objective 2: Incorporating a local mass transport coefficient in PNM for the ultimate goal of **studying the structure-performance relationship in VRFB electrodes**. In this objective a realistic geometry for the porous electrode was defined while the transport is simpler in contrast to objective 1, as it is a single phase transport problem. However, the fluid flow was added to the system of mass transport equations. Within

the PNM framework, steps were required to couple the fluid velocity with the reaction terms. A robust framework was developed for in-silico generation of novel fibrous materials and rapid iteration of designs for VRFB electrodes.

Objective 3: **Developing a framework to estimate diffusive mass transport conductance of conduits in PNM** accurately and efficiently. For this objective a deep learning framework was applied to estimate the diffusive conductance of conduits from real images of pore regions, thereby capturing the true geometry of the network. The deep learning model can then replace the time-consuming DNS methods and the erroneous analytical methods in estimating the diffusive conductance values. The final result of this objective increases the accuracy of PNM in diffusive mass transport behaviour and electrochemical modeling, as the diffusive conductance term exists in migrative conductance of species.

1.4. Thesis structure

This thesis is organized with a manuscript-based structure where each chapter is self-contained and addressing each objective of the thesis. Each objectives' chapter includes an introduction with relevant literature reviews to justify the motivation of the work presented in the chapter. Detailed theories and methodologies followed by results and discussions on findings are then provided. Each chapter ends with concluding marks and suggestions on future works. The structure of this thesis is as follows:

In chapter 2, background and theories relevant to the objectives of this thesis are provided. Only general literature review was included here since each subsequent chapter discusses the literature pertinent to its focus.

In chapter 3, a PNM framework is developed for modeling the multiphase transport in air electrodes of Zn-air flow batteries. A simple lattice network geometry is used as the porous catalyst layer, while the complex multiphase transport including dissolution of the oxygen is applied in the mass transport equations. Results and findings on the role of TPB on the electrode performance and the dependence of TPB on electrolyte distribution are presented. Next, the developed PNM is used for structural-performance analysis of the catalyst layer based on different pore size distributions.

In chapter 4, a PNM framework is developed for in-silico generation of novel structures for VRFB electrodes. The generated materials have complex structure, but in contrast to chapter 3 the mass transport is applied for a single phase flow. To include the velocity dependence of mass transfer coefficient the PNM geometry is modified. An image generation algorithm is used to generate fibrous materials with novel structures. Next, the developed PNM is used for structural-performance analysis of the generated structures.

In chapter 5, an image-based deep learning framework is developed to estimate the diffusive conductance of conduits in PNM. The deep learning model can be used to predict and assign physics properties of conduits, such as diffusive and migrative conductance in PNM of porous electrodes.

In chapter 6, key findings and conclusions from the three objectives are presented along with suggestions for future efforts and extensions of the research.

Chapter 2: Background and Theory

This chapter provides technical background and theory relevant to the objectives of the thesis, with a focus on modeling transport phenomena in porous electrodes.

2.1. Electrochemical devices

This section is focused on introducing the two electrochemical devices that are studied in this thesis. The basics of quantifying the performance of batteries are then explained along with justifications on the importance of studying porous electrodes.

2.1.1. Zinc-air flow battery

Zinc-air flow batteries have started to receive attention due to their high energy density since the fuel is a simple arbitrarily-sized hopper filled with zinc particles, which are an inexpensive and safe material [37]. Additionally, eliminating the need for a positive electrolyte effectively increases the energy density of the system. A schematic of a Zn-air flow battery is shown in Figure 2-1a. The battery system consists of a powdered metal as the anode, a porous air electrode as the cathode, and a membrane separator for electrical isolation while current collectors are connected to each electrode. In the air cathode the KOH electrolyte invades through the catalyst layer while the oxygen from the air diffuses through the electrode to the catalyst layer where it dissolves into the electrolyte and undergoes oxygen reduction reaction. The oxygen reduction reaction produces hydroxides from oxygen and water. The hydroxide ions react with the Zn metal and form zincate ions, which precipitates as ZnO, once the ions reach their solubility limit concentration. The electrochemical reactions in anode and cathode of ZAFB are as follows. For the zinc electrode:

$$\mathrm{Zn} + 4\mathrm{OH}^- \overset{r_{\mathrm{Zn}}}{\leftrightarrow} \mathrm{Zn(OH)}_4^{2-} + 2\mathrm{e}^- \tag{2-1}$$

$$\mathrm{Zn(OH)}_4^{2-} \overset{r_{\mathrm{ZnO}}}{\leftrightarrow} \mathrm{ZnO} + 2\mathrm{OH}^- + \mathrm{H_2O} \tag{2-2}$$

While for the air electrode:

$$\frac{1}{2}\mathrm{O_2} + \mathrm{H_2O} + 2\mathrm{e}^- \overset{r_{\mathrm{air}}}{\leftrightarrow} 2\mathrm{OH}^- \tag{2-3}$$

The oxygen reduction reaction takes place within the air cathode's catalyst layer porous structure, as schematically shown in Figure 2-1b. The reaction in the air electrode takes place at the interface of the solid

catalyst material, liquid electrolyte, and gas phases, the so-called triple phase boundary (TPB) region. The extent of the TPB region depends on various parameters such as the electrolyte invasion pattern and the microstructure of the porous catalyst layer. Therefore, to design better performing air electrode structures, it is necessary to understand the mechanisms of oxygen reduction reaction and the role of TPB and structural and operational parameters affecting the TPB. Part of this thesis (chapter 3) is therefore focused on understanding the role of TPB and structural-performance analysis of the porous catalyst layer in the Zn-air flow battery system.

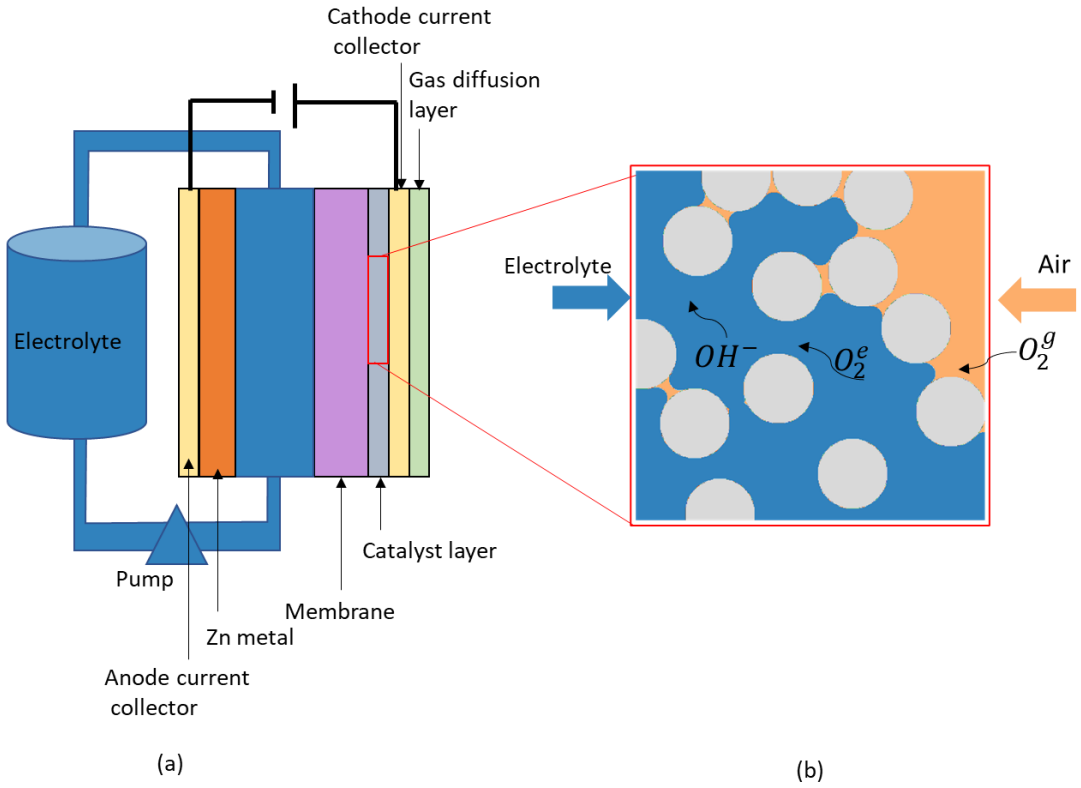

Figure 2-1 a) A schematic of a Zn-air flow battery b) A schematic of a porous catalyst layer and transport of species

2.1.2. Vanadium Redox flow batteries

Redox flow batteries (RFBs) are promising energy storage devices for large-scale, long-life applications such as stationary storage. The advantage of the flow battery over conventional batteries is that power generation and energy storage elements are decoupled, and therefore more stacks can be added when required to generate more power and larger electrolyte tanks can be added to increase amount of energy storage. Amongst different redox couples for RFBs, vanadium redox flow battery (VRFB) technology has been more developed. The advantage of VRFB to other RFBs is the use of the same material in cathodes

and anodes, thereby reducing the risk of cross-contamination in cell compartments, which is a degradation issue. A typical VRFB consists of a battery stack where the electrochemical reaction occurs to generate power, and separate electrolyte tanks where the solutions of electroactive species are stored as schematically shown in Figure 2-2 a. The electrochemical reactions during charge and discharge of a vanadium flow battery are as follows. For the cathodic electrode half-cell reaction:

$$VO^{2+} + H_2O - e^- \underset{\text{discharge}}{\overset{\text{charge}}{\rightleftharpoons}} VO_2{}^+ + 2H^+ \qquad (2\text{-}4)$$

And for the anodic electrode half-cell reaction:

$$V^{3+} + e^- \underset{\text{discharge}}{\overset{\text{charge}}{\rightleftharpoons}} V^{2+} \qquad (2\text{-}5)$$

The microstructure of the electrodes in VRFBs plays an important role on the fluid flow distribution and reactive transport, and accordingly the generated current/power of the battery. Figure 2-2b illustrates an example of a reactive fluid flow through a fibrous porous material from pore-scale simulation results. The red color indicates the electroactive species, which is consumed at the electrode surfaces (denoted by the dark blue spots). The fluid flow paths highly prefer regions of large pore size, resulting in channeling, and conversely constricted pore regions are starved of reactant. The transport here is influenced by both diffusion and convection. Not indicated here is the migration of ions due to electric field effects, which adds even further complexity to the system. This figure therefore illustrates how the structure of the electrode impacts the distribution of reactants, and that the reaction rates are unevenly distributed due to the heterogeneous nature of the electrode structure. Developing optimized electrode structures, with high permeability but also high reactive surface area and good mass transfer characteristics has been a top priority in the VRFB research. Part of this thesis (chapter 4) is therefore focused on developing a framework for structural-performance analysis of novel electrode structures in VRFBs.

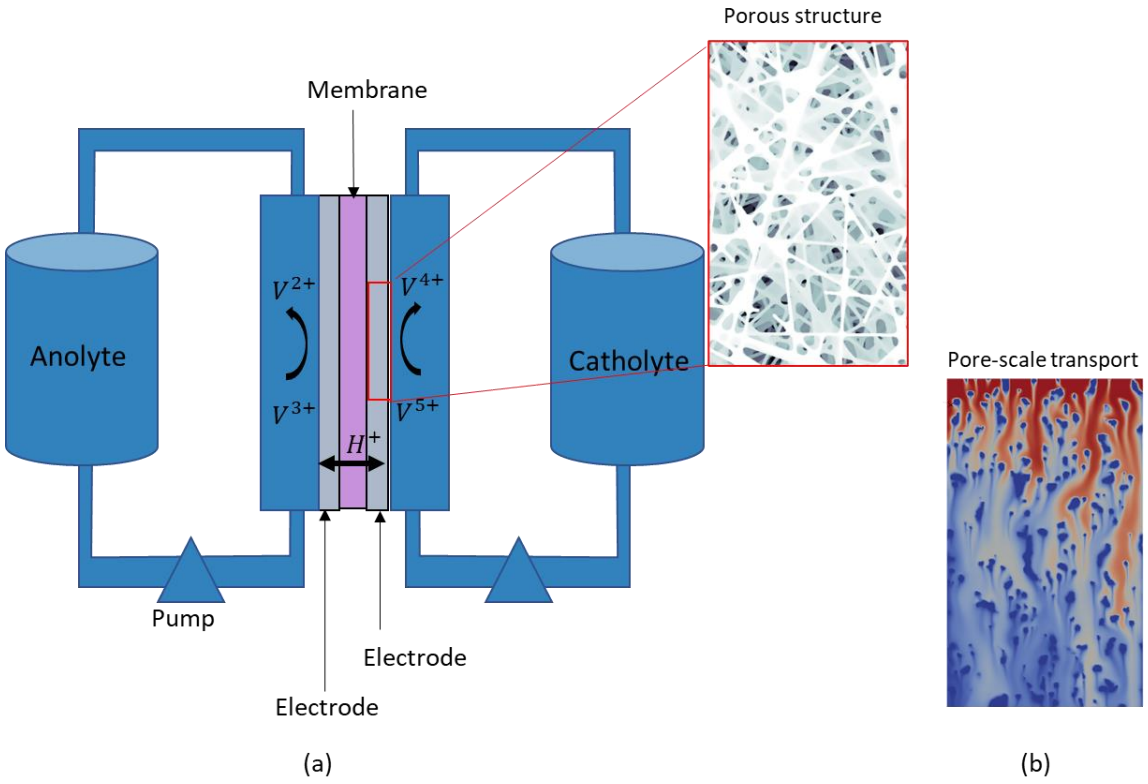

Figure 2-2 a) A schematic of a Vanadium redox flow battery b) A schematic of a porous electrode

2.1.3. Performance of electrochemical devices

The performance of flow-cell systems, which have an external supply of reactants that is in principle inexhaustible, can be quantified using the current-potential relationship or polarization curve. This is in contrast to a normal battery where capacity is the primary consideration. A polarization curve shows the steady-state dependence of cell potential on its current density [38]. A schematic of a polarization curve is shown in Figure 2-3. Each region in the polarization curve is relevant to a principal phenomenon or physics. For example, region a, b and c represent the effect of kinetics, ohmic losses and mass transfer, respectively.

In region a, the slope of the curve is initially high indicating a small amount of current generation leads to a fast drop in the cell potential. This region represents a kinetic controlled region at low current density (activation polarization). Kinetics of the reaction can be defined using Butler-Volmer equation [38], which indicates an exponential increase in current as voltage is applied.

In region b, the ohmic losses dominate the polarization behaviour. Ohmic losses are linearly proportional to current. In this linear region, kinetic losses are also increasing but much slower than ohmic losses as

kinetics are increasing proportional to the logarithm of the current. Therefore, this linear region is called ohmic region. The slope of the polarization curve in region b indicates the ohmic resistance of the electrolyte, which is mainly affected by the electrolyte conductivity and length [38].

In region c, mass transfer losses dominate the polarization behaviour at high current density. During the discharge reactants are transferred to the electroactive catalyst sites to undergo reaction at the electrode surface. The consumption of reactants leads to a concentration gradient between bulk electrolyte and electrode surface. The reactant concentration becomes zero and limiting current density is reached [38].

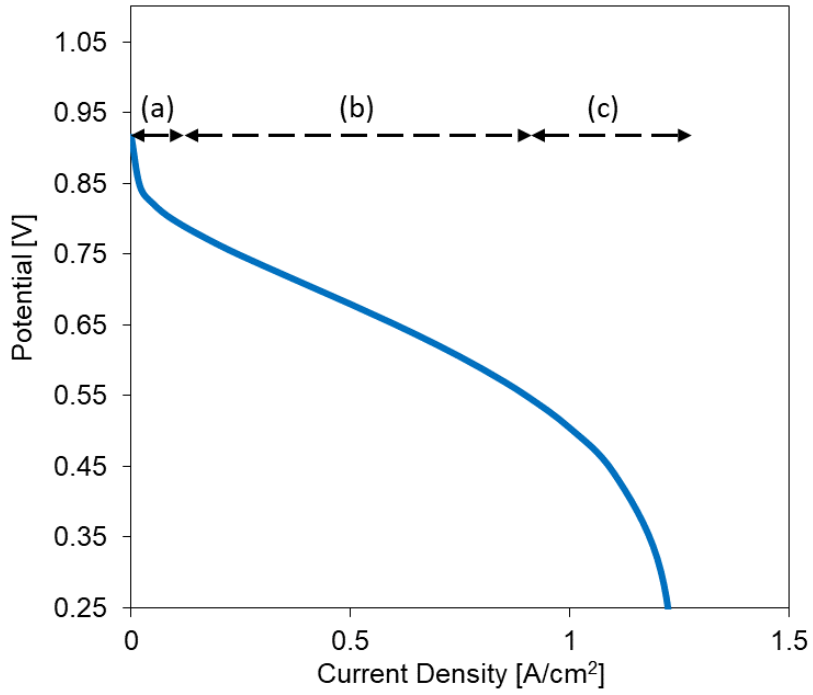

Figure 2-3 An example of an arbitrary polarization curve.

Depending on the system, the structures and properties of its components, and electrolytes the polarization curve is different in each electrochemical device. However, the contribution of kinetics, ohmic loss and mass transfer at low to high current densities is a common feature for all polarization curve [38]. Therefore, it is important to understand the effect of these mechanisms on the performance of the batteries. Analysis of polarization curve can be used to define operational or structural parameters that lead to a better performance. For example, using a thin electrolyte can reduce the ohmic loss, as it would be seen from a lower slope in moderate current region providing a higher current density. However, such simple conclusion was based on the use of a planar electrode. In a porous electrode the polarization curve is affected by the

microstructure of the electrode in a more complex way. To quantify the performance of VRFBs and Zn-air batteries in structural-performance analysis, the polarization curves can be used as a basis of performance measures. For example, when defining the performance in terms of the maximum power density or current density, the structural design and operational conditions that lead to a highest power/current density can be assumed to be the optimum design. Such cases are examined in chapter 3 and chapter 4 with a main focus on the microstructures of the electrodes.

2.1.4. Porous electrodes

Porous electrodes are used in various commercial energy storage devices instead of planar electrodes essentially because they can provide a larger interface for contact of active materials with the electrolyte liquid phase and in some applications with the gas phase [38], [39]. The increased surface area leads to increased power density and efficiency of the chemical reaction. Another advantage of a porous electrode is that its compactness can reduce the ohmic loss, as it reduces the length of the charge transport [39]. Other advantages include providing volume for storing reactants near the electrode surface, which accommodates the change in solid electrode volume during the discharge, such as in lead-acid batteries [38], [39]. Additionally, in air electrodes such as metal-air batteries the porous electrode structure promotes the transport of oxygen and creating a stable liquid-gas interface within porous catalyst layer promotes the oxygen reduction reaction. Therefore, the first step in designing better performing porous electrodes is to understand the transport mechanisms within the porous structure. However, studying transport in porous electrode includes more complications than planar electrodes. For example, ohmic loss and mass transfer occur in different directions within the porous structure and accordingly reaction is nonuniform [39]. To understand the transport mechanisms different numerical modeling techniques have been developed. In the next sections an overview of those techniques and their advantages and disadvantages are provided. As the focus of this thesis is based on pore network modeling framework, more details on that specific framework are provided.

2.2. Continuum-scale transport in porous electrodes

Continuum-scale modeling techniques are macroscopic modeling methods that use the average of variables over a volume of the electrode, the so-called representative elementary volume (REV). The REV in continuum-scale modeling is small in contrast to the electrode domain while large enough compared with individual pore regions [38], [39]. In macroscopic modeling the actual geometry of the pores and solid matrix are ignored and the volume-averaged quantities are assumed to be continuous in spatial and temporal space. In a porous electrode, the electrode is then modeled as the “superposition of two continua” [39] including electrolyte solution and matrix, meaning that at any point in the domain both continuum exist.

Therefore, variables such as electrolyte conductivity and diffusivity are calculated as effective properties instead of properties at the microscopic level within the porous electrode. Using the effective properties in the system of mass and charge transport equations, averaged values of velocity, species concentration and electrical potential are found. Macroscopic modeling is therefore computationally inexpensive due to this simplification of geometry and mathematical equations are sometimes even solved in one or two dimensions. However, actual geometric details of pores and matrix in electrode are ignored [39]. In this section modeling porous electrodes using macroscopic modeling is briefly explained.

2.2.1. Transport equations

The material balance for a species i in the electrolyte using volume-averaged method can be written as follows [39]:

$$\frac{\partial \varepsilon c_i}{\partial t} = a j_{in} - \nabla . N_i \tag{2-6}$$

where a is the specific interfacial area defined as surface area of pore walls per unit volume of the electrode domain. c_i is the average concentration of species i over the volume of the electrolyte solution in pores. With this definition εc_i is the amount of species per control volume [38]. j_{in} is the pore-wall flux density of species i averaged over the interfacial area of electrolyte-matrix [39] (species reaction rate at the interface [38]). N_i is the average flux density of species i over the cross-section of the electrode. Eq. (2-6) indicates that the concentration of species at a location within the electrode changes because of the electrochemical reaction ($a j_{in}$) and/or species transport ($\nabla . N_i$) [39].

A volume element in the electrode is assumed to be electrically neutral. Therefore, the divergence of total current density (matrix and electrolyte) becomes zero as follows [39]:

$$\nabla . \mathrm{i}_1 + \nabla . \mathrm{i}_2 = 0 \tag{2-7}$$

where i_1 and i_2 are the current density in matrix and electrolyte phase, respectively. In the solid matrix the current due to electrons transport is found from ohm's law as follows:

$$\mathrm{i}_1 = -\sigma \nabla \Phi_1 \tag{2-8}$$

where σ and Φ_1 are the effective conductivity of the solid phase and solid potential, respectively.

The current density in the electrolyte solution due to the transport of species i is defined as follows [39]:

$$\mathrm{i}_2 = F \sum_i z_i N_i \tag{2-9}$$

Combining Eq. (2-6), Eq. (2-9) and electroneutrality assumption in the electrolyte ($\sum z_i c_i = 0$) leads to the following equation:

$$\nabla . \mathrm{i}_2 = aF \sum_i z_i j_{in} = a i_n \tag{2-10}$$

where i_n is the average current density. Assuming a single electrode reaction, species reaction rate can be defined using Faraday's law [38]:

$$j_{in} = -\frac{s_i}{nF} i_n \tag{2-11}$$

where s_i is the stoichiometric coefficient for species i in the reaction, n is the number of electrons, F is the Faraday's constant. Substituting Eq. (2-11) into Eq. (2-6), species transport equation becomes as follows:

$$\frac{\partial \varepsilon c_i}{\partial t} = a \frac{s_i}{nF} i_n - \nabla . N_i = -\frac{s_i}{nF} \nabla . i_2 - \nabla . N_i \tag{2-12}$$

The faradic charge transfer from matrix to electrolyte can be described by a general Bulter-Volmer equation [39]:

$$\nabla . i_2 = a i_0 [\exp\left(\frac{\alpha_a F \eta_s}{RT}\right) - \exp\left(-\frac{\alpha_c F \eta_s}{RT}\right)] \tag{2-13}$$

where η_s is the surface overpotential defined as $\eta_s = \Phi_1 - \Phi_2 - U$. Φ_2 and U are the electrolyte potential and the open-circuit voltage, respectively. R is the universal gas constant and T is the absolute temperature. The average flux density of species i in a dilute electrolyte can be defined by the driving forces in the electrolyte using Nernst-Plank equation assuming advection, diffusion and migration driving forces [39]:

$$\frac{N_i}{\varepsilon} = -D_i \nabla c_i - z_i u_i F c_i \nabla \Phi_2 + \frac{\mathrm{v} c_i}{\varepsilon} \tag{2-14}$$

N_i and v are defined as flux density and bulk fluid velocity based on superficial area, which is the area of both matrix and pore. Therefore, $\frac{N_i}{\varepsilon}$ and $\frac{\mathrm{v}}{\varepsilon}$ can be interpreted roughly as the flux density and velocity in the electrolyte phase [39]. u_i is the ionic mobility and can be described by Nernst-Einstein equation as $u_i = \frac{D_i}{RT}$ [40]. Properties such as such as the diffusion coefficient and the mobility are estimated as effective properties. To estimate effective properties, the average structural effect of the porous medium is commonly defined by two parameters [38]. First parameter is porosity to account for the fact that within the porous electrode the area available for transport is smaller because of the presence of matrix. Second parameter is tortuosity (τ) of the porous medium which accounts for the fact that a species transport path is tortuous and

meandering because of the presence of solid [38]. For example effective diffusivity is estimated using Bruggeman correlation as $D_{eff} = D_0 \frac{\varepsilon}{\tau} = D_0 \varepsilon^{0.5}$ [18].

Continuum-based modeling methods are useful for studying operation of electrochemical devices or device geometry. However, they are not ideal for structural-performance analysis of porous electrodes due to three main reasons. Firstly, continuum-based modeling requires effective parameters such as effective diffusivity, conductivity, tortuosity and porosity; however, amongst those parameters the only actual structural parameter is porosity, while the rest are defined using correlations. The accuracy of the correlations are questionable however [17]. For example, to estimate effective diffusivity Brugmann's correlation [18] is widely used. However, for fibrous materials (e.g. VRFB electrode) Todamakis and Sotirchos [41] correlation was defined as $D_{eff} = D_0 \varepsilon \left[\frac{\varepsilon - 0.11}{1 - 0.11}\right]^{\beta}$, where due to the anisotropy in in-plane and through-plane direction in fibrous materials, different β are assumed for each direction. Both of these correlations have been examined in a study by Chen *et al.* [18] in comparison with a pore-scale modeling technique. Their study showed that although in-plane effective diffusivity using Todamakis and Sotirchos correlation matched with the pore-scale modeling result, Brugmann's correlation and through-plane Todamakis and Sotirchos can lead to overestimation of the effective diffusivity. The reason is that structural properties of fibrous materials are more complex and anisotropic that limits the applicability and accuracy of general correlations [18]. This conclusion reinforces the idea of using pore-scale modeling techniques for studying porous electrodes.

Secondly, continuum-based modeling techniques average the variables over a volume, therefore the detailed structure of the electrode is not captured. Such details are essential for design and manufacturing of optimum electrode structures. For example, a macroscopic model can inform about the general structural parameters such as the effect of porosity and permeability. However, these methods do not inform about parameters that can be directly used in experimental studies and designs. For example, the same value of permeability and porosity can be found in two different structures of foam materials and fibrous materials, whereas those two structures do not present the same performance. The lack of more structural information from continuum-based modeling can be avoided by using correlations that include structural parameters, such as fiber diameters. Such information can be used in experimental studies when creating fibrous electrodes. In this regards, in as study by Kok et al. [19], they used a continuum-based modeling approach to investigate the effect of fiber sizes on the performance. They incorporated the effect of fiber diameter by using Carman-Kozeny correlation in the estimation of permeability of the domain. Additionally, the fiber diameter was included in estimating the reactive surface area. Although their study presented additional

information to explore in experimental studies such as fiber diameter, their model was not capable of informing other important structural parameters such as the effect of anisotropy and alignment of fibers. Finally, although continuum-based models can be applicable in modeling single-phase transport in VRFB electrodes to provide some information on the structure and performance, their application on complex multiphase transport in Zn-air electrodes is even more limited. Modeling the air electrode requires two-phase flow, invasion of electrolyte using percolation theory and additional pore-scale information such as the extent of TPB regions, which are impossible to measure in a macroscopic modeling approach. Due to these limitations of macroscopic modeling tools, to capture the complex transport phenomenon at micro-scale and structural-performance analysis, pore-scale modeling techniques are more suitable. Pore-scale modeling approaches are explained in next sections.

2.3. Direct numerical simulations

With the advances in imaging techniques and availability of high-resolution images of porous media, pore-scale modeling approaches have attracted attentions in simulating porous electrodes of electrochemical devices. Direct numerical simulations (DNS) are pore-scale modeling methods that have the main advantage of capturing complex geometries up to the resolution limit of imaging techniques. DNS methods include various approaches, which can be divided into two main categories [28] of grid-based approach such as Finite Difference (FD) and Finite Element Method (FEM), and particle-based approach such as Lattice Boltzmann Method (LBM). In grid-based approaches, the electrolyte and matrix domain are discretized into computational meshes or nodes and the system of mass and charge transport equations are solved on the computational meshes or nodes. In LBM the void space is segmented into a lattice, on which the motion and collision of particles are simulated [35]. In this section, modeling porous electrodes using DNS approach is briefly explained. This provides context for the value of pore network modeling, and also provides background on DNS itself which is used in chapters 4 and 5 to some extent.

2.3.1. Transport equations

Fluid transport is defined by the continuity and Navier-Stokes equations [42]:

$$\nabla . u = 0 \tag{2-15}$$

$$\frac{\partial u}{\partial t} + (u.\nabla)u = -\frac{1}{\rho}\nabla p + \frac{\mu}{\rho}\nabla^2 u \quad (2\text{-}16)$$

where u is the electrolyte velocity, p is the pressure. ρ and μ are the density and the viscosity of the electrolyte, respectively. From the solution of the fluid flow equations, the pressure and velocity distribution in the electrolyte phase are found.

Transport of species in the electrolyte can then be defined using Nernst-Plank equation given advection, diffusion and migration as the driving forces for species movements [38], [39]:

$$\frac{\partial C_j}{\partial t} + u\,.\nabla C_j = D_j\nabla^2 C_j + \nabla.\left[\frac{z_j C_j D_j}{RT}\nabla\Phi\right] \quad (2\text{-}17)$$

where C_j is the concentration of species j, D_j is the diffusion coefficient of species j, and Φ is the electric potential in the electrolyte [10]. Due to electroneutrality in the electrolyte, Eq. (2-17) is applied for all species expect the supporting ion (e.g. SO_4^{2-} in VRFBs). The concentration of the supporting ion is found from $\sum z_j C_j = 0$. Charge transport within the electrode matrix (e.g. carbon fibers in VRFBs) given the charge conservation concept ($\nabla.J = 0$) can be defined as follows:

$$\nabla.(\kappa_s\nabla\Phi_s) = 0 \quad (2\text{-}18)$$

where κ_s is the electrical conductivity of the solid matrix and Φ_s is the electric potential in the solid phase. Charge transport within the electrolyte phase is defined as follows:

$$\nabla.\left[\left(\frac{F^2}{RT}\sum z_j^2 D_j C_j\right)\nabla\Phi + F\sum z_j D_j\nabla C_j\right] = 0 \quad (2\text{-}19)$$

The electrochemical reaction term is then added to Eq. (2-19) as a rate boundary condition at solid-electrolyte interface. The electrochemical reaction can be defined using a Butler-Volmer equation. For example, in a VRFB system, the rate of consumption/production of species can be defined as follows [20], [43]:

$$N_{IV}.\hat{n} = -N_V.\hat{n} = k\,(C_{IV}^s)^{\alpha_c}(C_V^s)^{\alpha_a}\left[\exp\left(\frac{\alpha_a F\eta}{RT}\right) - \exp\left(-\frac{\alpha_c F\eta}{RT}\right)\right] \quad (2\text{-}20)$$

where the multiplication factor for the exponential term on the right-hand side is the exchange current density, where C_{IV}^{s} and C_{V}^{s} are concentration of Vanadium species at the solid-liquid interface and k is the reaction rate constant. η is the overpotential defined as:

$$\eta = \Phi_s - \Phi_l - (E^0 + \frac{RT}{F}\ln\left(\frac{C_V}{C_{IV}}\right)) \tag{2-21}$$

where E^0 is the equilibrium potential. From Faraday's law given the fact that $J = FN$, the electrochemical reaction term for rate boundary condition in Eq. (2-19) is defined from Eq. (2-20).

The DNS solution of mass and charge transport provides the distribution of charge and species within the porous structure of electrodes. These pore-scale information along with the performance of electrodes can be analyzed for designing better performing electrodes. In studying VRFB electrode different studies were focused on using DNS methods. Qiu *et al.* [20] used finite volume method -to solve the system of species mass and charge transport equations in VRFB electrodes. Their study was focused on operational parameters to enhance the electrode performance. However, their analysis illustrated the non-uniform distribution of current and species within the porous electrode structure and the advantage of DNS in providing pore-scale information in contrast to macroscopic modeling. In a separate study, Qiu *et al.* [43] focused on three electrodes with different porosities and compared the distribution of species and losses within their microstructure. Their results showed that starvation of reactive species in some regions of the electrodes and low flow rates played an important role on limiting the performance of VRFB electrodes. In a separate study, Chen *et al.* [18] utilized LBM to study the effects of fiber diameter and porosity on the depletion rate of species in VRFB electrodes. They concluded that smaller fiber diameter results in a higher surface area and more efficient depletion rate of species. All of these DNS-based studies have shown that morphology and structure of the electrode is a dominant factor in electrode performance. However, DNS methods have a main drawback of being computationally expensive. For example, the lattice Boltzmann method, which is commonly used for solving the Navier-Stokes flow in porous media, was utilized in a previous stud by Chen *et al.* [25]. Despite their parallelized code, predicting effective properties of a porous catalyst layer domain required 320 CPU cores which took about 6 hours for simulation of oxygen diffusion and 2 hours for proton conduction [25]. Therefore, despite the accurate predictions of DNS methods, their application on performance analysis of various structures and multiphase flow is computationally expensive especially in large samples. Due to this drawback, pore-network modeling technique has attracted more attention in studying porous electrodes, as it is a cost-effective pore-scale modeling approach. PNM approach is explained in the next section.

2.4. Pore network modeling approach

Pore network modeling maps the phase of interest into a connected network of nodes and edges. In porous electrodes, the void space is mapped to a connected network of pores and throats corresponding to wide voids and narrow constrictions, respectively. Therefore, PNM simplifies the void space with smaller amount of information about pore geometry (e.g. radius, volume) and topology (e.g. coordinates, connections) [44]. Such simplification is the main reason for lower computational cost of PNM. Therefore, PNM is advantageous in contrast to DNS in terms of computational cost, especially in larger samples and where multiphase and more complex physics are involved. Electrochemical modeling of porous electrodes using PNM includes modeling fluid flow to find the distribution of velocity and pressure throughout the network followed by solving the systems of mass and charge transport to find the species concentration and electrical potential within the network. In this section, more details on PNM approach are provided.

2.4.1. Transport Equations

Transports in pore network models are modeled by applying the governing equations on discretized network of connected pores and throats. An example of a connected pore-throat-pore element in PNM with spherical pores and cylindrical throats geometry is shown in Figure 2-4. The region extending from center of one pore to the center of its neighbouring pore is the so-called conduit element and its conductance for transport phenomena is used in the system of equations in PNM. As the focus of this thesis is modeling transport phenomena at steady-state, the PNM formulations in this section are based on steady-state condition. For details on transient simulation using PNM see references [28], [45], [46]. For modeling steady-state stokes flow, assuming a Newtonian, incompressible fluid, the mass conservation around pore i is defined as follows [45]:

$$\sum_{j=1}^{N_i} q_{ij} = \sum_{j=1}^{N_i} G_{ij}^{h} \left(P_i - P_j\right) = 0, \quad i = 1,2,\dots,N_p \tag{2-22}$$

where j is the number of neighbors of pore i and q_{ij} is the flow rate between pore i and pore j. G_{ij}^{h} is the hydraulic conductance of the conduit element ij and N_p is the total number of pores in the network. G_{ij}^{h} can be estimated using resistors-in-series method from the conductance of each conduit's element. For transport "*tr*" the conduit conductance is calculated as follows:

$$\frac{1}{G_{tr,ik}} = \frac{1}{g_{tr,i}^{p}} + \frac{1}{g_{tr,ik}^{t}} + \frac{1}{g_{tr,k}^{p}} \tag{2-23}$$

where the conductance of each element depends on the transport properties (e.g. fluid viscosity in hydraulic transport) and geometrical properties of the element (e.g. diameter, length). For fluid flow transport assuming a cylindrical throat, the throat conductance can be defined from analytical solution of steady-state Navier-Stokes equation for flow in a cylindrical pipe. This results in Hagen-Poiseuille equation as follows [45]:

$$g_{ij}^{h} = \frac{\pi}{128\mu}\left(\frac{d_{ij}^{4}}{l_{ij}}\right) \tag{2-24}$$

where d_{ij} and l_{ij} are the diameter and length of the throat ij. Modeling a Stokes flow problem in a pore network is solving a system of linear equations resulting from the application of Eq. (2-22) to find unknown pressure values in each pore. It can now be clearly seen that the accuracy of defining G_{ij}^{h} highly affects the accuracy of the simulation. More details on estimating conductance values of PNM elements are explained in section 2.4.2.2.

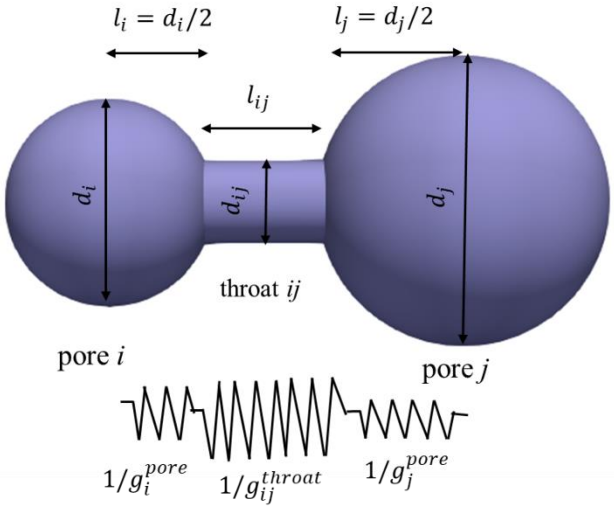

Figure 2-4 A schematic of a pore-throat-pore element in PNM.

Transport of species in the electrolyte can be defined using Nernst-Plank equations including the advection, diffusion and migration forces to describe the species movements. Using an upwind discretization scheme, Nernst-Plank equations in PNM framework is defined as follows [45]:

$$\sum_{j=1}^{N_i}\left[G_{d,ij}^{n}+max\left(q_{ij}-m_{ij}^{n},0\right)\right]c_i^n - \sum_{j=1}^{N_i}\left[G_{d,ij}^{n}+max\left(-q_{ij}+m_{ij}^{n},0\right)\right]c_j^n+S_i^n=0 \quad ,i = 1,2,\dots,N_p \tag{2-25}$$

where $G_{d,ij}^{n}$ is the diffusive conductance of conduit ij, and can be found using Eq. (2-23) from conductance of each element. For example, the diffusive conductance of a cylindrical throat ij can be found as follows [45]:

$$g_{ij}^{d}=D_{ij}^{n}\left(\frac{\pi d_{ij}^{2}}{4l_{ij}}\right) \tag{2-26}$$

where D_{ij}^{n} is the diffusion coefficient of species n at throat ij. m_{ij}^{n} in Eq. (2-25) is the migration rate of species n, and can be defined as follows:

$$m_{ij}^{n}=G_{m,ij}^{n}(\phi_i-\phi_j) \tag{2-27}$$

where ϕ_i is the electrolyte potential in pore i. $G_{m,ij}^{n}$ is the migrative conductance of conduit ij, and can be found using Eq. (2-23) from conductance of each element. The migrative conductance of throat ij is defined as follows:

$$g_{m,ij}^{\mathrm{n}}=\frac{z^{\mathrm{n}}F}{RT}g_{d,ij}^{\mathrm{n}} \tag{2-28}$$

Eq. (2-25) is applied for all the species in the electrolyte except the supporting ion, which can be found based on electroneutrality ($\sum_n z_i^n c_i^n=0$). The last term S_i^n is the reaction term and can be defined from Butler-Volmer kinetics using Faraday's law.

Charge conservation equation assuming electroneutrality in the electrolyte is as follows:

$$\sum_{j=1}^{N_i}G_{cond,ij}^{ionic}\left(\phi_i-\phi_j\right)=-F\sum_{n}^{nc}z^n\left[\sum_{j=1}^{N_{th}}G_{ij}^{n,diff}\,c_i^n-\sum_{j=1}^{N_{th}}G_{ij}^{n,diff}c_j^n\right]+I_{BV} \tag{2-29}$$

where $G_{cond,ij}^{ionic}$ is the ionic conductance of conduit ij and can be defined from Eq (2-23). Ionic conductance of pore element i with cross sectional area of A_i is defined as follows:

$$g_{ionic,i}^{electrolyte} = \frac{F^2}{RT}\left(\frac{A_i}{l_i}\right)\sum_k (z_i^n)^2 \; D_i^n c_i^n \tag{2-30}$$

I_{BV} can be defined from Butler-Volmer equation. For example, assuming a homogeneous simple one species reactant, current at pore i can be defined as follows [2]:

$$I_{BV} = A_{i_{rxn}} i_{0_{ref}} (c_i/c_{ref})[\exp\left(\frac{\alpha_a F \eta_i}{RT}\right) - \exp\left(-\frac{\alpha_c F \eta_i}{RT}\right)] \tag{2-31}$$

where $A_{i_{rxn}}$ is the reaction surface area of pore i and $i_{o_{ref}}$ is the exchange current density. η_i is the overpotential at pore i defined as:

$$\eta_i = \phi_s \; - \phi_i \; - OCV \tag{2-32}$$

where ϕ_s is the solid potential, and OCV denotes the open-circuit voltage. Charge transport equations for solid phase can be defined in PNM framework as studied by Khan *et al.* [27]. However, in this thesis the phase of interest for PNM was void space and the potential variation in matrix phase was assumed to be negligible due to a high conductivity in matrix phase [2], [28]. The system of charge and mass transport can be solved in an iterative scheme given the boundary condition and an initial guess for the unknown values. An iterative scheme the so-called Gummel iteration for transient solution of the equations was explained in details by Agnaou *et al.* [45]. At each Gummel iteration, the charge conservation equation and mass transport equations for each species are solved. The Gummel iterations continue until the difference between the unknown values for two successive iterations becomes smaller than a predefined tolerance. To ensure the convergence stability an under-relaxation method can be applied on the solution variables. In the existence of non-linear reaction terms, at each Gummel iteration an iterative method such as Picard iteration can be used to solve each individual mass and charge transport equations with a predefined convergence tolerance or maximum number of iterations [45]. As the focus of this thesis is PNM of porous electrodes, more details on PNM are given in the next section.

2.4.2. PNM details

2.4.2.1. Solving a simple diffusion in PNM

To demonstrate a steady-state solution of mass transport equations in PNM, a simple example of a single species diffusive mass transport for a simple 2D network as shown in Figure 2-5 is provided here. The conservation of mass at each pore i can be defined using Fick's law written as follows:

$$\sum_{j=1}^{N_i} G_{d,ij}\left(c_i - c_j\right) = 0, i = 1,2,\dots,N_P \tag{2-33}$$

Assuming a constant concentration boundary conditions at pores 1 ($c_1 = c_{inlet}$) and 6 ($c_6 = c_{outlet}$), and a linear reaction term $r_i = k_{rxn}c_i$ at pore 4 where k_{rxn} is assumed to be known reaction rate constant, the conservation of mass at each internal pore leads to following equations:

For pore 2:

$$G_{d,21}(c_2 - c_1) + G_{d,24}(c_2 - c_4) = 0$$

For pore 3:

$$G_{d,31}(c_3 - c_1) + G_{d,34}(c_3 - c_4) + G_{d,35}(c_3 - c_5) = 0$$

For pore 4:

$$G_{d,42}(c_4 - c_2) + G_{d,43}(c_4 - c_3) + G_{d,46}(c_4 - c_6) + k_{rxn}c_4 = 0$$

For pore 5:

$$G_{d,53}(c_5 - c_3) + G_{d,56}(c_5 - c_6) = 0$$

The system of linear equations can be rearranged into a matrix form as $AX = b$, where X is the vector of unknown variables (here the concentration of species at each pore), A includes the information on conduit conductance values and b includes information on boundary conditions. The coefficient matrix for mass transport equations above is shown in Table 2-1. The unknown vector X can then be found by solving the linear system using linear algebra methods. However, for more complex physics and large samples, sparse matrix solvers are commonly used to reduce the computational cost of the solver method. The solution of the system of equations gives the concentration values the at each pore. The concentration values at each throat can be defined as a weighted average of its connecting pores. The concentration distribution for arbitrary values of $c_{inlet} = 200, c_{outlet} = 100, k_{rxn} = 10^{-9}$ used in the boundary conditions is shown in Figure 2-6 a.

Table 2-1 Coefficient matrix for mass transport equations for PNM in Figure 2-5.

c_1	c_2	c_3	c_4	c_5	c_6	b
1	0	0	0	0	0	c_{inlet}
$-G_{d,21}$	$G_{d,21} + G_{d,24}$	0	$-G_{d,24}$	0	0	0
$-G_{d,31}$	0	$G_{d,31} + G_{d,34}$	$-G_{d,34}$	0	0	0
0	$-G_{d,42}$	$-G_{d,43}$	$G_{d,42} + G_{d,43} + G_{d,46} + k_{rxn}$	0	$-G_{d,46}$	0
0	0	$-G_{d,53}$	0	$G_{d,53} + G_{d,56}$	$-G_{d,56}$	0
0	0	0	0	0	1	c_{outlet}

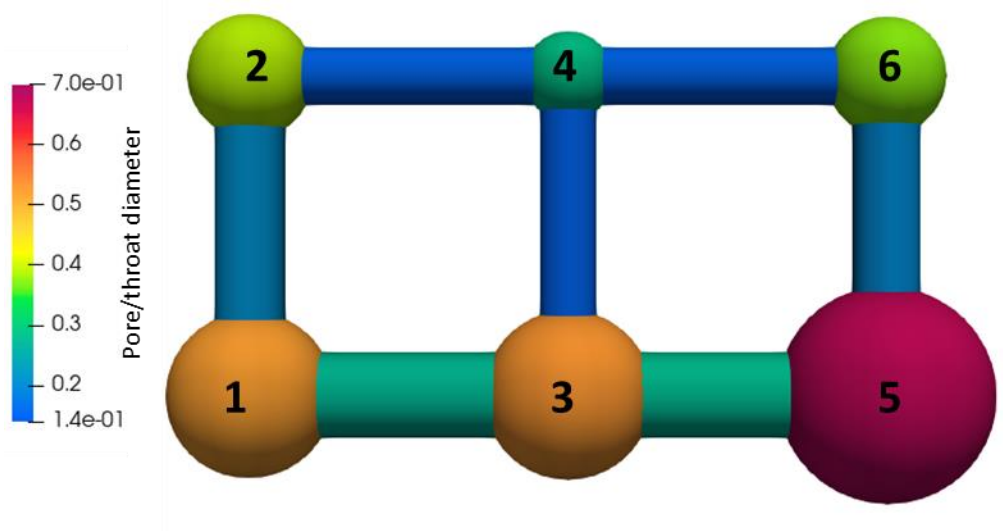

Figure 2-5 A schematic of a random cubic pore network in 2D.

Note that the source/sink term was assumed to be a simple linear reaction term. To include a non-linear reaction term in the system of equations, the source term needs to be linearized first. Assuming a non-linear

reaction source term $S = f(c_i)$, and initial guess of c_i as c_i^*, following formula studied by Patankar [47] can be used to linearize the function:

$$S = (S')^* x_i + (S^* - (S')^* x_i^*) = S_1 x_i + S_2 \tag{2-34}$$

where $(S')^*$ and $(S)^*$ denote the values of first derivative of the source term and the original source term at concentration of c_i^*. For example, in a simple power law reaction source term defined as $r_i = k_{rxn} c_i^n$ with a given order of n, Eq. (2-34) can be used to linearize the reactive term as follows:

$$r_i = S_1 c_i + S_2 = k_{rxn}(n-1) c_i^{*n} \times c_i + k_{rxn}(1-n) c_i^{*n} \tag{2-35}$$

S_1 and S_2 include c_i^* , which is the initial guess or the solution from previous iteration. Assuming a power law of order 2 for reaction term in pore 4, the linearized form of the reaction term will be as follows:

$$S = (2k c_4^*) c_4 - k(c_4^*)^2 = S_1 c_4 + S_2 \tag{2-36}$$

The matrix will be rearranged as shown in Table 2-2. The concentration distribution for arbitrary values of $c_{inlet} = 200, c_{outlet} = 100, k_{rxn} = 10^{-9}$ used in the boundary conditions is shown in Figure 2-6 b. Comparing Figure 2-6 a and Figure 2-6 b it can be seen that using the power law reaction term resulted in a lower value of species concentration at pore 4. This is because the power law reaction rate was higher than the linear reaction rate ($c_i > 1$), resulting in more consumption of species, thereby reducing the concentration of species by a larger amount.

Note that in electrochemical modeling, the non-linear reaction term is generally in the form of Butler-Volmer equation, which is a function of both concentration and potential. Therefore, the solution of coupled mass and charge transport equations is found using iterative algorithms, such as Gummel iteration explained the previous section [45]. More details on the iterative process are provided in chapter 3 and chapter 4.

Table 2-2 Coefficient matrix for mass transport equation including reaction term from Eq.(2-36)

c_1	c_2	c_3	c_4	c_5	c_6	b
1	0	0	0	0	0	c_{inlet}
$-G_{d,21}$	$G_{d,21} + G_{d,24}$	0	$-G_{d,24}$	0	0	0
$-G_{d,31}$	0	$G_{d,31} + G_{d,34}$	$-G_{d,34}$	0	0	0
0	$-G_{d,42}$	$-G_{d,43}$	$G_{d,42} + G_{d,43} + G_{d,46} + S_1$	0	$-G_{d,46}$	$-S_2$
0	0	$-G_{d,53}$	0	$G_{d,53} + G_{d,56}$	$-G_{d,56}$	0
0	0	0	0	0	1	c_{outlet}

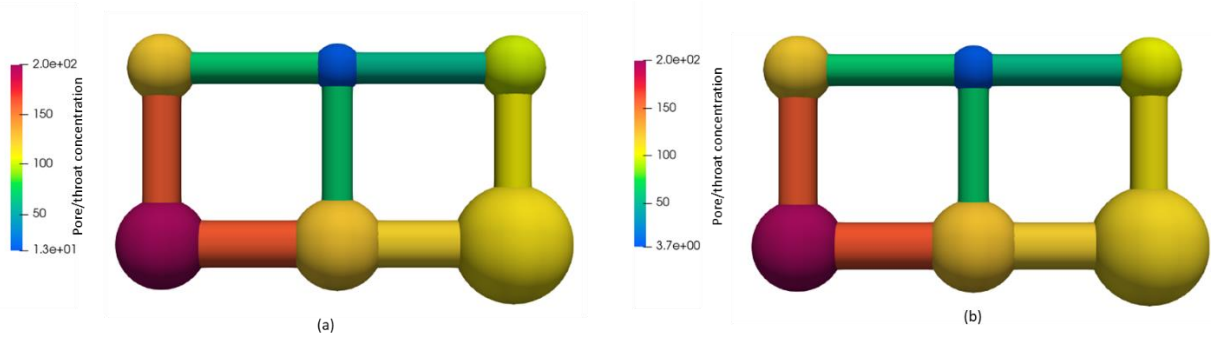

Figure 2-6 Solution of mass transport in the pore network model of Figure 2-5. a) Concentration distribution when reaction term is defined as $r = k_{rxn}c$. b) Concentration distribution when reaction term is defined as $r = k_{rxn}c^2$

2.4.2.2. Predicting conduit conductance

As explained in section 2.4.1, the accuracy of conduit conductance values affects the accuracy of PNM result [34], [35]. Hydraulic conductance estimation using Hagen-Poiseuille equation (Eq. (2-24)) was developed for fluid flow in cylindrical elements. However, in extracted networks original pore regions from the porous medium image have irregular shapes and cylindrical pore and throat elements are not the best representative of the real geometry's conductance. For example, Khan *et al.* [27] showed that the use of

truncated pyramids in PNM of Li-ion cathodes provides a better representation of the void space geometry and transmissibility. To calculate the conductance of non-cylindrical elements, the geometrical parameters in the conductance of each element can be lumped into a size factor (λ_i) parameter [48]. Based on this definition, the hydraulic conductance of each element i can then be defined as follows:

$$g_{h,i}^{p} = \frac{\lambda_i^{hyd}}{\mu_i} \tag{2-37}$$

where λ_i^{hyd} is found assuming a diverging or converging element with a varying cross-section. Assuming an element with varying cross-section, integrating over the pressure drop equation given in [48] with assumption of negligible inertial loss, the pressure drop equation becomes as follows [48]:

$$\frac{\Delta p}{Q} = 16\pi^2 \mu \int \frac{I_p^*}{A(x)^2} dx \tag{2-38}$$

where Q is the volumetric flow rare, I_p^* is the specific polar moment of inertia and A(x) is the cross-sectional area of the element. Based on the definition of hydraulic conductance, the ratio of flow rate to the pressure drop, hydraulic conductance of the element from Eq. (2-38) is as follows:

$$g_{h,i}^{p} = \frac{1}{16\pi^2 \mu_i \int_{l_i} \frac{I_p^*}{(A_i(x))^2} dx} \tag{2-39}$$

Comparing Eq. (2-39) with Eq. (2-37), the hydraulic size factor for element i is calculated as follows:

$$\lambda_i^{hyd} = \frac{1}{16\pi^2 \int_{l_i} \frac{I_p^*}{(A_i(x))^2} dx} \tag{2-40}$$

Assuming a pyramid pore element i in the network as schematically shown in Figure 2-7, λ_i^{hyd} will be:

$$\lambda_i^{hyd} = \frac{1}{\frac{8}{9}\pi^2 l_i \frac{d_i^2 + d_i d_{ij} + d_{ij}^2}{\left(d_i d_{ij}\right)^3}} \tag{2-41}$$

where d_i and d_{ij} are the diameter of pore i and throat ij.

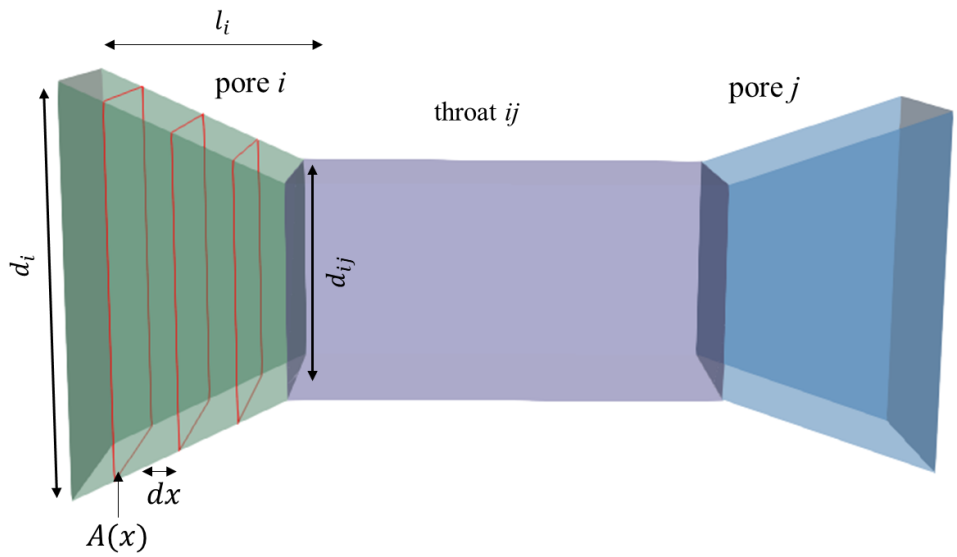

Figure 2-7 A schematic of a pyramid and cuboid pore and throat as a conduit element.

Similar to the hydraulic size factor, to calculate the diffusive conductance of non-cylindrical elements, the geometrical parameters of each element can be lumped into a diffusive size factor ($\lambda_{\mathrm{i}}^{diff}$) parameter [48]. Based on this definition, the diffusive conductance of each element i can then be defined as follows:

$$g_{diff,i}^{p} = \lambda_i^{diff} D_i \tag{2-42}$$

Assuming an element with varying cross-section, the diffusive mass flow rate through the element can be defined using Fick's law:

$$m_{diff} = -D\, A(x)\, \frac{dc}{dx} \tag{2-43}$$

Integrating the Eq. (2-43) over the length of the element i gives the following equation:

$$\frac{\Delta c}{m_{diff}} = \frac{1}{D} \int \frac{1}{A(x)} dx \tag{2-44}$$

From the definition of diffusive conductance, the ratio of diffusive mass flow rate to the concentration drop, the diffusive conductance for element i can be defined as follows:

$$g_{diff,i}^{p} = \frac{D_i}{\int_{l_i} \frac{1}{A_i(x)} dx} \tag{2-45}$$

Comparing Eq. (2-45) and Eq. (2-42), the diffusive size factor for element i is calculated as follows:

$$\lambda_i^{diff} = 1 / \int_{l_i} \frac{1}{A_i(x)} dx \tag{2-46}$$

Assuming a pyramid pore element i in the network (Figure 2-7), λ_i^{diff} will be:

$$\lambda_{(i\,|\,k)}^{diff} = \frac{1}{\frac{l_i}{d_i d_{ij}}} \tag{2-47}$$

Using the abovementioned size factors can provide a more accurate estimation of conductance of non-cylindrical elements in contrast to Hagen-Poiseuille equation or classic shape factor correlations [34], because the method includes arbitrary cross-sectional shapes as well as the gradual variation of cross-section in calculation of conductance [48]. However, estimating the conductance of conduits from the real image of conduit is the most accurate estimation [35]. Such estimation using DNS methods can be computationally expensive. In this thesis, a computationally efficient framework based on deep learning was developed to find conductance values from real images. More details are provided in chapter 5.

2.4.2.3. Predicting permeability in PNM

Permeability of a porous medium is an intrinsic parameter that indicates how easily fluid can flow through the medium. Permeability of porous electrodes is a characteristic of the electrodes and can be used as a validation parameter for comparing the accuracy of a PNM with experimental values or DNS methods. In fibrous electrodes such as VRFB electrodes, the permeability along the direction of alignment (x or y) the so-called in-plane permeability is commonly higher than the permeability perpendicular to the alignment (z) the so-called through-plane permeability. To find the permeability of a porous electrode using PNM, a flow algorithm can be applied with a constant pressure difference boundary condition or constant flow rate at the inlet/outlet of the flow direction. Once the pressure and flow rate values are found from the solution of the algorithm, the permeability (K) can be calculated using Darcy's law as follows:

$$K = -\frac{Q}{A}\frac{\mu}{\nabla P} \tag{2-48}$$

where Q is the volumetric flow rate at the inlet/outlet, A is the cross-sectional area of the porous domain at the inlet/outlet, and ∇P is the pressure gradient along the direction of flow.

2.4.2.4. Network extraction method

PNM's network and geometrical models can be categorized into two main categories: generated and extracted networks. Examples of a generated cubic network and an extracted network are shown in Figure 2-8. In generated networks, the network connections and geometry are generated using standard networks such as Cubic lattice, Delaunay, and Voronoi [49]. Geometrical data such as pores and throat sizes are assigned to the network elements to represent an arbitrary or real material's pore size distribution. Although standard Cubic lattice networks do not capture the real connectivity of the void space, they can be used as a good approximation of the porous medium when the porous sample's image is not available [2] or when the purpose of the study is to analyze phenomena at pore-scale [46], to test a PNM framework [45] or to reduce the complexity of the pore-scale study in multiphase or multi-physics problems [23]. In contrast to cubic lattice networks, generated networks based on Delaunay tessellations can be used as a better representative of porous domain for example fibrous materials. In a study by Gostick [50] on modeling a fibrous gas diffusion layer it was shown that a generated network based on Delaunay tessellations for void space and Voronoi tessellations for fibrous solid space was in good agreement with properties of available materials. However, to better capture the void space in porous samples based on real image data, extracted networks are advantageous as they directly map the void space into a connected network of pores and throats, thereby preserving the connectivity, topology and geometrical properties of pore regions [51]. Such networks are also advantageous in structural-performance analysis studies. For example, the species distribution can be used to find starved regions in a structure and use the pore-scale information for designing a better performing structure.

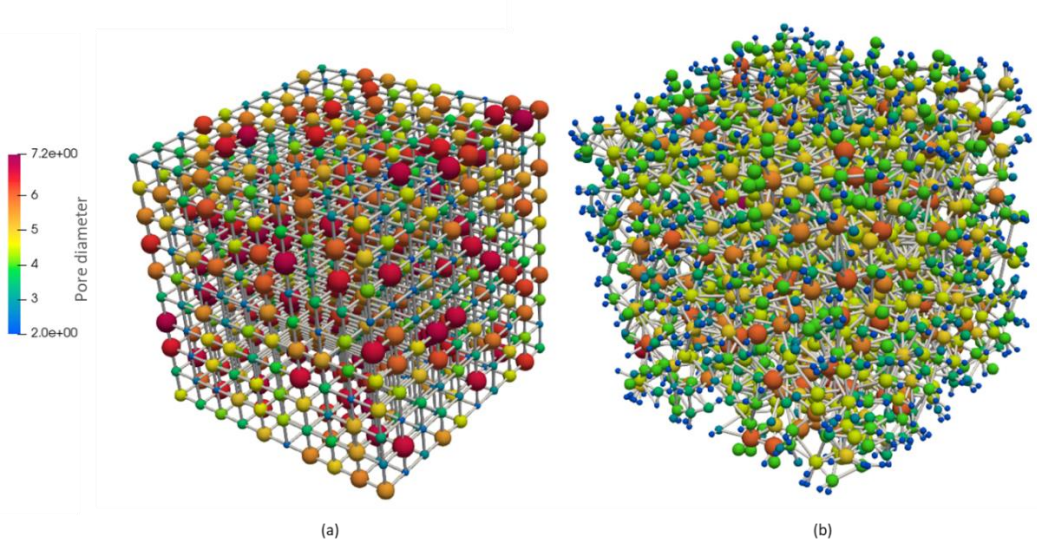

Figure 2-8 Examples of pore networks. a) A generated cubic network b) An extracted network

Extracted networks are created using pore network extraction methods, which utilize various image processing techniques on a volumetric image of the medium to map the void space into their corresponding network [51]. Different approaches have been developed for pore network extraction including the maximal ball, medial axis skeleton, and watershed segmentation [51]–[53]. In this thesis, a modified watershed-based approach presented by Gostick [51] was used. The algorithm in the study be Gostick [51] was originally developed for extracting a sub-network of the over-segmented watershed (SNOW) in high porosity materials. The general steps for extracting the pore network of a porous medium using SNOW algorithm are illustrated in Figure 2-9. For a given binary image of a porous medium (Figure 2-9a), first a distance transform map is created by replacing each void pixel with their distance value from nearby solid. Distance map creates cloud-like shapes that are denser in the centers shown as peaks of the distance transform (Figure 2-9b). Applying a maximum filter on distance map locates the distance peaks as centers of pore regions (Figure 2-9c). An algorithm to find and remove spurious peaks is then applied to prevent over segmentation [51]. The resulting peaks are then used as markers for finding the basins of the distance map and segmenting the pore regions in a marker-based watershed segmentation algorithm (Figure 2-9d). The network model is then extracted from the segmented image, in which each region corresponds to a pore and their connecting faces/channels are considered as throats (Figure 2-9e) [51], [54].

In a pore network model, the real geometry of segmented regions are mapped to a simplified geometry as shown Figure 2-9. Such simplification can reduce the accuracy of PNM, as the transport conductance values for each element are approximated over simplified shapes instead of the real geometry. To enhance the accuracy of PNM the conductance values can be estimated using DNS methods on the real image of pore to pore regions. However, applying DNS on each region is computationally expensive. To address this problem, the last objective of this thesis is focused on utilizing an image-based deep learning method to develop a framework for efficient estimation of conduit diffusive conductance values. A background and theoretical concepts related to deep learning are explained in the next section.

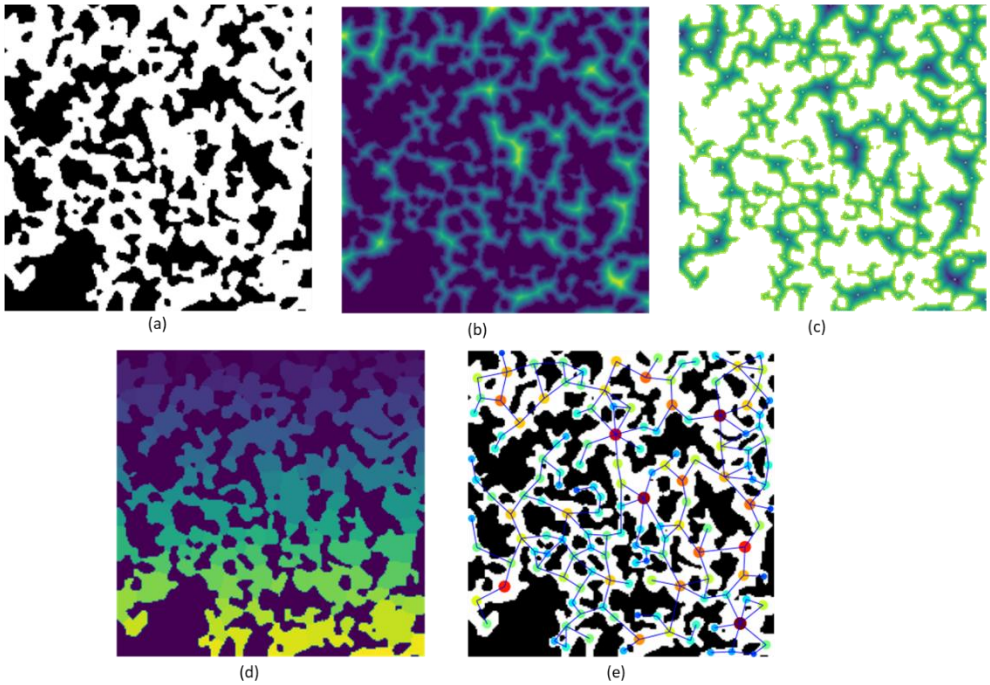

Figure 2-9 Illustration of the main steps in SNOW algorithm for a 2D randomly generated porous medium. a) The binary image of a randomly generated porous medium b) Distance map of the void space c) Peak points for watershed basins are shown as white dots within the distance map d) Segmented regions based on the watershed method e) The extracted network mapped on the binary image.

2.5. Introduction to deep learning

In this section a brief introduction to machine learning and deep learning concepts is provided. However, more details on the deep learning model in this study are provided in chapter 5.

2.5.1. Machine learning and deep learning

A machine learning (ML) algorithm is an algorithm that can learn from data [55] and define the best function that describes the relationships between features of the data [56]. A frequently quoted explanation of the learning process is the definition by Mitchell [57]: "A computer program is said to learn from experience E with respect to some class of tasks T and performance measure P , if its performance at tasks in T , as measured by P , improves with experience E ." A brief explanation and examples for each of these elements Task, Performance, and Experience are provided as follows [55].

Task T: A task indicates how the machine learning algorithm is processing an example. An example is defined as a collection of features and can be represented by a vector notation of $x \in R^n$, where each

element of x_i is a feature. These features are extracted from the data that need to be processed by ML. ML algorithms are capable of solving different tasks, such as regression, classification, anomaly detection, denoising, to name but a few. For example, in a regression task, the ML algorithm goal is to output a function $f: R^n \rightarrow R$ that can be used to predict a value [55].

Performance measure P: Performance measure is defined to evaluate the ability of the ML algorithm. Such measurements are defined specific to a task. For example, in a regression task the performance measure is defined as the accuracy or error rate of the model. Evaluating the performance measure is generally based on a set of data so-called test data that has not been used for training process. This evaluation ensures that the trained model can perform well on unseen data [55].

Experience E: Most frequently, the ML algorithm experiences a dataset to process. Based on the experience that the learning process is having, the learning algorithms can be categorized into supervised and unsupervised learning. In a supervised learning, the ML algorithm experiences a dataset of features where each example x has a label or target y. The ML algorithm can then be used to study and learn such dataset to predict y from x generally by estimating $p(y|x)$ (e.g. classification task). In an unsupervised learning, the ML algorithm experiences a dataset of features x and tries to learn the probability distribution $p(x)$ or properties of the distribution in a dataset (e.g. clustering task) [55].

In conventional ML methods a difficult step is to select the features that are important for the measurement. The process of feature selection requires expertise, statistical analysis, and sometimes repeated experiments on the data to find the best features [56]. Hand-engineering the features becomes more complicated when working with large data or complex high dimensional data, such as images. This problem is tackled by introducing deep learning methods. Deep learning is a sub-division of machine learning where deep neural networks are used as the basis of learning models [56]. In the last 10 years, deep learning methods have been rapidly developed mainly due to advances in computational resources and availability of "big data". Deep learning methods are advantageous over conventional machine learning methods in terms of feature extraction, as deep learning methods learn the useful features automatically from the raw data [56]. Additionally, deep learning methods have the capability to learn complex nonlinear functionality between input and output. Such advantages in deep learning are mainly due to the fact that the basis of its learning functions are deep neural network structures. A general overview of concepts and building blocks of deep learning models are explained in the next section.

2.5.2. Deep neural networks

As introduced in the previous section, the basic elements of deep learning approach are deep neural network models. A neural network model is a computational model that mimics the behaviour of the human brain [56] and includes three main component of input layer, hidden layer(s), and output layer. Deep learning networks are neural networks that have a large number of hidden layers (at least two) [56], hence the name "Deep" learning [56]. The basic elements in construction of deep neural networks are neural layers. Among different neural layers most common ones are fully connected layers and convolutional layers [58], as shown schematically in Figure 2-10. The fundamental differences between these two types of layers are their input/output structure and their mapping process. In a fully connected layer each unit is connected to all units of the previous layer whereas in a convolutional layer, each unit is connected to part of the units from previous layer [58]. Therefore, a fully connected layer does not have any assumption on the structure of the input whereas in a convolutional layer it is assumed that spatially close regions are semantically related. This assumption in convolutional layer is a significant advantage in processing image/video data. More details on convolutional layers will be provided in section 2.5.2.2. A deep learning model can be made by any combination of different layers, such as convolutional layer and fully connected layer. As a result, two common types of deep networks are feedforward networks and convolutional networks. A brief explanation of these two networks are provided in the next sections.

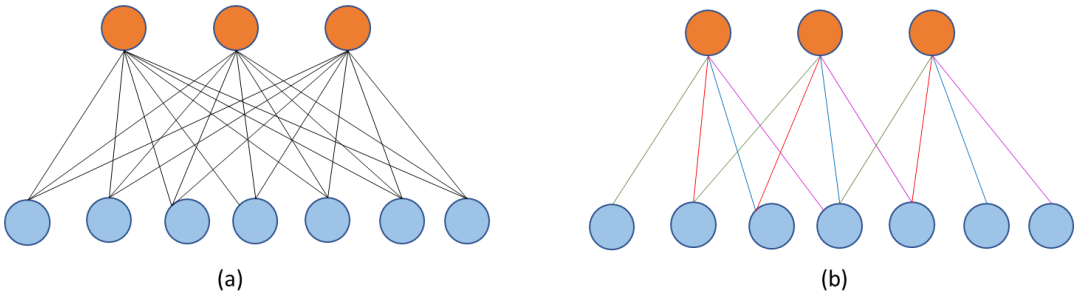

Figure 2-10 A schematic of two common types of neural layers. a) A fully connected layer b) A convolutional layer

2.5.2.1. Feed forward networks

A schematic of a simple feed forward neural network is shown in Figure 2-11, where neurons and their connections are shown as circles and arrows, respectively. The final goal of a feed forward network is to approximate a function F^*. [55]. The flow of information through a feedforward network can be defined using a chain rule as follows [59]:

$$F(x) = f_N(f_{N-1}\left(\dots\left(f_1(x)\right)\right)) \tag{2-49}$$

where N is the number of hidden layer, f_i is the function in layer i. In the forward pass, each neuron in a layer maps the input to output in a two step. First, the neuron calculates a weighted sum of the input values. Then, the calculated value is mapped through a mapping function (usually called activation function) to produce the output of the neuron. A simple example of an arbitrary neuron in a feed forward network is shown in Figure 2-12, where input vectors is represented as $x = [x_1, \dots, x_n]$, and weights of each connection is represented as $[w_1, \dots, w_n]$. First, the weighted sum of input values is calculated as follows:

$$z = \sum_{i=1}^{n} x_i w_i \tag{2-50}$$

To map the calculated value to the output value a non-linear activation functions ($f(.)$) can be applied on z, such as logistic $f(z) = 1/(1 + \exp(-z))$, hyperbolic tangent ($f(z) = (\exp(z) - \exp(-z))/(\exp(z) + \exp(-z))$, and rectifier function $f(z) = \max(0, z)$ [55]. Rectifier functions are commonly used and the neurons that use a rectifier activation function are commonly called rectified linear units (ReLUs).

Each of the connections between neurons contain a weight and training the network is essentially repeatedly updating the weights based on the network's error to find the optimum set of weights that can best model the patterns in data [56], thereby finding the F(x) that matches $F^*(x)$ [55]. A commonly used algorithm for training neural networks is the gradient descent algorithm [56]. In training a deep neural network, the gradient decent algorithm is used along with the backpropagation algorithm, where the gradient of an objective function with respect to weights of the network are found using the chain rule for derivatives in the backward direction. In this iterative algorithm based on the gradient of the error the weights are adjusted until the objective function is minimized [60].

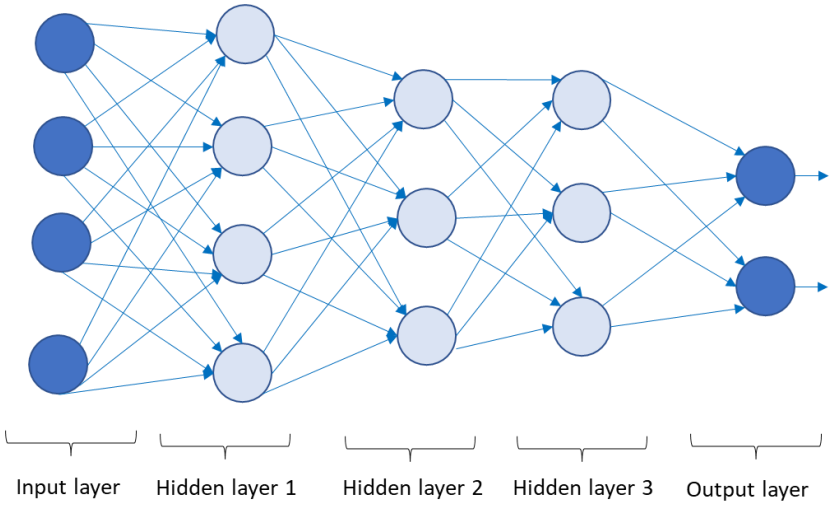

Figure 2-11 A schematic of a simple feed forward network

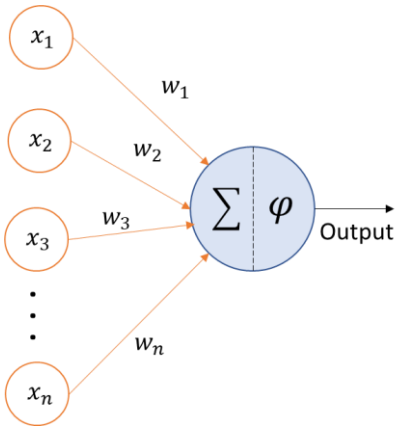

Figure 2-12 A schematic of a neuron in a feed forward network

2.5.2.2. Convolutional networks

Convolutional neural networks (CNNs) were developed for processing high dimensional data, such as images and texts [60]. The basic idea of CNNs is to extract local features using the early layers and combine the features into higher order information in the later layers [56]. The idea of local features and convolution was originated based on neuroscience concepts. For processing the inputs of the brain, neurons have a specific "field of view", the so-called local receptive field. As an example, when a person is touching something, this local receptive field is a small patch on their skin or when they look at a specific object the

local receptive field is defined as a part of their visual field [61]. The convolutional structure is based on a similar concept, where the local receptive field in an image is a local patch of voxels. In a convolutional layer within a CNN, the convolution is performed using different filters or kernels. Each convolutional kernel transforms a patch of grids in the input to one grid, where the size of the patch depends on the size of the kernel. A collection of these convolutional kernels then creates a convolutional layer.

In a convolutional layer i, the function f_i includes varieties of convolutional kernels $(g^1, \dots, g^{k-1}, g^k)$, where g^k is a linear function in the kth kernel. Assuming an input image I, g^k can be defined as follows [59]:

$$g^k(x,y) = \sum_{u=-m}^{m} \sum_{v=-n}^{n} \sum_{w=-d}^{d} W_k(u,v,w) I(x-u, y-v, z-w) \qquad (2\text{-}51)$$

where x, y, z are the location of the pixel in the image, $\mathrm{W_k}$ w is the weight of kth kernel, and $m, n,$ and w are the height, width and depth of the filter. A schematic of a convolutional layer followed by common layers in processing its output is shown in Figure 2-13. In each step of implementing the kernel on data, the nonlinear transformation of data has learnable weights. As too many learnable weights can be computationally expensive, they can be replaced by a fixed nonlinear transformation. A common non-linear transformation method is maxpooling, where in a maxpooling layer the maximum value of the input in the receptor fields is passed on as the output. A pooling layer reduces the size of the output, thereby providing a less computational cost for training process. A simple convolutional neural network can then be made by a stack of different types of layers, such as convolutional, activation, and pooling layers followed by fully connected prediction layers. Some examples of convolutional structures are LeNet, AlexNet, and Resnet models [62]. As in this thesis a residual network Resnet model was used, a brief explanation of the residual learning concept is provided in the next section. More details on the model are given in Chapter 5.

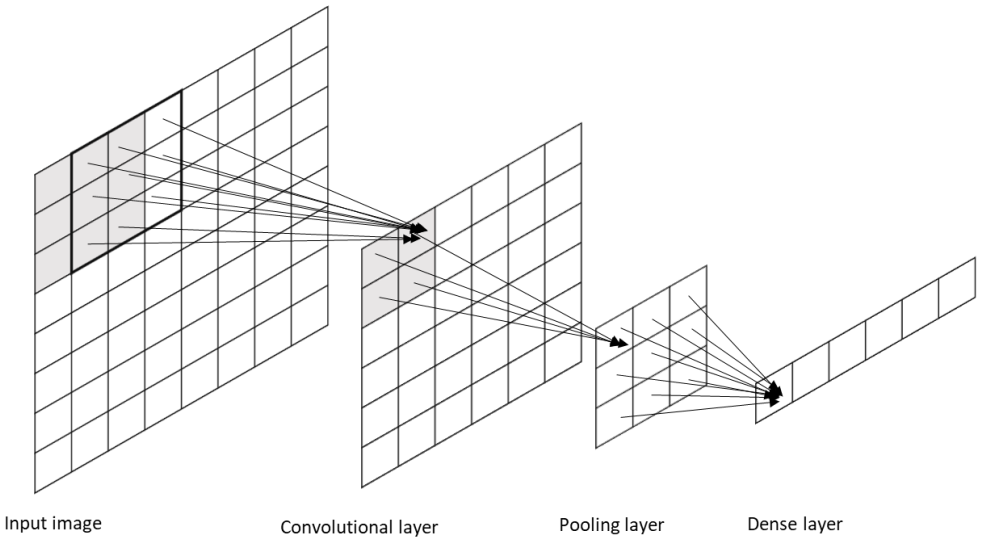

Figure 2-13 A schematic of a convolutional layer followed by a downsampling pooling layer and a dense layer

2.5.3. Residual networks

The basic idea for the development of residual networks was addressing a problem of signal strength reduction as it proceeds through deeper layers. In other words, a deeper network showed a higher training error in contrast to a shallow model. To prevent this issue, the idea of residual learning was introduced [63]. Assuming an input x and $\mathcal{H}(x)$ as the mapping that needs to be fit through a number of stacked layers, the idea of a residual learning is to let the stacked layers approximate a residual function $\mathcal{F}(x) = \mathcal{H}(x) - x$ instead of $\mathcal{H}(x)$. With this definition the mapping function is changed to $\mathcal{F}(x) + x$ [63]. This formulation can be added to neural networks by introducing bypass connections that skip a stack of layers. A schematic of a residual block is shown in Figure 2-14. As shown in Figure 2-14 a bypass connection provides the network with the opportunity to copy the activations from one residual block to the next, thereby parts of the signal can pass through deeper layers without losing its strength. In other words, more information is preserved to pass in deeper layers, which was the basic goal for making the network learn the residuals [62]. Based on the definition of the residual function, the formulation for a residual block shown in Figure 2-14 can be written as follows:

$$y = \mathcal{F}(x, \{W_i\}) + x \tag{2-52}$$

where x and y are inputs and outputs, respectively. $\mathcal{F}(x, \{W_i\})$ is the residual mapping function that needs to be learned. For example, in the illustrated residual block, $\mathcal{F} = W_2 f_{act}(W_1 x)$ where f_{act} is a rectifier activation function. $\mathcal{F} + x$ is implemented by a bypass connection and an addition operator. Bypass

connections are applicable to both fully connected layers and convolutional layers. In the fully connected layers the addition operator applies an element-wise addition, whereas in a convolutional layer the addition is applied on two feature maps in terms of channel by channel [63]. The residual learning enabled the residual deep learning models to have a large number of layers (e.g. 100) while reducing their training error in contrast to conventional deep learning models.

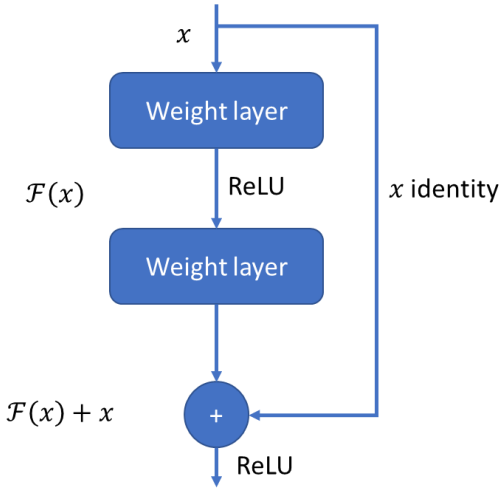

Figure 2-14 A schematic of a residual block

Chapter 3: The role of triple phase boundary and structure-performance relationship in Zn-air cathodes

3.1. Overview

Zinc-air flow batteries are a promising energy storage technology. Their performance depends on their porous cathodes where the oxygen reduction reaction (ORR) occurs. A key feature of the cathode is the invasion of electrolyte, creating the so-called triple phase boundary between air, electrolyte and catalyst, which is shown in this work to be an overly simplified picture. In this study a mathematical framework based on pore network modeling (PNM) was developed to better understand the interplay between electrode structure, transport of species and electrolyte invasion. The results suggest that increasing electrolyte volume provides highly branched invasion pattern and enhances performance up to a saturation of 0.7, whereas further invasion reduces air-liquid interfacial area and lowers the performance. Interestingly, at lower saturations (<0.3) the liquid structure is so excessively branched that hydroxide ions are unable to diffuse to the anode at a sufficient rate, resulting in supersaturation, which is a degradation problem. The pore size distribution of the catalyst layer also affects the performance with wider pore size distributions generally performing better. This work represents the first 3D PNM of a zinc-air cathode that includes all the key physics and transport mechanisms, enabling prediction of the structure-performance relationship of porous cathodes.

3.2. Introduction

Recent advances in energy storage technologies have focused on developing cost-effective large-scale batteries that can be installed anywhere and provide a large window for power and energy capacity. Metal-air flow batteries are a promising option as they are rechargeable and because they separate power and energy making them easily scalable. A main benefit of these batteries is the use of oxygen in air as the oxidant, which eliminates the need for a positive electrolyte, thereby significantly increasing the energy density of the system. Amongst different metal anodes, zinc is particularly appealing since it's cheap, abundant, and safe [37]. Despite the promise of Zn-air flow battery technology [64]–[66], they still need to be optimized to provide better performance and longer cycle-life. The properties of the porous air electrodes have a large impact on the performance since they must successfully support all the key modes of transport phenomena including invasion of electrolyte, oxygen reduction reaction (ORR), diffusion of ionic species, and conduction of electrons. The operation of the air electrode is based on the triple-phase boundary (TPB), which significantly complicates the situation [67].

To improve the performance and durability of Zn-air electrodes, it is necessary to understand the mechanisms of oxygen transport and ORR within the electrode's catalyst layer (CL), and specifically the role of the TPB. This region is thus named because reactions are envisioned to occur at the solid-gas-liquid interface where the three phases meet. The TPB is formed when liquid electrolyte from the anode penetrates partially into the cathode pore structure. The uninvaded pores remain filled with air and provide diffusion pathways for oxygen to the reactive sites. The solid walls of the pores are formed by the electrode material, which transfers electrons and provide the electrocatalytic surfaces for reactions [32]. The concept of TPB has been studied thoroughly in the context of solid oxide fuel cells (SOFC) [32], [68]–[71]; however, some details of TPB in SOFCs differs from that of Zn-air electrodes. Firstly, oxygen is insoluble in the ceramic electrolyte of SOFCs so the reaction truly takes place directly on TPB contacting the solid electrolyte. In a Zn-air cell, by contrast, the oxygen can dissolve into the electrolyte to react on the catalytic surface at the solid-liquid interface [31], [72]. Secondly, the TPB in an SOFCs is formed by the mixture of catalyst particles (i.e. Ni), electrolyte particles (i.e. yttria-stabilized zirconia), and a network of voids. This forms a classic percolation problem since some of the electrolyte particles may be disconnected from the membrane due to the random mixing. In a Zn-air cell, the TBP is created when electrolyte flows into the cathode via invasion percolation, meaning that all of the electrolyte is physically connected to the anode. Invasion percolation is a variation of percolation theory that can describe the process of fluid displacements in a porous medium at constant flow rate [73]. Moreover, the liquid distribution within the porous electrode can change with time as a result of various factors, such as changes in the void volumes.

The impact of pore-scale phenomena in Zn-air electrodes has not been thoroughly studied, and a deeper understanding of the multiphase behavior at the TPB is needed. The depth to which the electrolyte penetrates into the CL will impact the performance, but there is clearly an optimum. Insufficient electrolyte invasion will create very little TPB, while excessive invasion will destroy any existing TPB. The location of the optimum saturation will depend on the pore size distribution, spatial correlations, wettability, particle shape, anisotropy, and other structural factors [31], [74]. The effect of the electrolyte saturation on the performance of an air electrode invaded by phosphoric acid was experimentally studied by Mori *et al*. [75],who observed that saturation values higher than 0.8 reduced the performance of the electrode. However, the details of TPB was not studied in that work, yet understanding the pore scale processes is essential to designing electrodes with stable and optimum TPB distribution [31]. Gourdin *et al*. [76] used experimental results of polarization curves to study the performance behavior of $K-O_2$cathodes at different electrolyte volume. Although their result provided insights on the electrolyte saturation and surface area provided by TPB using Electrochemical Impedance Spectroscopy, the details of TPB location

in pore-scale, fluid flow invasion pattern and structural properties of the pore space were not studied. Electrolyte invasion within the CL can be well described by invasion percolation. Invasion percolation is a variation of percolation theory [73], [77]. One characteristic of invasion percolation is that the distribution of invading fluid has a self-similar fractal structure [78]–[80]. This fractal behavior is very good for creating large interfacial area between the liquid and gas, so the fluid invasion pattern plays an important role in achieving a large TPB in the cathode of a Zn-air battery. However, such a fractal structure may lead to long and tortuous transport paths for both oxygen and ion transport. It is thus essential to study the invasion pattern of the electrolyte at the pore-scale, and to analyze the structural parameters affecting the patterns such as size distributions of the constrictions in the void space. As liquid-gas interface exists in porous electrodes of Phosphoric acid fuel cells and Alkaline electrolyzer systems, the findings in this study could be generalized to other electrochemical systems applications.

Various mathematical models have been developed to study primary Zn-air batteries [81], [82]. These typically use 1D continuum formulations in the through-plane direction to investigate design parameters or to understand impact of operational conditions. Because they utilize continuum averaging of the porous components, they cannot resolve the transport process at the pore-scale, including the critical impact of the TPB distribution due to structural properties of the porous medium. In the classic work of Mao and White [81] as well as more recent works [83] the air cathode is assumed to be a flat plate with a high surface area to represent the air-water interface. The more recent work of Stamm *et al.* [82] treated the cathode as continuum with a uniform saturation field (between 0 and 1) predicted by assuming a capillary pressure vs saturation. These models require constitutive relationships for the air-electrolyte interfacial area and the effective diffusivities of each phase, which are correlated with the saturation. These correlations are very difficult to measure experimentally [84], [85], and are expected to vary with pore structure. Danner *et al.* [86] used a Lattice Boltzmann method to predict pressure-saturation parameters of bifunctional air electrodes in metal-air batteries, which was later used in continuum-based modeling of Li-air batteries [87]. Despite useful predictions about the precipitation of solid products in Li-air cathodes, their 1D model included the coexisting phases using macroscopic parameters (porosity and pressure) where the details of pore space structure and the variation in fluid-gas interface at pore-scale were ignored. Few models have been developed for Zn-air flow batteries [88], and these are all based on the continuum formulation and so are unable to investigate the impact of the TPB and pore structure on performance.

Clearly, a pore-scale model of the cathode is preferrable for studying the effects electrode pore structure and the TPB. It is possible to develop a so-called direct numerical simulation (DNS) which resolve the grains and voids of the electrode [43], [89]–[92]. These are computationally intensive and it remains a

challenge to incorporate two-phase flow [93]. Pore network modeling (PNM) is an alternative to continuum-based and DNS modeling techniques that offers several pivotal advantages. In PNMs the void space is mapped to a connected network of pores and throats representing the cavities and constrictions in the void space, respectively. Transport through the network occurs via this connected network where the conductance between each pore is based on the geometrical details of the constriction (i.e. diameter and length). This abstraction reduces the number of variables in the transport equations and hence reduces the simulation time enormously [13], [21], [35]. Another advantage of PNMs is that transport parameters such as tortuosity are an output of the model as they arise from the network topology and geometry rather than being supplied as an independently obtained correlation, which can be challenging to measure [27]. Most importantly for the present work, PNM has the ability to model the distribution of electrolyte using invasion percolation (IP) on the network [22], [80], [94]. The resulting fluid distributions more accurately represent the invasion patterns expected in a working electrode [95], [96]. PNMs allow simple coupling between transport and electrolyte invasion by adjusting the conductance of the throat connections according to their invasion status. While PNM has been used in modeling multiphase transport in fuel cells [22], [23], [97], [98], its application to air electrodes in Zn-air batteries has been limited. Zhu *et al*. [33] have presented a 2D PNM that focused on the invasion processes, though the underlying transport in the CL and ORR was not modeled. Their PNM was not geometrically rigorous and limiting the model to 2D significantly changes the fluid patterns. Nonetheless, their results do show the value of considering the TPB at the pore scale. In the present study, a 3D PNM was developed to study the role of TPB in the cathode's CL of a Zn-air battery, including the electrochemical reactions, multiphase transport, and the triple-phase boundary. The objective of this work was to utilize the developed PNM to investigate the effect of pore size distribution and electrolyte invasion pattern on the extent of TPB and the performance of the electrode, assessed by modeling polarization curves. In addition, since KOH precipitation is a known degradation mechanism [99], the effect of liquid phase tortuosity on hydroxide transport was studied and the maximum concentration of hydroxide ions in the electrode was reported for different operating condition. As a case study, the present work focused on the impact of pore size distribution on the polarization behavior of cells, which characterized the electrode performance. To the best of our knowledge this is the first 3D PNM of a Zn-air electrode, and we demonstrate that PNMs are an ideal tool for this application.

3.3. Model development

In this section the equations describing the various transport phenomena occurring in the air cathode's CL and on the TPB region are provided along with the steps to include those phenomena in pore network modeling. First, the pore network structure and geometrical properties of the CL pore network are

explained. Then, numerical equations for pore scale physics and transport algorithms are provided. Finally, the framework to solve the system of equations and obtain the results is presented.

3.3.1. Air cathode medium

To analyze the ORR in the Zn-air flow battery, this study includes only the air cathode half-cell as illustrated in Figure 3-1. The electrode includes a CL, and a gas diffusion layer that is connected to the current collector. To model the cathode compartment with pore-scale resolution while maintaining a reasonable computational cost, the domain was limited to only the porous CL, with the GDL and the membrane treated as boundary conditions. It was found that the gas phase transport was not a significant factor, thus neglecting the transport processes in the gas diffusion layer was justified.

The hydrophobicity of the materials in CL and the pore architecture affects the distribution of the triple phase interface of gas, liquid electrolyte, and solid catalysts as shown in Figure 3-2. The sensitivity of the electrode performance to the electrolyte invasion and the CL structure (pore size distribution) were investigated in this study.

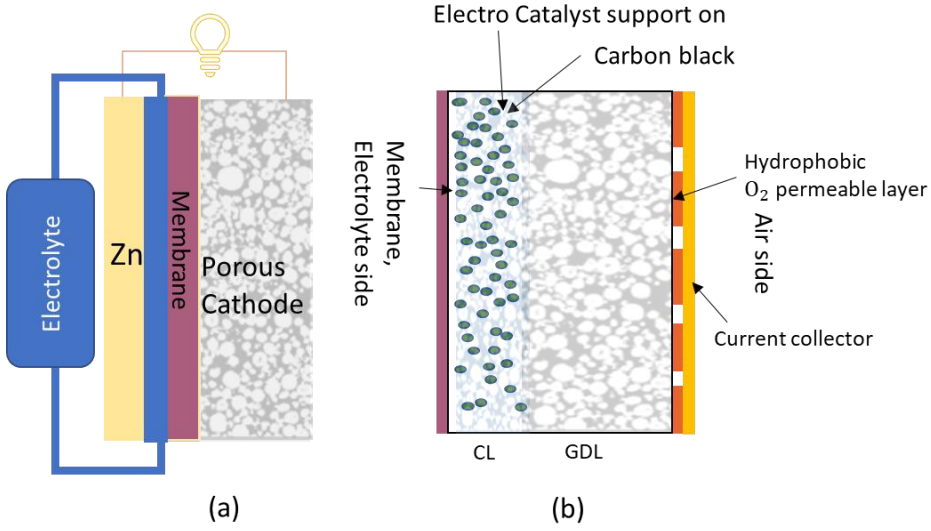

Figure 3-1 A schematic of a Zn-air flow battery. a) The flow battery includes cathode and anode compartments with electrolyte tank. b) The cathode compartment containing CL and GDL as the computational domain and membrane and air inlet as the boundaries. We assume that the electrolyte has invaded the CL from membrane side.

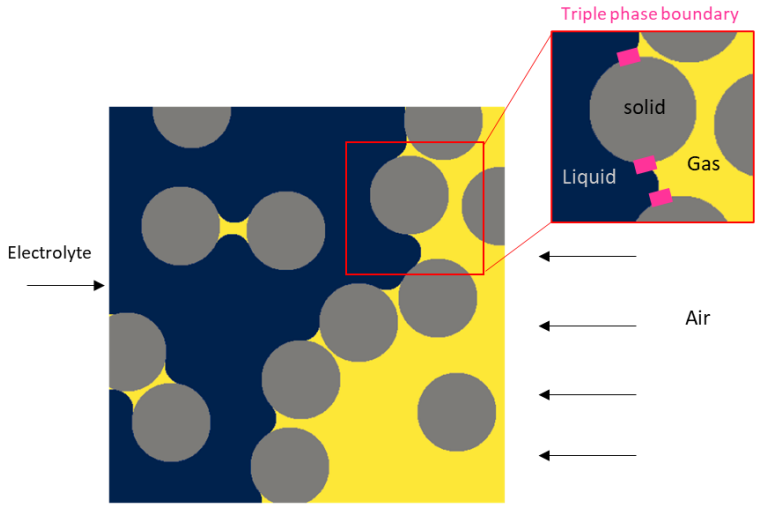

Figure 3-2 A schematic of the TPB in an air cathode. Spherical particles are the backbone porous layer containing active materials (CL). Electrolyte invasion occurs in the catalyst layer of the air electrode. The oxygen in the air dissolves and diffuses into the electrolyte while undergoing ORR upon contacting the active materials.

3.3.2. Pore network structure

In this study, the void space of an air cathode's CL was represented as a pore network, defined as a connected network of pores (nodes) and throats (edges). Figure 3-3 shows the representative pore network model used here, which is based on a cubic lattice topology for simplicity. Obtaining an experimental tomogram of the entire CL of a Zn-air electrode is challenging due to the small size of the pores ($< 200\ nm$) and the relatively large thickness of the CL (of order 100 μm) and a suitable tomogram was consequently not available for this study. A representative cubic network was used as a first approximation of the CL structure. For validation purposes, a random distribution of pore sizes was used with pores spanning between 25 and 250 nm. This size range was obtained from an SEM micrograph as outlined in Appendix B. The effect of the pore size distribution is studied in section 3.4. In all cases, the throat diameter was taken as 0.8 of the lower size of the two connected pores. This value was chosen to provide a sufficient porosity of 0.4, while providing a distribution of sizes for narrow constrictions (throats). The pores and throats are assumed to be cubes and cuboids, respectively, which determines the geometrical properties (i.e. volume and surface area), as well as the pore transport conductance (see section 3.3.3.2). The computational domain of the pore network contains only the pores of the CL, with boundary conditions at the interfaces with the gas diffusion backing layer on atmospheric side and the membrane-liquid electrolyte on the anode side. The PNM in this study was implemented in OpenPNM [49].

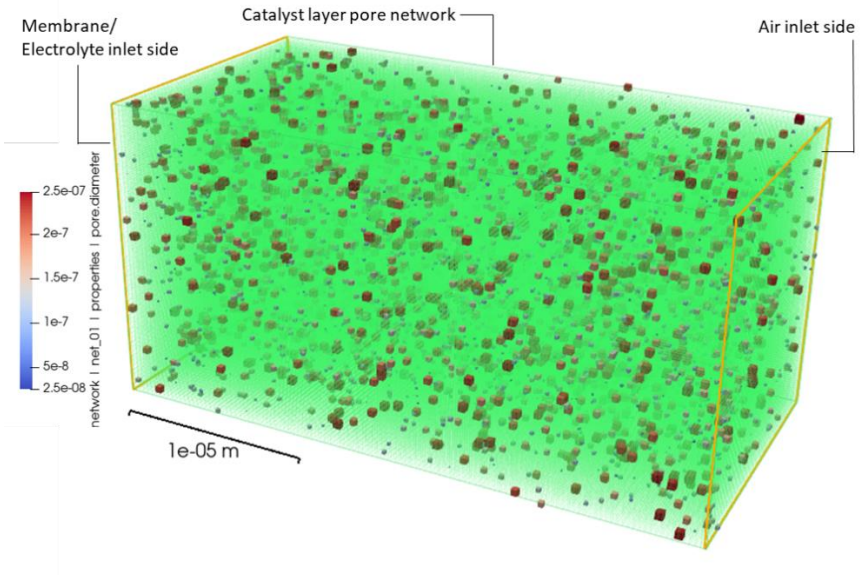

Figure 3-3 A representation of a pore network model used in this study. Cubic pores are colored by their diameter size. For a better visualization purpose, only a fraction of pores enlarged by a factor of 1.5 is shown and the cuboid throats are not shown for better visualizations. However, the connections are shown as green wireframe. The pore network demonstrates a typical model in this study, while the network architecture, geometry, and pore/throat sizes will vary in different investigations in this study.

3.3.3. Transport calculations

The transport phenomena in the air cathode are shown in Figure 3-4 and include diffusion of oxygen from the gas diffusion layer, dissolution of oxygen into the electrolyte at electrolyte-gas interface, diffusion of the dissolved oxygen through the electrolyte, ORR on catalyst sites (assumed to be uniformly distributed on the pore walls), diffusion and migration of the produced ions (OH^-), and the ionic conduction of the electrolyte. As explained earlier, TPB terminology better describes the ORR in solid oxide fuel cells, whereas the ORR in Zn-air cathode occurs at electrolyte-catalyst interface, which is a two-phase (liquid-solid) interface [31], [74]. Therefore, in this study the term TPB will not be used. To distinguish between different regions in the CL, three regions were defined as shown in Figure 3-4. The electrolyte-gas interface was defined at the interface throat locations where the dissolution of oxygen takes place. The invaded pores that are connected to these interfaces were defined as “near interface pores”. The remaining invaded pores that are located further from the interface were defined as remaining electrolyte-filled pores. With this definition, it was assumed that all electrolyte-filled pores were reactive, though the bulk of the reaction occurs near the interface. The pore network was partially invaded by the electrolyte using invasion percolation to a specific saturation, and the rate of the ORR was computed for various applied voltages

under steady state conditions to compute a polarization curve. The ORR produces hydroxide ions (OH^-), the charge carrier in the electrolyte phase:

$$\frac{1}{2}O_2 + H_2O + 2e^- \overset{r_{ORR}}{\leftrightarrow} 2OH^- \tag{3-1}$$

The PNM of the CL was developed based on the following assumptions: 1) steady state conditions; 2) no electrolyte convection in the CL; 3) The diffusion coefficients in the electrolyte depend only on the initial KOH concentration; 4) Reactions only occur in the electrolyte-filled pores; 5) The rate of the ORR (r_{ORR}) in each pore is proportional to the oxygen concentration in the pore. The reaction area of each reactive pore was defined by adding half of the surface area of the connected throats to the pore surface area. Mathematical details of each transport phenomena are described in the following sections.

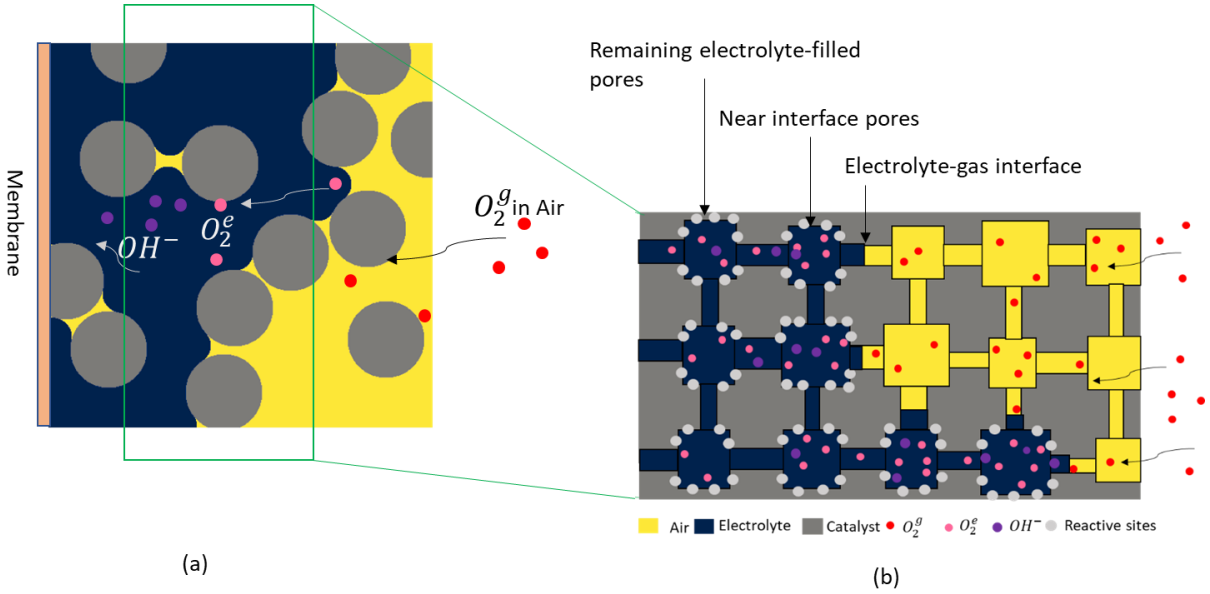

Figure 3-4 a) A schematic of the oxygen transport in a Zn-air cathode. Oxygen molecules are represented as red dots, dissolved oxygen as pink dots, and hydroxide ions are represented as purple dots. b) A schematic of the electrode's pore network model in 2D. The interface of electrolyte-air represents the electrolyte-gas interface. Reactive pores include near interface pores and remaining electrolyte-filled pores.

3.3.3.1. Electrolyte-air Interface

To model the electrolyte invasion in the CL, an IP algorithm was employed. Invasion percolation considers fluid injection and menisci movement in porous materials based on capillary forces presented by the void space constrictions. During invasion of a non-wetting fluid, capillary forces resist the invasion of narrower constrictions, so wider constrictions are preferentially invaded. Once a pore is invaded by electrolyte, its

neighboring throats are labeled as accessible, and the process repeats by invading the throat with the next minimum entry pressure [100]. The entry pressure of the electrolyte into the air filled pores was estimated using the Washburn equation [101]:

$$P_{c,i} = -2\sigma\frac{cos\theta}{r_i} \tag{3-2}$$

where $P_{c,i}$ and r_i are the capillary entry pressure and radius of pore i, respectively; σ and θ are the surface tension of the electrolyte and the contact angle of the electrolyte with the solid.

The electrolyte invasion inlet was the membrane-CL interface and periodic boundary conditions were imposed on 4 sides of the network in the y and z directions perpendicular to the direction of invasion. A periodic boundary condition allows the fluid exiting one boundary to enter at the opposite boundary. Such periodic boundary condition are necessary to eliminate wall effects and provide a continuous internal flow throughout the porous domain [94], [102]–[104]. This is especially important at lower saturations below the percolation threshold, where the size of a representative elementary volume is infinite, since the invasion front shows self-similarity over many length scales. Periodic connections were added to the PNM by creating additional throats that connect the pores on the opposite walls of the network. The sizes of these throats were determined in the same manner as described above.

3.3.3.2. Diffusion and reaction of oxygen

Oxygen diffusion through the CL was modeled by Fickian diffusion. The mass balance of oxygen around pore i is as follows:

$$\sum_{j=1}^{N_i} G_{d,ij}^{O_2}\left(c_i^{O_2} - c_j^{O_2}\right) = S_i^{O_2} = -\nu_{O_2} \times r_{ORR} = 0.5 \times r_{ORR} \tag{3-3}$$

where $G_{d,ij}^{O_2}$is the diffusive conductance of the conduit that is connecting pores i and j and can be found using a resistors-in-series model (see below); $c_i^{O_2}$ is the concentration of the oxygen in pore i; $S_i^{O_2}$ is oxygen consumption by reaction; and ν_{O_2} is the stoichiometry coefficient of O_2 in Eq. (2-1) i.e. 0.5. Within the CL, $S_i^{O_2}$ is zero in all gas filled pores, and positive in all wetted pores, not only those near the electrolyte-gas interface.

The value of r_{ORR} at the reactive sites can be calculated using the Butler-Volmer kinetic model [105]:

$$r_{ORR} = \frac{J_0 A_i}{n_e F}\left(\frac{c_i^{O_2}}{c_0}\right)\left[\exp\left(\frac{\alpha_a F}{RT}\eta_c\right) - \exp\left(-\frac{\alpha_c F}{RT}\eta_c\right)\right] \quad (3\text{-}4)$$

where J_0, n_e, α_a and α_c are the exchange current density, the number of electrons in reaction Eq. (2-1), and the charge transfer coefficients for the anode and the cathode, respectively; c_0 is a reference concentration; η_c is the cathode overpotential; and F, R, and T are Faraday's constant, the universal gas constant, and the temperature, respectively. Ignoring the IR loss in the anodic compartment, η_c is defined as follows:

$$\eta_c = \phi_s - \phi_l - V_{oc} \quad (3\text{-}5)$$

where ϕ_s, ϕ_l, and V_{oc} are the solid potential, local electrolyte potential and open circuit voltage, respectively. A constant electric potential for the solid phase was assumed due to the relatively high conductivity of the carbon electrodes, which was equal to the applied voltage.

In Eq. (3-3), the value of $G_{d,ij}^{O_2}$ can be defined using the resistors-in-series model as shown in Figure 3-5. This model was used for all transport processes, and its general formulation is as follows:

$$\frac{1}{G_{tr,ij}} = \frac{1}{g_{tr,i}^{p}} + \frac{1}{g_{tr,ij}^{t}} + \frac{1}{g_{tr,j}^{p}} \quad (3\text{-}6)$$

where $g_{tr,(i\,|\,ij\,|\,j)}^{p|t}$ is the conductance of the transport mechanism of interest "*tr*" for each element (half pore/throat/half pore) in the conduit. For a diffusive mass transport mechanism, the diffusive conductance of each element can be explicitly calculated based on Fick's first law of diffusion. The diffusive conductance of pore i is as follows:

$$g_{d,i}^{p} = \frac{D_{i,k} A_i}{L_i} \quad (3\text{-}7)$$

where $D_{\mathrm{i,k}}$ is the molecular diffusivity of species k, A_i is the cross-sectional area of the pore i, and L_i is the length of the element. The diffusive conductance of pore j and throat ij can be defined in a similar way as for pore i in Eq. (3-7). Therefore, for the specific transport mechanism of oxygen diffusion, $G_{d,ij}^{O_2}$ in Eq. (3-3) can be calculated using Eq. (3-6) and Eq. (3-7), given the molecular diffusivity of oxygen (D_{i,O_2}). Note that for a conduit at the electrolyte-gas interface region, the value of $G_{d,ij}^{O_2}$ will be corrected to incorporate the dissolution of oxygen into the electrolyte. This correction is explained in the next section.

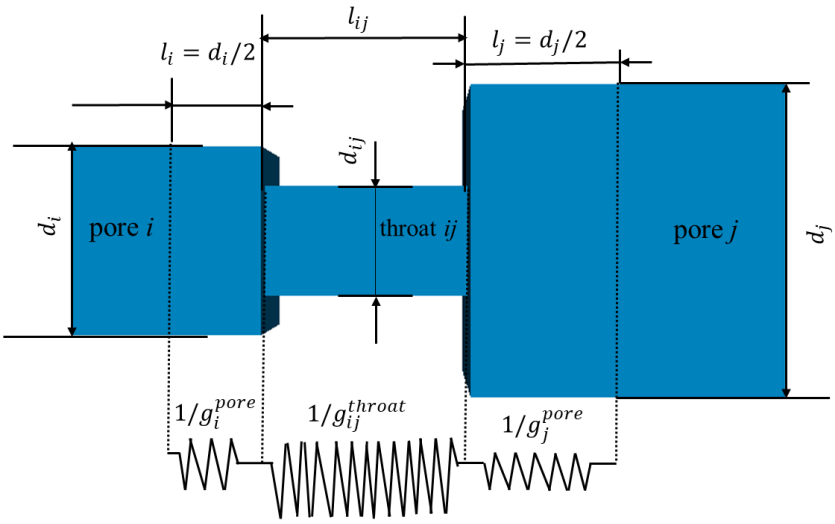

Figure 3-5 A schematic of simple cube and cuboid geometry for a pore-throat-pore element as one conduit. The conduit elongates from the centroid of one pore and includes their connecting throat and half of two pores. The corresponding conductance of the conduit is calculated using a resistors-in-series theory on its elements (half pore-throat-half pore) from Eq. (3-6).

3.3.3.3. Oxygen solubility

The dissolution of the oxygen in the electrolyte was modeled by Henry's Law. The oxygen solubility was calculated as a linear function of the partial oxygen pressure as follows [82]:

$$C_{O_2} = H_{O_2}^{c,p} P_{O_2} \tag{3-8}$$

where $H_{O_2}^{c,p}$ is Henry's constant and P_{O_2} is the partial oxygen pressure. The dissolved oxygen then diffuses through the partially invaded electrode and participates in the ORR. To implement Henry's law in the PNM, the solubility was incorporated into the mass transport resistance/conductance of a conduit element at the interface of water and air (where the dissolution occurs). A conduit element filled with water and air is illustrated in Figure 3-6. The diffusive resistance of this conduit includes two parts: First, the resistance from the center of the electrolyte-filled pore to the liquid-gas interface. Second, the resistance from the interface to the center of the air-filled pore. To derive the mass flow rate at the interface of an arbitrary conduit, it was assumed that the interface boundary was at the middle of the throat. Therefore, pore i and half of throat ij are occupied by the electrolyte phase α, while pore j and the remaining half of the throat are occupied by the air phase β. The resulting concentration profile in the conduit is schematically shown in Figure 3-6.

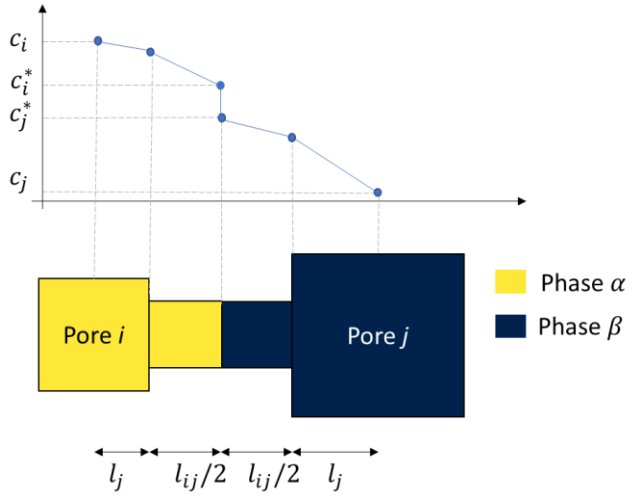

Figure 3-6 A schematic of mass partitioning at the interface of electrolyte-air contact region. It is assumed that the interface boundary locates at the middle of the throat.

The mass flow rate of the conduit is calculated as (see Appendix A):

$$m_{ij} = \hat{G}_{ji}(c_i - H_{ij}c_j) \tag{3-9}$$

where H_{ij} is the dimensionless Henry's constant:

$$H_{ij} = H_{gas}^{c,c} = \frac{C_{aq}^{gas}}{C_{gas}^{gas}} \tag{3-10}$$

where C_{aq}^{gas} is the concentration of gas species (oxygen) in the electrolyte phase and C_{gas}^{gas} is the concentration of the gas species in the gas phase. As the $H_{gas}^{c,p}$ is conventionally reported in references [82], $H_{gas}^{c,c}$ can be calculated from $H_{gas}^{c,p}$ assuming an ideal gas behavior for oxygen:

$$H_{ij} = H_{gas}^{c,c} = RTH_{gas}^{c,p} \tag{3-11}$$

Therefore, the oxygen solubility defined in Eq. (3-8) is incorporated into the mass flow rate in the form of dimensionless Henry's constant, calculating from Eq. (3-11). Finally, $\hat{G}_{ji}$ can be derived (see Appendix A):

$$\hat{G}_{ji} = \left(\frac{1}{g_i^p} + \frac{0.5}{g_{ij}^t}\right) + H_{ij}\left(\frac{1}{g_j^p} + \frac{0.5}{g_{ij}^t}\right) \tag{3-12}$$

$\hat{G}_{ji}$ along with the mass flow rate Eq. (3-9) was used to define the dissolution of oxygen and mass transport at the electrolyte-gas interface region.

As the solubility of oxygen in KOH electrolyte is a function of molarity of the solution, H_{ij} (given in Table 3-2) can be calculated from oxygen solubility values at a specified KOH concentration. Oxygen solubility (S) are found as follows[106]:

$$logS = log1.26 \times 10^{-3} - 0.1746\, C_{KOH} \tag{3-13}$$

For a 7M KOH solution:

$$S = 10^{-4.12} = 7.58 \times 10^{-5} \left[\frac{mol}{l}\right] = 0.075\, [\frac{mol}{m^3}] \tag{3-14}$$

As Eq. (3-13) from Davis et al.[106] were presented at $P_{O2} = 750\ torr = 101080\ Pa$, the value of $H_{gas}^{c,p}$ can be calculated from its definition:

$$H_{gas}^{c,p} = \frac{C_{aq}}{P_{gas}} = \frac{0.075}{101080} = 7.42 \times 10^{-7} [mol_{gas}/m^3 Pa] \tag{3-15}$$

Substituting $H_{gas}^{c,p}$ value in Eq. (3-11), the Henry's constant is found as follows:

$$H_{gas}^{c,c} = RTH_{gas}^{c,p} = 8.314 \times 298 \times 7.42 \times 10^{-7} = 1.838 \times 10^{-3} \tag{3-16}$$

The value of Henry's constant can also be calculated using the formulation used by Stamm et al. [82], where Sechenov constant was used to calculate the oxygen solubility based on KOH concentration (salting out). As an additional check, Henry's constant was calculated applying Sechenov constant. A value of $H_{gas}^{c,c} = 1.85 \times 10^{-3}$ was obtained from calculations, which matched the value found in Eq. (3-16).

3.3.3.4. Transport of ionic species

The ionic species in the electrolyte are K^+ and OH^-. Assuming a high concentration of KOH, the K^+ cation mass transport equation is not solved in the system of ionic species transport equations, as it is assumed to be abundant in the supporting electrolyte. Therefore, only the cation was considered when applying the electroneutrality condition and calculating the electrolyte conductivity, with the cation assumed to be present in balance.

The transport of OH^- through the electrolyte occurs by diffusion and migration, which can be modeled by the Nernst-Planck equation [45], [107], [108]. Agnaou *et al*. [45] presented the PNM formulation of the Nernst Planck equation. In the present work there was no convection, the upwind scheme was used to discretize the migration term, and the electroneutrality assumption was applied, giving the following:

$$\sum_{j=1}^{N_i}\left[G_{d,ij}^{\mathrm{OH}}+\max\left(-m_{ij}^{\mathrm{OH}},0\right)\right]c_i^{\mathrm{OH}}-\sum_{j=1}^{N_i}\left[G_{d,ij}^{\mathrm{OH}}+\max\left(m_{ij}^{\mathrm{OH}},0\right)\right]c_j^{\mathrm{OH}}=S_i^{\mathrm{OH}} \\ =-\nu_{\mathrm{OH}}\times r_{ORR}=-2\times r_{ORR} \tag{3-17}$$

where $G_{d,ij}^{OH}$ is the OH^- diffusive conductance in the conduit ij. $G_{d,ij}^{\mathrm{OH}}$ can be calculated using the resistors-in-series model defined in Eq. (3-6) where the diffusive conductance of each element is found from Eq. (3-7) given the OH^- diffusion coefficient $D_{i,\mathrm{OH}}$. m_{ij}^{OH} is the migration rate of OH^- which can be defined as follows:

$$m_{ij}^{\mathrm{OH}}=G_{m,ij}^{\mathrm{OH}}(\phi_i-\phi_j) \tag{3-18}$$

where ϕ_i and ϕ_j are the electrolyte potential at pore i and j, respectively. $G_{m,ij}^{\mathrm{OH}}$ is the migrative conductance and can be calculated using the resistors-in-series defined in Eq. (3-6), where the migrative conductance of pore i is defined as follows:

$$g_{m,i}^{\mathrm{OH}}=\frac{z^{\mathrm{OH}}F}{RT}g_{d,i}^{\mathrm{OH}} \tag{3-19}$$

where $z^{\mathrm{OH}}$is the valence of OH^-, and $g_{d,i}^{\mathrm{OH}}$ is the OH^- diffusive conductance of pore i found from Eq.(3-7) using OH^- diffusion coefficient.

3.3.3.5. Charge conservation

The charge conservation around pore i assuming electroneutrality is as follows [45], [107]:

$$\sum_{j=1}^{N_i}G_{cond,ij}^{ionic}\left(\phi_i-\phi_j\right)=S_i^{charge}=-F\sum_{n}^{nc}z^n\left[\sum_{j=1}^{N_{th}}G_{ij}^{n,diff}\,c_i^n-\sum_{j=1}^{N_{th}}G_{ij}^{n,diff}c_j^n\right]+I_{BV} \tag{3-20}$$

where ϕ_i is the potential of the electrolyte. S_i^{charge} is the source term which includes electroneutrality term and the rate of the charge generation (current) from Butler-Volmer kinetics. $I_{BV}$is nonzero at the electroactive sites where ORR occurs. z_i^n is the valence of ionic species n. $G_{cond,ij}^{ionic}$ is the ionic conductance of the conduit, which can be calculated using the resistors-in-series model defined in Eq. (3-6), where the ionic conductance of pore i is defined as follows:

$$g_{ionic,i}^{electrolyte}=\frac{F^2}{RT}\left(\frac{A_i}{L_i}\right)\sum_{k}(z_i^n)^2\,D_i^nc_i^n \tag{3-21}$$

where z_i^n, D_i^n,and c_i^n are the valence of ionic species n, Diffusion coefficient and concentration of species n, respectively. The electroneutrality condition $\sum_n z^n c^n=0$ is applied on the electrolyte solution.

Therefore, $c^{\mathrm{K}^+} = c^{\mathrm{OH}^-}$. Applying electroneutrality into Eq. (2-30) the ionic conductance of pore i can be simplified as a function of c^{OH^-}:

$$g_{ionic,i}^{electrolyte} = \frac{F^2}{RT}\left(\frac{A_i}{L_i}\right)[D_i^{\mathrm{K}^+} + D_i^{\mathrm{OH}^-}]c_i^{\mathrm{OH}^-} \tag{3-22}$$

Similarly, the electroneutrality term in the LHS can be simplified as a function of c^{OH^-}. The second term in the LHS is found from Butler-Volmer kinetics defined in Eq. (3-4) $I_{BV} = n_e F r_{ORR}$.

The boundary condition for the charge balance equation was imposed on the electrolyte-membrane interface by calculating the ohmic loss in the cell components as given in Eq. (3-23)Assuming an average ohmic loss of IR_{ohmic}, the potential on the boundary ($\phi_{mem-bound}$) is calculated using Ohm's law. The generated current can be calculated by summing the current rates ($I_{i,BV}$) in the pore network. R_{ohmic} is the ohmic resistance of the membrane and other components that can be calculated by Pouillet's law [2] with known values of the components' dimensions and conductance given in [88] and Table 3-2:

$$\phi_{mem-bound} = R_{ohmic} I_{BV} = \left(\sum_{k}^{n_{comp}} \frac{\delta_k}{\sigma_k A_k}\right)\left(\sum_{i} I_{i,BV}\right) \tag{3-23}$$

where δ_k, σ_k, and A_k are thickness, conductivity, and area of the component k in the cell. Given the high conductivity of the Zn electrode $O(10^7)$ $[\frac{\mathrm{S}}{\mathrm{m}}]$and air cathode $O(10^4)[\frac{\mathrm{S}}{\mathrm{m}}]$, the ohmic loss in the electrodes were assumed to be negligible. Therefore, the ohmic loss was calculated for membrane, electrolyte channel and other components in the cell [88]. Relevant calculated parameters given in Table 3-2 were found [88], [109] as follows:

Membrane effective conductivity (σ_{mem}):

Given the porosity of the membrane ($\varepsilon_{\mathrm{sep}}$) from [88], assuming a tortuosity of $\tau_{sep} = (\frac{1}{\varepsilon_{sep}})$ for the porous membrane, σ_{mem} can be found as follows:

$$\sigma_{mem} = \sigma_{electrolyte} \times \frac{\varepsilon}{\tau} = 60 \times \left(\frac{0.5}{2}\right) = 15\ S/m \tag{3-24}$$

Electrolyte channel thickness ($\delta_{electrolyte\ channel}$):

The ohmic resistance in [88] was calculated based on δ_{zinc} for the anode compartment and $\delta_{electrolyte\ channel}$ for the electrolyte channel. As $\delta_{electrolyte\ channel}$ was not, based on the reference information and shown setup it was assumed that the given δ_{anode} in their supplementary info includes

both $\delta_{electrolyte\ channel}$ and δ_{zinc}. The value of $\delta_{electrolyte\ channel}$ was then calculated as the difference between δ_{anode} $(0.00615\ m)$ and $\delta_{zinc}(0.00115\ m)$, which resulted in the value of $5 \times 10^{-3} m$.

Electrolyte channel conductivity ($\sigma_{electrolyte\ channel}$):

Electrolyte channel conductivity in [88] was assumed to be a function of KOH concentration ($\sigma = f(C_{\mathrm{KOH}})$). However, the function was not provided. Therefore, the conductivity of the 7M KOH electrolyte was found from an empirical relationship given in [109] as follows:

$$\sigma = -2.041(M) - 0.0028(M^2) + 0.005332(M.T) + 207.2\left(\frac{M}{T}\right) + 0.001043(M^3) - 0.0000003(M^2.T^2) \quad (3\text{-}25)$$

where M and T are molarity and temperature, respectively. Substituting $M = 7$ and $T = 298$ into Eq. (3-25), results in $\sigma = 61.77\ S/m$. As stated in [109] the regression model in Eq. (3-25) had an average of 2% deviation from reference experimental data. Therefore, an approximate value of $60\ S/m$ was used for $\sigma_{electrolyte\ channel}$ in this study.

3.3.3.6. Coupling mass and charge transport

The charge conservation boundary condition depends on the current, which itself is unknown and a function of mass transport rate. Therefore, the mass and charge transport equations are coupled, with the concentration of the species and the electrolyte potential as unknown variables. To solve the system of equations an iterative framework was used, as illustrated in Figure 3-7. The proposed algorithm may diverge if the initial guess is not close enough to the actual solution, so a relaxation factor ω was used [2]. In each iteration, the value of the unknown variables was updated as $X_i^{iter+1} = \omega\, X_i^{iter+1} + (1-\omega)\, X_i^{iter}$. Once the systems of equations were solved, the distribution of the electrolyte-gas interface was then analyzed to investigate the CL's parameters that affect the electrode's performance. When simulating a polarization curve the results from the previous voltage were used as inputs to the next voltage, providing a good initial guess which helped speed and stability.

The value of relaxation factor in a range of (0,1) was defined based on the range of applied cell voltage [2]. At cell voltage close to open circuit the kinetic overpotential is relatively small. Therefore, the reaction rate and consumption of species is relatively small, which leads to an approximately uniform concentration distribution. Therefore, at the beginning of the discharge and close to open circuit voltage, the coupling between mass and charge transport is weak. As a result, a larger relaxation factor at the early stages of discharge is sufficient for convergence. On the other hand, at the later stages of discharge as the cell voltage is reduced farther from open circuit voltage, the coupling between mass and charge transport physics

becomes stronger. As a result, a smaller relaxation factor was required to reach convergence [2]. The relaxation factor for the reference case generated in section 3.4.1 was defined using a trial and error, as given in Table **3-1**. Similarly, relaxation factors were fine tuned for other networks generated in section 3.4.4. However, for future works it is recommended to automatically define an adaptive relaxation factor by defining a function to adaptively change the value of the relaxation factor. A simple outline of the function could take in an initial value of the relaxation factor (ω_0), residual error from previous step ($error_0$), error at the current step ($error$), and a minimum and maximum value of the relaxation factor ($\omega_{min}, \omega_{max}$). The function could calculate the relaxation factor to adaptively increase or decrease. For example, if $error > error_0$, (meaning we need a smaller relaxation factor) the function could return $\omega = \omega_0 \times 0.8$. Otherwise, if $error \leq error_0$ (meaning we don't need a smaller relaxation factor) the function could return $\omega = \omega_0 \times 1.5$. This adaptive definition is advantageous over constant value of relaxation factor, as it reduces the computational costs of the trial and error and the number of iterations to reach the convergence.

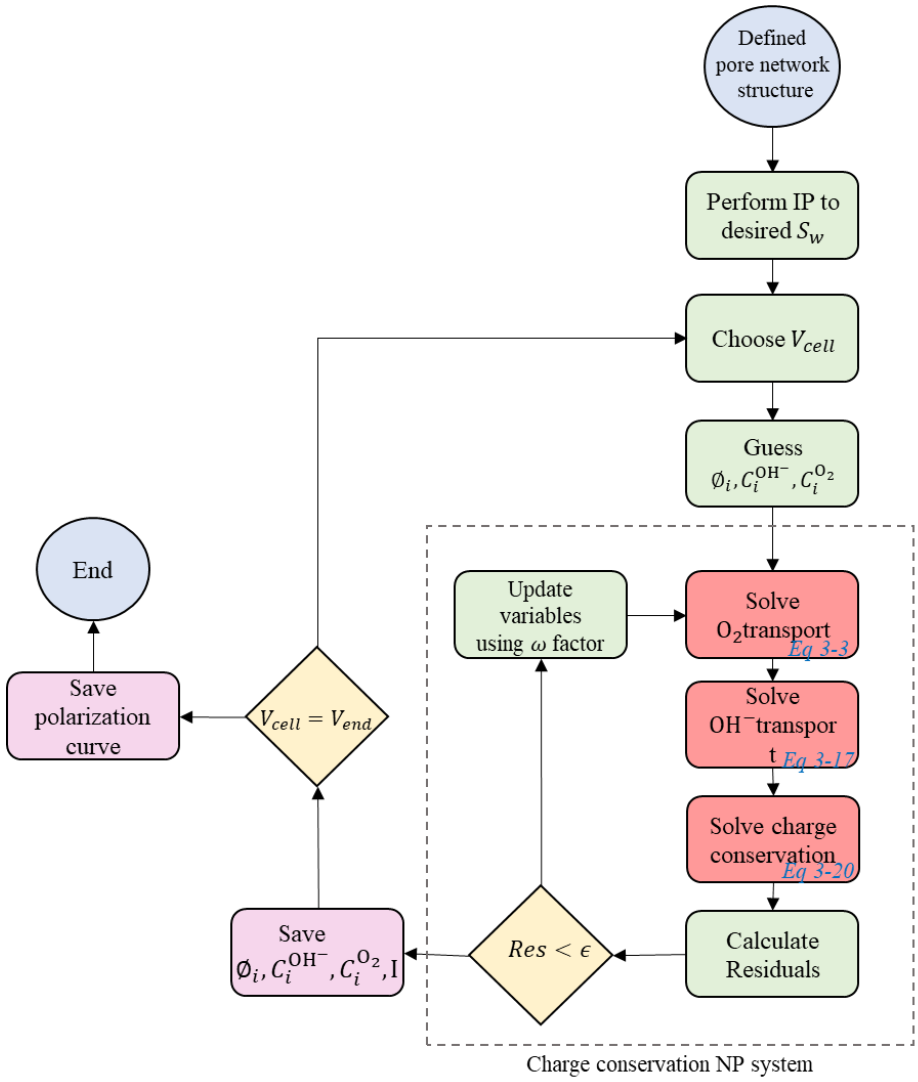

Figure 3-7 The flow chart of the framework to model the Zn-air cathode

Table 3-1 Defined relaxation factors for convergence in the reference pore network model

Applied voltage	Relaxation factor
$0 < V_{cell} \leq 0.8$	0.2
$0.8 < V_{cell} \leq 0.9$	0.3
$0.9 < V_{cell} \leq 1.1$	0.4
$1.1 < V_{cell} < 1.2$	0.8
$1.2 \leq V_{cell} < V_{oc}$	1

3.4. Modeling Results and Discussion

3.4.1. The effect of the electrolyte saturation on electrolyte-gas interface length

To verify the modeling framework, a cubic network was generated based on the data from Lao-atiman *et al*. [88]. The pore size distribution and porosity of the CL was not reported in their experimental data so a random distribution with sizes 25 and 250 nm was used based an SEM micrograph (Appendix B) and a porosity of 40% was used based on the typical average porosity for catalyst layers [99], [105]. The random distribution was created using a random generator to sample from a uniform distribution over the defined size range. To reduce the computational cost, the cross-sectional dimension of the cell was reduced to 15 μm by 15 μm, while the CL thickness was remained constant. The network dimension was [30,15,15] μm corresponding to a domain size of [120,60,60] pores in the x, y, and z directions. The spacing of the cubic network was 0.25 μm, which resulted in a network porosity of 40%. The details of the parameters used in the PNM are given in Table 3-2. The KOH concentration was 7 M, which is reported as an optimum molarity to provide a high electrolyte conductivity [88], [109]. All physical properties of the model including KOH concentration, diffusivity of ions, and partial pressure of the oxygen were the same as the reported experimental data. The fitted parameters were the exchange current density (j_0), electrolyte saturation, and the thickness of other components, which were manually adjusted to fit the model result with the experimental data. Figure 3-8 shows the simulated polarization curve compared with the experimental data, and reasonable agreement was obtained. As the electrolyte saturation was not included in the experimental data, the CL saturation was fitted to 0.85, which was found from the saturation values corresponding to the high performance and ensures the electrolyte has reached the CL-GDL interface.

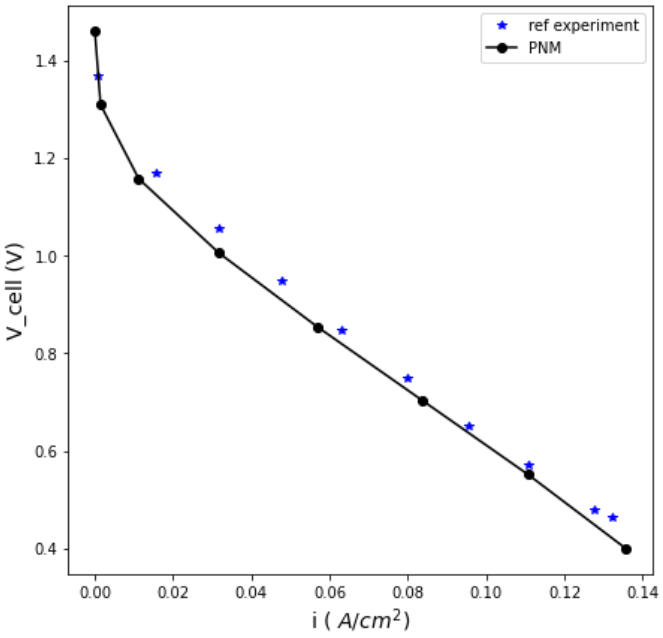

Figure 3-8 Comparison of the PNM polarization curves with experimental data by Lao-atiman et al. [88] assuming a fitted saturation value of 0.85.

The available experimental data did not include the saturation of the CL, which is challenging to measure experimentally. However, in the present study the effect of the electrolyte saturation on the performance of electrode was investigated. The invasion of the electrolyte at 4 selected saturations are illustrated in Figure 3-9. For illustration purpose, pores and throats are shown as spheres and wireframes, and the air-filled pores are masked so that the only visible pores are the electrolyte-invaded pores.

Figure 3-10a shows the cell polarization behavior for varying CL saturation between 0.1 and 0.9. Increasing the electrolyte saturation does not necessarily increase the maximum generated power, with peak power generation occurring at a saturation of 70%. This can be understood by considering the fraction of pores where a reaction is *possible* (i.e. any electrolyte filled pore) versus the fraction of pores where the reaction is *actually occurring* at a significant rate (i.e. pores near the phase boundary). Although dissolved oxygen can physically reach any electrolyte-filled pore, the reality is that due to limited solubility and low diffusion coefficient the oxygen concentration rapidly drops so that the ORR rate rapidly becomes negligible. As a result, most of the reaction occurs at near interface pores. As the saturation increases so does the number of pores at the air-electrolyte interface, and thus the peak power increases with saturation. However, at high saturations above 0.9, the fraction of pores at the air-electrolyte interface decreases towards 0 as all the

pores become filled with electrolyte. This is also reflected in the polarization curves as the observed peak power drops beyond a saturation of 0.7. To illustrate this trend, Figure 3-10b shows the fraction of the surface area of electrolyte filled pores which lie near the interface as a function of the electrolyte saturation in the CL. The peak of this curve also occurs within the saturation range of 0.6-0.8. This behavior in the performance agrees with experimental works where the increase and decrease in the performance of air electrodes were observed with increasing electrolyte volume [31], [74]–[76]. Another way to evaluate the performance of the electrode is to plot the current density versus electrolyte saturation, as shown in Figure 3-10c for three applied voltages. At each applied voltage, a peak current density occurs when the saturation of the CL is around 0.7-0.8, though this shift to slightly higher values at the higher voltages.

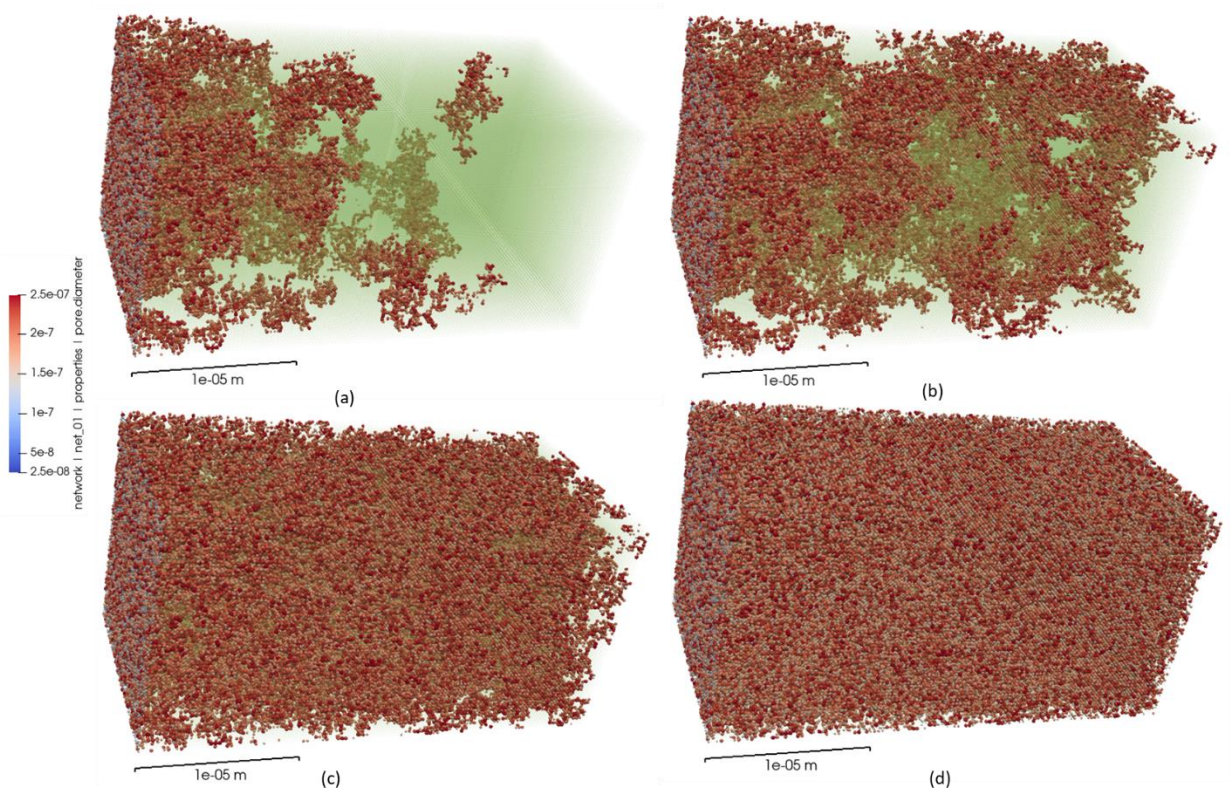

Figure 3-9 Invasion of electrolyte at different saturation (electrolyte volume). Only electrolyte-filled pores are shown (colored by pore diameters) for a better illustration purpose. a) Electrolyte invading at $S_w = 0.1$. b) Electrolyte invading at $S_w = 0.2$. At this point electrolyte front has additional fingers/branches providing additional triple phase boundaries. The breakthrough front is not completely blocking the air side. c) Electrolyte invading at $S_w = 0.4$. At this point the electrolyte front has grown in three dimensions occupying more pores which creates a more uniform front. d) Electrolyte invading at $S_w = 0.7$. The breakthrough front is blocking more pores at the air side. At this point and further invasion, the electrolyte has occupied most of the CL and the electrolyte-gas interface length will be reducing to a minimum value.

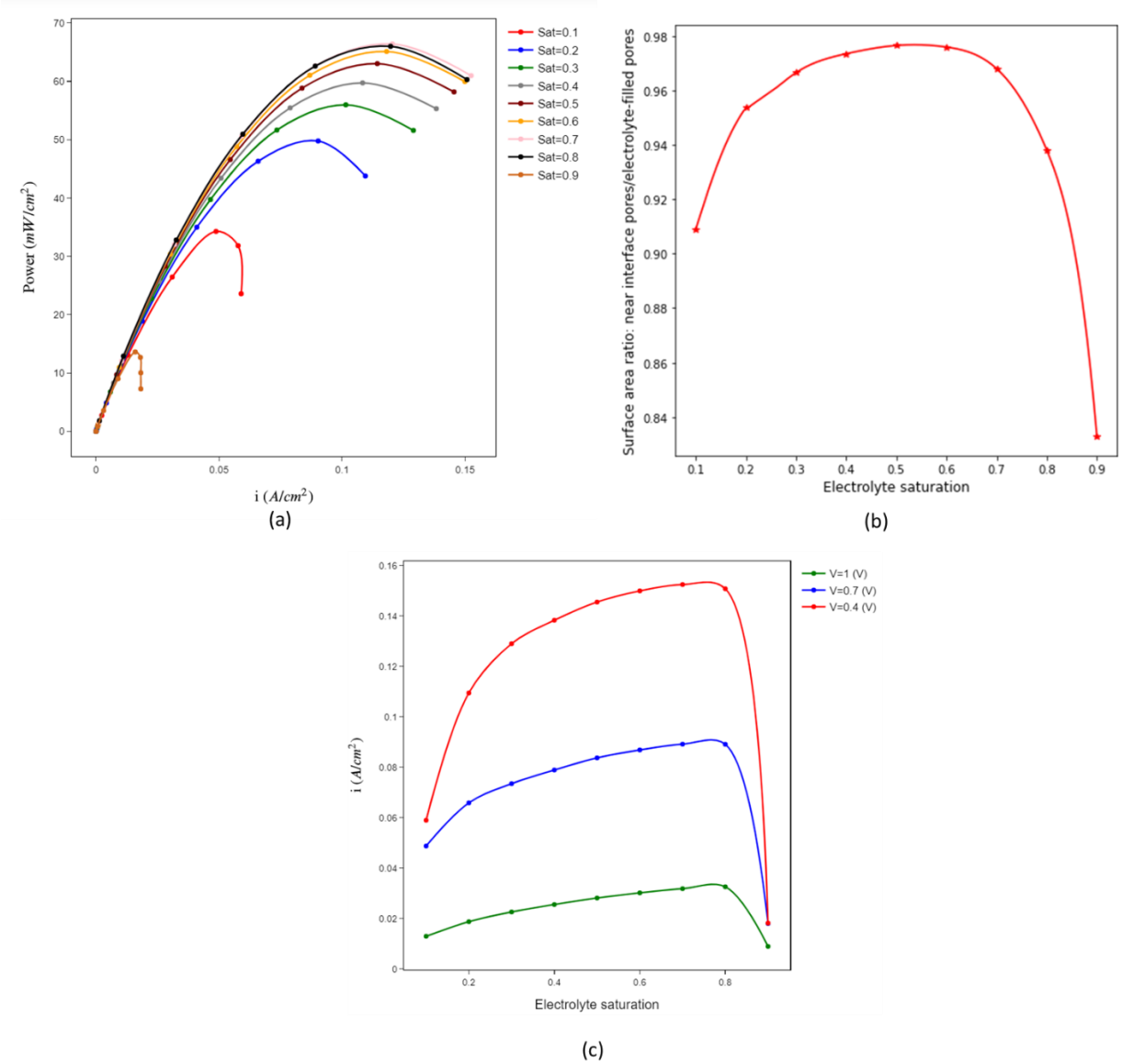

Figure 3-10 a) Power and current density curves at each saturation of the electrolyte. b) The surface area ratio of near interface pores to all electrolyte-filled pores vs saturation of the electrolyte. c) The change of current density by increasing invading electrolyte volume. Each curve shows the increasing and decreasing trend at a constant cell potential.

Table 3-2 Summary of the parameters used in this study

Parameter	Value	Units	Description	source
δ_m	2×10^{-4}	m	Membrane thickness	[88]
σ_{mem}	15	S/m	Membrane effective conductivity (porosity=0.5 and tortuosity=2 applied)	Calculated from [88]
$\delta_{electrolyte\ channel}$	5×10^{-3}	m	Electrolyte channel thickness	Calculated from [88]
$\sigma_{electrolyte\ channel}$	60	S/m	Electrolyte channel conductivity	Calculated from [88],[109]
σ_{other_comp}	20	S/m	Other components' conductivity	[88]
δ_{other_comp}	6.1×10^{-3}	m	Other components' thickness	Fitted parameter
j_0	0.9	A/m^2	Exchange current density	Fitted parameter
c_0	8.452	mol/m^3	Reference concentration of oxygen	[88]
α_c, α_a	0.5	-	Cathodic, Anodic transfer coefficient	[88], [105]
H_{ij}	1.838×10^{-3}	-	Dimensionless Henry's constant	Calculated from [106]
$D_{O_2,air}$	2.3×10^{-5}	m^2/s	Oxygen diffusivity in air	[88]
$D_{O_2,elec}$	0.6×10^{-9}	m^2/s	Oxygen diffusivity in Electrolyte	[106]
$D_{\mathrm{OH}^-,elec}$	5.27×10^{-9}	m^2/s	OH^- diffusivity in Electrolyte	[110]
$D_{\mathrm{K}^+,elec}$	1.2×10^{-9}	m^2/s	K^+ diffusivity in Electrolyte	[88]
$C_{\mathrm{o}_2,inlet}$	8.452	mol/m^3	Inlet oxygen concentration	[88]

3.4.2. Electrolyte saturation and tortuosity

The void space in a porous CL includes a broad range of pore sizes providing a heterogeneous pore space, which results in a fractal or highly branched fluid invasion front. Ionic transport paths through the fluid phase are therefore quite tortuous [111], [112]. To quantify this effect, a network-based tortuosity parameter was used [111], [113], [114], defined as the ratio of the shortest path length (L_{min_i}) to the straight-line length (L_{s_i}) [111] as follows:

$$\tau_i = \left(\frac{L_{min_i}}{L_{s_i}}\right)^2 \tag{3-26}$$

The shortest path between each pore i and the membrane interface was found using the Dijkstra algorithm [112], [115] with equal weights on each connection since the pores were equally spaced. The straight-line length for each pore i was calculated as the direct or Euclidean distance from the membrane face to the pore center. This metric is explored here to examine the effect of saturation on tortuosity of the invasion front. Tortuosity of the invasion front hinder the transport of produced ions towards the anode. As a result, the increase in produced OH^- concentration in tortuous regions results in an increase in the KOH concentration. The concentration of KOH can exceed its solubility limit , meaning that KOH can precipitate in the CL pores, which is a key degradation mechanism for these systems [99]. Figure 3-11(a & b) shows the fluid configuration at two saturations at relatively low saturation values of $S_w = 0.1$ and $S_w = 0.2$, with each pore colored based on the calculated tortuosity (Eq. (3-26)) at this location. Some pores show a very high tortuosity, exceeding 100. This is due to the highly fractal nature of the invasion front [78]. Thus, an ion formed near the electrolyte-gas interface in the CLs shown in Figure 3-11(a & b) has to follow a narrow tortuous path through many pores before reaching the main electrolyte backbone, from where it can be transported more easily to the anode. Figure 3-11(c & d) show the same data with only pores having a tortuosity greater than 40 visible. This illustrates that the highest tortuosity pores are located in the long fingered regions, which make up much of the near interface pores. This also shows that the number of pores with an unusually high tortuosity is decreases when the saturation increases from 0.1 to 0.2. To further illustrate this trend, Figure 3-12 shows the cumulative tortuosity distributions for a range of saturations. It is apparent that once saturation exceeds 0.2 the number of pores with high tortuosity decreases significantly. This suggests that the CL should be operated with saturations greater than about 0.3 to reduce the number of pores which have very high tortuosity, since these will have high OH^- concentrations to drive the mass transfer, and thus could be subject to KOH precipitation if the solubility limit is reached.

The sudden drop in tortuosity between $S_w = 0.2$ and $S_w = 0.3$ may be explained by the percolation threshold for this system which is around $S_w \approx 0.25$ (bond percolation on a cubic lattice with a random distribution of bond entry values). Below the percolation threshold, the correlation length of the largest

invaded cluster becomes infinite [116], [117]. The results for $S_w < 0.25$ are impacted by this in two ways. Firstly, a high tortuosity is obtained since the electrolyte pathways are highly fractal. Secondly, the results are variable between realizations since the domain size was limited, whereas the representative elementary volume (REV) of the porous medium becomes infinite.

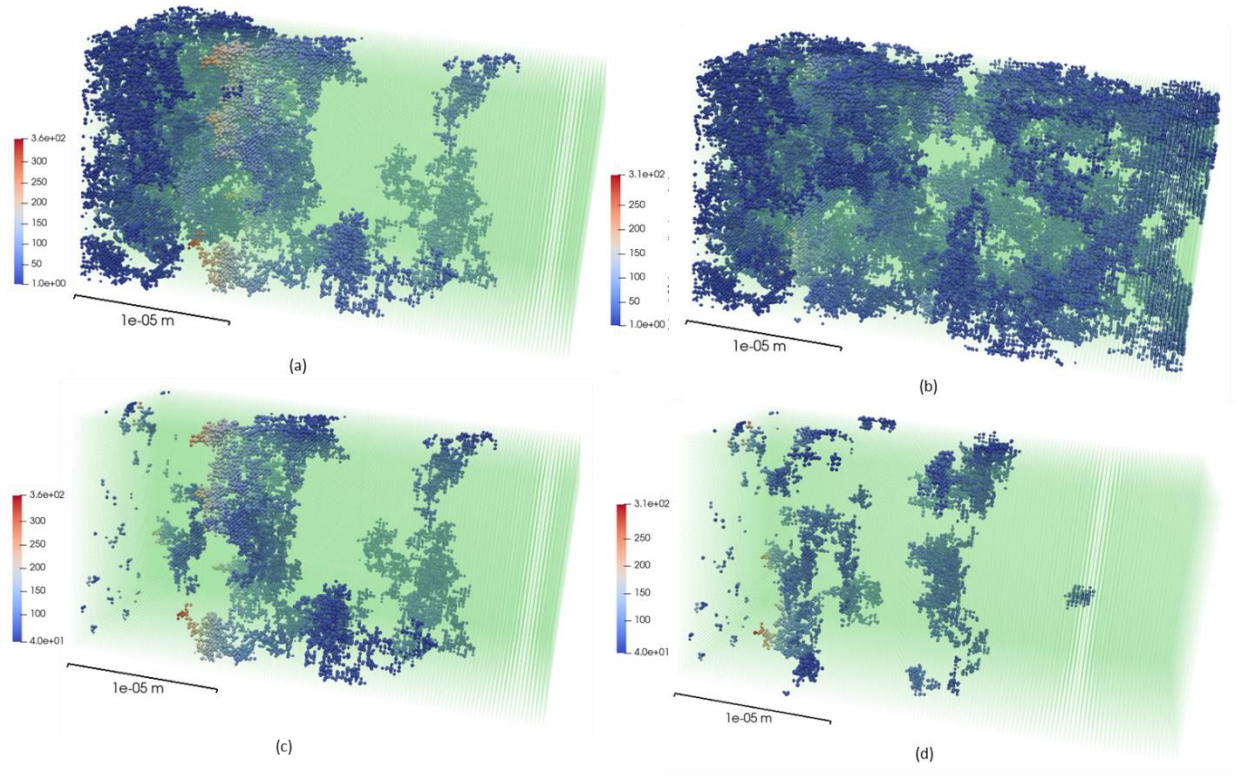

Figure 3-11 a) Tortuosity of invaded pores in the CL. a) Tortuosity at $S_w = 0.1$ b) Tortuosity at $S_w = 0.2$ c) Pores with tortuousity greater than or equal to 40 at $S_w = 0.1$ d) Pores with tortuosity greater than or equal to 40 at $S_w = 0.2$

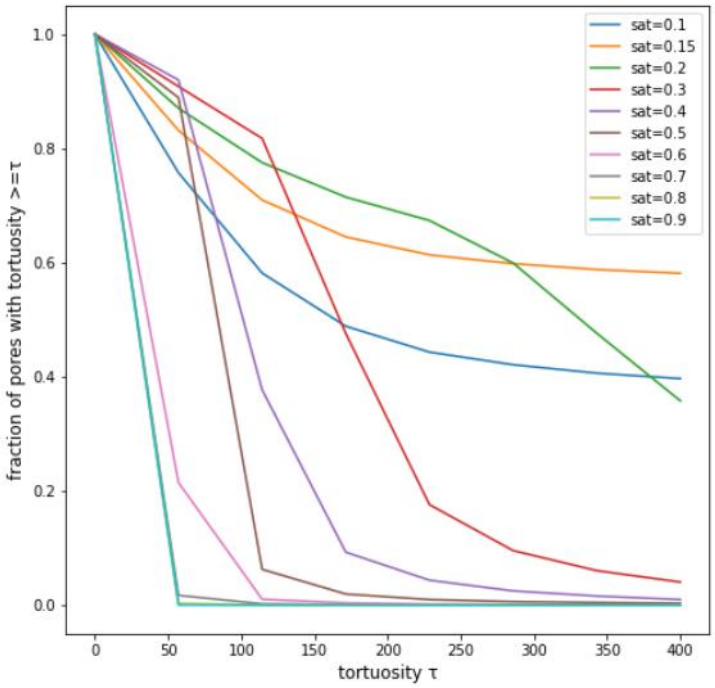

Figure 3-12 a) Plot of fraction of pores with tortuosity greater than or equal to the stated value in x axis. Each line in the plot shows the values at a specific electrolyte saturation.

3.4.3. Hydroxide concentration distribution

Given the extremely high tortuosity observed at lower saturations, the distribution of OH^- concentration was explored, to determine conditions and regions where the solubility limit for KOH (15 M) [110] may be exceeded. Exceeding this limit leads to the precipitation of KOH in the CL which blocks the mass transport paths and reduce the performance of the air electrode. A contour plot of the maximum OH^- concentration in the CL as a function of the electrolyte saturation and current density is shown in Figure 3-13. The color at each saturation and current density in the contour plot corresponds to the maximum value of the OH^- concentration observed in the CL under these conditions. The contours with concentration equal to and greater than 15 M were colored red to indicate that precipitation of KOH may occur under these conditions. At low to intermediate saturation (0.1-0.4) and higher current density, the OH^- concentration can exceed the KOH solubility limit (red-color regions). In contrast, at higher saturation values (0.4-0.8) the maximum observed OH^- concentration remains below the solubility limit at all current densities. Therefore, an intermediate to high electrolyte saturation is preferable for both electrode performance (higher current density), and for preventing KOH precipitation. In terms of cell degradation this result suggests that attempts to avoid electrolyte leakage into the GDL by operating at low saturation may induce precipitation. This trade-off is worthy of deeper study and should be the subject of future work.

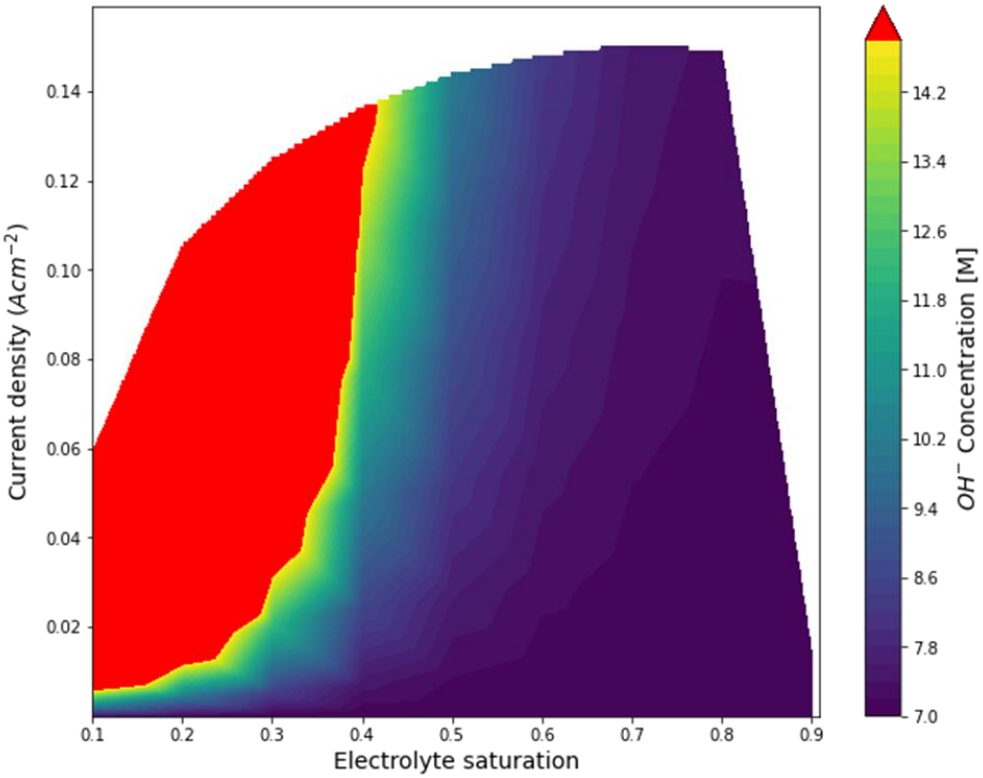

Figure 3-13 Contour plot of maximum OH^-concentration at different electrolyte saturation and current density. The red region with $C_{OH^-} > 15$ M represent the condition where the KOH will precipitate in the invaded electrolyte which is known to be a degradation mechanism. This contour plot can be used as a guide in choosing an optimum operational conditions and electrolyte invasion saturation for the CL to prevent the KOH precipitation and CL degradation.

3.4.4. The effect of the pores size distribution on the invasion front and cell performance

The pore size distribution (PSD) of the CL strongly affects the invasion pattern and subsequently the electrolyte-gas interface. In the above discussions a random distribution was used, but it is also interesting to study the impact of other distributions on the expected cell performance. The PSD of the CL is a particularly relevant parameter to investigate because it can be adjusted by altering the particle size distribution and/or calendering processes, which is experimentally feasible. Three networks were generated with dimensions of [30,15,15] µm corresponding to a domain size of [120,60,60] pores in the x, y, and z direction. Alternative pore size distributions were then generated using a Weibull function with varying parameters, giving the distributions shown in Figure 3-14. The distributions included a wide PSD, a moderate PSD and a narrow PSD option, which span the ranges of sizes seen in the SEM micrograph shown in Appendix B. The pore and throat size distributions of the previous results (from section 3.4.1) are

included in Figure 3-14 for comparison. A complete set of cell performance simulations was performed with each option so the impact of PSD on saturation distribution and subsequent cell polarization behavior could be seen. The electrolyte invasion pattern at two different saturations of 0.1 and 0.3 for the three different PSDs is shown in Figure 3-15(a-f). Given that the saturation in each row is equal, the differences in the fluid configuration are striking. For the narrow PSD the invading fluid spans the entire domain at $S_w = 0.1$ (Figure 3-15(c)). For the wide PSD at $S_w = 0.3$ (Figure 3-15(d)), there are large regions of uninvaded pores. A comparison of the invasion front's saturation profile along the x-axis (the through-plane direction) is shown in Figure 3-15(g-i). At low saturations the profiles vary widely throughout the domain, indicative of electrolyte fingers with pockets of air interspersed. This invasion configuration is beneficial since it increases the electrolyte-gas interface length by creating more branches of electrolyte-filled pores at electrolyte-air interface. The saturation profiles become flatter as the electrolyte saturation increases since only small clusters of invaded pores remain.

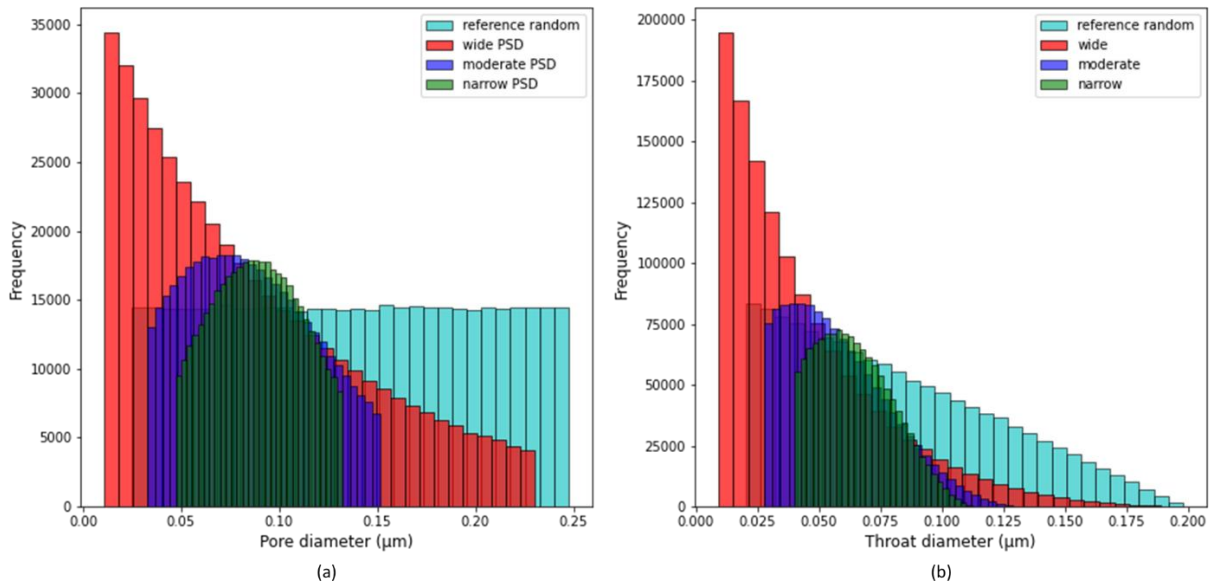

Figure 3-14 Network elements size distribution. a) Three Weibull pore size distribution with shape=1,2,3. Random pore size distribution from previous results are shown for comparison. b) Corresponding throat size distributions of the pore networks. Throat sizes are defined as a fraction of minimum pore size that is connected to the throat (0.85). Throat size distribution from previous results are shown for comparison.

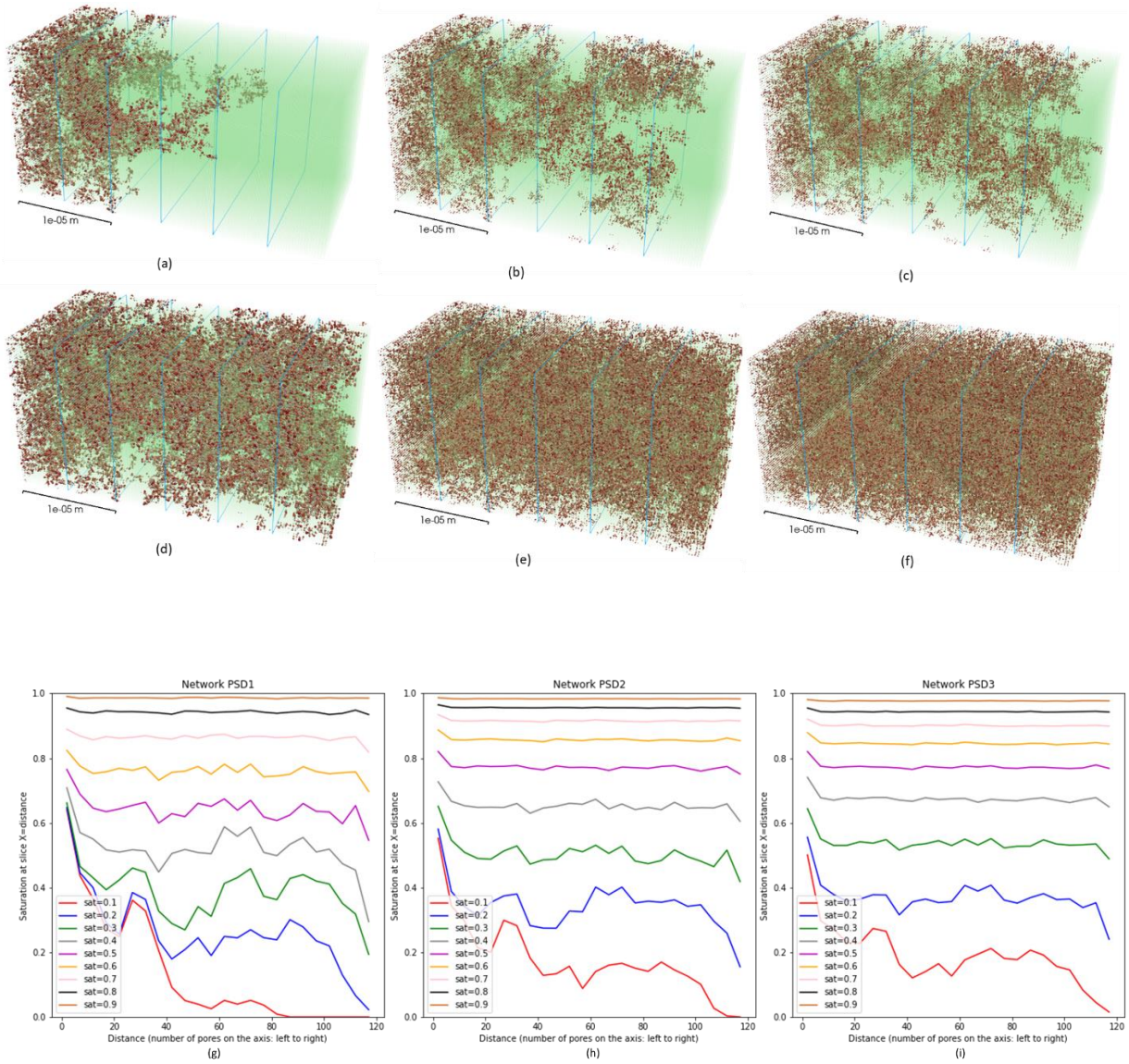

Figure 3-15 Electrolyte invasion in three PSD. a,b,c) Saturation=0.1 for wide, moderate, and narrow PSD, respectively. d,e,f) Saturation=0.3 for wide, moderate, and narrow PSD, respectively. g,h,i) Electrolyte saturation at each vertical slice (distance=X) in the network in three PSDs for electrolyte saturation step 0.1 to 0.9.

The key insight from these simulations is that the invasion pattern in each PSD is quite different, which will result in different electrolyte-gas interface and electrolyte tortuosity. These differences in the invasion pattern of each PSD also affects the performance of the electrode, as shown in Figure 3-16a. All three distributions have a similar peak power output around 70 mW/cm^2. The narrow PSD has a substantially higher peak power at lower saturation, while the wide PSD allows for a higher total saturation before the

performance collapses. This behaviour can be explained in terms of the electrolyte distribution and the number of electrolyte-gas interface throats for each network, as shown in Figure 3-16b. As the porosity of these three PSD is about half of the porosity of the previous results, the peak performance of only these three PSDs is the focus of analysis here. However, the previous results are included in Figure 3-16 for comparison. The peak performance corresponds very closely with the peak of number of interface throats. The wide PSD has a larger proportion of small pores which are the last to be invaded. These pores allow oxygen gas to transport deeper into the domain, even at very high saturations. This could be a useful feature since it allows the electrode to continue functioning even if high saturation is reached. On the downside, the wider distribution means that at lower saturation, the electrolyte is confined to the subset of large pores which reduces the amount of TBP created and leads to lower performance. These results clearly demonstrate that pore size distributions can be manipulated to obtain improved performance, but a more exhaustive study for an optimum distribution will be the focus of future work. It also remains to be seen if complex distributions can actually be realized in a lab.

As it was mentioned in section 3.4.3, it is important to operate the electrode under conditions where the concentration of KOH in the CL does not exceed its solubility limit. Therefore, the maximum concentration of OH^- in each PSD were examined at their peak performance. The maximum concentration of OH^- at the peak performance of wide, moderate and narrow PSD were $8.4\ M$, $8.2\ M$, and $8.2\ M$, respectively. These values indicate that KOH does not precipitate at the conditions corresponding to peak performance in these CLs. Note that the peak performance of wide, moderate and narrow PSD occurs at intermediate to high saturations ($0.5 - 0.8$) which matches well with saturation ranges shown in Figure 3-13. Although Figure 3-13 was developed based on a random PSD, its prediction was applicable (with some approximation) for these three PSDs.

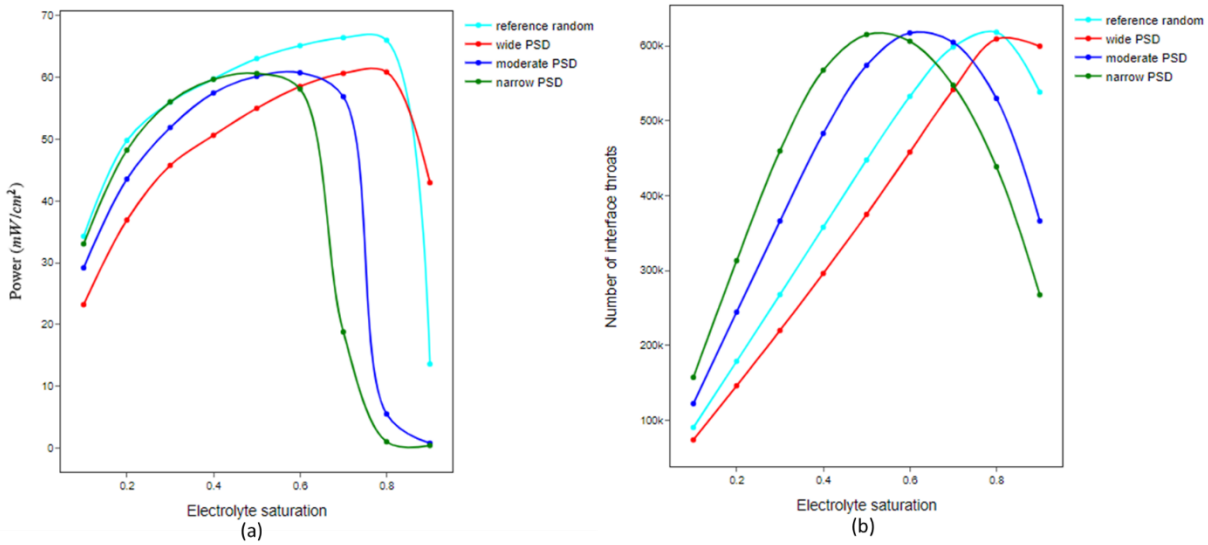

Figure 3-16 a) Power peak of the three PSDs vs the electrolyte saturation. The curve for previous results (reference random) is shown for comparison. b) Electrolyte-gas interface length (number of interface throats) of three PSDs vs electrolyte saturation. The curve for previous results (reference random) is shown for comparison.

3.5. Conclusions

A framework to model the CL of Zn-air flow batteries was developed based on PNM. This model allowed a detailed study of the electrolyte-gas interface and its effect on the cell performance. PNM was uniquely suited to this study since it can incorporate multiphase transport at the pore-scale in complex structures with computational ease. It was shown that the amount of electrolyte invasion and its pattern arising from the pore structure play an important role on the extent and configuration of the electrolyte-gas interface, and subsequently cell performance. The results showed that increasing the electrolyte saturation to provide more reaction sites (electrolyte filled pores) does not always increase the cell performance. As the invasion proceeds to higher saturations, the peak power reaches a maximum and then decreases. The behavior is explained by considering that the reaction predominantly occurs in the near interface pores, despite the fact that oxygen can dissolve into the electrolyte and be transported to pores deeper within the electrolyte phase [31], [75]. The peak amount of electrolyte-gas interface occurs at intermediate saturations, with the exact value depending on the pore size distribution.

The true utility of the PNM was in the detailed pore-scale information it provided, with respect to the interaction between the electrolyte-gas interface and its impact on electrode performance. In addition to the electrolyte-gas interface size, the effect of electrolyte saturation on tortuosity was studied. At lower

saturations the electrolyte front was shown to be highly tortuous which resulted in severely restricted transport of OH^-, such that concentrations exceeding solubility limit of KOH were observed. Such results can be used as a guide for the selection of the electrode structure and operating conditions to prevent KOH precipitation which may cause electrode degradation.

The importance of pore size distribution was studied to investigate how this could impact cell performance. Pore size distributions are potentially adjustable in the lab, so this study aimed to provide some guidance on the ideal structures. Although the maximum attainable peak power was close for all cases, it was found that CLs with wider pore size distributions continued to function well at higher saturations, while narrow PSD were more easily flooded. In contrast, CLs with narrow PSDs did perform better at low to intermediate saturations. It remains to be explored whether more elaborate structures could provide additional benefits. To the best of our knowledge, this is the most rigorous PNM developed for studying the electrolyte-gas interface and ORR in a metal-air cathode, with realistic 3D geometry and coupled multiphysics. The results of this work can be used as a guide in the design of the pore size distribution of the CL and the amount of electrolyte invasion (e.g. by altering wettability and/or electrolyte pressure). Future works can be focused on investigating the model's application on other electrochemical systems such as Phosphoric acid fuel cells and Alkaline electrolyzers, where porous electrodes operate with liquid-gas interface. Additionally, it would be of interest to use a heterogenous reaction for the ORR. For this purpose, a suggestion is to define the mass transfer coefficient in the pore network element and compare the results of concentration distribution in the electrolyte phase with direct numerical simulation results for validation purposes at pore-scale. Another future research could be developing a framework to solve the system of mass and charge transports using a simultaneous approach instead of the sequential approach to reduce the computational cost that is currently involved in the iterative method.

Chapter 4: Structure-performance relationship in multi-layer VRFB electrodes

4.1. Overview

Vanadium redox flow batteries (VRFBs) are a promising technology for large-scale and durable energy storage applications. The microstructure of the porous electrode affects the performance of these batteries. To guide the design of novel fibrous materials, identifying optimized electrode structures has become an active research area. However, to design optimal electrode microstructures for VRFBs it is crucial to study varieties of structural parameters and design cases using a modeling tool with low computational cost. In this study, a pore network modeling (PNM) framework was developed to study the effects of multi-layer electrodes on VRFB electrode performance. In contrast to previous experimental works that were focused on multi-layer structure of the same material, this study explores the effect of different microstructures at each layer. Using an image generation algorithm, different fibrous materials were artificially generated from which pore networks were extracted. The pore network framework also included a modification by introducing additional throat nodes in the network geometry. The new nodes were added to capture the heterogeneity in velocity distribution and accommodate a velocity dependence of mass transfer coefficient. Using polarization curves from PNM the performance of different structures was compared. The results in this study showed that in a multi-layer structure, the flow rate distribution depends on the arrangement of the layers. Putting a highly permeable layer near the membrane provides an alternative preferential path for fluid to distribute throughout the electrode thickness and to supply those regions with reactive species. Therefore, such electrode design results in a higher reaction rate and current density. Although this study was focused on multi-layer structures in VRFBs, the proposed PNM framework can be used to study the effect of other structural parameters within porous electrodes.

4.2. Introduction

Redox flow batteries (RFBs) are a promising energy storage technology that are being developed to support sustainable energy generation like wind and solar, which require some form of large-scale storage to buffer the mismatch between supply and demand. Amongst different redox couples for RFBs, vanadium redox flow battery (VRFB) technology has attracted more attention due to the use of the same material in cathodes and anodes, thereby reducing the risk of cross-contamination in cell compartments, which is a degradation issue. RFBs including VRFBs are electrochemical reactors and each component, such as the porous electrodes and membrane separator, contributes to the overall efficiency and performance of the system [118] as well as its durability [6]. The main roles of the porous electrode are to provide high surface area for electrochemical reactions (reaction), while being conductive to transfer electrons (conduction) [3] and permeable for electrolyte flow (convection). The efficiency of these transport processes is largely dictated by the structural properties of the electrode such as pore and fibers sizes, porosity, and fiber orientation. Therefore, ongoing efforts are focused on optimizing the porous electrode structure to provide VRFBs with better performance and lower operational cost [118].

The effect of structural properties on electrode performance has been the subject of numerous studies. Forner-Cuenca *et al.* [8] compared cloth and non-woven structures and found that the large spaces between the tows of the woven cloth provided enhanced permeability to flow while the denser regions inside each tow provided reactive surface area. The weaker performance of the non-woven electrode can be explained by the work of Wong *et al.* [119] who visualized the reaction distribution using a fluorescing tracer and transparent flow field. This revealed pronounced channeling in the nonwoven structures, which left many sections of the electrode starved of reactants. Together, these studies stress the key role that the porous structure plays on the transport processes occurring during the electrochemical reaction in these flow-through electrodes, though neither authors suggested novel designs. In addition to supporting flow and providing reactive surface area, diffusion and ion transport in the electrode are also crucial. In an early experimental study by Aaron *et al.* [120] it was found that merely stacking 3 standard sheets of electrode material (non-woven) substantially outperformed a single sheet. This clearly demonstrated the importance of providing increased surface area for the reaction, despite creating increased transport lengths for the reactive species. Following this, Tucker *et al.* [121] explored the impact of layered electrodes more deeply, including up to 6 layers, and also varying compression and therefor porosity. They found that 3 layers with 25% compression performed best since too many layers and too much compression both negatively impacted the ability of ions to transport to the reaction sites. Clearly there are many competing objectives,

suggesting that the search for an optimum electrode design would benefit from a numerical performance model that incorporates the structure of the electrode.

The ability to create fibrous materials in lab provides a wide range of design opportunities for electrodes, though it would be time consuming to perform experiments on each candidate structure. To design electrode materials more efficiently, a computational model that describes the local distribution of species and transport phenomena within the porous structure of the electrode is required. Various modeling techniques have been used for studying VRFBs for different purposes. Volume averaged models are the most common approach for studying the electrode properties and cell performance [15], [16], [122]. These models assume the electrode is a homogeneous continuum domain with macroscopic properties such as porosity, permeability, and tortuosity. Although those models provide insights into macroscopic trends such as increasing permeability with increasing the porosity [43], they do not capture the microstructure at pore-scale level for detailed structural-performance analysis. Or in other words, they do not provide a recipe for how to make a customized electrode, only what properties it should have. For instance, He *et al.* [123] used a finite element method (using COMSOL [122]) to explore the impact of porosity gradients in the electrode with porosity increasing from the membrane side to the flow field side. Their results in a serpentine flow field showed that with such a design electrochemical reaction can occur more uniformly throughout the through-plane direction in contrast to an electrode with a constant porosity, which may result in higher reaction rates near the flow field or membrane depending on the porosity. Although a porosity gradient may be enticing, it is not clear how to obtain it in the lab. Moreover, it is almost certain that the correlations used for other porosity dependent properties (e.g., tortuosity) will not apply to any arbitrary electrode structures, which can take on many forms such as reticulated foams, sintered grains, or highly aligned fibers.

In contrast, direct numerical simulations on volumetric images of an actual microstructure can resolve transport phenomena at pore-scale level, making them a useful tool to study the transport phenomena in porous structures, without the limitation of continuum models mentioned above. Chen at al. [18] used the lattice-Boltzmann method (LBM) to study the effect of electrode porosity and fiber diameter on its permeability and transport of reactive species. Their results showed that at a constant porosity, reducing fiber diameter results in increased surface area and decreased permeability, which lead to rapid depletion of reactive species. At a constant fiber diameter, reducing porosity results in a similar effect. Although their study included a large number of stochastically generated fibrous images, their analysis did not include other structural parameters such as fiber orientation, nor did they incorporate the electrochemical performance and polarization behavior. Applying LBM on voxel images of porous materials is extremely computationally expensive, and this is even more limiting when considering the additional physics required

to include electrochemical performance. Qiu *et al.* [42] also used LBM to study electrolyte flow through the porous electrodes, while the coupled charge and mass transport equations were solved using finite volume method. Their work was focused on the effect of operational conditions on the cell performance and yielded valuable results on the distribution of species and current; however, structural parameters were not studied. To address the issue of high computational cost, some studies have turned to machine learning. Wan *et al.* [124] developed a genetic algorithm to find optimum structural parameters that resulted in optimum surface area and permeability values. To calculate the values of surface area and permeability they have developed a machine learning framework that maps the structural properties of fibrous materials to the objective parameters. They have concluded that that smaller fiber diameters and more alignment of fibers provide optimum surface area and permeability, which is supported by existing experimental data [125]. Although their framework included different structural properties including fiber diameter, alignment, and porosity, their results were limited to the effect of structural properties on surface area and permeability. Therefore, electrochemical performance of the generated materials and operational conditions were not considered.

Clearly there is a need for a modeling framework that captures the pore-scale information while being computationally efficient. Pore Network Modeling (PNM), where the porous domain is modeled as a connected network of pores and throats can provide pore-scale resolved information while being computationally inexpensive. Sadeghi *et al.* [2] used PNM to study the effect of electrode microstructure on the performance of H-Br flow batteries. Their study showed the value of fiber alignment to increase flow battery performance by locally increasing the fluid velocity. This was the first PNM study to model the full electrochemical polarization behavior of a redox flow battery and demonstrated the direct impact of structure on performance; however, their work was based on simple cubic networks, which have simplified assumptions about the network structure. So, although their study pointed to a potential avenue for structural optimization, it was not apparent how an actual electrode might look. Since the porous structure of the electrodes have such an important impact on performance, it is essential to investigate the real porous electrodes characteristics. Lombardo *et al.* [28] developed a PNM for modeling redox flow battery electrodes that pioneered the use of the Nernst-Planck equations in the pore network scheme. Their study was limited to exploring the effect of migration and convection terms on the distribution of species and current within the network, therefore, the structural properties of the material were not investigated. Simon *et al.* [126] studied the effect of commercial electrode microstructures on performance, but they only used PNM to model the fluid flow through the electrode and find the pressure distribution. They then resorted to a 1D continuum-based model for modeling transport of species and finding the mass transport coefficient. Their results showed that best performance was seen in cloths with high permeability and mass-transfer

coefficient. Despite their comprehensive study on available commercial materials, their work was limited to looking at the effect permeability values of existing materials. Designing new materials requires exploration of many structural parameters such as fiber alignment, diameter, and their effect on the electrode performance. Moreover, using a 1D continuum-based model for electrochemical modeling limits the investigations to averaged properties instead of detailed pore-scale information. Heijden *et al.* [29] applied PNM to simulate the electrochemical processes in RFB porous electrodes, with the added feature that mass transfer resistance was included in the reaction term, so the bulk and surface concentrations in pores could differ. They also limited their study to commercially available materials, then focused on the impact of flow rates, which alters the pore-level mass transfer. Although their results can be used as a guide for selecting an ideal operational condition for a given electrode structure, the effect of migration of species and further structural parameters were not included. Moreover, their mass transfer coefficients were independent of local velocities and the effect of velocity was applied as a correction factor. This limits the application of their model for studying heterogeneous fibrous materials where local velocity values vary significantly, such as the excessive channeling observed by Wong *et al.* [119] . Therefore, there is a need for a PNM-based framework to study fibrous materials with different structural parameters and analyze their performance while rigorously including the effect of heterogeneity in velocity and mass transfer coefficients, since this is the only way to fully capture the impact of structural changes on performance.

As mentioned earlier, different studies suggested that multi-layer structure for electrodes provides a better performance in RFBs. In this study, a framework based on PNM was developed to explore the concept of multi-layered structures in terms of the structure-performance relationship. The first step was generating images of fibrous materials with different structural parameters [127]–[129] from which the pore network was extracted. Several substantial and important modifications were required to the pore network framework itself, such as including throat nodes. This was necessary to compute the pore-scale, velocity dependent mass transfer coefficients since fluid velocity is only defined in throats. This modification is also closer to reality as the reaction occurs at the fiber surfaces which define the throat constrictions. Next, their resulting pore network model was used to solve the system of Nernst-Plank mass and charge transport equations, incorporating mass transfer limitation into the reaction terms. The developed PNM was validated based on experimental polarization data in literatures [130]. Finally, the developed framework was used to study the performance of different multi-layer electrode structures and their impact on RFB performance and operating cost.

4.3. Model development

4.3.1. Cathode medium

The present study is focused on modeling the positive electrode half-cell of the VRFB as illustrated in Figure 4-1a. The findings obtained for this half-cell are equally valid for the counter electrode as well, but for the sake of simplicity only one electrode was considered. All comparisons to literature data were therefore limited to half-cell studies which eliminate polarization effects at the counter electrode. The cathode domain included an electrolyte channel to distribute the electrolyte and reactants, a polymer membrane that allowed the transport of protons from the cathode towards the anode, a porous electrode where the electrochemical reactions occurred, and current collectors. Due to symmetry, the domain was defined to span from the center of the inlet channel, across a full rib, and a half of the outlet channel, as shown in Figure 4-1b. As the effect of cell length on modeling result is assumed to be negligible [131], to reduce the computational cost a fraction of electrode length was modeled with dimensions given in Section 4.4.1. Because the main goal of this study was to investigate the structural properties of porous electrodes, the computational domain was limited to only the porous electrode, with the flow channels, current collectors and the membrane treated as boundary conditions. Generating the fibrous material image and pore network extraction methods are explained in following sections.

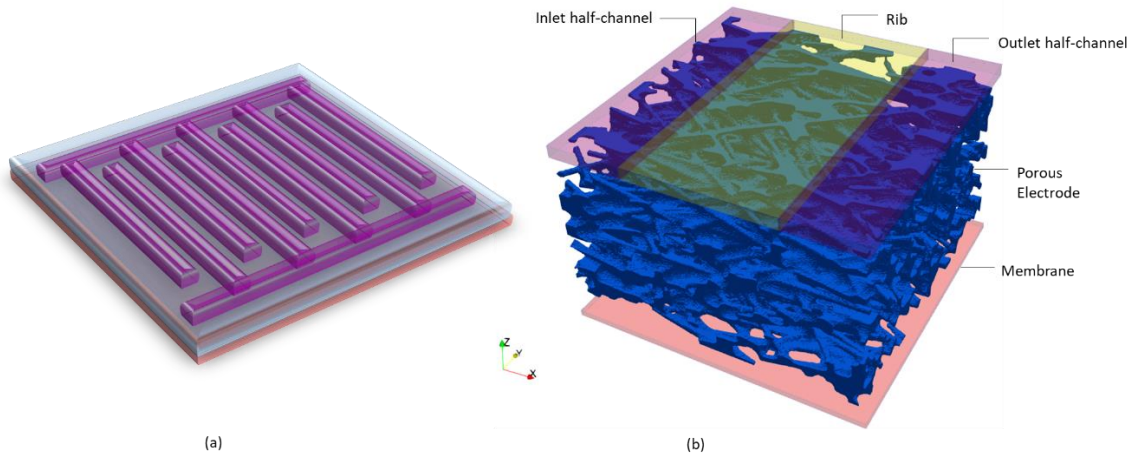

Figure 4-1 a) Schematic of a VRFB cathode medium with an interdigitated flow field. b) Modeling domain, which includes a half-channel, rib, and a half-channel.

4.3.1.1. Fibrous materials generation

In this section the developed algorithms for generating random fibrous materials are explained. First, the algorithms to generate random materials without binders are defined. Second, the developed image processing framework to include binders are explained. Fibrous materials with binders were used for validation purposes in Section 4.4.1.

To generate random fibrous images overlapping cylinders were inserted into a blank image (PoreSpy's *cylinders generator* was used [132]). The main assumptions for the algorithm are that fibers have a circular cross section (cylindrical fibers), have negligible curvature, and are allowed to intersect [124]. The algorithm takes in the structural properties of the fibrous material including number of fibers or porosity, fiber diameter, and fibers' 3D orientations to generate a random fibrous material with the given properties. The 3D fiber orientation includes the polar angle (φ) and azimuthal angle (θ) of the fibers, defined as through-plane and in-plane orientation degree [124]. Additional parameters such as maximum length of the fibers and iterations can also be defined. The algorithm can be used to generate a fibrous material with either a given number of fibers or a given porosity as follows:

A) Assuming a predefined number of fibers, each fiber is generated with a random starting point in the domain, then oriented at random angles of φ and θ out of XY plane (polar) and within the XY plane (azimuthal), respectively, within the range of 0 to maximum predefined value to create the final image of the fibrous material. Special attention was given to adjust each fiber's length to span throughout the domain, if not defined.
B) Assuming a predefined porosity the algorithm first estimates an initial value for the number of fibers to be added in the domain, based on a rough estimation of the fibers' length and volume. The assumption for initial estimation of porosity is based on the fact that for a given domain volume vol_{total}, when potentially overlapping fibers are randomly inserted into the domain the total volume of added fibers is vol_{added} and the porosity can be estimated as $\exp\left(-\frac{vol_{added}}{vol_{total}}\right)$. Once the number of fibers is estimated (n_{fibers}), the algorithm inserts a small fraction of n_{fibers} into the domain using the method explained above (part A) and calculates the true volume of fibers. Then additional fibers are inserted into the domain. This process repeats for a predefined maximum number of iterations, resulting in an image with a porosity close to the predefined porosity.

When simulating electrospun materials later in this work, only overlapping fibers are necessary. However, when validating the present workflow comparison is made to commercial fibrous mats which include

carbonaceous binder to hold the fibers together. Consequently, it was necessary to simulate the presence of binder in some images. A schematic of the steps to include binder in a generated fibrous material is shown in Figure 4-2. First, a random binary image of fibrous material (pore = 1, solid = 0) with given properties is generated using cylinders generator algorithm described above. Figure 4-2a shows an example of a generated image with number of fibers of 600, and maximum φ and θ angles of 15 and 45, respectively. Note that the voxel size was chosen to be 1 μm, therefore fiber radius was defined as 4 voxels. Next, the distance map of the void space was calculated using Euclidean distance transform giving the result shown in Figure 4-2b. A threshold was then applied to distance map to create a mask of all voxels greater than a distance R from the solid (Figure 4-2d). This mask was then dilated with a spherical structuring element of radius R as shown in Figure 4-2c. The choice of R depends on the number of fibers, target porosity, and desired volume fraction of binder. This morphological dilation defines the void space, so any voxels previously attributed to void but not part of the dilation represent additional solid phase around the fibers, and is concentrated in the areas where fibers are overlapping. This process mimics the accumulation of binder at the fiber intersections that is observed in microscope images. The resulting image is the final image for pore network modeling where fibers and binder are labeled as 0, and void space is labeled as 1. A segmented image of the fibrous material is shown in Figure 4-2e, where void space, fibers and binders are labeled as 1, 0, and 2, respectively. Although binder is generally microporous, these pores do not contribute to the flow due to their small size, and do not contribute to the reaction since they are largely starved of reaction, hence the binder is treated as solid in the subsequent network extraction step. The final solid structure, including both fibers and binder is shown in Figure 4-2f.

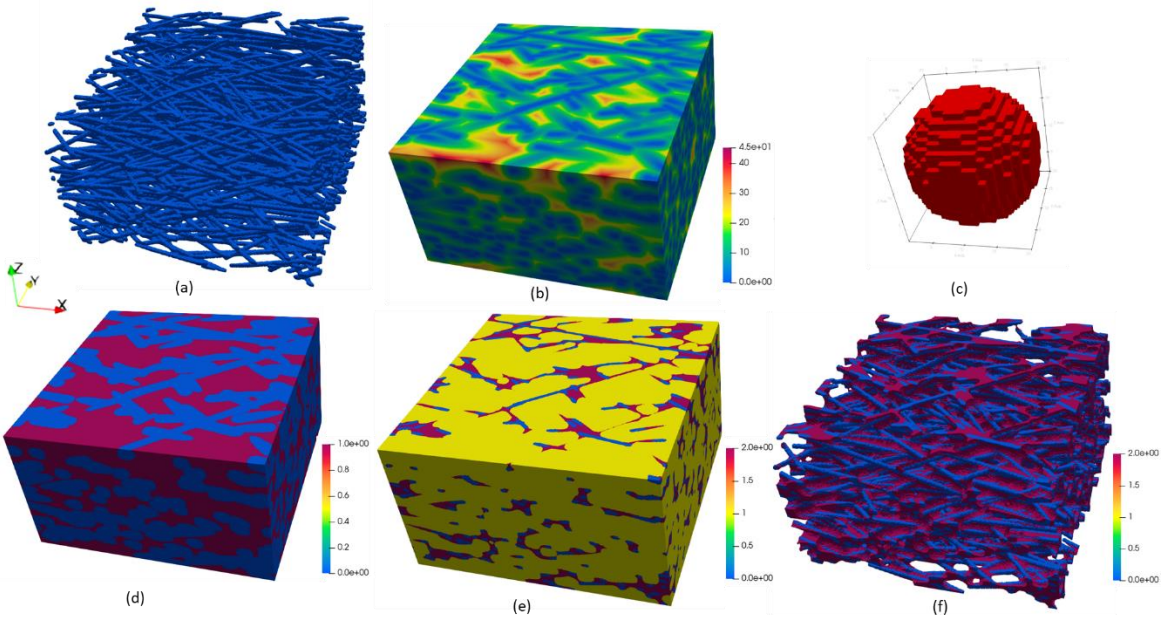

Figure 4-2 An example of the steps for creating a random fibrous material including binders. a) Random fibrous material generated using PoreSpy's *cylinder generator* method b) Distance map of the void space c) A spherical structuring element with radius R used for morphological image processing d) Masked image e) Segmented image of the dilation result including void (yellow), fibers (blue) and binders (red). f) Final image of the fibrous material including fibers and binders.

4.3.2. Network extraction

The SNOW algorithm [51] was used for extracting pore networks of the generated fibrous materials. SNOW is a pore network extraction method based on watershed segmentation approach with a main benefit of reducing network extraction errors for high-porosity materials. During network extraction the void space is segmented into pore regions using modified watershed segmentation [51]. The segmented image is then mapped to a connected network of pores and throats, where each region corresponds to a pore and the connecting face between neighbouring regions corresponds to a throat. In traditional network modeling the balance equations are solved on the pores, and this is where chemical reactions would be included since reactions are functions of concentration. In this study, however, it was necessary to augment this paradigm since the reaction is also a function of mass transfer to the fiber surface [133], which requires knowing the local fluid velocity, but this is only known in the throats. To include the both concentration dependent

reactions and the mechanism of mass transfer from bulk to the solid-liquid interface, the network geometry was modified to include additional nodes positioned at the centroid of original networks' throats. Defining computational nodes on throat locations were previously implemented in other applications such as heat transfer [134] and mineral dissolution [135]. More details about mass transfer coefficients and their dependence on velocity are explained in Section 4.3.3.3.

The process of adding throat nodes to the network is illustrated in a flow chart shown in Figure 4-3. To create the additional nodes in the network model, first new throat nodes were added at the centroids of original throats, followed by trimming the original throats. New throat connections were then added to the network to connect new throat nodes to their neighbouring pores, which were previously connected by original throats. The geometrical properties of the new throat nodes such as diameter were assigned from the original throat diameter. As these additional nodes are reactive, their reaction surface area was calculated as sum of half of the surface area of their neighbouring pores.

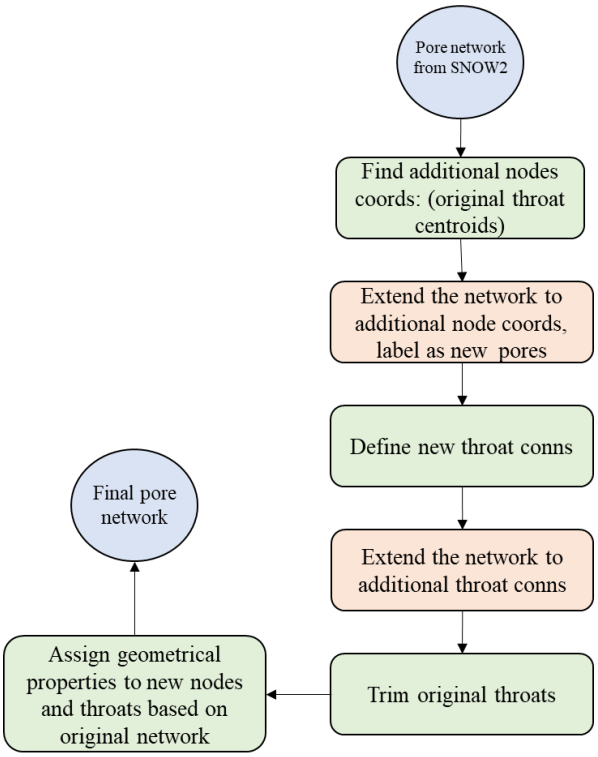

Figure 4-3 A flow chart of modifying the geometry of extracted network to accommodate additional nodes for PNM.

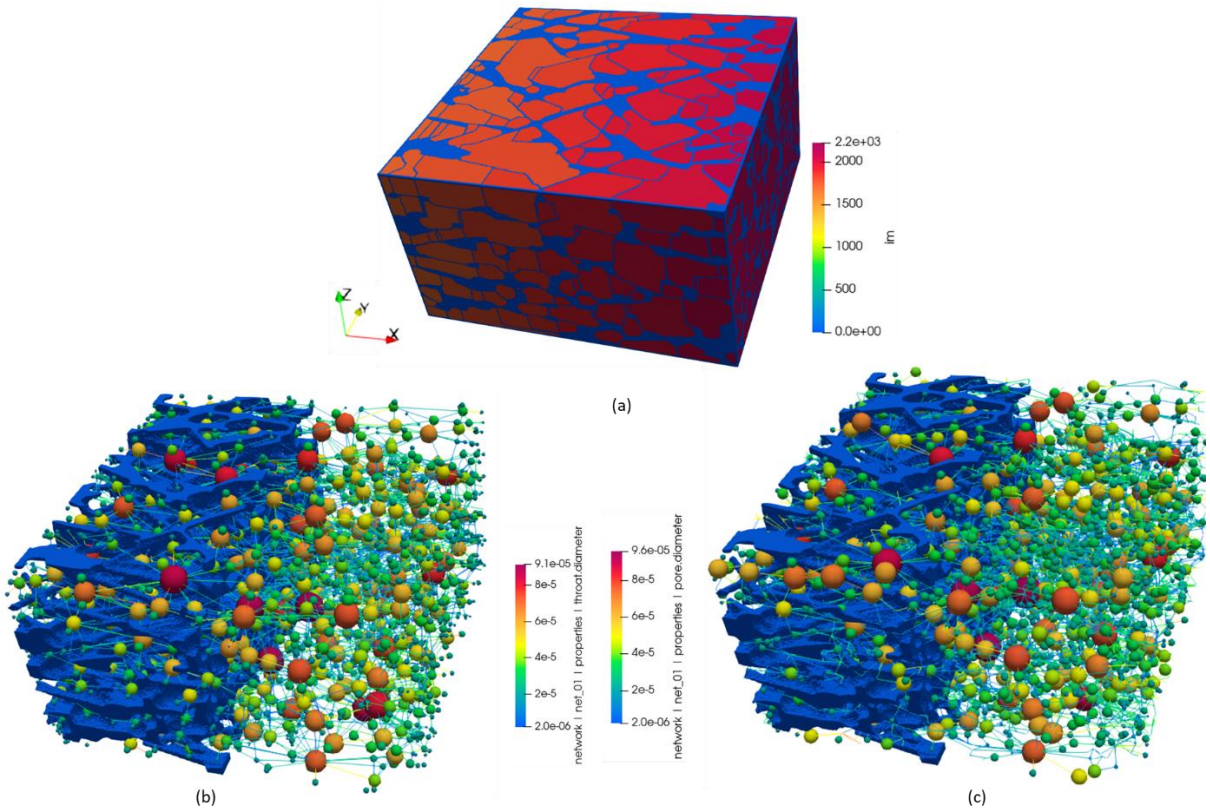

Figure 4-4 Comparison of original extracted network and geometry updated network with additional nodes for a random fibrous image. a) Segmented regions in network extraction b) Original network extracted using *Snow2* algorithm in PoreSpy. Only for visualization purposes pores and throats are shown as sphere and wireframes. c) Network with updated geometry where additional nodes are located at previous network's throat center.

Figure 4-4 shows an example of the original network and modified network, which was extracted from the fibrous image in Figure 4-2. Note that only for visualization purposes, the network pores and throats are shown as spheres and cylinders. The geometry of the pore network is actually modeled using connected pyramids, where the intersection of joined pyramids are assumed to be cuboid throats with the length of 1 voxel as shown in Figure 4-5. A schematic of two pore regions in the original extracted network and their corresponding pore network elements are shown in Figure 4-5. These connected regions form a conduit which extended from the center of one pore to the center of the neighbouring pore (Figure 4-5b). The transport properties of the modified network conduits were defined using the information from the original network (such as diffusive and hydraulic size factors) to ensure the geometry modification does not change

effective properties (e.g. permeability) of the resulting pore network. More details on defining conduits' transport properties are explained in Section 4.3.3. The developed PNM was implemented using open-source software PoreSpy [132] and OpenPNM [49].

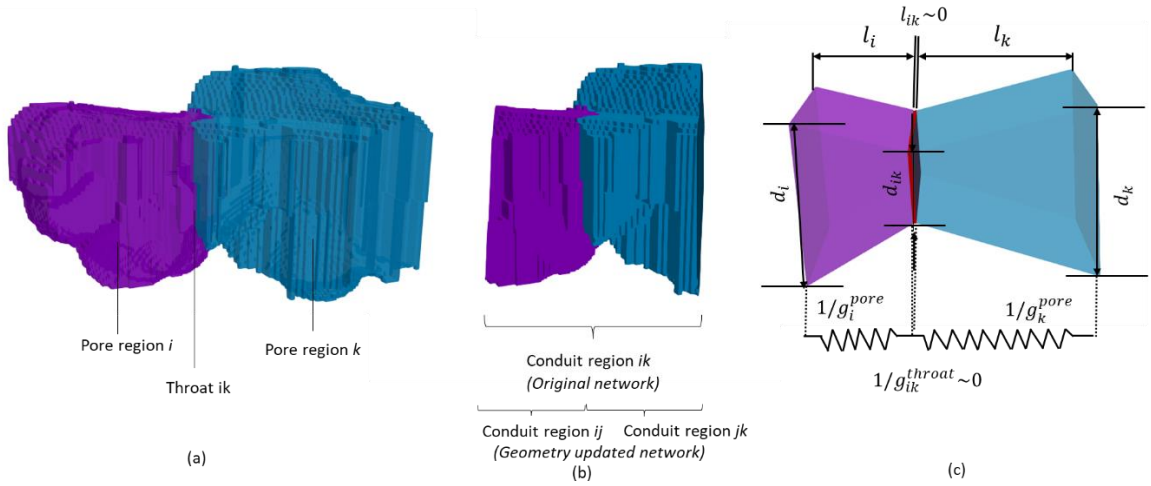

Figure 4-5 A schematic of conduit regions and their corresponding PNM element. a) Two connected pore regions from segmented image of a porous domain. b) Conduit regions include 3D image of the connected pores extending from pore i's centroid to pore k's centroid. c) Corresponding PNM element of the conduit region in part b from original extracted network. Pores and their connecting throat are modeled as pyramids and cuboid. In the updated network creating an additional node on throat location (node not shown here) breaks the conduit into two conduits of ij and jk.

4.3.3. Transport Equations

The transport phenomena in the cathode include advection-diffusion-migration of species, and charge transport including reaction kinetics. During the discharge, the reaction at the VRFB positive electrode is as follows:

$$VO_2^+ + e^- + 2H^+ \rightarrow VO^{2+} + \mathrm{H_2O} \qquad (4\text{-}1)$$

where for simplicity VO_2^+ and VO^{2+} ions are denoted as V^{5+}, and V^{4+} in the remaining sections. The PNM of the porous electrode was developed based on the following assumptions: 1) Steady state condition, and 2) diffusion coefficients in the electrolyte depend only on the initial electrolyte concentration. Mathematical details of each transport phenomena are described in the following sections.

4.3.3.1. Stokes Flow

Electrolyte flow through the porous electrode is described by Steady-state Stokes flow, assuming a single phase, Newtonian fluid for the electrolyte [45]. The mass balance for an arbitrary pore *i* is then defined as follows:

$$\sum_{j=1}^{N_i} G_{h,ij}\left(p_i - p_j\right) = 0, i = 1,2,\dots,N_P \tag{4-2}$$

where p_i, and p_j are pressure values in pore *i* and *j*, respectively. $G_{h,ij}$ is the hydraulic conductance of the conduit ij , which includes pore i and newly added nodes j (located at the throat centroids of originally extracted network). Conductance of conduits in the modified network can be found from the conductance of conduit elements in the original network ($G_{tr,ik}$) using resistors-in-series model as schematically shown in Figure 4-5c. The general formulation of the resistors-in-series model for a transport mechanism *tr* in a conduit containing pore i, throat ik, and pore k is as follows:

$$\frac{1}{G_{tr,ik}} = \frac{1}{g^p_{tr,i}} + \frac{1}{g^t_{tr,ik}} + \frac{1}{g^p_{tr,k}} \tag{4-3}$$

where $g^{p|t}_{tr,(i\,|\,ik\,|\,k)}$is the conductance of transport 'tr' for each element in the conduit. For a flow mass transport problem, the hydraulic conductance of pore i element can be defined using Hagen–Poiseuille model as follows [45]:

$$g^p_{h,i} = \frac{\pi}{128\mu}\left(\frac{d_i^4}{l_i}\right) \tag{4-4}$$

where d_i and l_i are the diameter and length of pore i. The hydraulic conductance of pore k and throat ik in the conduit can be found in a similar manner as for pore i using Eq. (4-4). As throats are defined as the intersecting plane between the pyramid pores ($(l^t \approx 0) \ll l^p$) their resistance was assumed to be negligible. Therefore, the right-hand side of Eq. (4-3) includes only pore i and pore k. Hagen–Poiseuille model was developed for cylindrical elements, but in the extracted network the pore regions have irregular shapes. Assuming an intersecting pyramids conduit in originally extracted network, the conductance of each pore element can be found based on a correction size factor ($\lambda^{hyd}_{(i\,|\,k)}$) [48]:

$$\lambda^{hyd}_{(i\,|\,k)} = \frac{1}{\int_{l_i} \frac{I_p^*}{\left(A_{(i\,|\,k)}(x)\right)^2}\,dx} \tag{4-5}$$

where I_p^* is the specific polar moment of inertia and $A(x)$ is the cross-sectional area of the element. Given the pore diameter d_i and throat diameter d_{ij} , $\lambda_{(i\,|\,k)}^{hyd}$ will be:

$$\lambda_{(i\,|\,k)}^{hyd} = \frac{1}{\frac{8}{9}\pi^2 l_i \frac{d_i^2 + d_i d_{ij} + d_{ij}^2}{\left(d_i d_{ij}\right)^3}} \tag{4-6}$$

The conductance of each element can then be defined as:

$$g_{h,(i|k)}^{p} = \frac{\lambda_{(i\,|\,k)}^{hyd}}{\mu_{(i|k)}} \tag{4-7}$$

Now that the conductance of elements in the originally extracted network are defined, the hydraulic conductance of conduits in modified network can be found using resistors-in-series model as shown in Figure 4-5. The hydraulic conductance of conduit ij ($G_{h,ij}$) containing pore i and newly added node j will be equal to $g_{h,i}^{p}$. Similarly, the hydraulic conductance of conduit jk ($G_{h,jk}$) containing newly added node j and pore k will be equal to $g_{h,k}^{p}$. Assigning conductance values for PNM elements based on the originally extracted network ensures that additional nodes do not affect the characteristics of the domain such as permeability of the network.

Fluid flow boundary conditions:

For modeling the fluid flow in porous electrode, a constant inlet flow rate or inlet velocity boundary condition was applied at the boundary between the porous electrode and inlet channel. The average velocity of the inlet channel in an interdigitated flow model was found based on the total volumetric flow rate (Q_T) and channel geometry [136], [137]:

$$v_{in} = \frac{Q_T}{N_{c,in} W_c L_c} \tag{4-8}$$

where W_c and L_c are the width and length of the channel, respectively. $N_{c,in}$ is the number of inlet channels in the interdigitated flow field. To accommodate this boundary condition, a fictitious inlet pore was added to the network geometry. This fictitious pore was only connected to the pores in the cathode located at the interface of porous electrode and inlet channel (inlet pores). A conductance value of infinity was assigned to the throats connecting the fictitious pore and inlet pores. Once the flow simulation was solved, the fictitious pore was removed from the network. At the boundary between the porous electrode and outlet half channel, a constant pressure equal to zero was assigned to the outlet pores. A no-flux boundary condition was assumed for other remaining boundaries.

4.3.3.2. Species transport

At the positive half-cell the electrolyte which includes water and ionic species (V^{5+}, V^{4+}, H^{+}, and SO_4^{2-}) flows through the porous electrode. The transport of ionic species within the porous electrode includes advection, diffusion, and migration. The mass transport of ions except for SO_4^{2-} was modeled using the Nernst-Planck equation [45], [107], [108], while the concentration of SO_4^{2-} was calculated based on the electroneutrality condition ($\sum_n z_i^n c_i^n = 0$). The molar flux of species n based on the Nernst-Planck formulation developed by Agnaou *et al.* [45] using an upwind discretization scheme is as follows:

$$\sum_{j=1}^{N_i} \left[G_{d,ij}^n + max\left(q_{ij} - m_{ij}^n, 0\right)\right] c_i^n - \sum_{j=1}^{N_i} \left[G_{d,ij}^n + max\left(-q_{ij} + m_{ij}^n, 0\right)\right] c_j^n + S_i^n = 0 \quad , i = 1, 2, \dots, N_p \tag{4-9}$$

where $G_{d,ij}^n$ is the diffusive conductance of conduit ij. q_{ij} is the electrolyte flow rate at throat ij. m_{ij}^n is the migration rate of species n. Migrative and diffusive conductance of conduit ij can be calculated from originally extracted network (conduit ik) using a similar resistors-in-series approach explained in Section 4.3.3.1. The diffusive conductance of pore i element in original network can be defined as follows:

$$g_{d,i}^p = \frac{D_{i,k} A_i}{L_i} \tag{4-10}$$

where $D_{\mathrm{i,k}}$ is the molecular diffusivity of species k, A_i is the cross-sectional area of the pore i, and L_i is the length of the element. Assuming an intersecting pyramids conduit in originally extracted network, the conductance of each pore element can be found based on a correction size factor ($\lambda_{(i\,|\,k)}^{diff}$) defined as follows [48]:

$$\lambda_{(i\,|\,k)}^{diff} = 1 / \int_{l_i} \frac{1}{A_{(i\,|\,k)}(x)} dx \tag{4-11}$$

Given the pore diameter d_i and throat diameter d_{ij} , $\lambda_{(i\,|\,k)}^{diff}$ will be:

$$\lambda_{(i\,|\,k)}^{diff} = \frac{1}{\frac{l_i}{d_i d_{ij}}} \tag{4-12}$$

The corrected diffusive conductance of pore elements can then be found as:

$$g^{p}_{d,(i|k)} = D_{(i|k)}\lambda^{diff}_{(i\,|\,k)} \tag{4-13}$$

Similar to Section 4.3.3.1, the diffusive conductance of conduit ij ($G_{d,ij}$) containing pore i and newly added node j will be equal to $g^{p}_{d,i}$.

The volumetric flow rate q_{ij} can be calculated as follows:

$$q_{ij} = G_{h,ij}(p_i - p_j) \tag{4-14}$$

The migration rate of species n can be calculated as follows:

$$m^{n}_{ij} = G^{n}_{m,ij}(\phi_i - \phi_j) \tag{4-15}$$

where $G^{n}_{m,ij}$ is the migrative conductance of conduit ij, found from resistors-in-series model, where the migrative conductance of each element (pore/throat) is calculated as follows:

$$g^{\mathrm{n}}_{m,i} = \frac{z^{\mathrm{n}}F}{RT}\, g^{\mathrm{n}}_{d,i} \tag{4-16}$$

where z^{n} is the valence of species n, and $g^{n}_{d,i}$ is the diffusive conductance of pore element i, found from Eq. (4-11).

The last term in Eq. (4-9) is the reactive source term defined as follows:

$$S^{n}_{i} = \frac{rate\ of\ reaction}{\vartheta \times F} \tag{4-17}$$

where ϑ is species stoichiometric coefficient in reaction (4-1) and F is Faraday's constant. Rate of reaction can be defined using Butler-Volmer kinetic model, which will be explained in Section 4.3.3.4. Note that S^{n}_{i} is non-zero in reactive nodes.

Species transport boundary conditions:

At the inlet pores a constant concentration boundary condition was assigned for transport of species ($V^{5+}, V^{4+}, \mathrm{H}^{+}$). The inlet concentration for each species was defined based on the initial molarity of the vanadium electrolyte (M_V), sulphuric acid, and state of charge (SOC) as follows:

$$c_{V^{5+}} = SOC \times M_V \quad (4\text{-}18)$$

$$c_{V^{4+}} = (1 - SOC) \times M_V \quad (4\text{-}19)$$

$$c_{H^+} = M_{acid} - (1 - SOC) \times M_V \quad (4\text{-}20)$$

$c_{so4^{2-}}$ was defined based on electroneutrality in the electrolyte solution.

At the outlet pores, an outflow boundary condition was applied, which means the gradient of the species concentration is zero [24].

4.3.3.3. Mass transfer coefficient

The electrochemical reaction in the porous electrode takes place at the solid-liquid interface at reactive nodes. Therefore, the reaction rate is controlled by the mass transfer of species from the bulk solution to solid-liquid interface. The rate of mass transfer to the interface is proportional to the concentration difference and the interfacial area [133], and the proportionality is defined as mass transfer coefficient. The mass transfer in terms of rate can then be defined as follows:

$$R_i^n = k_m A(C_b^n - C_s^n) \quad (4\text{-}21)$$

where R_i^n is the rate of transport of species *n* at the interface, k_m is the mass transfer coefficient, A is the interfacial area, and C_s^n and C_b^n are the concentration at the interface and in the bulk solution, respectively. The physical meaning of mass transfer coefficient is that it's the rate constant for transport of species from bulk solution to the interface and it has the dimension of velocity [133]. Many different correlations have been developed to calculate the mass transfer coefficient depending on the flow and geometry of the system. A common form is to define the mass transfer correlation based on dimensionless parameters Sherwood (Sh) and Reynolds (Re) number as follows [133]:

$$Sh = a \times Re^b, k_m = Sh \times (D/l) \quad (4\text{-}22)$$

where D is the diffusion coefficient of species, l is the characteristic length. For fibrous materials, many correlations use fiber diameter (d_f) as characteristic length and interstitial velocity as the velocity used in Re [138]–[140]. However, those correlations apply to mass transfer at the continuum scale, while the PNM approach requires correlations that apply to individual throats. Additionally, depending on the range of Re at relatively low Re, which is the case for VRFBs some correlations provide a higher estimation error outside their range of application [141]. Correlations can be found based on flow over a single cylinder or single fiber using experimental methods [140], [142], however, it has been found that those correlations

overestimate the mass transport rate because flow around a single fiber differs enough from flow through a conduit defined by a constriction between several fibers [141]. Therefore, to determine a suitable local mass transfer coefficient for use within the PNM framework, a series of simulations were performed, which imitates the experimental steps used to define global correlations. The details of the PNM simulation and assumptions are as follows: For a range of inlet flow rate (resulting in a range of global Re), the Stokes flow algorithm followed by advection-diffusion algorithm was applied on the PNM to find the global mass transfer coefficient of the domain. It was assumed that the system was under mass transfer control, which is equivalent to limiting current conditions in experimentally developed correlations [139]. Therefore, the concentration at the solid surface was set to zero. It was confirmed that the bulk concentrations did not change significantly from inlet to outlet, as is required by the definition to use Eq.(4-21). The advection-diffusion algorithm was then applied with a constant inlet concentration at the inlet pores ($C_i^n \approx C_b$) of the network (left), and outflow boundary condition at the outlet pores (right). Therefore, the advection-diffusion algorithms solves for following mass transport equation for V^{5+} species [143]:

$$\sum_{j=1}^{N_i}\left[G_{d,ij}^n + max\left(q_{ij},0\right)\right]c_i^n - \sum_{j=1}^{N_i}\left[G_{d,ij}^n + max\left(-q_{ij},0\right)\right]c_j^n = -k_{m\_local}A_{rxn_i}(c_i^n) \quad (4\text{-}23)$$

where $k_{m_local}$was defined using local Re (with characteristic length of d_f) in newly added nodes (reactive nodes):

$$k_{m\_local} = \alpha Re^{\beta}(D/d_f) \quad (4\text{-}24)$$

where local Re was defined based on velocity values at throat nodes. A range of α and β were defined for each simulation. The value of k_{m_global} at each inlet flow rate was found as:

$$k_{m-global} = total\ reaction\ rate/A_{rxn_{total}}(C_b^n - 0) \quad (4\text{-}25)$$

Given the fact that $k_{m-global}$= $Sh_{global} \times (D/df)$ [139] and $Re_{global} = \frac{\rho v_{in}}{\mu d_f \varphi}$, the global correlation for Sh_{global} vs Re_{global} was found using least square regression model based on calculated Sh_{global} and Re_{global}. The resulting global correlations were then compared with existing literatures for flow in fibrous materials and flow over single fiber/cylinder [139]–[141]. The final value of local formulation (α , β in Eq.(4-24)) was then selected such that their corresponding global correlation matches the existing literature trend within an acceptable accuracy. As shown in Figure 4-6, the global correlation is within the range of correlations developed for fibrous materials [139], [141]. The corresponding global and local correlations are $Sh_{global} = 0.825\ \mathrm{Re}_{\mathrm{global}}^{0.73}$and $Sh_{local} = 1.0\ Re_{local}^{0.7}$, respectively.

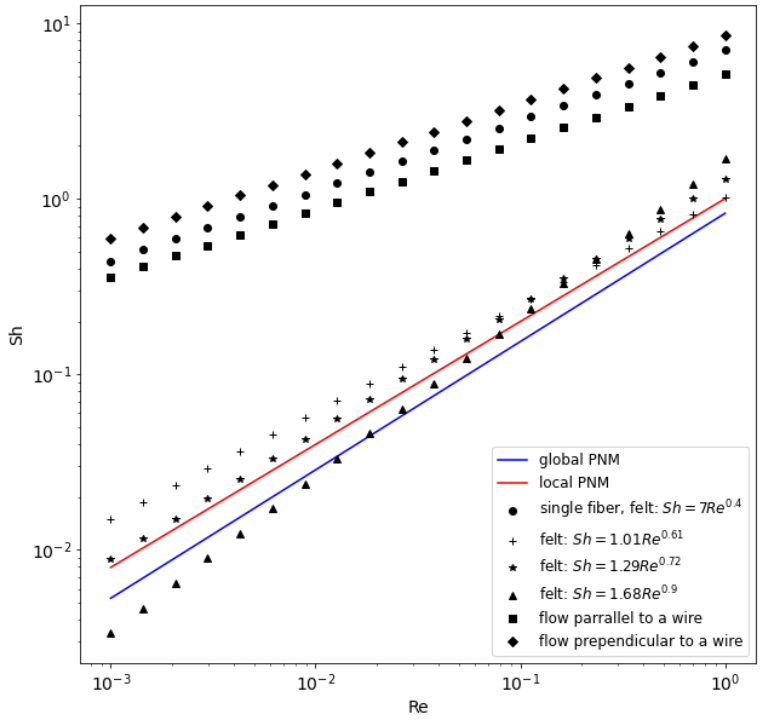

Figure 4-6 Plots of Sh vs Re correlations. Correlations for local and global mass transfer coefficient using PNM results are shown as solid lines. Correlations from previous works are extrapolated to the range of Re in the plot and shown using different markers from following references: circle [140], plus [139], star [139], triangle [141], square [144], diamond [144].

4.3.3.4. Charge transport

The flow of electric current in the porous electrode occurs through both the electrolyte phase (ionic current) and solid phase (electronic current). Due to the relatively high conductivity of the carbon electrodes, the potential loss within the carbon electrode was assumed to be negligible. Therefore, a constant electric potential for the solid phase was assumed ($\nabla\varphi_s = 0$), which was equal to the applied voltage. In the electrolyte phase, the charge conservation around pore i assuming electroneutrality ($\sum_n z^n c^n = 0$) is as follows [28], [45]:

$$\sum_{j=1}^{N_i} G_{cond,ij}^{ionic}\left(\phi_i - \phi_j\right) = S_i^{charge} = -F\sum_{n}^{nc} z^n \left[\sum_{j=1}^{N_{th}} G_{ij}^{n,diff} c_i^n - \sum_{j=1}^{N_{th}} G_{ij}^{n,diff} c_j^n\right] + I_{BV} \quad (4\text{-}26)$$

where ϕ_i is the electrolyte potential at pore i. S_i^{charge} is the source term or right-hand side (RHS) of the equation including electroneutrality source term and the generated current from Butler-Volmer reaction kinetics [28]. I_{BV} is nonzero at reactive sites. z_i^n is the valence of species n. $G_{cond,ij}^{ionic}$ is the ionic conductance of conduit ij, which can be defined using resistors-in-series model, where ionic conductance of pore elements were defined as follows:

$$g_{ionic,i}^{electrolyte} = \frac{F^2}{RT}\left(\frac{A_i}{L_i}\right)\sum_k (z_i^n)^2 \, D_i^n c_i^n \tag{4-27}$$

Given the diffusive size factors defined for pyramid pores, ionic conductance of pore elements is corrected as follows:

$$g_{ionic,i}^{electrolyte} = \frac{F^2}{RT}\lambda_i^{diff}\sum_k (z_i^n)^2 \, D_i^n c_i^n \tag{4-28}$$

The current generated from electrochemical reaction can be defined using Butler-Volmer equation as follows [130], [145], [146]:

$$I_{Rxn} = k_0 A_{rxn_i} F\left[C_s^{\mathrm{V}^{4+}} exp\left(\frac{\alpha_a F}{RT}\eta_c\right) - C_s^{\mathrm{V}^{5+}} exp\left(-\frac{\alpha_c F}{RT}\eta_c\right)\right] \tag{4-29}$$

where k_0 is the reaction rate constant, $C_s^{\mathrm{V}^{4+}}$ and $C_s^{V^{5+}}$ are the concentration of V^{4+} and V^{5+} at the solid-liquid interface, respectively; α_a and α_c are the charge transfer coefficients for the anode and cathode; F, R, and T are Faraday's constant, the universal gas constant, and the temperature, respectively; η_c is the electrode overpotential and assuming a negligible IR loss in the anode (for a half-cell model where anode includes hydrogen reaction and is used as a pseudo reference electrode [130]), η_c can be defined as follows [2]:

$$\eta_c = \phi_s - \phi_l - V_{oc} \tag{4-30}$$

where ϕ_s, ϕ_l, and V_{oc} are solid potential, electrolyte potential and equilibrium/open-circuit voltage, respectively.

The concentration of active species at the interface can be calculated from their concentration in the bulk solution from mass transfer equation defined in Eq. (4-21). Rewriting Eq. (4-21) for reduced and oxidized species, we'll have:

$$I_{Rxn} = Fk_m A(C_s^n - C_b^n) \tag{4-31}$$

Combining Eq. (4-29) and Eq. (4-31), the Butler-Volmer kinetics including the mass transfer resistance between the bulk solution and interface is defined as follows [130]:

$$I_{Rxn} = \frac{k_0 A_{rxn_i} F}{1 + \frac{k_0}{h_m}\left[exp\left(\frac{\alpha_a F}{RT}\eta_c\right) + exp\left(-\frac{\alpha_c F}{RT}\eta_c\right)\right]}\left[C_b^{\mathrm{V}^{4+}}\, exp\left(\frac{\alpha_a F}{RT}\eta_c\right) - C_b^{\mathrm{V}^{5+}}\, exp\left(-\frac{\alpha_c F}{RT}\eta_c\right)\right] \tag{4-32}$$

Substituting Eq. (4-32) into the charge conservation Eq. (4-26) provides the final formula for charge conservation as a function of $C_b^{\mathrm{V}^{4+}}$, $C_b^{\mathrm{V}^{5+}}$, and electrolyte potential ϕ_l.

Charge transport boundary conditions:

At the electrode-membrane interface, a Dirichlet boundary condition was applied equal to the IR loss in the membrane. The value of the potential at the electrode-membrane interface was defined based on the generated current and the ohmic resistance of the membrane (R_{mem}) using Ohm's law. The generated current was calculated as the summation of the current rates ($I_{i,BV}$) in the pore network. The membrane resistance was calculated based on Pouillet's law [2] as $R_{mem} = \frac{\delta_m}{\sigma_m A_m}$, where δ_m, σ_m, and A_m are thickness, conductivity, and area of the membrane. At the remaining pores in the porous electrode an electroneutrality diffusive flux source term was applied to the RHS of charge equations. As the electrical conductivity of the fibrous material is assumed to be significantly greater than the electrolyte conductivity, the transport equations for solid electrode potential were not solved. Rather, a constant distribution of potential ϕ_s equal to applied voltage (V_{cell}) was assumed.

4.3.3.5. Solving equations

A flow chart of the developed framework for solving Nernst-Plank system of equations is shown in Figure 4-7. The fluid flow through the porous electrode was described by Stokes flow Eq. (4-2). In the first step of numerical solution, the system of linear equations for fluid flow was solved to find the pressure and velocity distribution within the pore network. Next, the coupled system of mass and charge transport equations were solved using an iterative algorithm shown in Figure 4-7, where the concentration of species and electrolyte

potential values were the unknown variables. As the charge transport equation is highly non-linear, the iterative algorithm may diverge, if the initial guess of the variable is not close to the actual solution. To prevent this issue a relaxation factor ω was defined, which was adaptively changed at each voltage range based on the convergence error [2]. Therefore, at each iteration in the charge conservation Nernst-Planck loop, the unknown variables were updated as $X_i^{iter+1} = \omega\, X_i^{iter+1} + (1-\omega)\, X_i^{iter}$. Once the systems of equations were solved at a specified cell voltage, their results were used as input at the next voltage, providing a good initial guess and speed for the algorithm.

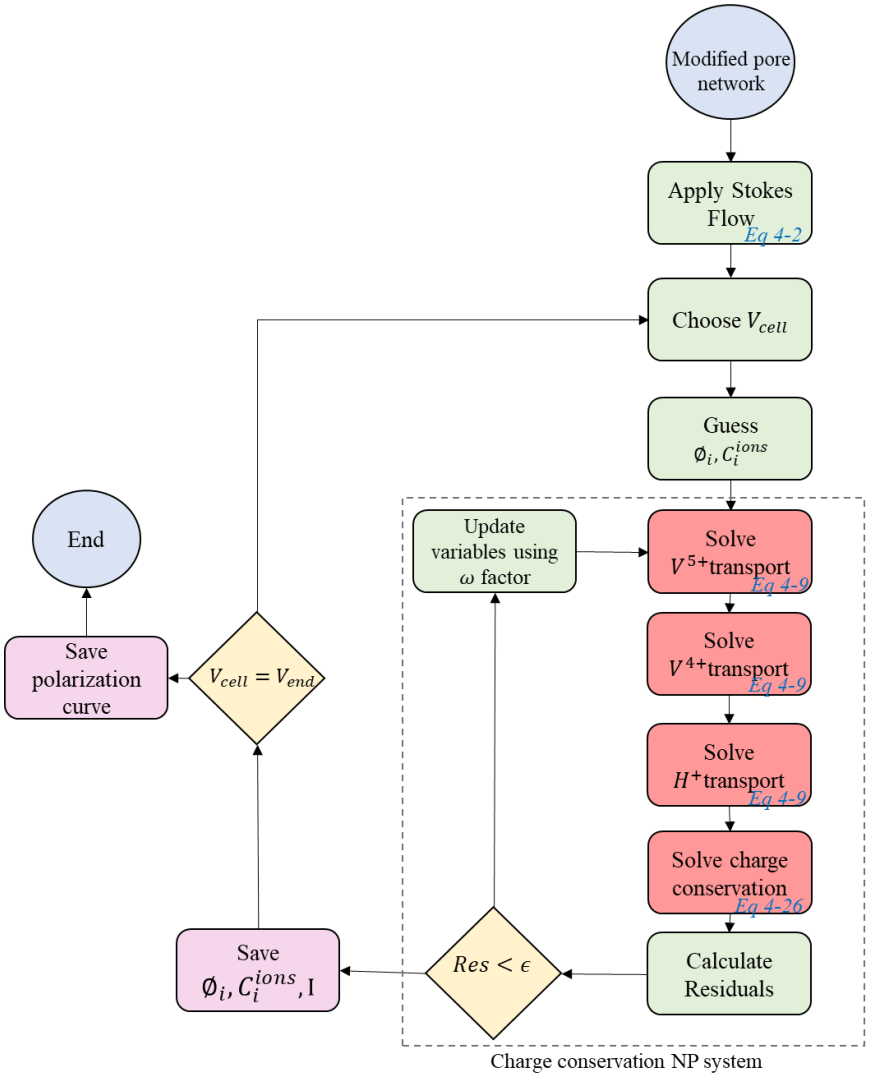

Figure 4-7 A flow chart of the developed algorithm to solve the Nernst-Plank system of mass and charge conservation and create a polarization curve.

4.4. Validation

To validate the modeling framework with experimental data, polarization data for a VRFB half-cell with an interdigitated flow field design by Messaggi *et al.* [130] was used as the reference. The reference experimental data were based on a commercial fibrous material SGL 39AA as the cathode electrode. However, because a 3D image of the fibrous material was not available, the developed algorithm in Section 4.3.1.1 was used to digitally generate a fibrous material with properties close to SGL 39AA. Fibrous material generation, network extraction and electrochemical performance results are presented in the following sections.

4.4.1. Fibrous material generation and characteristics

To create fibrous materials an initial range of $\varphi = [5,15,25]$ and $\theta = [45,90]$ was defined. The domain size for generating random fibrous images was $[2000,500,280]$ voxels with resolution of 1 μm, fiber diameter of 8 μm [12].The thickness of the porous electrode was selected based on nominal thickness of SGL 39AA (280 μm) [119], [130], [136], assuming that the effect of compression on transport was negligible. A key step in the fiber image generation algorithm was to define the number of fibers and the radius of structuring element to apply morphological image processing.

It was found that the candidate fibrous materials generated with fiber orientation parameters of $\varphi = 15$ and $\theta = 45$, provided a closer match to the known values of permeability. Calculating the pore size distribution (PSD) and permeability of the candidate images, the material with properties closest to the SGL 39AA was selected for modeling purposes. The selected material had an initial porosity of 0.89 (number of fibers = 900) and final porosity of 0.6 (radius of structuring element = 25). The selected generated image and its PSD are shown in Figure 4-8. The PSD of the generated fibrous material was found by applying a porosimetry simulation based on morphological image opening (i.e., using PoreSpy's *porosimetry* filter). As the PSD of the reference material was not given by Messaggi *et al.* [130], the PSD of an SGL 39AA from Forner-Cuenca *et al.* [8] was used as a reference for comparison. Assuming minimum and maximum differential saturation of 0 and 1 for data from [8], the generated PSD's differential saturation was normalized between 0 to 1 for comparison. As shown in Figure 4-8b, the generated image has a slightly smaller average pore size in contrast to the reference data from experimental mercury intrusion porosimetry (MIP) [8]. This was expected because porosimetry filter operates on inscribed spheres so only breaches a throat opening at the smallest radii of curvature [51]. For example, considering a throat opening with an aspect ratio above 1, the capillary pressure value can be found as follows [51]:

$$\frac{P_c}{\sigma} = 2H = \frac{1}{R_1} + \frac{1}{R_2} \tag{4-33}$$

where P_c, σ are the capillary pressure and surface tension, respectively. R_1 and R_2 are the radii of the throat. In a flattened throat $R_2 \neq R_1$ and larger value of R_2 leads to a smaller value of P_c. Therefore, flattened throats in fibrous materials would be invaded at a lower capillary pressure in MIP in contrast to image-based method, resulting in a larger pore size in PSD from interpretation of capillary pressure curves. More details about the difference between these two methods have been explained in the study by Gostick [51]. Permeability calculations of the generated material are explained in next section.

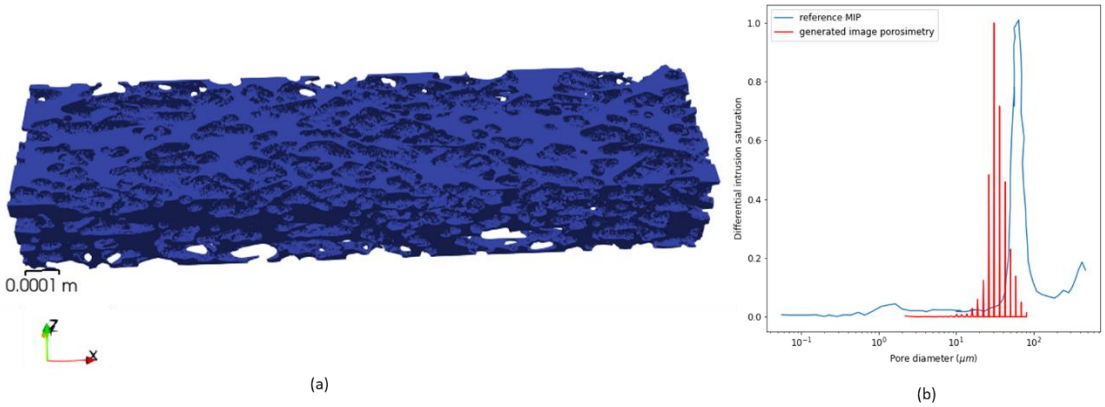

Figure 4-8 a) Generated fibrous material image b) Pore size distribution of the generated fibrous material (red) and an SGL 39AA sample (thickness of 320 um, geometric area of 1.7 cm by 1.5 cm) reproduced from [8](blue).

4.4.2. Pore network extraction and permeability

Pore network and geometry for the generated fibrous image was created in two steps. First, a pore network of the porous domain was extracted (using PoreSpy's *snow2* algorithm). Then, the throat-node framework described in Section 4.3.2 was applied on the original extracted network. The resulting pore network is shown in Figure 4-9. To characterize the generated material, the permeability of the material was calculated using the PNM framework. The permeability in the in-plane and through-plane directions were 5.81 D and 20.48 D, respectively, which matches with values in references for SGL 39AA within an acceptable accuracy [130], [136]. To further confirm the suitability of the generated images and accuracy of the PNM permeability, LBM simulations were used to calculate the permeability of the generated image. However, due to the computational cost of LBM and the need for the use of higher resolution image for through-plane direction for a fibrous material with binder, the in-plane permeability was calculated for a smaller domain of [500, 500, 280] voxels, which was cropped from the image. LBM simulation was performed using an open-source package MPLBM-UT [147], which is built upon the open-source package Palabos [148]. To

apply a single-phase simulation, a constant pressure gradient was defined between the inlet and outlet of the domain. D3Q19 lattice was used as descriptor and Bhatnagar-Gross-Krook (BGK) collision model was used to define the dynamics of fluid flow. The simulation with a pre-defined maximum iteration steps continues until the steady state is reached when the standard deviation of the average energy falls below a pre-defined threshold [149]. In-plane permeability of the cropped image from LBM and PNM were 27.1 D and 32.66 D, respectively.

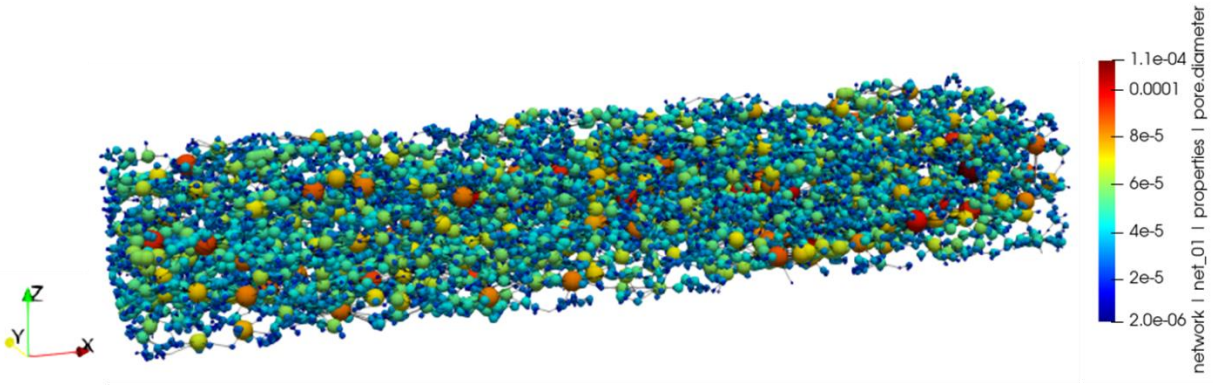

Figure 4-9 Pore network of the generated image in Figure 4-8. Only for visualization pores and throats are shown as spheres and wireframes. Spheres diameters are scaled as half of pore diameters for better visualizations and are colored by pore sizes. Wireframes opacity was reduced to 0.1, as the focus of this figure was pore sizes.

4.4.3. Electrochemical performance validation

The developed PNM framework shown in Figure 4-7 was applied to the pore network model of the generated image. As the reference experiments were based on a constant flow rate, their corresponding inlet flow rate for the modeling electrode domain of half channel-rib-half channel was calculated using Eq. (4-8). For a total flow rate of 20 ml/min, channel width of 1 mm and length of 5 cm, number of inlet channels as 12.5 [130], the average velocity at inlet channel was found as $v_{in} = 5.24 \times 10^{-4}$, resulting in PNM half-channel inlet flow rate of $Q_{in} = v_{in}A_{in} = 1.32 \times 10^{-10}$. Therefore, the PNM results at inlet flow rates of 6.6×10^{-11} , 1.32×10^{-10}, 3.96×10^{-10} m^3/s correspond to the reference experiment's total flow rates of 10, 20, and 60 ml/min. The simulations were performed at a SOC of 0.6 with parameters given in Table 4-1 to obtain polarization curves. The only fitting parameters were k_0 and $\sigma_{membrane}$, which were found from fitting the model to experimental results. As shown in Figure 4-10, polarization curves from the PNM results matches the experimental curves for all three flow rates within an acceptable error given the approximate nature of the generated image of the electrode. For visualization purpose, the concentration distribution of V^{5+} in the PNM at each flow rate is shown in Figure 4-11. As shown in Figure 4-11, as the flow rate increases, higher concentrations are seen throughout the network, because a higher

flow rate supplies the reactive zones with reactive species to replenish the regions, whereas at lower flow rates those regions near the membrane and outlet are exhausted.

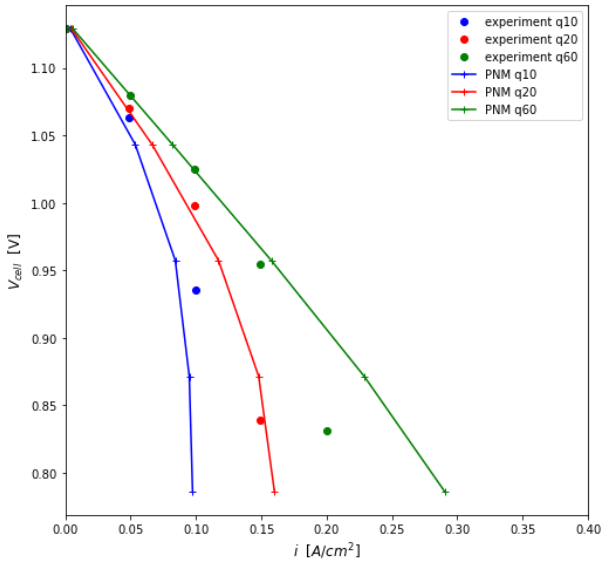

Figure 4-10 Polarization curves from modeling results (solid lines) and experimental data of an interdigitated flow from [130] (dots) at total flow rates of 10 ml/min, 20 ml/min, and 60 ml/min and SOC = 0.6. Note that for modeling a half-channel rib and half-channel, the inlet channel flow rates were calculated based on average channel velocity corresponding to the experimental data's flow rate using Eq. (4-8).

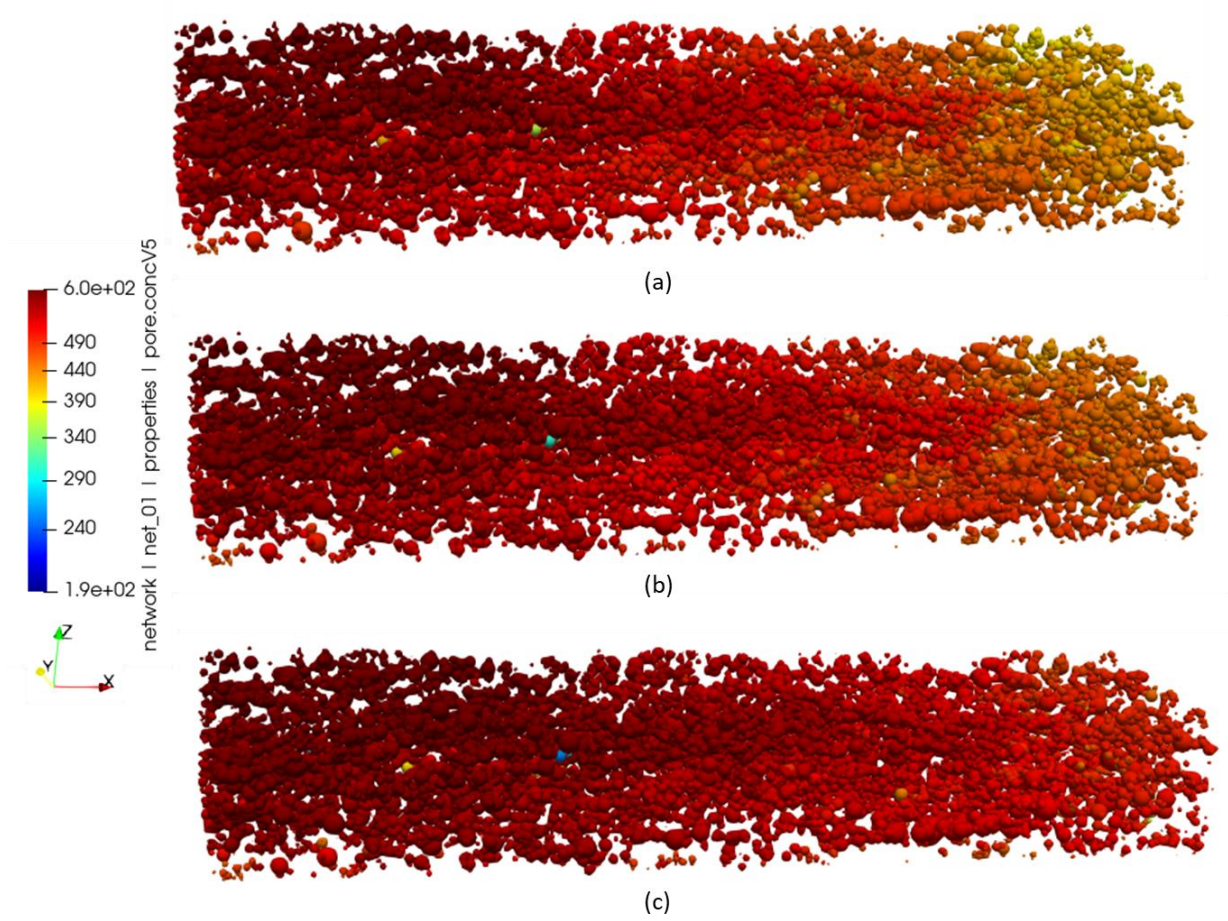

Figure 4-11 Concentration distribution of V^{5+} within pore network at $V_{cell} = 0.7$ V for modeling results. Inlet flow rates for a half-channel rib and half-channel medium were calculated based on Eq. (4-8) corresponding to total flow rates of a) 10 ml/min b) 20 ml/min , c) 60 ml/min in reference experiments from [130].

Table 4-1 Summary of the parameters used in this study

Parameter	Value	Units	Description	source
δ_m	125×10^{-6}	m	Membrane thickness	[130]
σ_m	2	S/m	Membrane conductivity	Fitted parameter
k_0	5×10^{-7}	m/s	Reaction rate constant	Fitted parameter
α_c, α_a	0.5	-	Cathodic, Anodic transfer coefficient	[130]
ρ	1350	kg/m^3	Electrolyte density	[130]
μ	0.005	$Pa.s$	Electrolyte viscosity	[130]
$D_{V^{4+}}$	3.9×10^{-10}	m^2/s	V^{4+} diffusivity in electrolyte	[130], [150]
$D_{V^{5+}}$	3.9×10^{-10}	m^2/s	V^{5+} diffusivity in electrolyte	[130], [150]
D_{H^+}	9.312×10^{-9}	m^2/s	H^+ diffusivity in electrolyte	[130], [150]
$D_{SO_4^{2-}}$	1.065×10^{-9}	m^2/s	SO_4^{2-} diffusivity in electrolyte	[150]
M_V	1000	mol/m^3	Vanadium electrolyte molarity	[130]
M_{acid}	5000	mol/m^3	Sulphuric acid molarity	[130]

4.4.4. A note on velocity dependence of mass transfer coefficient

As explained in Section 4.3.3.3, the mass transfer coefficient was assumed to be velocity dependent. To confirm the validity of this assumption in the developed PNM, the results are compared with a PNM assuming a velocity independent mass transfer coefficient as $k_m = 2D/l$ with a characteristic length of reactive pore diameter (d_p) [29]. Firstly, a histogram of k_m values using velocity dependent and independent assumptions are compared as shown in Figure 4-12. It is obvious that the latter assumption overestimates k_m values. This conclusion was stated in the study by Heijden *et al.* [29], where they used a correction factor for k_m values at different inlet flow rates to account for the dependence of k_m to variations in velocity. Secondly, the polarization curves for the PNM using both methods are compared. As shown in Figure 4-13, a velocity independent k_m overestimates the performance of the battery assuming that reaction is not mass transfer limited. This comparison demonstrates the importance of mass transfer resistance in VRFBs, which is a broad field of research and requires further investigations in future works.

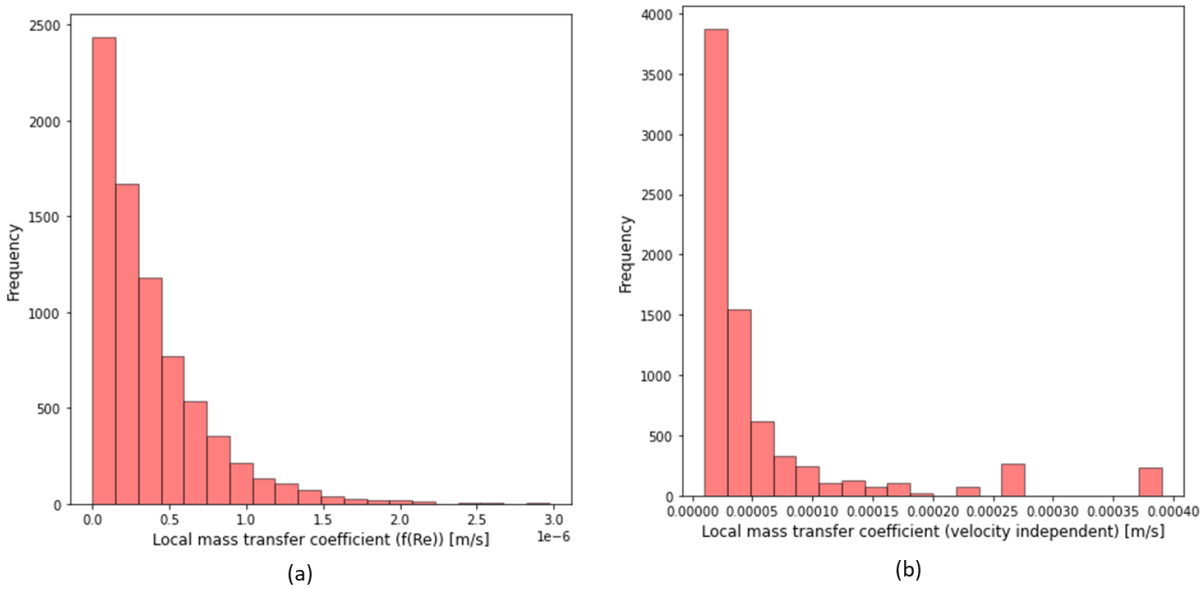

Figure 4-12 Histograms of mass transfer coefficients at reactive nodes in the PNM for inlet flow rate corresponding to 10 ml/min a) Local mass transfer coefficients were defined based on the local correlation found in Section 4.3.3.3:$k_m = (1.0\ Re^{0.7})\ \left(\frac{D}{d_f}\right)$. b) Local mass transfer coefficients were defined as velocity-independent in [29]: $k_m = 2D/l$.

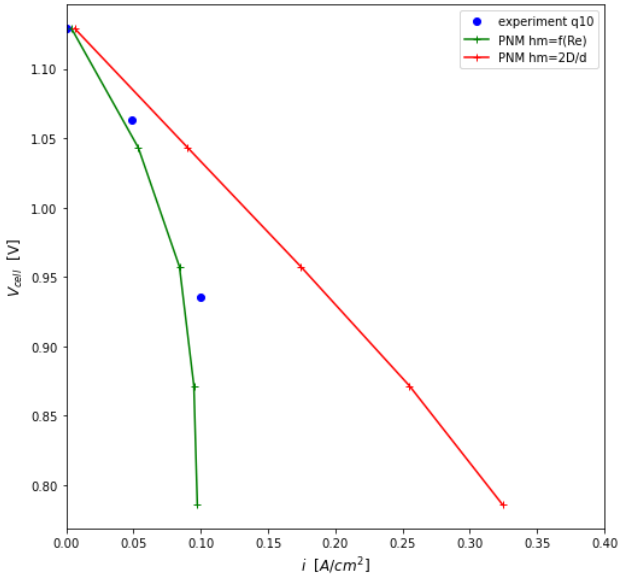

Figure 4-13 Comparison of polarization curves of the PNM at inlet flow rate of $6.6 \times 10^{-11}\ m^3/s$ (corresponding to total flow rate of 10 ml/min in experimental result) using velocity dependent mass transfer coefficient and velocity independent mass transfer coefficient. The experimental curve from [130] is shown for comparison.

4.5. Results: Multi-layer structures

As the structure of the fibrous electrode affects the performance of the cell, different structures were explored here to examine their performance using the developed PNM framework. The main goal was to utilize PNM to study different structures at pore-scale to find an improved design that provided better performance and lower operational cost. The results of creating multi-layer structure and their structural-performance analysis are presented in the following sections. Crucially, the final structure suggested by this study can be directly made in the lab using a technique like electrospinning since all the structural details are known.

4.5.1. Creating structures

The building blocks of multi-layer structures were individually generated fibrous materials which were stacked into layers, inspired by the approach of Tucker *et al.* [121]. Using the framework developed in Section 4.3.1.1, for a maximum $\varphi = 20$ and $\theta = 90$, three random fibrous materials were generated with low, medium, and high porosity values of 0.7, 0.8, and 0.9. Note that the fiber diameter, domain size of each layer and channel, land dimensions for their resulting electrode model were chosen to be the same as validation model in Section 4.4. Cross sectional views of the generated fibrous materials are shown in Figure 4-14a while 3D visualizations are provided in Appendix C. In-plane and through-plane permeability of the generated images were calculated using PNM as presented in

Table 4-2. Using the generated materials, 18 multi-layer electrode structures containing different combinations of 2 and 3 layers were created, plus 3 single layer structures. A schematic of 2-layer structures containing different layers is shown in Figure 4-14b, where the layers with high, medium and low porosity are denoted as “H”, “M”, and “L”, respectively. Each multi-layer structure was named based on the order of its layers starting from the electrode-channel side ($z = z_{max}$) to electrode-membrane side ($z = 0$). As an example, structure “L-H” in Figure 4-14b contains the layer with porosity of 0.7 near the channel ($z = 560\ \mu m$) and the layer with porosity of 0.9 near the membrane ($z = 0$). The 3-layer structures were named in a similar way as schematically shown in Figure 4-14c.

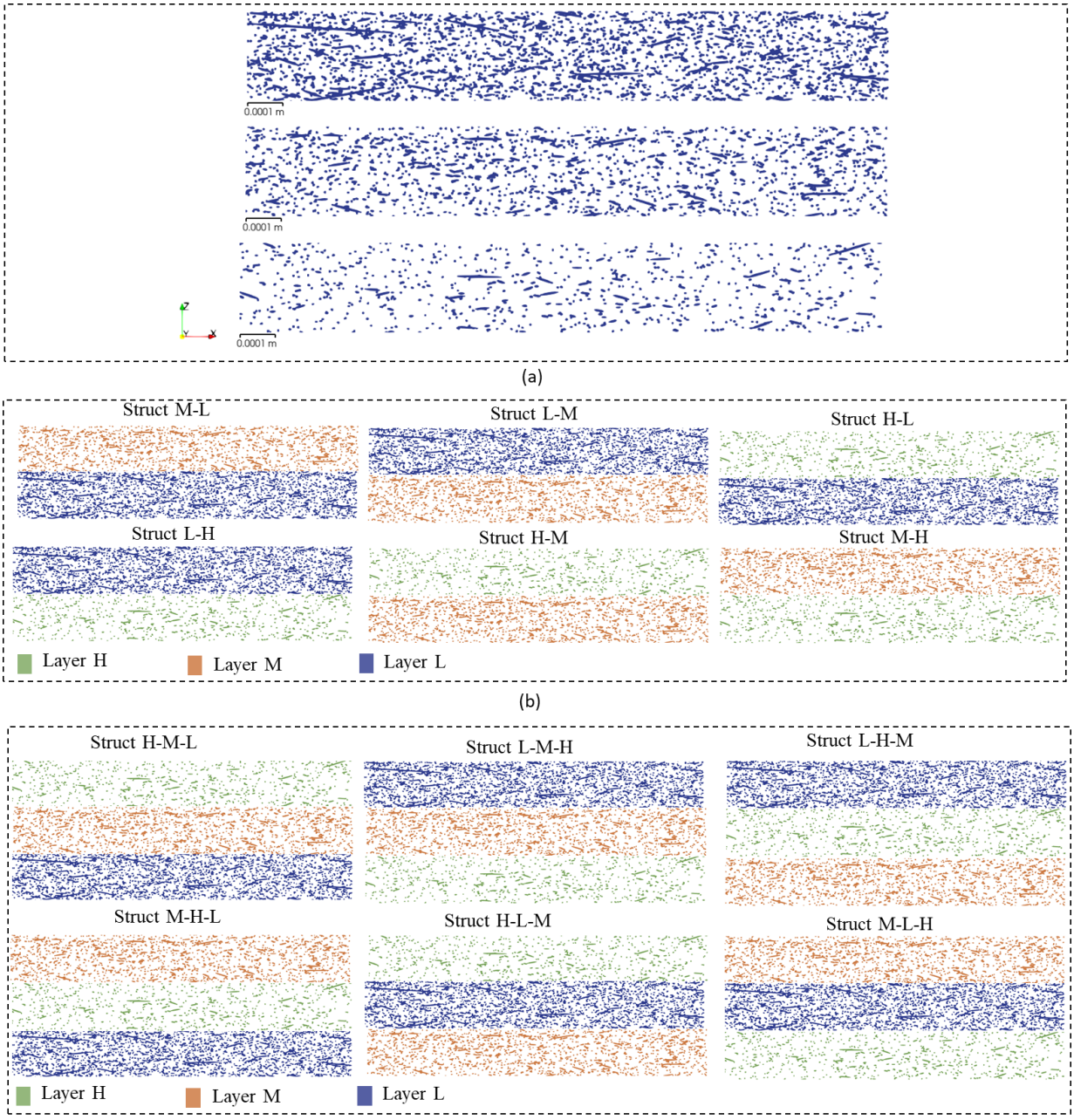

Figure 4-14 a) Cross sectional view of the generated fibrous materials as building blocks of multi-layer structures. Each view is extracted from 3D visualization in xz plane at y = 250 voxel. Top) layer with porosity = 0.7 Middle) layer with porosity = 0.8 Bottom) layer with porosity = 0.9. b) A schematic of layers orders in each 2-layer structure containing different layers c) A schematic of layers orders in each 3-layer structure containing different layers.

Table 4-2 Properties of the generated layers

Layer	Porosity	In-plane permeability (D)	Through-plane permeability (D)
Low porosity (“L”)	0.7	5.39	3.79
Medium porosity (“M”)	0.8	13.89	9.49
High porosity (“H”)	0.9	45.52	29.23

4.5.2. Relative performance of the structures

The developed PNM framework was applied to each multi-layer structure to compare the performance of different structures. The electrochemical performance of the electrodes was compared at a constant inlet flow rate of $6.6 \times 10^{-11}\ m^3/s$ using similar boundary conditions and membrane properties that were used for validation section. Initial comparison was performed on the generated novel multi-layer structures containing different layers. Finally, a thorough comparison of all generated structures was performed in Section 4.5.5.

4.5.3. 2-layer structures

The polarization curves of PNM for 2-layer structures are shown in Figure 4-15a. In general, in a two-layer structure, better performance is seen when the layer with higher permeability/porosity is located near the membrane. As shown in Figure 4-15a, structures L-M, L-H, M-H show better performance in contrast to the structure where the layer with relatively higher permeability is located near the channel (struct M-L, H-L, H-M). This is because when an interdigitated flow field is used, both in-plane and through-plane permeability play a role in fluid flow distribution and mass transfer. When a layer with lower permeability is located far from the channel, the fluid follows the paths with least resistance (i.e., of high permeability) near the channel while regions near the membrane are deprived of reactant. Therefore, the lower amount of flow near the membrane regions leads to lower reaction rate and performance (current/power density), accordingly. To compare the results in pore-scale, the V^{5+} concentration and fluid flow distribution in struct H-L and L-H, where an increase of 57.9% in performance was seen from changing the order of the layers, are shown in Figure 4-16. In structure H-L (Figure 4-16a), the region near the membrane has lowest concentration values supporting the conclusion that mass transport limitation negatively affected the performance. In contrast L-H (Figure 4-16b), the region near the membrane has higher concentration values as a result of better fluid flow distribution. The flow rate distributions in Figure 4-16c and d support this conclusion. Note that these two structures H-L and L-H have the same porosity and permeability, while

providing different microstructures due to the arrangement of their layers. A similar story is seen when M-L and M-H combinations are used, but the differences in the performance are less extreme.

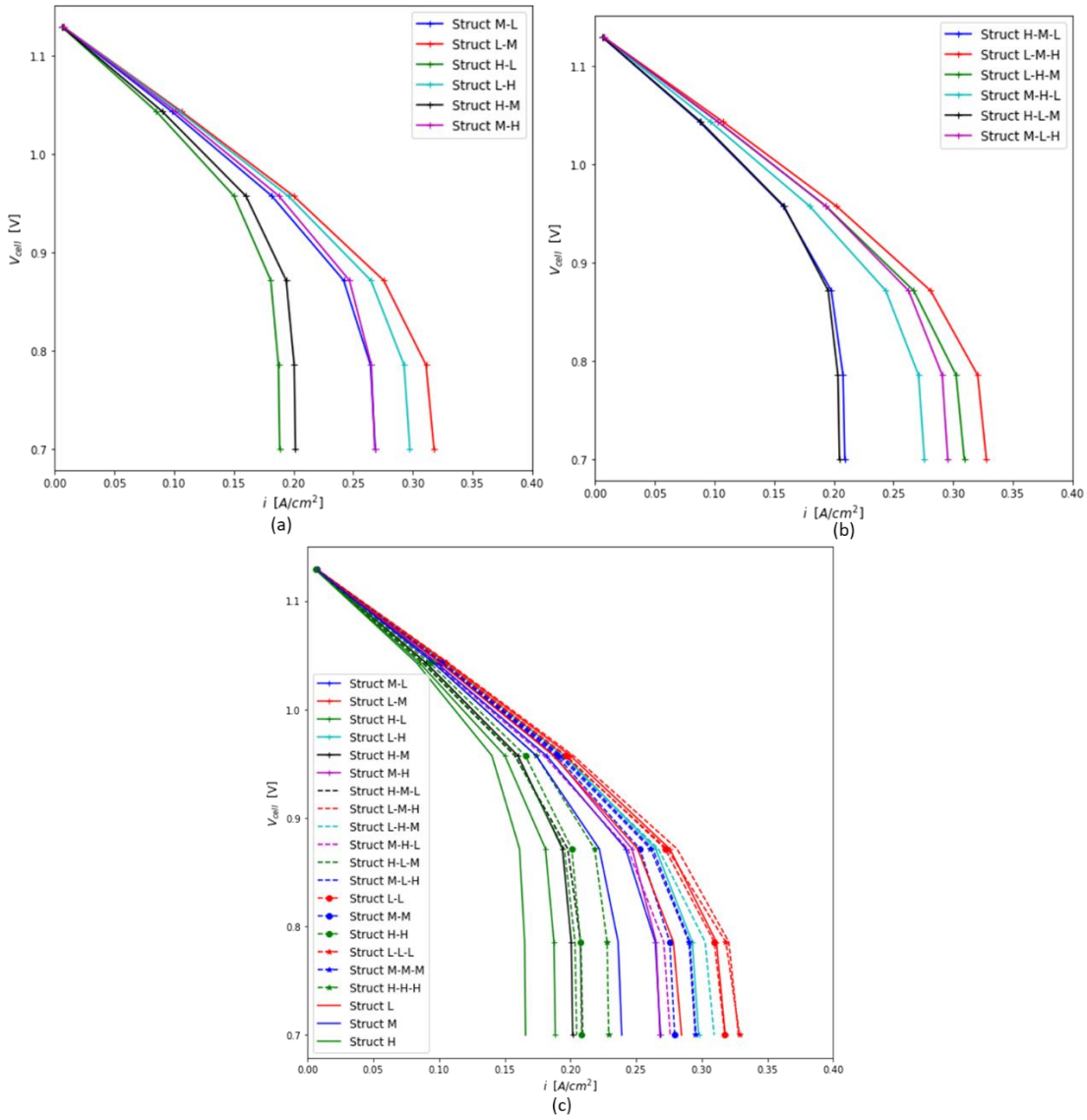

Figure 4-15 Comparison of polarization curves of PNMs at inlet flow rate of $6.6 \times 10^{-11}\ m^3/s$ a)The generated 2-layer structures with different layers b)The generated 3-layer structures with different layers c) All multi-layer structures including structures with similar layer and single layer structures.

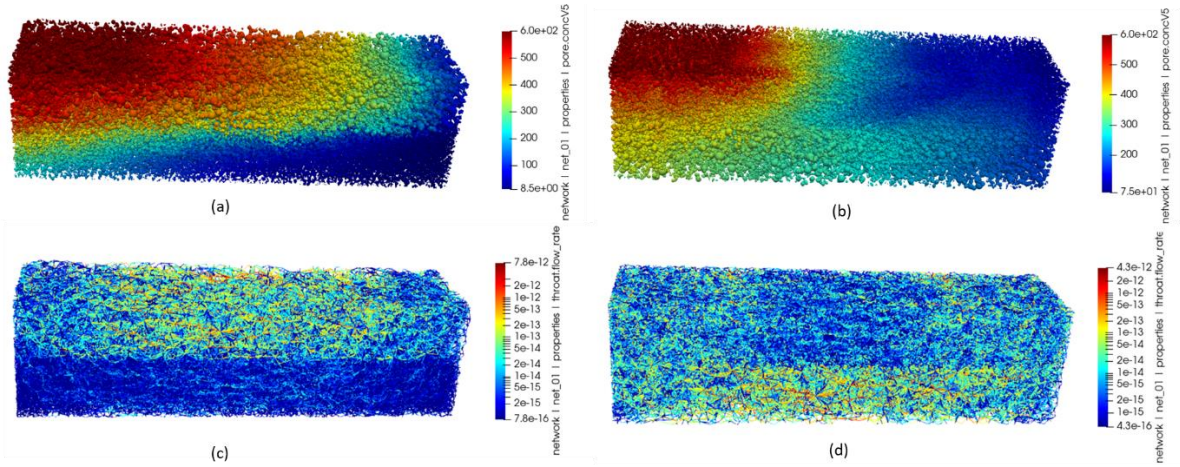

Figure 4-16 Distribution of V^{5+} concentration and fluid flow rate within pore network at $V_{cell} = 0.7$ V for 2-layer structures. For visualization purposes, only pores are shown as spheres (a,b) and throats are shown as wireframes (c,d). a) Concentration distribution of V^{5+} in Struct H-L. b) Concentration distribution of V^{5+} in Struct L-H. c) Fluid flow rate distribution in throats in Struct H-L d) Fluid flow rate distribution in throats in Struct L-H.

4.5.4. 3-layer structures

In order to more deeply explore the impact of various layers and their ordering, simulations were performed with 3 layers as well. The polarization curves of PNM for 3-layer structures are shown in Figure 4-15b. In general, in a 3-layer structure, higher performance is seen where layers with higher permeability are located near the membrane (struct L-M-H, L-H-M, M-L-H) whereas the opposite order provides a worse performance (struct H-M-L, M-H-L, H-L-M). However, the best performance was seen in struct L-M-H, where the structure's porosity and permeability increased through the electrode thickness (z direction) from the lowest porosity layer near the channel to highest porosity layer near the membrane. The V^{5+} concentration and fluid flow distribution in struct H-M-L and struct L-M-H, where an increase of 56.7% in performance was seen from changing the order of the layers, are shown in Figure 4-17. In struct H-M-L (Figure 4-17a), the exhausted region near membrane correspond to a lower flow rate (Figure 4-17e), whereas in struct L-M-H those regions have higher flow rate (Figure 4-17f) and concentration (Figure 4-17b). This trend is similar to the trend seen in 2-layer structures. Although the 3-layer structure generally provided a higher performance in contrast to 2-layer structures, the gain in their performance was found to be on average 3.35% in better performing structures (e.g. 4% gain in struct L-H-M in contrast to struct L-H), and 7.5% in low performing structures (e.g. 10% gain in struct M-L-H in contrast to struct M-L). Due to such small gain in the performance, it may be reasonable to select a 2-layer structure instead of a 3-layer structure to reduce the cost of additional material and operations. However, it is noteworthy that a 3-layer structure

with additional high permeability layer near the membrane can lead to a lower pressure drop within the system, thereby reducing the pumping cost (not studied in this section).

Amongst the 3-layer structures with worse performance, placing the highest permeability layer in the middle provided a better performance (struct M-H-L). The reason is this layer provides a least resistance path for fluid to flow near the third layer (near the membrane) and enhances the positive effect of mass transport in those regions. The V^{5+} concentration and fluid flow distribution in struct M-H-L and H-L-M as shown in Figure 4-17 support this conclusion.

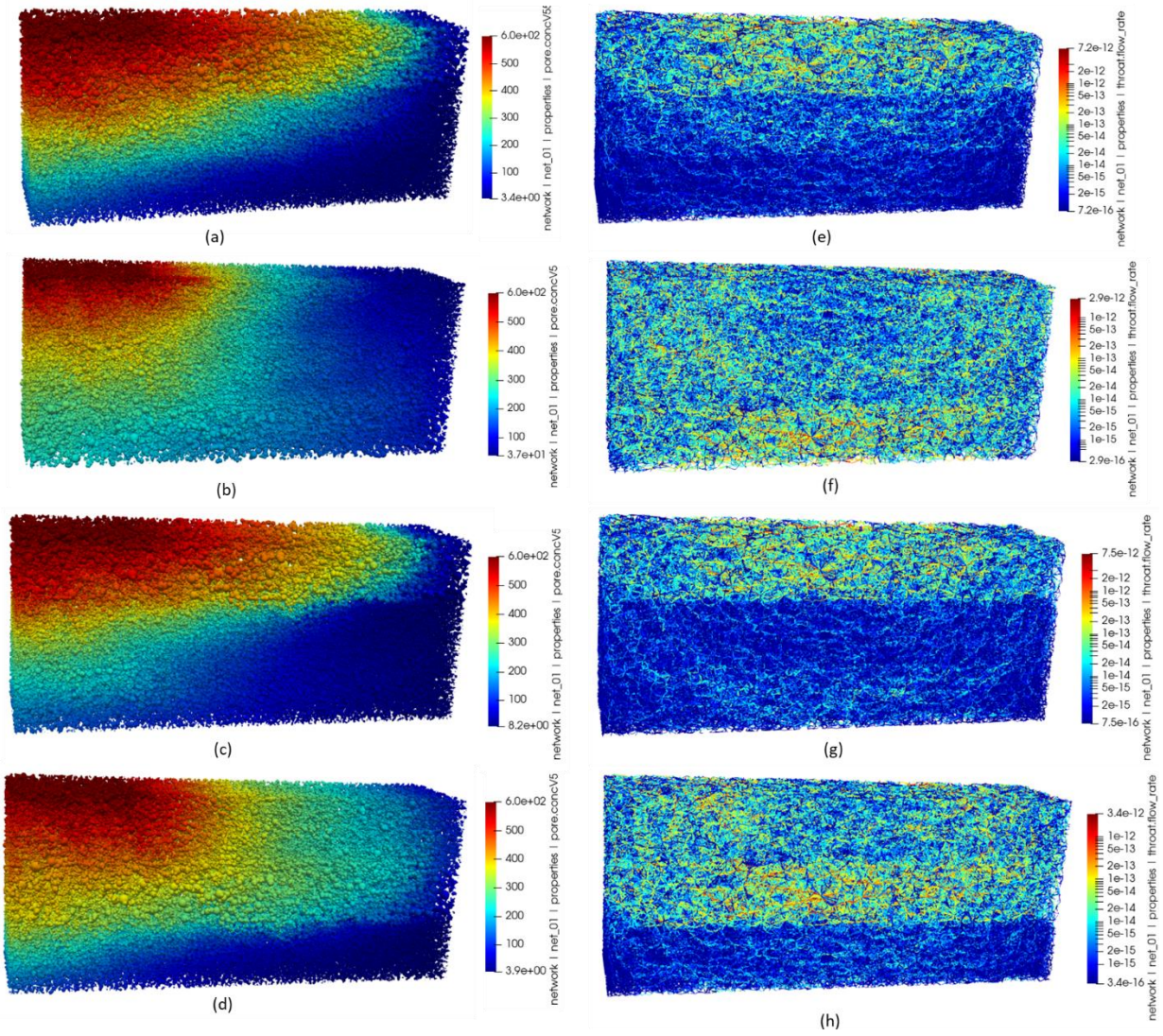

Figure 4-17 Distribution of V^{5+} concentration (left) and fluid flow rate (right) within pore network at $V_{cell} =$ 0.7 V for 3-layer structures. For visualization purposes, only pores are shown as spheres (left) and throats are shown as wireframes (right). Left) Concentration distribution of V^{5+} in a) Struct H-M-L. b) Struct L-M-H. c) Struct H-L-M. d) Struct M-H-L. Right) Fluid flow rate distribution in throats in e) Struct H-M-L. f) Struct L-M-H. g) Struct H-L-M. h) Struct M-H-L.

4.5.5. Comparison with single structures

In previous sections to rationalize the improvements in limiting current density of novel multi-layer structures the microstructure design and transport at pore-scale were examined. For a more comprehensive comparison, the developed PNM was applied on single-layer structures as well as stacks of the same

structure. The polarization curves for these structures and previous structures from Sections4.5.3 and 4.5.4 are shown in Figure 4-15c. As shown in Figure 4-15c, the lowest and highest limiting current density belongs to the single layer struct H and multi-layer struct L-L-L. However, at a constant inlet flow rate comparison purely based on limiting current density includes ambiguity, because the effect of pumping cost is not included. For instance, amongst single layer structures the structure with lowest porosity provides the highest limiting current density which is expected since it has the highest volumetric surface area, but it is the least efficient structure based on the pumping cost as a consequence of higher pressure drop required to apply the fixed flow. The pressure drop vs limiting current density for the generated structures is shown in Figure 4-18a. It can be seen that the novel multi-layer structures with the arrangement of lower permeability layers near the channel are located at the bottom right region of the scatter plot where a desired balance of low pressure drop (operational cost) and high current density can be achieved in contrast to other structures, which are located at the two ends of high pressure drop or low current density. To quantify this trend, a more comprehensive and fair comparison requires normalizing the performance in terms of both limiting current density and pressure drop (which is used here as a proxy for pumping cost). In this regard, the ratio of $i_{lim}/\Delta P$ was defined, for which a higher value indicates a rough estimate of a more efficient structure. The bar chart of the defined ratio for each generated structure is shown in Figure 4-18b, where each column is colored by the limiting current density of the structure. As shown in Figure 4-18b, a multi-layer structure in general provides a higher value of this ratio while the best ratio for single layer structures was found in the struct H, which is mainly due to a low pressure drop while its current density is the lowest of all cases (colored as dark blue). Amongst multi-layer structures the structures with higher permeability layer near the channel provided a higher ratio. However, it can be seen from their color (colored as dark and light blue) that their high value of the ratio was not as a result of high current density but low pressure drop. Therefore, a more desired balance between current density and pressure can be achieved in columns that show still relatively high value of the $i_{lim}/\Delta P$ ratio while providing a relatively high current density (colored as orange/red). For example, a wide selection range based on this balance can be found in the multilayer structures in Figure 4-18b spanning from M-H-L to L-M-H. It is noteworthy that although the defined ratio includes both generated current and pressure loss, more thorough investigation on the pumping cost are required to find a balance between the desired target of power and cost, which would be of interest for future works.

Another note on the polarization curves is that although in the single structure cases including single and multi-layers of the same structure, the structure with lower porosity provided a higher limiting current density, this was not the case for multilayer structures that contained different microstructure at each layer. For instance, struct H-L and H-M have lower porosity in contrast to struct H-H, while providing a lower

limiting current density as shown in Figure 4-15c. This observation supports the importance of pore-scale modeling and studying microstructure properties and anisotropy within the electrode in VRFBs.

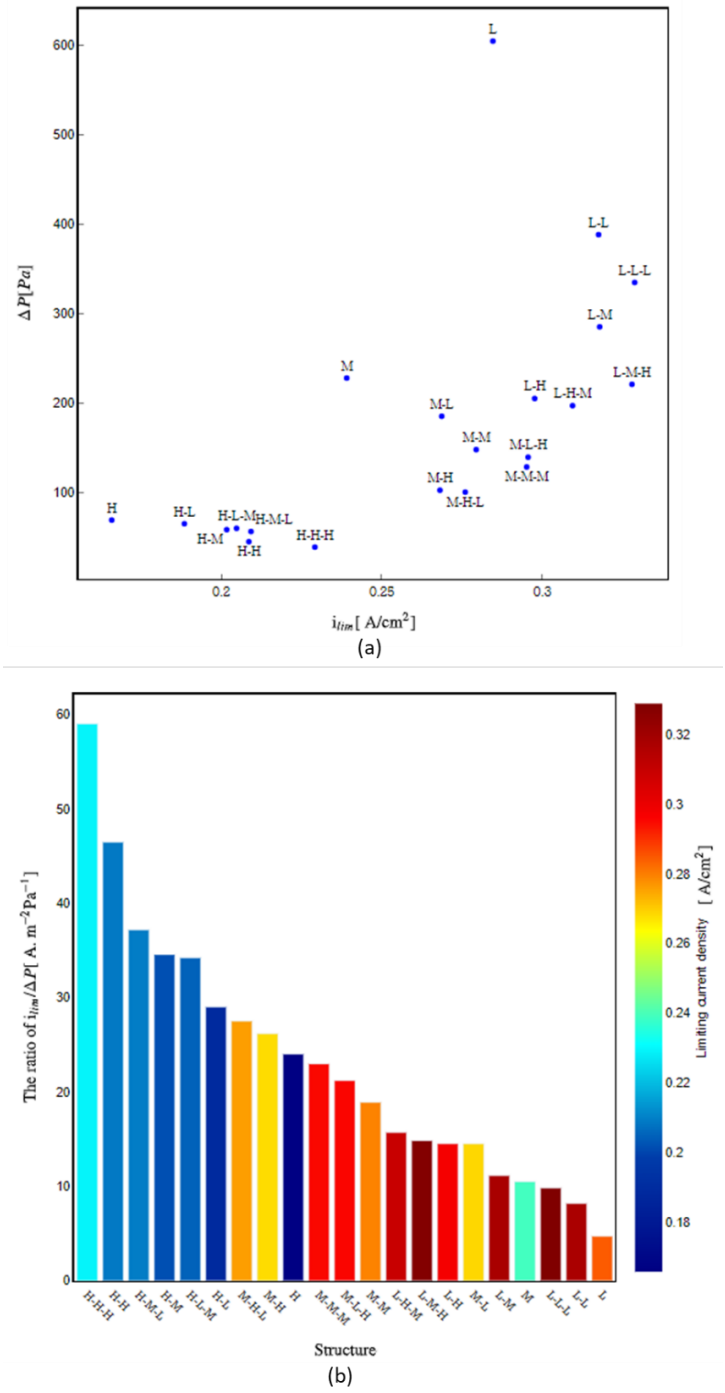

Figure 4-18 a) Pressure drop vs limiting current density for each generated structure. b) Ratio of $i_{lim}/\Delta P$ for each generated structure.

4.6. Conclusion

In this study, a PNM was developed to study the effects of novel electrode structures on the performance of VRFBs. Previous experimental studies showed that an electrode containing multiple layers of the same material can enhance the performance of RFB electrodes [120], [121]. To further investigate the effect of microstructures on the electrode performance, this study was focused on exploring the idea of multi-layer structure, each with different porosity and permeability, using PNM framework. A workflow was defined to generate fibrous microstructures with desired structural properties. The extracted network was then modified by introducing additional nodes in the center of each throat locations to allow the application of velocity dependent of mass transfer coefficients in each network conduit. An iterative algorithm was used for solving the Nernst-Plank system of mass and charge transport equations in PNM framework. The proposed PNM framework was first validated based on experimental polarization data available in literature [130]. Multi-layer structures with 2 and 3 layers were then created from generated images of fibrous materials with porosity of 0.7, 0.8, and 0.9 as low, medium and high porosity layers. It was shown that in both 2-layer and 3-layer structures, the structure with higher permeable layer near the membrane and lower permeable layer near the channel provides highest performance in terms of current density, with an increase of around 57% over the cases with an opposite order for the arrangement of the layers. Concentration of species and flow rates at the pore-scale were analyzed to rationalize the observed improvement. In high performing structures, higher flow rates were seen in the near-membrane regions, providing the reactive surface area with sufficient reactive species. These regions were otherwise starved of reactant in least performing structures, as flow bypassed the cell via the high permeability layer under the ribs. It was also shown that multi-layer cases with different layers can have the same overall porosity while providing a different performance due to the difference in their microstructures, which demonstrates the importance of studying the microstructures at pore-scale.

Additionally, as the balance between the generated current and pumping cost is essential in operation of VRFBs a final comparison was performed on the generated structures based on the ratio of limiting current density to the pressure loss. The comparison included the generated structures as well as single and multi-layer structures of the same material. It was seen that in single layer structures and multi-layer structures of the same material, the least efficient structure in terms of current density had the most efficient value in terms of pressure loss. However, this trend was not completely straightforward for multi-layer structures with different types of layers. For selecting the desired structure and operational conditions it is important to analyze both pumping cost and the generated current. However, more detailed comparison of these two

parameters is the focus of future works. Results from this study demonstrated the transport behaviour in pore-scale and its effect on macroscopic performance of the electrode.

Future research areas can be studying other parameters such as the effect of fiber orientations and compression on electrode performance, including pumping cost analysis. The framework could be applied on a large dataset of generated images with a wider range of structural properties to further analyze the structure-performance relationship and design parameters. Extending the framework for modeling the entire battery cell including the counter electrode as well as both charging and discharging would be of interest. Another future research could be developing a multi-scale PNM framework to include the transport phenomena in the binders materials if present.

Chapter 5: A deep learning framework to estimate diffusive conductance of conduits in extracted pore networks

5.1. Overview

Pore network modeling (PNM) based on networks extracted from tomograms is a well-established tool for simulating pore-scale transport behavior in porous media. A key element of this approach is the accurate determination of pore-to-pore conductance values, which is a complex task that greatly affects the accuracy of flow and diffusive mass transport studies. Classic methods of conductance estimation based on analytical solutions and shape factors only apply to simple pore geometries, whereas real porous media contain irregular-shaped pores. Although direct numerical simulations (DNS) can accurately estimate conductance considering pores' real morphology, it has a high computational cost that becomes infeasible for large tomograms. The present work remedies this problem using a deep learning (DL) approach, with a specific focus on diffusional transport which has received less attention than hydraulic conductance. A convolutional neural network (CNN) model was trained to estimate diffusive conductance of PNM elements from volumetric images of porous media. The developed framework estimates the diffusive conductance by analyzing individual pore-to-pore 3D images isolated from the tomogram to fully capture the topology and shapes. A key outcome of the present work is that only images of the pore regions are used as input data, avoiding excessive preprocessing time for data preparation. The results of the diffusive conductance prediction show good agreement with the test data obtained by DNS method, with 0.94 R^2 prediction accuracy and a speedup of 500x in prediction runtime.

5.2. Introduction

Diffusive transport occurs in a variety of porous media applications such as geological storage of radioactive nuclear waste [151], [152], catalyst supports [153], and electrodes [154], [155]. The use of pore-scale modeling and simulation techniques to understand the structure-performance relationship of porous materials is common in engineering design, such as optimizing performance of porous components, distribution of catalyst materials, morphology control of undesired deposition [156], and others [157], [158]. The two main approaches for pore-scale simulations of transport in porous materials are direct numerical simulations (DNS), and pore network modeling (PNM) [52]. DNS methods such as the lattice Boltzmann method (LBM) and the finite element method (FEM) have the advantage of probing detailed geometrical features up to the resolution limit of the available image [159]. Their accurate predictions come at a high computational cost that prohibits application in more complex problems such as multiphysics,

coupled nonlinear and transient transport problems, and large samples where there are billions of unknowns [13]. This is in addition to challenges related to building accurate FEM computational grids. On the other hand, PNM is a viable alternative for these large and complex problems due to its vastly lower computational cost [22], [45], [157], [160]–[162]. In PNM the porous medium is abstracted as a connected network where wider void regions are defined as pores (nodes) that are connected by narrower constrictions referred to as throats (edges). This simplification reduces the numbers of variables in the discrete transport equations by orders of magnitude and hence reduces the simulation time concomitantly [13], [21], [35]. However, the necessary simplifications to obtain the speed-up decrease the modeling fidelity [163]. The accuracy of PNM predictions depends on the precise description of the pore space geometry, which is used in the computation of transport conductance values [54]. A connected pore-throat-pore element in the PNM is defined as a conduit and the estimation of conduit's conductance for mass transport has been an active research area since the PNM technique was developed [35], [36], [164]–[167]. The conduit conductance for a simple cylindrical geometry can be obtained from an analytical solution of the governing transport law (i.e. Fick's law); however, for real pore morphologies the cylindrical approximation loses accuracy. Hence, many attempts have been made to adjust the analytical solution by adding correction factors or shape factors to account for the complex geometry encountered in extracted networks [163], [166], [168]–[170]. Most of these efforts have focused on correcting for the deviation of the cross-section from circularity, but they neglect the impact of the diverging and converging nature of the cross-section along its axis. Changes in the constriction have particularly important effects on the diffusion transport conductance [164] which is the focus of the present work. An alternative to analytical methods based on shape factor is to use DNS to estimate the diffusive conductance of each individual pore network element [35], [36]. In this approach, the transport conductance is back-calculated from the DNS results without any arbitrary selection of the pore size and shape information, since the full impact of the conduit geometry is captured in the DNS result. Although this increases the PNM accuracy, it is computationally expensive to conduct this analysis on every tomogram for which a pore network is extracted. A promising alternative, explored herein, is to employ machine learning (ML) algorithms to estimate the conduit's conductance with a relatively low computational cost compared to the DNS approach.

Image-based deep learning (DL) methods have proven to be a powerful tool in classification problems such as cancer detection and disease diagnosis [59], age prediction [171] where a property of interest is predicted based on only image datasets. They can also be used for regression problems, and in the porous media literature have been used to predict properties such as porosity, permeability, and pores size distribution[172]–[177]. More complex physics-based information has also been obtained. For instance Santos *et al.* who used CNNs to estimate the gas density profiles in nanopores of shale samples [178]. The

advantage of using CNNs over using regular neural network models to predict effective properties of porous media was established in a previous work [179], which attributed the success to its convolutional architecture which explicitly assume that spatially close inputs are semantically related. This assumption is an advantage in image data where the features are obviously spatially related. In the present study, a CNN framework was developed to extract and learn the spatial features of random irregular-shaped conduit images and predict diffusive conductance values.

The prospect of using ML to estimate the conductance of PNM elements has recently attracted attention [180]. The general idea is that sub-images of each conduit can be extracted from the full tomogram, by performing a watershed segmentation to identify pore regions, then each pair of pores are analyzed to predict their conductance. Both Miao *et al.* [181] and Rabbani *et al.* [180] trained a model to predict hydraulic conductance, such that Darcy flow could be simulated in the resultant PNM. Because they both focused on hydraulic conductance, the physics were dominated by the throat constriction, to the extent that in both cases the ground truth or training data was generated by using LBM to simulate flow through the throat cross-section only, neglecting the effect of the larger pore bodies. Both groups then estimated some relevant geometrical parameters about the throat size and/or shape (convex hull convexity and circularity [181], and diameter of an inscribed sphere [180]) for training the ML model. In other words, the ML model was trained to predict the given conductance values obtained by DNS simulations on the throat cross-section, from knowledge of only a few geometrical properties of the throat. There are two key limitations to this approach. First, viscous flow is highly dependent on the tightest throat constriction (*i.e.*, $\sim R^4$ where R is the radius of the conduit), whereas diffusion is less sensitive to this (*i.e.*, $\sim R^2$) and thus more impacted by the size and shape of the entire conduit. Therefore, obtaining training data based only on transport through the throat constriction is insufficient. Second, since the entire conduit is of interest, it becomes much less obvious which specific geometrical properties should be extracted and provided to the ML model as input. Moreover, this would require extracting multiple metrics using tools that are themselves computationally demanding (*i.e.*, fast marching method, skeletonization, local thickness, *etc.*). It is therefore an open question how to best leverage ML to estimate diffusive conductance values for use in PNMs.

The proposed workflow in this study is based on training a CNN model to predict the diffusive conductance of pore network elements based on only images of neighboring pore region pairs. The presented study estimates the diffusive mass transport properties and tackles defining challenge of previous ML-based methods by using a non-preprocessed image-based framework. This framework trains a DL model simply by providing a voxel image of two connected pore regions, with each region labeled. This is the smallest

possible amount of preprocessing that can be done on input data. The proposed framework substantially decreases the preprocessing time and resolves the challenge of finding conduits features. The DL model can be used to predict and assign physics properties of conduits (diffusive conductance) in pore network models of porous media. This approach can be generalized in the future to predict other properties. This manuscript is organized as follows. First, the theoretical background and the methodology of the framework are explained. Then, the DL data and trained model are described. Finally, the pore network simulation results and their comparison with currently available PNM approaches [152], [163], [166] and DNS methods are presented and discussed.

5.3. Theoretical background

5.3.1. PNM formulation and conduit conductance

Diffusion of a species in a conduit is described by Fick's first law:

$$J_n = -\left(\frac{D_n A}{L}\right)\Delta C_n, \tag{5-1}$$

where J_n and C_n are the diffusive mass flux of species n, and its concentration, respectively. In Eq. (5-1), D_n is the diffusion coefficient of species n in the solvent (note that this is the diffusion coefficient in an open space, not an effective diffusivity), and A and L are the area and length of the conduit. If the conduit is a straight cylinder, A and L are well defined; however, if the conduit's shape is irregular and cross-section area along its length varies, these become *effective* values A_e and L_e, respectively. Specifically, when the conduit connecting pores i and j is irregular shaped, Eq. (5-1) should be amended as follows [152]:

$$J_e = -\frac{D_n A_e \Delta C_{ij,n}}{L_e} = -G_{ij}^{diff}\Delta C_{ij,n} \tag{5-2}$$

where G_{ij}^{diff} is the overall diffusive conductance of the conduit connecting pores i and j. Applying this expression to each conduit in the network and enforcing mass conservation at every pore i yields the following system of equations, assuming steady-state:

$$\sum_{j=1}^{N} G_{ij}^{diff}\left(c_{i,n} - c_{j,n}\right) = 0, \;\; i = 1,2,\dots,k \tag{5-3}$$

where N is the total number of pores connected to pore i and k the total number of pores in the network. Modeling Fickian diffusion in a pore network requires solving this system of linear equations (Eq. (5-3)) assuming relevant boundary conditions are applied. This results in concentration values in each pore of the network. It is apparent that G_{ij}^{diff} values directly affect the accuracy of the simulation, so a network extraction tool must be able to reliably determine these values.

A conduit is described with the combination of ½ of pore i, ½ of pore j, and the throat connecting them. Given that a conduit has three elements in series, G_{ij}^{diff} is the cumulative conductance of each element which can be defined based on the linear resistor theory for resistors connected in series by:

$$G_{ij}^{diff} = \left(\frac{1}{g_i^{diff}} + \frac{1}{g_{ij}^{diff}} + \frac{1}{g_j^{diff}} \right)^{-1} \tag{5-4}$$

where $g_{(i \mid ij \mid j)}^{diff}$ is the conductance of each element (half pore i/throat ij/half pore j) in the conduit.

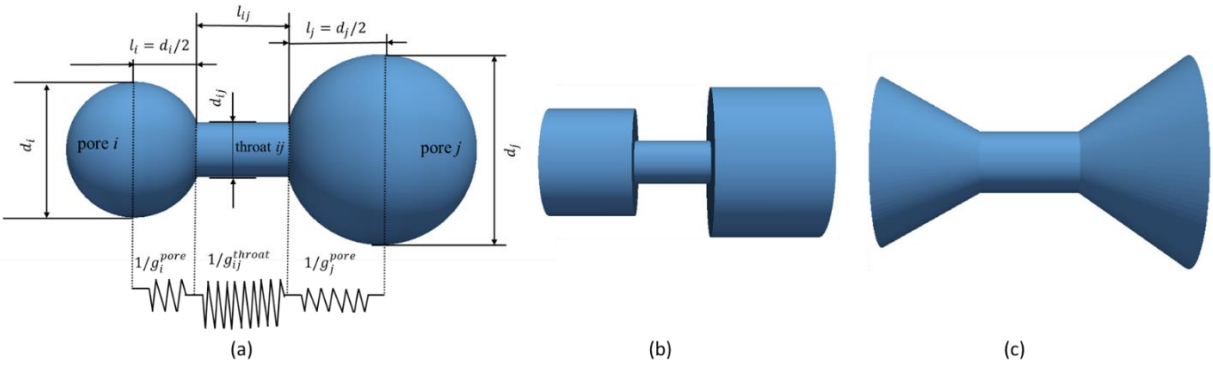

Figure 5-1 A schematic of different geometries for a pore-throat-pore element as one conduit. a) Simple sphere and cylinder geometry. The conduit elongates from the centroid of one pore and includes their connecting throat and half of two pores. The corresponding conductance of the conduit is calculated using the linear resistor theory for resistors connected in series on its elements (half pore-throat-half pore) from Eq (5-4) [43]. b) Cylindrical tubes for pores and throats, referred as geometry-based method. c) An example of a conical frustum and cylinder. The corresponding conductance of the conduit is calculated using the series of resistors model with a correction, referred as shape factor based method.

Figure 5-1 shows a pore-throat-pore conduit and different regular shapes that can be assigned to pores. In the conventional approach for calculating conductance, each element in the conduit is usually assumed to be a cylindrical tube (Figure 5-1b). This arrangement, referred to herein as geometry-based conductance model [98], yields:

$$g_i^{diff} = \frac{\pi D}{4} \left(\frac{d_i^4}{l_i} \right), \tag{5-5}$$

where d_i and l_i are the diameter and length of the elements. Equation (5-5) applies to pores i and j and the throat ij. The length l of a pore is its radius as shown on Figure 5-1a. Inserting equation (5-5) into Eq. (5-4) yields G_{ij}^{diff} values, which can then be used in Eq.(5-3). To determine g_i^{diff} from tomograms, it is necessary to extract meaningful values of d_i and l_i of the pore and throat elements. This is a challenging

task in complex 3D media where the void space is highly irregular in shape, and the pores and throats cannot be completely distinguished.

As explained in the Introduction, different studies have proposed shape factor correction models to salvage the use of the geometrical model for irregular geometries. A more accurate shape factor correction can be obtained by accounting for a variable cross-section in a pore/throat [48]. Assuming a diverging conduit of connected conical frustums and cylinder, as shown in Figure 5-1c, the shape factor ($S^{diff}_{(i\,|\,ij\,|\,j)}$) can be calculated as:

$$S^{diff}_{(i\,|\,ij\,|\,j)} = 1/\int \frac{dx}{A_{(i\,|\,ij\,|\,j)}(x)}$$
$$S_i = \frac{d_i d_t \pi}{4 l_i}, S_j = \frac{d_j d_t \pi}{4 l_j}, S_t = \frac{\pi d_t^2}{4 l_t}, \tag{5-6}$$

where the shape factors are multiplied by geometry-based diffusive conductance of each element as mentioned above:

$$g^{diff}_{i\_shape\_factor} = S_i^{diff} g_i^{diff}, \tag{5-7}$$

In this study, shape factor based conduit conductance values are calculated for comparisons, using Eq. (5-7). Despite its advantages over geometry-based method (Eq.(5-5)), the diffusive conductance calculated based on the shape factor method still results in erroneous predictions of overall effective diffusivity of the network compared to a DNS method using the image.

5.3.2. Image-based framework

Instead of attempting to extract accurate values for quantities describing the geometry, it is possible to find G_{ij}^{diff} using DNS instead. This can be achieved by performing DNS of diffusion on each sub-image representing two neighboring pores and calculating G_{ij}^{diff} using Eq.(5-2). This approach would provide increased accuracy, but is computationally expensive given that a typical tomogram may require thousands of such mini-simulations. So, although this has been demonstrated to be feasible [35] it is not generally practiced.

The objective of the proposed workflow is to overcome the issues of estimating the diffusive conductance of PNM elements accurately and rapidly. For this purpose, a DL model was trained to predict diffusive conductance of pore network elements with only images of the pore-to-pore regions as the input data. The bounding box containing a pair of pore-to-pore region is referred as region of interest (ROI). The input image data included random irregular-shaped images of the ROIs extracted from segmented regions of randomly generated porous media images. The randomness in the shapes of ROIs is because of

segmentation on randomly shaped void space of each porous medium. The details of generated images are given in section 5.3.3. The ground truth data was calculated by implementing diffusion DNS on the pore-to-pore images. A CNN model was then built and trained on the image dataset. The trained model was used to predict the diffusive conductance of unseen image datasets. The model performance was assessed based on prediction accuracy and runtime. Note that the framework was initially implemented for both two-dimensional (2D) and three-dimensional (3D) images. The final model presented in this study was developed based on 3D images. However for visualization purposes, the 2D samples are shown in the framework and in the figures in following sections. The workflow in this study is illustrated in Figure 5-2. Details of each step in the workflow are presented in the next sections.

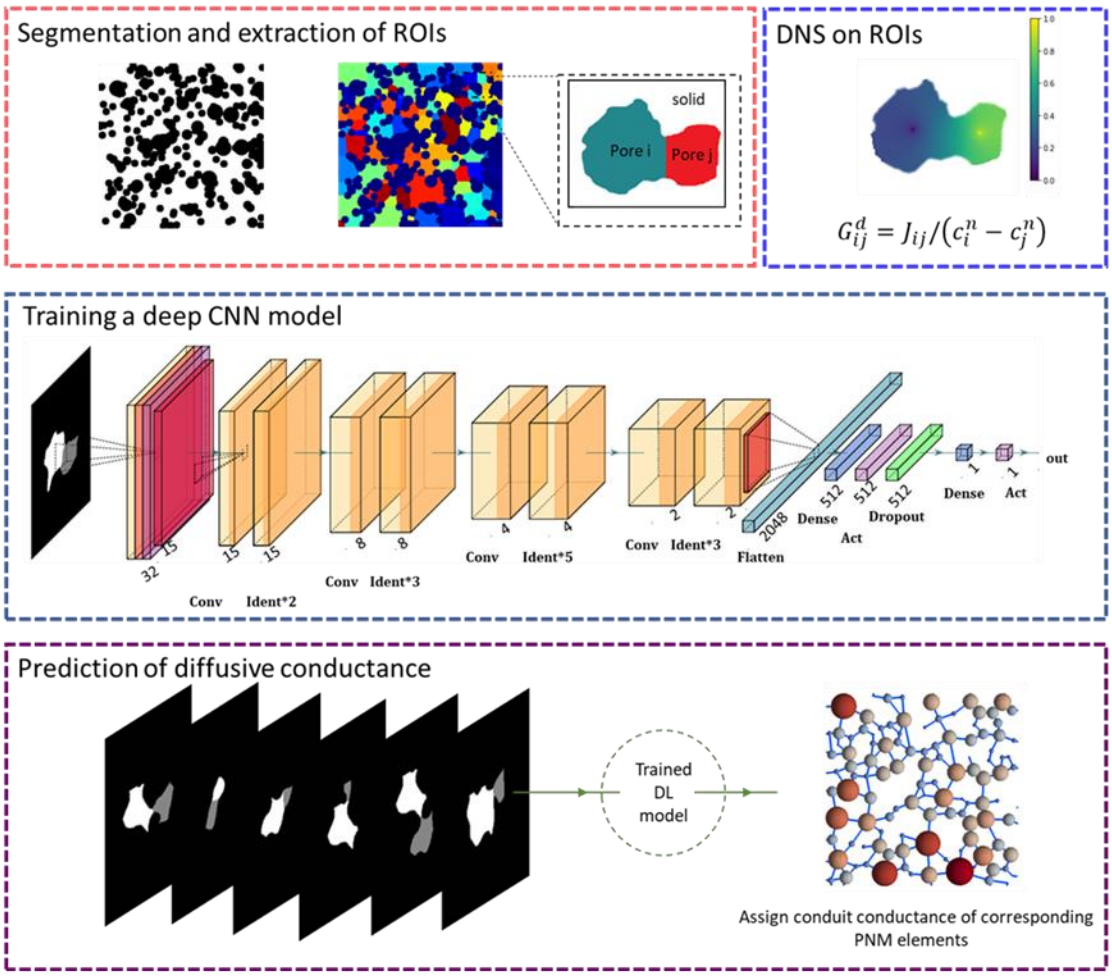

Figure 5-2 A flow chart of the proposed algorithm. It starts by applying an improved watershed segmentation (SNOW algorithm[51]) on binary images of porous media (top left). For each region of interest (ROI) in the segmented image (real shapes of pore-throat-pore element) the diffusive transport is simulated using DNS to find its diffusive conductance value (top right). Labeled images of these regions are passed to a DL model (Resnet 50[63]) to extract their features and train on existing images with their DNS conductance as the ground truth data (middle). The model performance is then assessed with a non-biased test dataset (bottom).

5.3.3. Preparation of the training dataset and ground truth labels

To cover a large variety of geometrical shapes, topologies, and geometrical complexities in the training data, synthetic images of porous media were generated. For training a DL model, synthetic image generation can provide a large number of samples, which is difficult to obtain from a limited number of real porous media images. The 3D images of random porous media were generated using PoreSpy's random polydisperse_spheres generator [132]. PoreSpy is an open-source collection of image analysis tools used to

extract information from 3D images of porous materials. PoreSpy's polydisperse_spheres generator module creates an image of randomly placed, overlapping spheres with a distribution of radii, and the shape and overall distribution of the void/solid phase are varied. The distribution of overlapping spheres' radii was defined using Scipy's [182] statistical normal distribution function. To include varieties of realizations close to real geometries, a wide range of porosities (0.35-0.8) were used to generate the random images.

The generated images are sets of 3D binary images from which a pore network can be extracted. For this study, sub-images (ROIs) of the pore-to-pore regions of pore network elements were required. These ROIs can be captured from watershed segmentation of images. Image segmentation is the first step towards pore network extraction where the binary image of the porous medium is divided into segmented pore regions. In this work, a custom marker-based watershed segmentation method (SNOW method [51]) in PoreSpy was used to segment the porous media images (Figure 5-3a). Each region in the segmented image corresponds to a pore, and the constriction to its neighboring region corresponds to a throat in the pore network model (Figure 5-3b bottom). Therefore, the ROI for this study is two neighboring areas in a segmented image of a porous medium that corresponds to a pore-throat-pore element (conduit) in the pore network model(Figure 5-3b top).

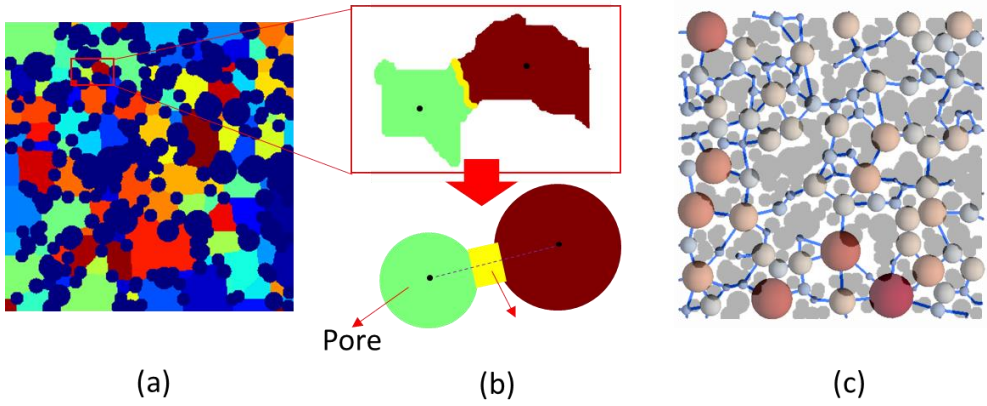

Figure 5-3 Illustration of the watershed segmented image and an ROI for a 2D randomly generated porous medium. a) Segmented regions based on watershed method. b) Two neighboring pore regions segmented image (top) and their corresponding pore and throat model in a PNM (bottom). c) Pore network connections in the void space.

The corresponding pore network of the segmented image is illustrated in (Figure 5-3c). The framework developed in this study only requires the information of the image before network extraction (i.e., Figure 5-3a). Therefore, the input images of the framework are ROIs of the segmented samples. For each ROI, two connected pore areas were labeled 1 and 2 and the rest of the segmented image was labeled 0 and

treated as non-conducting phase. Flipping the labeling of the regions in every ROI did not notably alter the predicted conductance of the conduit.

This label-based description of the pairs was found to work as well or better than other different preprocessing steps, such as distance transform, in terms of DL model performance. The labeled image of pore-throat-pore captures the shapes and irregularities of pore regions and the location of the throat as shown in Figure 5-4. Therefore, the converging and diverging parts of the conduit shape are also well captured. The labeled ROI images were defined as input data for the DL workflow. The resolution of all images was 1 $pixel^{-1}$. Therefore, the framework is independent of the resolution of the images, as the diffusive conductance values are calculated in terms of voxels with the dimension of 1/pixel in 2D and 1/voxel in 3D.

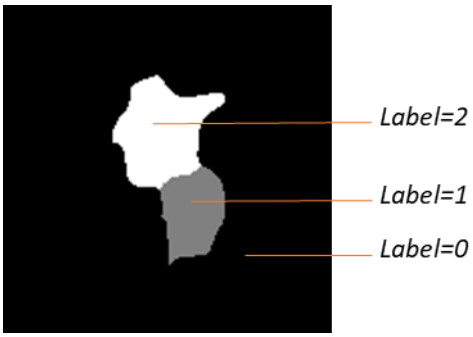

Figure 5-4 A sample input image for the ML algorithm. It includes two connected pore regions extracted from the whole medium segmented void space. To remove the effect of label values on the algorithm, solid-phase along with the regions other than ROI are labeled as 0. Two connected pore regions in the ROI are labeled as 1, and 2, respectively.

To improve representativity of the images dataset and remove any bias related to image generation, augmentation methods including rotations and flips were used. [59], [183].

These ROI images were also computational domains for calculating the ground truth data. A diffusion problem at the pore-scale over the conduit was defined and solved using DNS (finite difference method) as described in Figure 5-5. A square (or cubic for 3D conduits) grid was used to discretize the computational geometry. For each ROI, Dirichlet concentration boundary conditions were imposed on the centroids of the two pore regions. After solving the resulting linear system of equations, the diffusive conductance was computed using in Eq. (5-2) [152] with concentrations averaged over the portions of the domain within the two inscribed spheres (or circles for 2D images) (see Figure 5-5 (c)). In the rest of this work, the DNS based conductance values are referred as the ‘ground truth’.

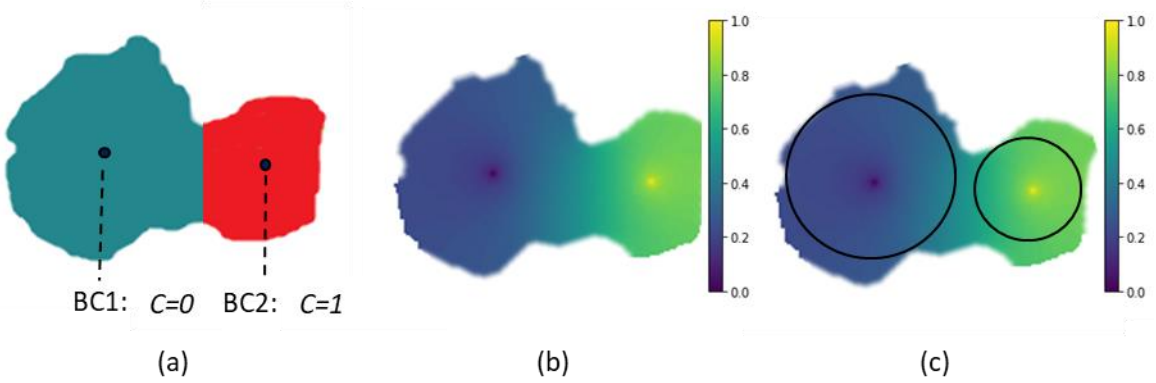

Figure 5-5 Steps towards the calculation of 2D conduits diffusive conductance using DNS. a) After meshing the conduit using a square (hexahedral for 3D conduits) grid, Dirichlet concentration boundary conditions were imposed at the pores centroid. b) Concentration color map resulting from the solution of the diffusion problem. c) An illustration of the portions of the 2 regions lying within the corresponding inscribed circle (sphere for a 3D conduit). Surface (volume for 3D conduits) average concentration over the inscribed circles (spheres in 3D) are used for the calculation of conduit's effective properties (i.e., the diffusive conductance). An inscribed circle is the largest circle that can fit into a pore region [51] while having the pore's centroid as a center. Inscribed circles are obtained during the network extraction using PoreSpy [132].

5.3.4. Deep learning model

The building blocks of a simple CNN are stacks of convolutional layers (CL) followed by maxpooling layers and a fully connected layer as the last layer to produce the output [58]. A CL extracts the patterns and features of an image by applying filters to the image [61]. The CNN architecture in this study was developed based on a residual network model Resnet50 [63] that is advantageous in addressing "vanishing gradient problem" in conventional deep networks [184]. The vanishing gradient problem is addressed by adding bypass connections where parts of the transformed image can pass through deeper layers without losing their strength (Figure 5-6 c). The CNN structure in this study is illustrated in Figure 5-6. The developed model is a 3D Resnet50 that takes in 3D voxelated images of ROIs as input. However, for illustration purpose a 2D image is shown in Figure 5-6.The model starts with a 3D CL with a cubic kernel that sweeps on a padded input image to extract features directly from images. The CL is followed by a batch normalization layer where the convoluted input image is normalized based on the samples in the same mini-batch. The resulting image is passed to an activation layer with an activation function of rectified linear unit (ReLU) $f(x) = \max(0, x)$. Downsampling is then applied to the image using a maxpooling layer. The remaining building blocks of the network are convolutional and identity blocks. Convolutional and identity blocks include a pattern of convolution, batch normalization, and activation layer with bypasses explained

above (Figure 5-6 b,c) [63]. After a series of convolutional blocks and identity blocks, the last block of the network starts with a pooling layer. The output of this layer is then flattened to be fed into a dense layer. A dropout layer at the end was used to prevent the overfitting problem and increase computational efficiency.

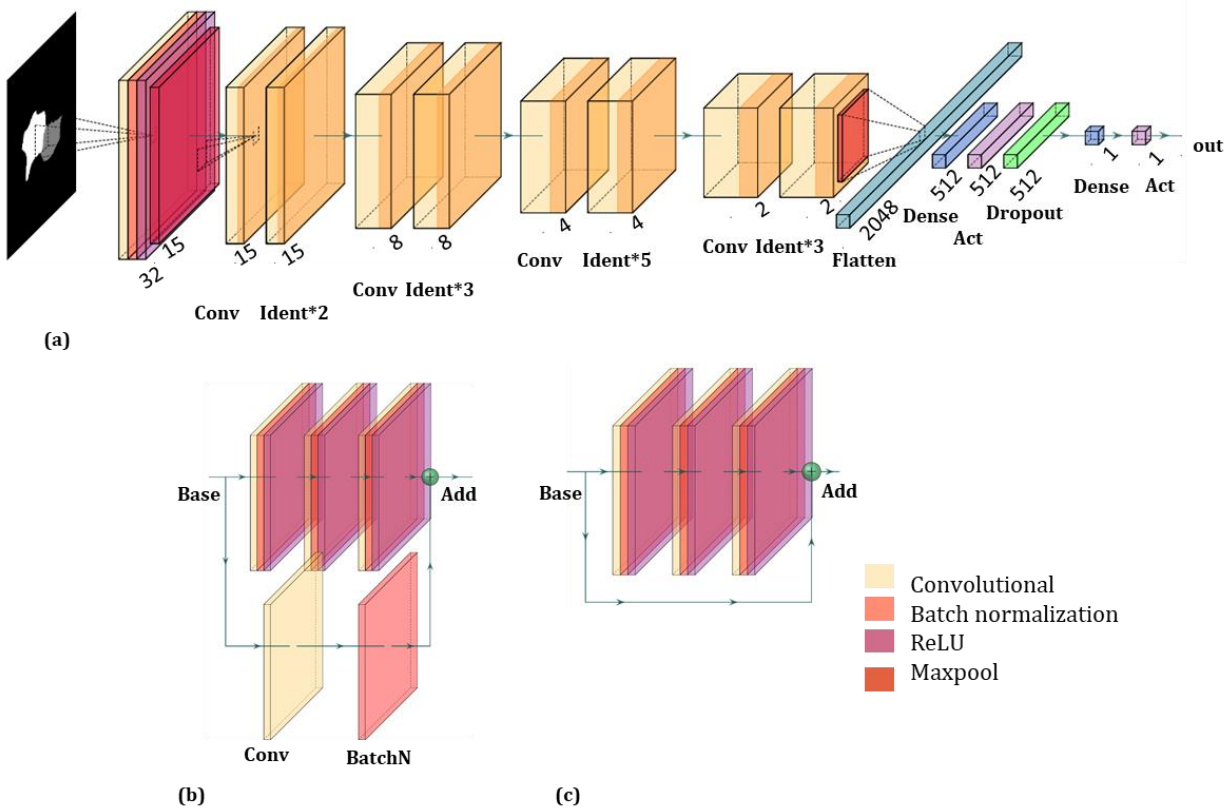

Figure 5-6 The architecture of the CNN model used in this study. a) Resnet model. b) A convolutional block (conv blocks are repeatedly used in the Resnet model with different kernel sizes. c) An identity block (identity blocks are repeatedly used in the Resnet model), the bypass identity connection allows the input to pass through the cell without modifications.

5.4. Results and discussion

5.4.1. Training process

The workflow for training the DL model was developed in Python [185] using TensorFlow [186]. From a dataset containing 24,465 images of pore pairs, the training and validation sets were randomly selected in a way that 80% of the images were used as training data and 10% of the images were used as validation

dataset. To assess the prediction performance of the model for unseen data, the remaining 10% of the images were used. The target data was normalized with min-max scaling between [0,1] based on training dataset. The loss function for this regression problem was defined as the MSE between the predicted and target values of diffusive conductance. This function was selected among other functions including Huber and root mean squared error (RMSE). The objective of the optimization process in CNN learning is to minimize this loss function as described in Eq.(5-8).

$$\text{Loss} = \frac{1}{n}\sum_{i=1}^{n}\left(Y_i - \acute{Y}_i\right)^2, \tag{5-8}$$

where n is the number of data (labeled images of two regions), Y is the vector of target values and $\acute{Y}$ is the vector of predicted values of diffusive conductance.

The model was fitted in the training process by minimizing the MSE loss function using Adam Optimizer with a learning rate of 10^{-4}. The prediction accuracy was defined as R^2 (coefficient of determination) accuracy which indicates the proportion of variance of target values that were defined by variables in the model as following: [47]:

$$R^2(Y, \acute{Y}) = 1 - \frac{\sum_{i=1}^{n}(Y_i - \acute{Y}_i)^2}{\sum_{i=1}^{n}(Y_i - \bar{Y})^2}, \tag{5-9}$$

where $\bar{Y}$ is the average of target values calculated as $\bar{Y} = \frac{1}{n}\sum_{i=1}^{n} Y_i$.

It must be emphasized that training the model requires setting the hyper-parameters of the DL algorithm and adapting its architecture to the task. This was done by performing the training several times, adjusting one parameter at a time, and assessing the performance and accuracy of the model to find the best values for each parameter. Using this process, a batch size of 16 was and a dropout probability of $P = 0.5$ were selected as the best values in terms of memory and accuracy efficiency. To increase the memory efficiency of the workflow all the input and output files were saved in Hierarchical Data Format (HDF) files [187].

The framework was developed on a machine with 2.10GHz Intel Xeon CPU. Model training was implemented on a GPU architecture using Nvidia Quadro RTX 8000 graphics card. Each epoch of training took approximately 8.2 minutes to run. Training the model took about 13.7 hours. After training, the model predicted conductance of 2,447 images of 3D conduit test data in 9.32 seconds with R^2 accuracy of 0.97. That is approximately 0.0038 sec to predict each target label. In contrast, predicting the diffusive conductance on those conduit images using DNS method takes between 2-10 seconds (average 3.5) depending on the size of the image for the test dataset. DNS based runtime increases as the size of each pair of image becomes larger. This performance difference can become quite substantial when networks are extracted from images containing 1,000's of conduits. The trained DL model takes in tensors of large number of images and can predict the results within seconds. As the number of conduit images increases, the computational cost of DL-based prediction does not increase significantly. On the other hand, the DNS-

based prediction of larger number of images becomes more time consuming. A detailed comparison of these two PNM methods is shown in the next sections.

5.4.1.1. Training and validation loss

The loss values for training and validation datasets in each epoch of the training are shown in Figure 5-7. The decreasing trend in training and validation errors indicates an improvement in the CNN model capability to estimate target values as more epochs are completed. The training and validation errors reached a plateau of approximately $MSE = 2.7563 \times 10^{-4}$ and $MSE = 3.3711 \times 10^{-4}$ at 100 epochs, respectively. The trend indicates that overfitting or underfitting did not occur when the model was stopped at 100 epochs. However, we observed that before epoch 85, the validation loss is lower than the training loss. There are two main reasons that can lead to this trend in early stages of the training until reaching an optimum point of a good fit (epoch 100). First, because there is a competition between optimization and generalization, the optimization tends to update the model to best perform on the training data whereas the generalization tends to have a model that performs well on unseen data (test or validation data). At the early stages of the training, these two concepts are correlated [188] and the model can be underfit, meaning that there is still room for improvement of the model and the network has not captured all important patterns in the training data. At the later stages of the training, the generalization stops improving and the model starts to overfit meaning that the model is learning the patterns that are more specific to the training data. A good fit will be where both optimization and generalization are in balance and the training and testing loss are low but not very much different in terms of order of magnitude. This condition of a good fit was reached at epoch 100. Second, this may be related to the use of dropout layers to prevent overfitting [188]. During the training the dropout layer drops some of output features of the layer so that the optimization focuses on the most important patterns in the training data instead of all patterns, thereby allowing the network to generalize better (perform better on unseen data). As more epochs are processed, the trained network improves and both training and validation loss become closer until they reach a plateau near epoch 100.

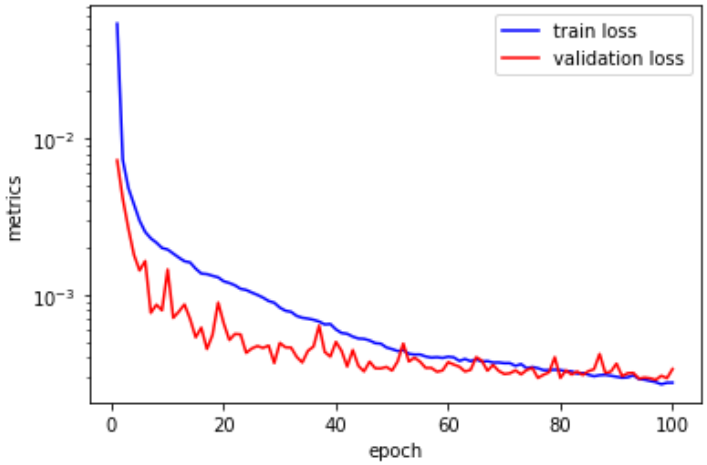

Figure 5-7 Loss function values for the training and validation dataset for 100 epochs (semi-log scale).

5.4.2. Prediction

5.4.2.1. Prediction accuracy

The ability of the trained model to predict diffusive conductance of unseen data (vs Fickian diffusion equation solution obtained by DNS method described in Section 5.3.3) was then assessed. Prediction results for unseen data shown in Figure 5-8 indicate a high accuracy of prediction up to $R^2 = 0.97$.

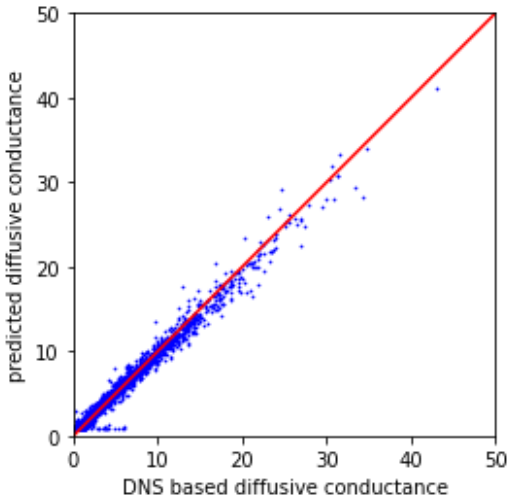

Figure 5-8 Predicted diffusive conductance vs DNS based diffusive values (ground truth) for 2,447 test images tested on the fitted model.

To compare the proposed framework with traditional methods of estimating diffusive conductance, a separate larger dataset of 6,163 conduit images were used as the test data. The conduit images were

extracted from a new set of 14 randomly generated images. The DL-based prediction results for these unseen images are shown in Figure 5-9.

After extracting the conduit images the DL prediction runtime for 6,163 conduits was 13s whereas the DNS prediction was 2.5 hrs. The advantage of using DL-based framework to predict the values is more noticeable here, as after increasing the number of images from 2,447 (shown in Figure 5-8) to 6,163 (shown in Figure 5-9) the DL-based prediction runtime does not increase significantly (from 9.32s to 13s), which is about 4 seconds increase while still remaining in the order of seconds. On the other hand, the DNS-based prediction runtime increases significantly (from 1.5 hrs to 2.5 hrs), which is about 1 hour increase in runtime.

For comparison, also shown in Figure 5-9 are the conductance values for the same set of images but calculated with the basic geometrical method and shape factor based method both discussed in section 5.3.1. The geometry-based conductance values (Eq. (5-5)) and shape factor based methods (Eq. (5-7)) are underestimating/overestimating the conduits' conductance resulting in a higher estimation error. The accuracy of these methods to estimate diffusive conductance can be even lower in more irregular-shaped geometries and heterogeneous media. As shown in Figure 5-9, geometry-based conductance values have a large deviation from ground truth values resulting in the lowest estimation accuracy. This demonstrates the inaccuracy of conductance values calculated based on simplified geometries. Attempting to correct these geometrically computed values using shape factors improves the overall result marginally, as shown in Figure 5-9c. Despite some improvement, the shape factor based method still presents a large deviation from ground truth data as degrees of irregularities in pore shapes increase. The main reason is shape factor methods are only partially successful in that they do not account for the diverging/converging nature of the conduits. Conduit features such as diverging/converging section, shape and more complicated features that cannot be quantified as a factor such as spatial features were automatically extracted in a CNN framework. As shown in Figure 5-9a, the trained DL model estimated conductance values for unseen images of conduits with the highest accuracy ($R^2 = 0.94$) in contrast to traditional geometrical and shape factor based methods (Figure 5-9). However, there are some points where the predicted conductance is much lower than the DNS value (the points along the bottom close to the horizontal axis). To find the reason for the deviation, the volumetric image of pore-to-pore regions corresponding to those points were investigated. It was found that those regions either contained a connecting throat of one to two voxels or had a slit-like geometry embedded into their large neighboring pore. Examples of such ROIs are shown in
Figure 5-10. These two types of properties are rare in the segmented image dataset and are not a desired property for PNM in general. Therefore, these images were because of the original image's highly constricted region, and image segmentation method that could be improved to modify the segmentation.

To compare the DL predicted values with shape factor method visually, an example of a randomly generated porous sample with the size of 100^3 voxels is shown in Figure 5-11. The extracted network model and part of the segmented image of the porous sample is shown in Figure 5-11a. The pores are represented as spheres (shrink to half of their size) and throats are represented as cylinders with a constant thickness of 5 voxels. This scaling of the size was done only for visualization purpose. In other words, the pore network model and its geometry model used for calculating the diffusive conductance includes the real values of pore and throat sizes. Predicted values of conduit conductances from DL model is shown in Figure 5-11b. Each throat is colored by the predicted conductance value, which spans on a range of [0.25,16] for this porous sample. The DL prediction accuracy was $R^2 = 0.94$ while the shape factor method's prediction accuracy was $R^2 = 0.65$. Therefore, the DL method predicted the conductance values more accurate than the shape factor method. To compare the predicted diffusive conductances in more details, the percent error of estimated conductance of each individual conduit was calculated using $percent\ error = \left|\frac{estimated\ value - DNS\ value}{DNS\ value}\right| \times 100$. As a visual comparison, the percent errors of DL conductance and shape factor method conductance are shown in Figure 5-11c,d. For better distinction of the difference in the errors, only the throats with percent error smaller or equal to 10% were colored in Figure 5-11c,d. The throats with percent error higher than 10% were represented by thin green lines in Figure 5-11c,d. As shown in Figure 5-11c, the minority (15% of all conduits in the network) of the percent error are higher than 10%, whereas in Figure 5-11d, the majority (96% of all conduits in the network) of the percent error are higher than 10%. This comparison shows the advantage of DL method over the shape factor method to predict the conductances of conduits. Images shown in
Figure 5-10 and Figure 5-11 were visualized in ParaView[189].

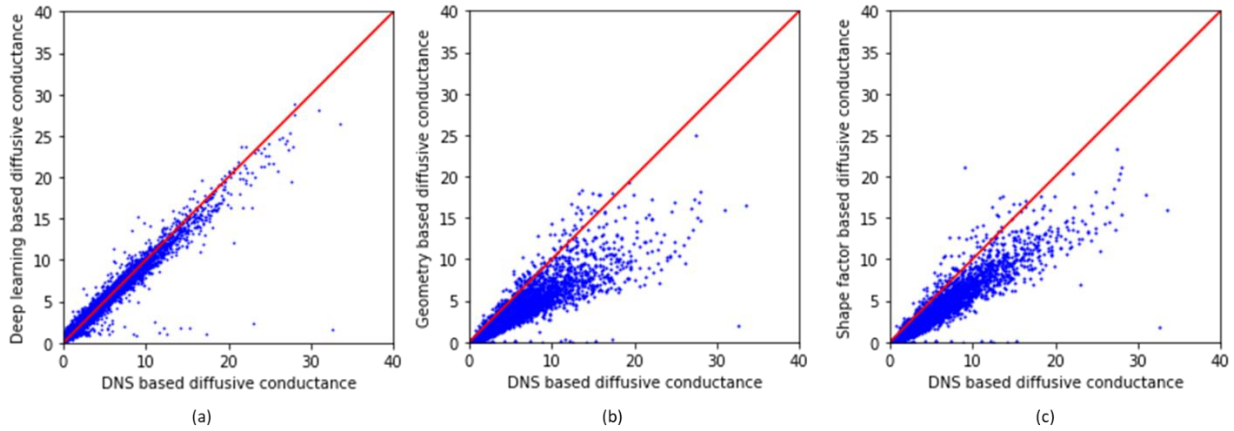

Figure 5-9 Predicted diffusive conductance obtained by different methods vs DNS based values for 6,163 test images. a) Predicted diffusive conductance using DL model vs ground truth values, $R^2\ accuracy = 0.94$. b) Geometry-based diffusive conductance vs ground truth values, $R^2\ accuracy = 0.62$. c) Shape factor based diffusive conductance vs ground truth values, $R^2\ accuracy = 0.71$.

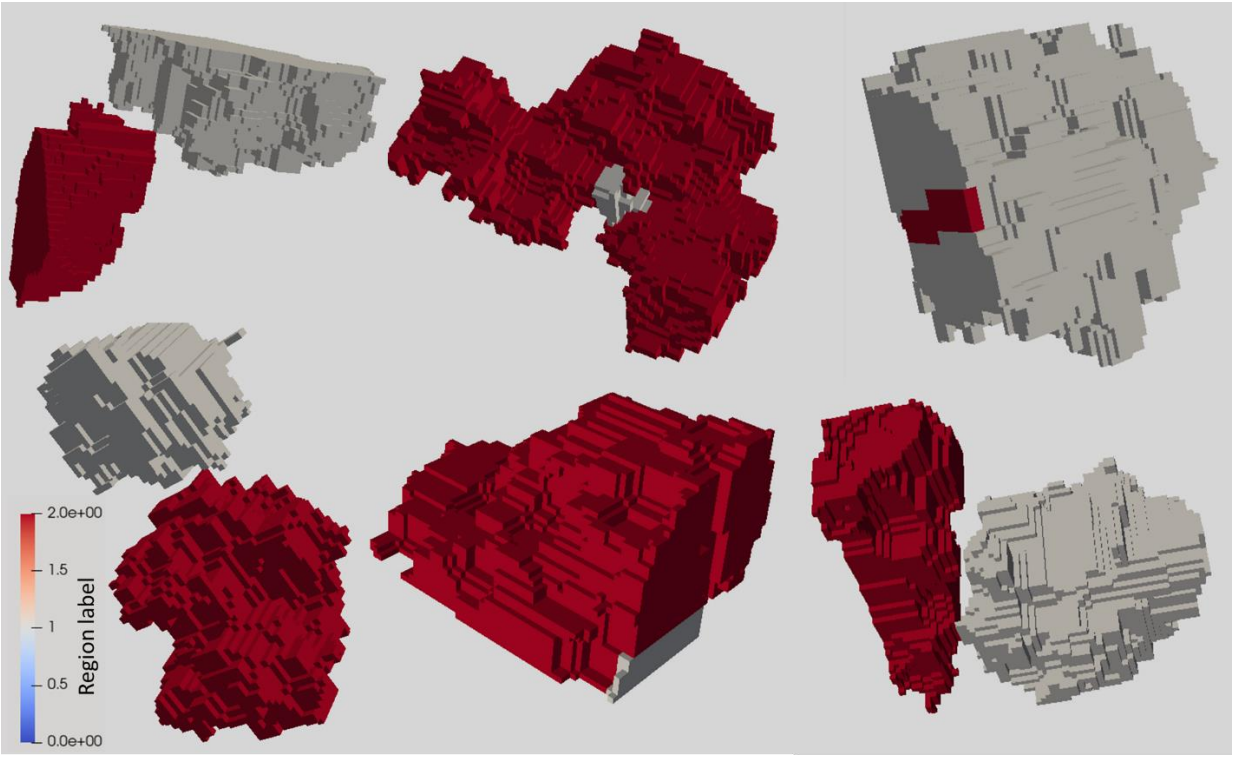

Figure 5-10 Examples of ROIs (from 6,163 test images) that the trained model predicts their diffusive conductance with the least accuracy. These ROIs correspond to the scatter points in Figure 5-9a that are along the bottom close to the horizontal axis.

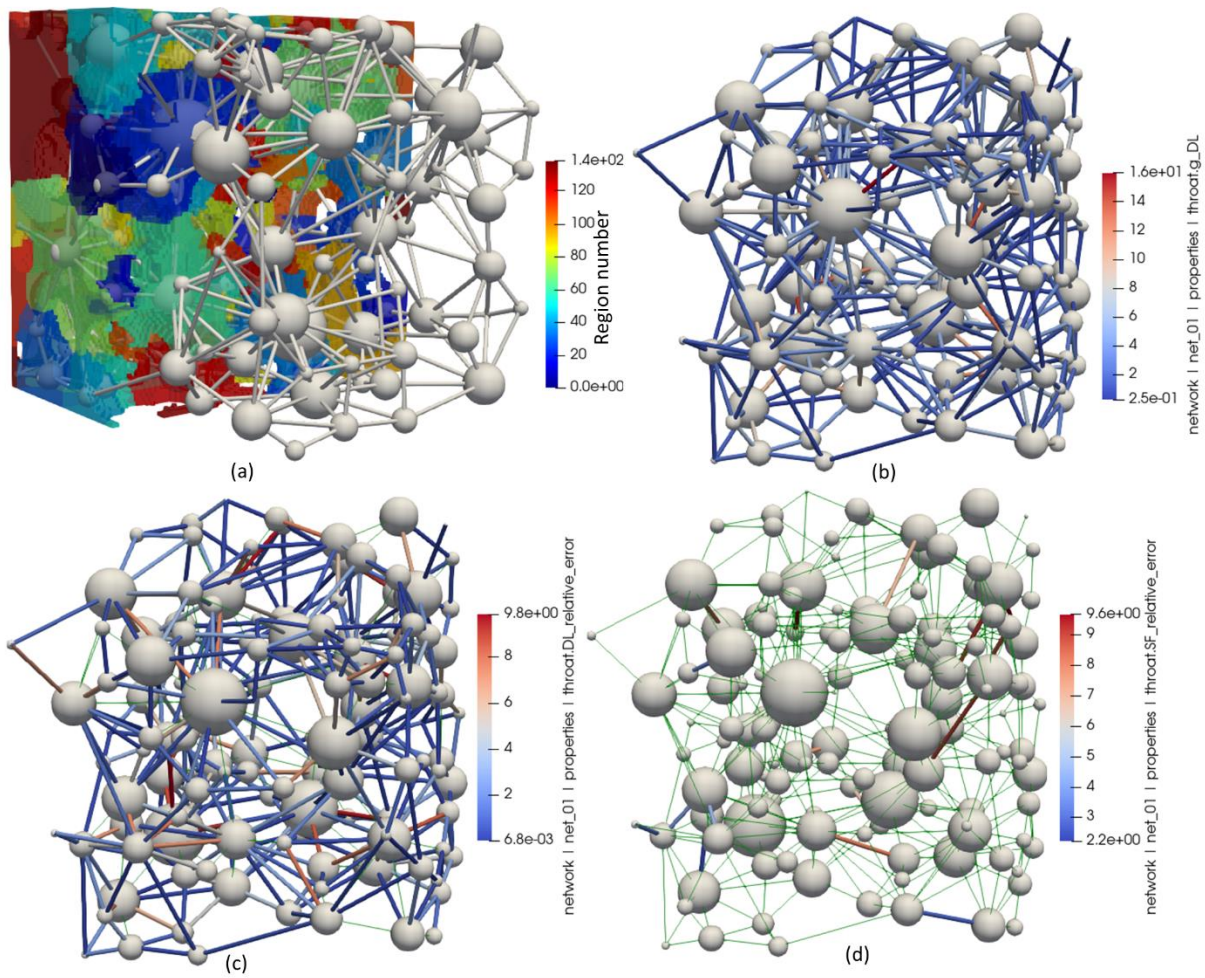

Figure 5-11 Pore network visualization of a randomly generated porous sample. a) Part of the segmented image of the porous sample with the extracted pore network of the sample's void space. Each segmented region is colored by its index value. b) The pore network throats are colored by predicted diffusive conductance of conduits using the DL method. c) The pore network throats are colored by the percent error of DL-based conductance method. The throats with higher than 10% error are distinguished with thin green lines. The DL prediction accuracy for diffusive conductance of all conduits in the network was $R^2 = 0.94$. d) The pore network throats are colored by the percent error of shape factor-based conductance method. The throats with higher than 10% error are distinguished with thin green lines. The shape factor prediction accuracy for diffusive conductance of all conduits in the network was $R^2 = 0.65$.

5.4.3. Deep learning-based PNM Comparison with DNS on the entire domain

The accuracy of PNM results using the local diffusive conductance values found from the proposed DL framework was assessed with reference to the results from the DNS method on the entire domain. The formation factor prediction for 15 randomly generated synthetic porous media calculated using PNM with DNS-based conduit conductance, DL-based conduit conductance, PNM with geometry-based conduit

conductance, and shape factor based conduit conductance in comparison with the full DNS results on the entire images is shown in Figure 5-12. The formation factor was calculated from the effective diffusivity of the domain. Applying a Dirichlet boundary condition for inlet and outlet concentration on each domain, assuming a diffusion coefficient of 1, effective diffusivity and formation factor were calculated as follows:

$$D_{eff} = \frac{J_A \times L}{\Delta C_n \times A}, \qquad F = \frac{1}{D_{eff}}, \tag{5-10}$$

where J_A and F are the molar rate of species transport through the domain, and the formation factor of the domain, respectively.

The DL-based PNM can estimate the diffusive mass transport behavior in these porous media samples within acceptable accuracy while requiring considerably less computational time in contrast to the DNS method. After extracting the images of the conduits, the average runtime to estimate the conduit conductance of 6,542 image samples of 3D conduits using the DNS method was 3.5 hrs, whereas the predictions using the trained DL model was done in 16.5s.

R^2 accuracy of each PNM approach to estimate formation factor in contrast to DNS on the entire medium for these 15 cases were: -1.17, 0.49, 0.87, and 0.84 for geometry-based conductance model, shape factor based model, DNS-based model, and DL-based model, respectively. Assuming a baseline of 0 for R^2 accuracy of a model that always predicts the average value of a target, a negative R^2 can be analyzed as a scenario where the model predicts worse than the baseline.

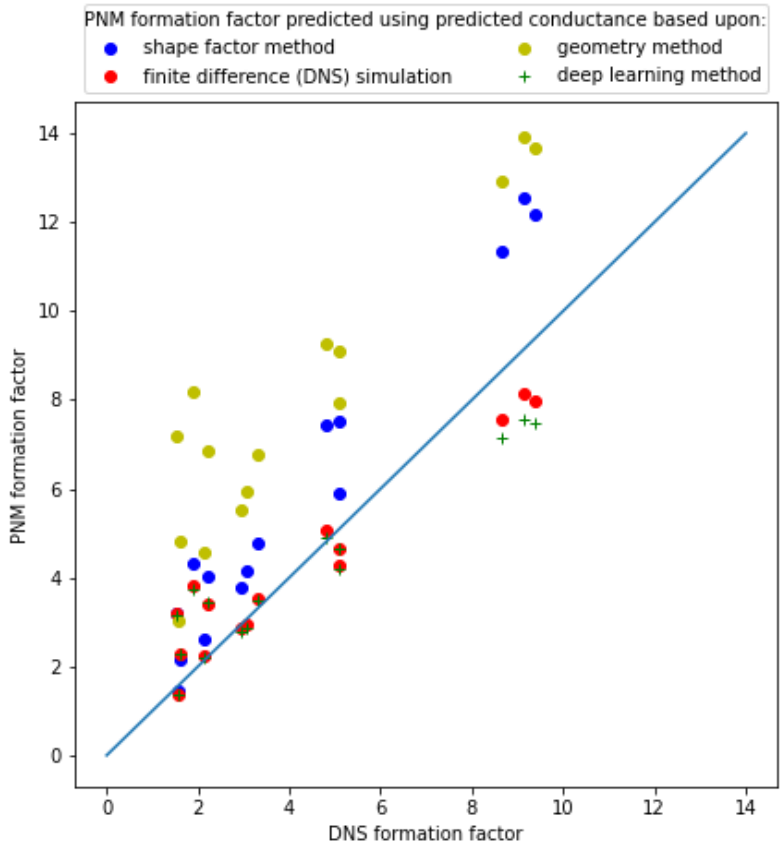

Figure 5-12 A plot of formation factor calculated using PNM vs DNS for 15 images. Blue dots data points are the PNM with shape factor based diffusive conductance, red dots data points are the PNM with finite difference-based diffusive conductance, yellow dots data points are the PNM with geometrical diffusive conductance, and green plus data points are the PNM with our DL-based diffusive conductance.

The comparison shown in Figure 5-12 demonstrates the advantage of DL-based PNM models both in terms of time and accuracy. However, the domain size for the 15 presented samples were not large enough to capture the significance of DL-based PNM in terms of time in contrast to the finite difference-based PNM approach. For this purpose, a separate comparison was applied on randomly generated porous samples of the same porosity (0.75) with different sizes. As the size of the samples increases, the advantage of runtime saving in DL-based PNM becomes more significant as shown in Figure 5-13. The runtime reported for PNM models includes pore network extraction, extraction of conduit pairs, prediction of conductance as well as Fickian diffusion simulation. The runtime for network and image extraction increases as the size of the domain becomes larger while the runtime for predicting diffusive conductance using DL-based model does not increase significantly. Despite the increase of time for extracting the network and conduit images, it should be noted that once the network is extracted, the same network can be used for fast simulation of transport phenomena and other simulation purposes in the porous sample.

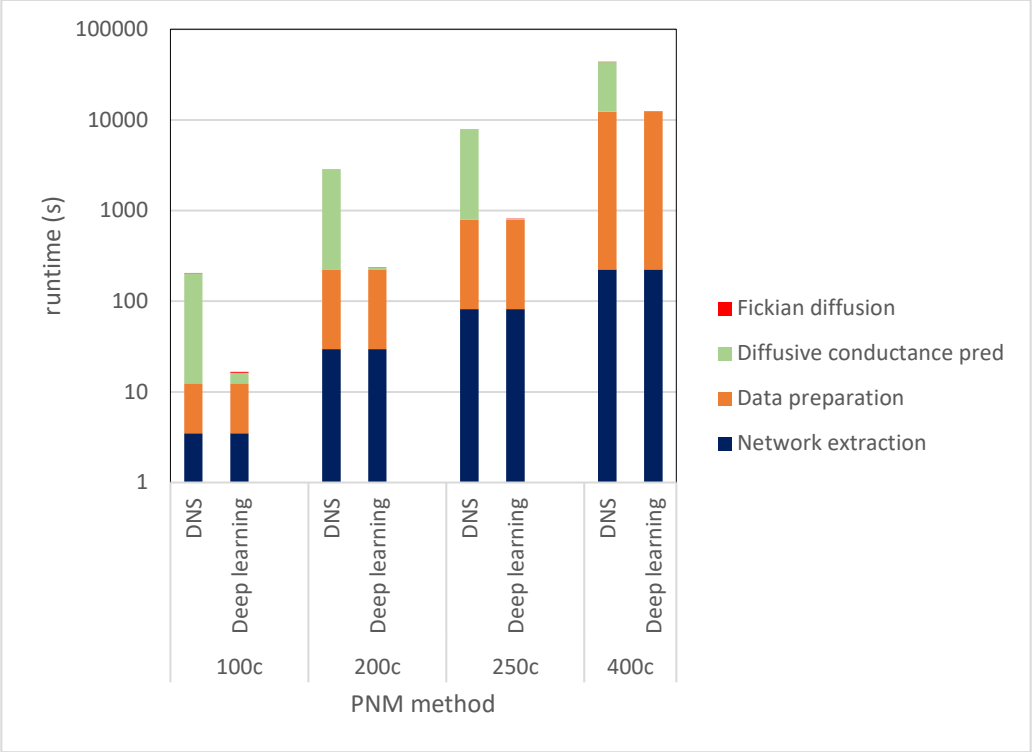

Figure 5-13 Runtime to create a PNM and implement a Fickian diffusion transport through the domain using finite difference based conduit conductance method (DNS) and DL based method. Each bar indicates the steps applied on 4 randomly generated porous sample with size of $100^3, 200^3, 250^3, and\ 400^3$. These steps include extracting the network, preparing images of conduits, predicting the diffusive conductance of conduits, and applying a diffusive mass transport throughout the network.

5.5. Conclusion

A DL-based framework was developed to estimate diffusive conductance of conduit elements in pore network models using only images of pore-to-pore regions as the input data. The proposed framework is the first to estimate diffusion conductance rather than hydraulic conductance, and crucially uses only the images rather the more complex metrics obtained from images, greatly simplifying and accelerating its end use. The capability of the DL model to estimate the conduits' diffusive conductance was assessed with a non-biased test dataset. The test dataset contained a large number of porous media realizations with various morphologies, topologies, and geometrical complexities. The accuracy of the DL model to estimate diffusive conductance of irregular-shaped conduits was compared with the accuracy of conventional methods to calculate conductance values including geometry-based and shape factor based approaches. The DL model predicted diffusive conductance of test images within 0.94 R^2 accuracy, whereas geometry-based and shape factor based methods estimated conductance values within 0.62 and 0.71R^2 accuracy,

respectively. The speedup in predicting diffusive conductance using the DL model compared to computing them using DNS was on average 500x. Therefore, the developed framework was both massively faster than DNS and much more accurate than geometry-based methods. Ultimately, the predicted formation factor and/or effective diffusivity of full extracted networks was much more accurate than using geometry-based methods for conductance, leading to more predictive pore network models based on extractions from tomograms. The framework was trained on randomly generated sphere pack materials. For other types of porous material samples, the trained model can be retrained on a portion of new samples using transfer learning and can be used for prediction on the rest of the samples. Retraining the model would also offer a reduced training time as the current model's weights and trainable parameters need only be fine-tuned with new samples. The proposed DL framework was included in PoreSpy's pore network extraction module (porespy.network), and they are compatible with OpenPNM's diffusive conductance models for pore network modeling of transport phenomena. The codes of the proposed framework are available online in the PMEAL group's github profile [190]. Future works could be extending the framework for estimating hydraulic conductance of conduits. Although the basis of the comparison for prediction accuracy was mainly R^2 accuracy, it is recommended to use multiple metrics such as relative errors, RMSE to evaluate the prediction accuracy in future works. It would also be interesting to develop a framework to generate a wide range of random individual ROI images as an alternative to extracting the ROI regions from porous samples. However, this idea requires further investigation to ensure the dataset is a good representative of ROI regions in a range of porosity and types of porous samples.

Chapter 6: Conclusions and future work

The overall goal of this thesis was to apply pore network modeling to the study of transport processes in porous electrodes, with an emphasis on VRFB electrodes and Zn-air cathodes. This goal required addressing several knowledge gaps in the field of pore network modeling since they have not historically been applied to these types of multiphysics systems. The resultant pore network framework was the applied to unravel the structure-performance relationship of the electrodes to provide insights into the design and operation of these systems. A summary of each objective and key findings in this study are explained in the next section.

6.1. Summary and conclusions

In chapter 3, a PNM framework was developed for electrochemical modeling of the porous catalyst layer of Zn-air flow batteries. The focus of the study was to properly capture the liquid-gas interface and investigate its role on the performance of the electrode. The model included electrolyte invasion using invasion percolation algorithm that mimics a drainage process in a porous medium, which subsequently required including dissolution of oxygen, multiphase transport, and electrochemical kinetics into the PNM framework. The developed framework was utilized to analyse the effect of electrolyte saturation on the extent of liquid-gas interface and electrode performance. It was found that as the invasion of electrolyte proceeds, the generated power increases up to a maximum value and decreases afterwards. Such increase and decrease trend in the performance matched the changes of the extent of liquid-gas interface, reinforcing the hypothesis that the oxygen reduction reaction is predominantly occurring in the regions closest to the liquid-gas interface, but not necessarily at the 'triple phase boundary' as is generally assumed. In addition, the effect of electrolyte invasion on tortuosity of the electrolyte cluster at pore-scale was studied. It was found that at relatively low non-wetting phase saturations the electrolyte cluster presented a highly tortuous path that hinders the mass transport of produced OH^- and may eventually result in precipitation of KOH, which is a degradation issue. Existence of highly tortuous path had a more detrimental effect on the accumulation of OH^- at lower to intermediate saturations and higher current densities. Finally, the developed model was used for structure-performance analysis of the catalyst layers based on three pore size distributions. It was concluded that a catalyst layer with narrower pore size distribution performs better at lower saturations whereas a catalyst layer with wider pore size distribution continues to perform better at higher saturations. The developed framework was the first 3D PNM of zinc-air cathode that included all the key physics and transport mechanisms.

In chapter 4, a PNM framework was developed for modeling of VRFB porous electrodes. The focus of the study was structure-performance analysis of novel electrode structures. For this purpose, a workflow was defined to generate fibrous materials with pre-defined structural properties. Extracted networks of the fibrous materials were then modified with additional throat nodes to include the velocity dependent of mass transfer coefficients in the pore network conduits. This modification was crucial, as it was shown that using a velocity independent mass transfer coefficient could lead to overestimation of mass transport behaviour. The developed framework was used to generate novel multi-layer structures with different porosity and permeability. Various 2-layer and 3-layer structures were generated, and their performance were analyzed along with pore-scale information, such as distribution of flow and reactive species. PNM results showed that when using an interdigitated flow field, placing the layer with higher permeability near the membrane and the layer with lower permeability near the flow channels provides a better performance in contrast to the opposite order. However, it was shown that the selection of an optimum design purely based on the limiting current density is ambiguous, as a desired balance between the limiting current density and pressure loss within the electrode is required. The novel multi-layer structures were then compared with structures with similar layers in terms of operational parameters including limiting current density and pressure drop. It was shown that in general the multi-layer structures with different layers provide a better balance in terms of both parameters. This model provides the basis for future investigations into the structure-performance relationship of novel electrode structures, including in-silico designs, allowing for much more rapid innovation in this area.

Chapter 5 was dedicated to developing a deep learning framework to predict the diffusive mass transport conductance of PNM elements more accurately and efficiently. The accuracy of the ML model was evaluated with a large test dataset of unseen images with diffusive conductance values from the DNS as ground truth data. The deep learning based prediction accuracy was also compared with classic analytical methods of estimating diffusive conductance. It was shown that the prediction accuracy for the developed framework was higher than classic analytical-based methods while providing a 500x speed up in contrast to DNS methods. The developed framework can be used in electrochemical modeling of porous electrodes for estimating diffusive and migrative transport properties, and dispersion in PNM, as the same parameter exists in those transport phenomena. The developed framework was the first deep learning based method to estimate the diffusive conductance of PNM elements based on only images of conduits as input data, while previous frameworks were focused on only hydraulic conductance estimation and multiple extracted features as input data.

The findings presented in this thesis have notable implications for design studies of Zn-air cathodes and VRFB electrodes, which are popular technologies for large-scale energy storage projects. The developed frameworks can be utilized for other pore-scale applications where multiphase transport and mass transfer resistance are important to be captured. Finally, the frameworks in this thesis helped contributions to OpenPNM and PoreSpy and expanded the open-source ecosystem.

6.2. Suggestions for future works

From the Zn-air study in chapter 3, the followings are recommended:

- Applying the framework on extracted networks of real images of air cathode catalyst layers, which could demonstrate the effect of new structural parameters, such as particle size distribution.
- Including convection in the mass transport of species.
- Including mass transfer coefficient in the reaction term.
- Developing a framework for simultaneous solution of Nernst-Plank equations instead of the developed sequential methods to avoid the computational cost of iterative approach.
- Applying the framework on other devices with liquid-air interface, such as electrolyzers.

From the VRFB study in chapter 4, the followings are recommended:

- Including pumping cost in evaluating the performance of electrodes.
- Extending the framework for other structural parameters, such as fiber orientations.
- Extending the framework for a wider range of generated images for further structure-performance analysis.
- Investigating the range of application of local mass transfer correlation.
- Extending the framework for modeling the entire battery cell including the counter electrode as well as both charging and discharging.
- Developing a multi-scale framework to include the transport in binder materials if present.

From the deep-learning based study in chapter 5, the followings are recommended:

- Extending the framework for wider range of porous material types, such as anisotropic fibrous materials.
- Extending the framework for estimating hydraulic conductance values, extending the metrics of accuracy to include other types of measurements, such as relative errors.
- Investigating the possibility of generating individual ROI images by developing an image generation framework.

References

[1] K. T. Cho, P. Ridgway, A. Z. Weber, S. Haussener, V. Battaglia, and V. Srinivasan, "High Performance Hydrogen/Bromine Redox Flow Battery for Grid-Scale Energy Storage," *J. Electrochem. Soc.*, vol. 159, no. 11, pp. A1806–A1815, 2012, doi: 10.1149/2.018211jes.

[2] M. A. Sadeghi *et al.*, "Exploring the Impact of Electrode Microstructure on Redox Flow Battery Performance Using a Multiphysics Pore Network Model," *J. Electrochem. Soc.*, vol. 166, no. 10, pp. A2121–A2130, 2019, doi: 10.1149/2.0721910jes.

[3] C. Ding, H. Zhang, X. Li, T. Liu, and F. Xing, "Vanadium flow battery for energy storage: Prospects and challenges," *J. Phys. Chem. Lett.*, vol. 4, no. 8, pp. 1281–1294, 2013, doi: 10.1021/jz4001032.

[4] X. Han *et al.*, "Metal–Air Batteries: From Static to Flow System," *Adv. Energy Mater.*, vol. 8, no. 27, pp. 1–28, 2018, doi: 10.1002/aenm.201801396.

[5] J. Houser, A. Pezeshki, J. T. Clement, D. Aaron, and M. M. Mench, "Architecture for improved mass transport and system performance in redox flow batteries," *J. Power Sources*, vol. 351, pp. 96–105, 2017, doi: 10.1016/j.jpowsour.2017.03.083.

[6] D. You, H. Zhang, and J. Chen, "Theoretical analysis of the effects of operational and designed parameters on the performance of a flow-through porous electrode," *J. Electroanal. Chem.*, vol. 625, no. 2, pp. 165–171, 2009, doi: 10.1016/j.jelechem.2008.10.027.

[7] M. Gencten and Y. Sahin, "A critical review on progress of the electrode materials of vanadium redox flow battery," *Int. J. Energy Res.*, vol. 44, no. 10, pp. 7903–7923, 2020, doi: 10.1002/er.5487.

[8] A. Forner-Cuenca, E. E. Penn, A. M. Oliveira, and F. R. Brushett, "Exploring the Role of Electrode Microstructure on the Performance of Non-Aqueous Redox Flow Batteries," *J. Electrochem. Soc.*, vol. 166, no. 10, pp. A2230–A2241, 2019, doi: 10.1149/2.0611910jes.

[9] "Transforming our world: the 2030 Agenda for Sustainable Development," no. Resolution 70/1. United Nations, 2015.

[10] G. Qiu, C. R. Dennison, K. W. Knehr, E. C. Kumbur, and Y. Sun, "Pore-scale analysis of effects of electrode morphology and electrolyte flow conditions on performance of vanadium redox flow batteries," *J. Power Sources*, vol. 219, pp. 223–234, 2012, doi: 10.1016/j.jpowsour.2012.07.042.

[11] B. K. Chakrabarti *et al.*, "Modelling of redox flow battery electrode processes at a range of length scales : a review," *Sustain. Energy Fuels*, pp. 5433–5468, 2020, doi: 10.1039/d0se00667j.

[12] A. A. Wong, S. M. Rubinstein, and M. J. Aziz, "Direct visualization of electrochemical reactions and heterogeneous transport within porous electrodes in operando by fluorescence microscopy," *Cell Reports Phys. Sci.*, vol. 2, no. 4, p. 100388, 2021, doi: 10.1016/j.xcrp.2021.100388.

[13] M. J. Blunt *et al.*, "Pore-scale imaging and modelling," *Adv. Water Resour.*, vol. 51, pp. 197–216, 2013, doi: 10.1016/j.advwatres.2012.03.003.

[14] L. Xiao *et al.*, "Pore-Scale Characterization and Simulation of Porous Electrode Material for Vanadium Redox Flow Battery : Effects of Compression on Transport Properties Pore-Scale Characterization and Simulation of Porous Electrode Material for Vanadium Redox Flow Batter," 2020, doi: 10.1149/1945-7111/aba4e3.

[15] H. Al-Fetlawi, A. A. Shah, and F. C. Walsh, "Non-isothermal modelling of the all-vanadium redox flow battery," *Electrochim. Acta*, vol. 55, pp. 78–89, 2009, doi: 10.1016/j.electacta.2009.08.009.

[16] D. You, H. Zhang, and J. Chen, "A simple model for the vanadium redox battery," *Electrochim. Acta*, vol. 54, no. 27, pp. 6827–6836, 2009, doi: 10.1016/j.electacta.2009.06.086.

[17] B. Tjaden *et al.*, "Tortuosity in electrochemical devices : a review of calculation approaches Tortuosity in electrochemical devices : a review of calculation approaches," vol. 6608, 2018, doi: 10.1080/09506608.2016.1249995.

[18] L. Chen, Y. L. He, W. Q. Tao, P. Zelenay, R. Mukundan, and Q. Kang, "Pore-scale study of multiphase reactive transport in fibrous electrodes of vanadium redox flow batteries," *Electrochim.*

Acta, vol. 248, pp. 425–439, 2017, doi: 10.1016/j.electacta.2017.07.086.
[19] M. D. R. Kok, J. E. Soc, M. D. R. Kok, A. Khalifa, and J. T. Gostick, "Multiphysics Simulation of the Flow Battery Cathode : Cell Architecture and Electrode Optimization Multiphysics Simulation of the Flow Battery Cathode : Cell Architecture and Electrode Optimization," 2016, doi: 10.1149/2.1281607jes.
[20] G. Qiu, A. S. Joshi, C. R. Dennison, K. W. Knehr, E. C. Kumbur, and Y. Sun, "3-D pore-scale resolved model for coupled species/charge/fluid transport in a vanadium redox flow battery," *Electrochim. Acta*, vol. 64, pp. 46–64, 2012, doi: 10.1016/j.electacta.2011.12.065.
[21] Q. Xiong, T. G. Baychev, and A. P. Jivkov, "Review of pore network modelling of porous media: Experimental characterisations, network constructions and applications to reactive transport," *J. Contam. Hydrol.*, vol. 192, pp. 101–117, 2016, doi: 10.1016/j.jconhyd.2016.07.002.
[22] M. Aghighi and J. Gostick, "Pore network modeling of phase change in PEM fuel cell fibrous cathode," *J. Appl. Electrochem.*, vol. 47, no. 12, pp. 1323–1338, 2017, doi: 10.1007/s10800-017-1126-6.
[23] M. Aghighi, M. A. Hoeh, W. Lehnert, and G. Merle, "Simulation of a Full Fuel Cell Membrane Electrode Assembly Using Pore Network Modeling," *J. Electrochem. Soc.* ·, vol. 163, no. 5, pp. F384–F392, 2016, doi: 10.1149/2.0701605jes.
[24] M. A. Sadeghi, M. Agnaou, J. Barralet, and J. Gostick, "Dispersion modeling in pore networks: A comparison of common pore-scale models and alternative approaches," *J. Contam. Hydrol.*, vol. 228, no. October 2019, p. 103578, 2020, doi: 10.1016/j.jconhyd.2019.103578.
[25] L. Chen, G. Wu, E. F. Holby, P. Zelenay, W. Tao, and Q. Kang, "Lattice Boltzmann Pore-Scale Investigation of Coupled Physical-electrochemical Processes in C / Pt and Non-Precious Metal Cathode Catalyst Layers in Proton Exchange Membrane Fuel Cells," *Electrochim. Acta*, vol. 158, pp. 175–186, 2015, doi: 10.1016/j.electacta.2015.01.121.
[26] S. Jung *et al.*, "Estimation of Relative Transport Properties in Porous Transport Layers Using Pore-Scale and Pore-Network Simulations," *J. Electrochem. Soc.*, vol. 168, no. 6, p. 064501, 2021, doi: 10.1149/1945-7111/ac03f2.
[27] Z. A. Khan *et al.*, "Probing the Structure-Performance Relationship of Lithium-Ion Battery Cathodes Using Pore-Networks Extracted from Three-Phase Tomograms," *J. Electrochem. Soc.*, vol. 167, no. 4, p. 040528, 2020, doi: 10.1149/1945-7111/ab7bd8.
[28] A. Gayon Lombardo, B. A. Simon, O. Taiwo, S. J. Neethling, and N. P. Brandon, "A pore network model of porous electrodes in electrochemical devices," *J. Energy Storage*, vol. 24, no. January, p. 100736, 2019, doi: 10.1016/j.est.2019.04.010.
[29] M. van der Heijden, R. van Gorp, M. A. Sadeghi, J. Gostick, and A. Forner-Cuenca, "Assessing the Versatility and Robustness of Pore Network Modeling to Simulate Redox Flow Battery Electrode Performance," *J. Electrochem. Soc.*, vol. 169, no. 4, p. 040505, 2022, doi: 10.1149/1945-7111/ac5e46.
[30] C. E. Wood *et al.*, "Combining electrochemical and imaging analyses to understand the effect of electrode microstructure and electrolyte properties on redox flow batteries," vol. 306, no. November 2021, 2022, doi: 10.1016/j.apenergy.2021.117678.
[31] K. Kinoshita, *Electrochemical Oxygen Technology*. John Wiley & Sons, 1992.
[32] Y. Chen, D. Su, Y. Chen, Z. Zhu, and W. Li, "Three-phase interface-assisted advanced electrochemistry-related applications," *Cell Reports Phys. Sci.*, vol. 2, no. 10, p. 100602, 2021, doi: 10.1016/j.xcrp.2021.100602.
[33] M. Zhu, H. Ge, X. Xu, and Q. Wang, "Investigation on the variation law of gas liquid solid three phase boundary in porous gas diffusion electrode," *Heliyon*, vol. 4, no. 8, p. e00729, 2018, doi: 10.1016/j.heliyon.2018.e00729.
[34] T. W. Patzek and D. B. Silin, "Shape factor and hydraulic conductance in noncircular capillaries: I. One-phase creeping flow," *J. Colloid Interface Sci.*, vol. 236, no. 2, pp. 295–304, 2001, doi: 10.1006/jcis.2000.7413.
[35] Y. Sholokhova, D. Kim, W. B. Lindquist, and W. Brent Lindquist, "Network flow modeling via

lattice-Boltzmann based channel conductance," *Adv. Water Resour.*, vol. 32, no. 2, pp. 205–212, 2009, doi: 10.1016/j.advwatres.2008.10.016.
[36] C. Xie, A. Q. Raeini, Y. Wang, M. J. Blunt, and M. Wang, "An improved pore-network model including viscous coupling effects using direct simulation by the lattice Boltzmann method," *Adv. Water Resour.*, vol. 100, pp. 26–34, 2017, doi: 10.1016/j.advwatres.2016.11.017.
[37] W. Yu *et al.*, "Toward a new generation of low cost, efficient, and durable metal-air flow batteries," *J. Mater. Chem. A*, vol. 7, no. 47, pp. 26744–26768, 2019, doi: 10.1039/c9ta10658h.
[38] T. F. Fuller and J. N. Harb, *Electrochemical engineering*. Hoboken, New Jersey : Wiley, 2018.
[39] J. Newman and K. E. Thomas-Alyea, *Electrochemical systems*. Hoboken, New Jersey: John Wiley & Sons, 2004.
[40] X. L. Zhou, T. S. Zhao, L. An, Y. K. Zeng, and X. H. Yan, "A vanadium redox flow battery model incorporating the effect of ion concentrations on ion mobility," *Appl. Energy*, vol. 158, pp. 157–166, 2015, doi: 10.1016/j.apenergy.2015.08.028.
[41] M. M. Tomadakis and S. V Sotirchos, "Ordinary and Transition Regime Diffusion in Random Fiber Structures," vol. 39, no. 3, pp. 397–412, 1993.
[42] G. Qiu, A. S. Joshi, C. R. Dennison, K. W. Knehr, E. C. Kumbur, and Y. Sun, "Electrochimica Acta 3-D pore-scale resolved model for coupled species / charge / fluid transport in a vanadium redox flow battery," *Electrochim. Acta*, vol. 64, pp. 46–64, 2012, doi: 10.1016/j.electacta.2011.12.065.
[43] G. Qiu, C. R. Dennison, K. W. Knehr, E. C. Kumbur, and Y. Sun, "Pore-scale analysis of effects of electrode morphology and electrolyte flow conditions on performance of vanadium redox flow batteries," *J. Power Sources*, vol. 219, pp. 223–234, 2012, doi: 10.1016/j.jpowsour.2012.07.042.
[44] Q. Sheng, "Pore-To-Continuum Multiscale Modeling of Two-Phase Flow in Porous Media," no. May, 2013.
[45] M. Agnaou, M. A. Sadeghi, T. G. Tranter, and J. T. Gostick, "Modeling transport of charged species in pore networks: Solution of the Nernst–Planck equations coupled with fluid flow and charge conservation equations," *Comput. Geosci.*, vol. 140, no. April, p. 104505, 2020, doi: 10.1016/j.cageo.2020.104505.
[46] M. Mckague, H. Fathiannasab, M. Agnaou, M. Amin, and J. Gostick, "Extending pore network models to include electrical double layer effects in micropores for studying capacitive deionization," *Desalination*, vol. 535, no. February, p. 115784, 2022, doi: 10.1016/j.desal.2022.115784.
[47] Patankar, *Numerical heat transfer and fluid flow*. .
[48] M. Akbari, D. Sinton, and M. Bahrami, "Viscous flow in variable cross-section microchannels of arbitrary shapes," *Int. J. Heat Mass Transf.*, vol. 54, no. 17–18, pp. 3970–3978, 2011, doi: 10.1016/j.ijheatmasstransfer.2011.04.028.
[49] J. Gostick *et al.*, "OpenPNM: A Pore Network Modeling Package," *Comput. Sci. Eng.*, vol. 18, no. 4, pp. 60–74, 2016, doi: 10.1109/MCSE.2016.49.
[50] J. T. Gostick, J. E. Soc, and J. T. Gostick, "Random Pore Network Modeling of Fibrous PEMFC Gas Diffusion Media Using Voronoi and Delaunay Tessellations Random Pore Network Modeling of Fibrous PEMFC Gas Diffusion Media Using Voronoi and Delaunay Tessellations," 2013, doi: 10.1149/2.009308jes.
[51] J. T. Gostick, "Versatile and efficient pore network extraction method using marker-based watershed segmentation," *Phys. Rev. E*, vol. 96, no. 2, pp. 1–15, 2017, doi: 10.1103/PhysRevE.96.023307.
[52] H. Dong and M. J. Blunt, "Pore-network extraction from micro-computerized-tomography images," *Phys. Rev. E - Stat. Nonlinear, Soft Matter Phys.*, vol. 80, no. 3, pp. 1–11, 2009, doi: 10.1103/PhysRevE.80.036307.
[53] Z. Jiang, K. Wu, G. Couples, M. I. J. Van Dijke, K. S. Sorbie, and J. Ma, "Efficient extraction of networks from three-dimensional porous media," *Water Resour. Res.*, vol. 43, no. 12, pp. 1–17, 2007, doi: 10.1029/2006WR005780.

[54] T. G. Baychev *et al.*, *Reliability of Algorithms Interpreting Topological and Geometric Properties of Porous Media for Pore Network Modelling*, vol. 128, no. 1. Springer Netherlands, 2019.
[55] I. Goodfellow, Y. Bengio, and A. Courville, *Deep Learning*. MIT Press, 2016.
[56] J. D. Kelleher, *Deep Learning*. MIT Press, 2019.
[57] T. M. Mitchell, *Machine learning*. New York : McGraw-Hill, 1997.
[58] T. Hope, Y. S. Resheff, and I. Lieder, *Learning TensorFlow: A Guide to Building Deep Learning Systems*, 1st ed. O'Reilly Media, Inc., 2017.
[59] Z. Hu, J. Tang, Z. Wang, K. Zhang, L. Zhang, and Q. Sun, "Deep learning for image-based cancer detection and diagnosis − A survey," *Pattern Recognit.*, vol. 83, pp. 134–149, 2018, doi: 10.1016/j.patcog.2018.05.014.
[60] Y. Lecun, Y. Bengio, and G. Hinton, "Deep learning," *Nature*, vol. 521, no. 7553, pp. 436–444, 2015, doi: 10.1038/nature14539.
[61] B. Ramsundar and R. B. Zadeh, *TensorFlow for Deep Learning: From Linear Regression to Reinforcement Learning*, 1st ed. O'Reilly Media, Inc., 2018.
[62] A. S. Lundervold and A. Lundervold, "An overview of deep learning in medical imaging focusing on MRI," *Z. Med. Phys.*, vol. 29, no. 2, pp. 102–127, 2019, doi: 10.1016/j.zemedi.2018.11.002.
[63] K. He, X. Zhang, S. Ren, and J. Sun, "Deep residual learning for image recognition," *Proc. IEEE Comput. Soc. Conf. Comput. Vis. Pattern Recognit.*, vol. 2016-Decem, pp. 770–778, 2016, doi: 10.1109/CVPR.2016.90.
[64] S. Clark, A. Latz, and B. Horstmann, "A review of model-based design tools for metal-air batteries," *Batteries*, vol. 4, no. 1, pp. 1–26, 2018, doi: 10.3390/batteries4010005.
[65] Q. Liu, Z. Pan, E. Wang, L. An, and G. Sun, "Aqueous metal-air batteries: Fundamentals and applications," *Energy Storage Mater.*, vol. 27, no. October 2019, pp. 478–505, 2020, doi: 10.1016/j.ensm.2019.12.011.
[66] A. Khor *et al.*, "Review of zinc-based hybrid flow batteries: From fundamentals to applications," *Mater. Today Energy*, vol. 8, no. January, pp. 80–108, 2018, doi: 10.1016/j.mtener.2017.12.012.
[67] S. Ren, X. Duan, S. Liang, M. Zhang, and H. Zheng, "Bifunctional electrocatalysts for Zn-air batteries: Recent developments and future perspectives," *J. Mater. Chem. A*, vol. 8, no. 13, pp. 6144–6182, 2020, doi: 10.1039/c9ta14231b.
[68] W. Kong, M. Zhang, Z. Han, and Q. Zhang, "A theoretical model for the triple phase boundary of solid oxide fuel cell electrospun electrodes," *Appl. Sci.*, vol. 9, no. 3, 2019, doi: 10.3390/app9030493.
[69] X. Deng and A. Petric, "Geometrical modeling of the triple-phase-boundary in solid oxide fuel cells," *J. Power Sources*, vol. 140, no. 2, pp. 297–303, 2005, doi: 10.1016/j.jpowsour.2004.08.046.
[70] P. Vijay, M. O. Tadé, Z. Shao, and M. Ni, "Modelling the triple phase boundary length in infiltrated SOFC electrodes," *Int. J. Hydrogen Energy*, vol. 42, no. 48, pp. 28836–28851, 2017, doi: 10.1016/j.ijhydene.2017.10.004.
[71] J. D. Fehribach and R. O'Hayre, "Triple Phase Boundaries in Solid-Oxide Cathodes," *SIAM J. Appl. Math.*, vol. 70, no. 2, pp. 510–530, 2009.
[72] J. S. Lee *et al.*, "Metal-air batteries with high energy density: Li-air versus Zn-air," *Adv. Energy Mater.*, vol. 1, no. 1, pp. 34–50, 2011, doi: 10.1002/aenm.201000010.
[73] D. Wilkinson and J. F. Willemsen, "Invasion percolation: A new form of percolation theory," *J. Phys. A. Math. Gen.*, vol. 16, no. 14, pp. 3365–3376, 1983, doi: 10.1088/0305-4470/16/14/028.
[74] W. Xu, J. Xiao, D. Wang, J. Zhang, and J. Zhang, "Effects of Nonaqueous Electrolytes on the Performance of Lithium / Air Batteries," *J. Electrochem. Soc.*, vol. 157, no. 2, 2010, doi: 10.1149/1.3269928.
[75] T. Mori, J. Imahashi, T. Kamo, K. Tamura, and Y. Hishinuma, "Phosphoric Acid Absorption and Performance of Gas Diffusion Electrode," *J. Electrochem. Soc.*, vol. 133, no. 5, p. 896, 1986.
[76] G. Gourdin, N. Xiao, W. McCulloch, and Y. Wu, "Use of Polarization Curves and Impedance Analyses to Optimize the 'triple-Phase Boundary' in K-O 2 Batteries," *ACS Appl. Mater. Interfaces*, vol. 11, no. 3, pp. 2925–2934, 2019, doi: 10.1021/acsami.8b16321.

[77] R. Chandler, J. Koplik, K. Lerman, and J. F. Willemsen, “Capillary displacement and percolation in porous media,” *J. Fluid Mech.*, vol. 119, pp. 249–267, 1982, doi: 10.1017/S0022112082001335.
[78] C. C. Barton and P. R. La Pointe, *Fractals in petroleum geology and earth processes*. Springer Science & Business Media, 2012.
[79] R. Lenormand and C. Zarcone, “Invasion percolation in an eetched network: Measurement of a fractal dimension,” *Phys. Rev. Lett.*, vol. 54, no. 20, pp. 2226–2229, 1985, doi: 10.1103/PhysRevLett.54.2226.
[80] V. Berejnov, A. Bazylak, D. Sinton, and N. Djilali, “Fractal Flow Patterns in Hydrophobic Microfluidic Pore Networks: Experimental Modeling of Two-Phase Flow in Porous Electrodes,” *J. Electrochem. Soc.*, vol. 157, no. 5, p. B760, 2010, doi: 10.1149/1.3332623.
[81] Z. Mao, “Mathematical Modeling of a Primary Zinc/Air Battery,” *J. Electrochem. Soc.*, vol. 139, no. 4, p. 1105, 1992, doi: 10.1149/1.2069348.
[82] J. Stamm, A. Varzi, A. Latz, and B. Horstmann, “Modeling nucleation and growth of zinc oxide during discharge of primary zinc-air batteries,” *J. Power Sources*, vol. 360, pp. 136–149, 2017, doi: 10.1016/j.jpowsour.2017.05.073.
[83] E. Deiss, F. Holzer, and O. Haas, “Modeling of an electrically rechargeable alkaline Zn-air battery,” *Electrochim. Acta*, vol. 47, no. 25, pp. 3995–4010, 2002, doi: 10.1016/S0013-4686(02)00316-X.
[84] T. G. Tranter, P. Stogornyuk, J. T. Gostick, A. D. Burns, and W. F. Gale, “A method for measuring relative in-plane diffusivity of thin and partially saturated porous media: An application to fuel cell gas diffusion layers,” *Int. J. Heat Mass Transf.*, vol. 110, pp. 132–141, 2017, doi: 10.1016/j.ijheatmasstransfer.2017.02.096.
[85] T. G. Tranter *et al.*, “Pore Network Modelling of Capillary Transport and Relative Diffusivity in Gas Diffusion Layers with Patterned Wettability,” *J. Electrochem. Soc.*, vol. 167, no. 11, p. 114512, 2020, doi: 10.1149/1945-7111/ab9d61.
[86] T. Danner, S. Eswara, V. P. Schulz, and A. Latz, “Characterization of gas diffusion electrodes for metal-air batteries,” *J. Power Sources*, vol. 324, pp. 646–656, 2016, doi: 10.1016/j.jpowsour.2016.05.108.
[87] B. Horstmann, T. Danner, and W. G. Bessler, “Precipitation in aqueous lithium-oxygen batteries: A model-based analysis,” *Energy Environ. Sci.*, vol. 6, no. 4, pp. 1299–1314, 2013, doi: 10.1039/c3ee24299d.
[88] W. Lao-atiman, K. Bumroongsil, A. Arpornwichanop, P. Bumroongsakulsawat, S. Olaru, and S. Kheawhom, “Model-based analysis of an integrated zinc-air flow Battery/Zinc Electrolyzer System,” *Front. Energy Res.*, vol. 7, no. FEB, pp. 1–15, 2019, doi: 10.3389/fenrg.2019.00015.
[89] P. Meakin and A. M. Tartakovsky, “Modeling and Simulation of Pore-Scale Multiphase Fluid Flow and Reactive,” *Rev. Geophys.*, vol. 47, no. 2008, pp. 1–47, 2009, doi: 10.1029/2008RG000263.1.INTRODUCTION.
[90] Y. L. Fu, B. Zhang, X. Zhu, D. D. Ye, P. C. Sui, and N. Djilali, “Pore-scale modeling of oxygen transport in the catalyst layer of air-breathing cathode in membraneless microfluidic fuel cells,” *Appl. Energy*, vol. 277, no. July, 2020, doi: 10.1016/j.apenergy.2020.115536.
[91] P. P. Mukherjee, C. Y. Wang, Q. Kang, and C. Y. Wang, “Pore-scale modeling of two-phase transport in polymer electrolyte fuel cells - Progress and perspective,” *Energy Environ. Sci.*, vol. 4, no. 2, pp. 346–369, 2011, doi: 10.1039/b926077c.
[92] D. Zhang *et al.*, “Understanding the role of the porous electrode microstructure in redox flow battery performance using an experimentally validated 3D pore-scale lattice Boltzmann model,” *J. Power Sources*, vol. 447, no. March 2019, p. 227249, 2020, doi: 10.1016/j.jpowsour.2019.227249.
[93] J. T. Gostick, N. Misaghian, J. Yang, and E. S. Boek, “Simulating volume-controlled invasion of a non-wetting fluid in volumetric images using basic image processing tools,” *Comput. Geosci.*, vol. 158, no. November 2021, p. 104978, 2021, doi: 10.1016/j.cageo.2021.104978.
[94] J. T. Gostick, M. A. Ioannidis, M. D. Pritzker, and M. W. Fowler, “Impact of Liquid Water on Reactant Mass Transfer in PEM Fuel Cell Electrodes,” *J. Electrochem. Soc.*, vol. 157, no. 4, p.

B563, 2010, doi: 10.1149/1.3291977.
[95] L. Furuberg, J. Feder, A. Aharony, and T. Jøssang, “Dynamics of invasion percolation,” *Phys. Rev. Lett.*, vol. 61, no. 18, pp. 2117–2120, 1988, doi: 10.1103/PhysRevLett.61.2117.
[96] D. Stauffer, *Introduction to percolation theory*. London ; Philadelphia: Taylor & Francis, 1985.
[97] T. Tranter, J. Gostick, A. Burns, and W. Gale, “Pore Network Modeling of Compressed Fuel Cell Components with OpenPNM,” *Fuel Cells*, vol. 16, 2016, doi: 10.1002/fuce.201500168.
[98] J. T. Gostick, M. A. Ioannidis, M. W. Fowler, and M. D. Pritzker, “Pore network modeling of fibrous gas diffusion layers for polymer electrolyte membrane fuel cells,” *J. Power Sources*, vol. 173, no. 1, pp. 277–290, 2007, doi: 10.1016/j.jpowsour.2007.04.059.
[99] D. Schröder and U. Krewer, “Model based quantification of air-composition impact on secondary zinc air batteries,” *Electrochim. Acta*, vol. 117, pp. 541–553, 2014, doi: 10.1016/j.electacta.2013.11.116.
[100] C. Quesnel, R. Cao, J. Lehr, A. Kietzig, A. Z. Weber, and J. T. Gostick, “Dynamic Percolation and Droplet Growth Behavior in Porous Electrodes of Polymer Electrolyte Fuel Cells,” *J. Phys. Chem.*, vol. 119, p. 22934−22944, 2015, doi: 10.1021/acs.jpcc.5b06197.
[101] E. W. Washburn, “Note on a Method of Determining the Distribution of Pore Sizes in a Porous Material,” *Proc. Natl. Acad. Sci. U. S. A.*, vol. 7, no. 4, p. 115—116, Apr. 1921, doi: 10.1073/pnas.7.4.115.
[102] A. Federbush and Y. Kantor, “Percolation perspective on sites not visited by a random walk in two dimensions,” *Phys. Rev. E*, vol. 103, no. 3, p. 32137, 2021, doi: 10.1103/PhysRevE.103.032137.
[103] S. Liu, X. Liu, F. Chen, L. Wang, and W. Ge, “A study on periodic boundary condition in direct numerical simulation for gas–solid flow,” *Chinese J. Chem. Eng.*, vol. 28, no. 1, pp. 236–241, 2020, doi: 10.1016/j.cjche.2019.04.025.
[104] W. Yang, Z. Zhou, D. Pinson, and A. Yu, “Periodic boundary conditions for discrete element method simulation of particle flow in cylindrical vessels,” *Ind. Eng. Chem. Res.*, vol. 53, no. 19, pp. 8245–8256, 2014, doi: 10.1021/ie404158e.
[105] K. D. Huang, T. Sangeetha, W. F. Cheng, C. Lin, and P. T. Chen, “Computational fluid dynamics approach for performance prediction in a Zinc-Air Fuel Cell,” *Energies*, vol. 11, no. 9, 2018, doi: 10.3390/en11092185.
[106] R. E. Davis, G. L. Horvath, and C. W. Tobias, “The solubility and diffusion coefficient of oxygen in potassium hydroxide solutions,” *Electrochem. Acta*, vol. 12, pp. 287–297, 1967.
[107] S. Moshtarikhah, N. A. W. Oppers, M. T. de Groot, J. T. F. Keurentjes, J. C. Schouten, and J. van der Schaaf, “Nernst–Planck modeling of multicomponent ion transport in a Nafion membrane at high current density,” *J. Appl. Electrochem.*, vol. 47, no. 1, pp. 51–62, 2017, doi: 10.1007/s10800-016-1017-2.
[108] K. Krabbenhøft and J. Krabbenhøft, “Application of the Poisson-Nernst-Planck equations to the migration test,” *Cem. Concr. Res.*, vol. 38, no. 1, pp. 77–88, 2008, doi: 10.1016/j.cemconres.2007.08.006.
[109] R. J. Gilliam, J. W. Graydon, D. W. Kirk, and S. J. Thorpe, “A review of specific conductivities of potassium hydroxide solutions for various concentrations and temperatures,” *Int. J. Hydrogen Energy*, vol. 32, no. 3, pp. 359–364, 2007, doi: 10.1016/j.ijhydene.2006.10.062.
[110] D. R. Lide, *CRC handbook of chemistry and physics*, vol. 85. CRC press, 2004.
[111] B. Ghanbarian, A. G. Hunt, R. P. Ewing, and M. Sahimi, “Tortuosity in Porous Media: A Critical Review,” *Soil Sci. Soc. Am. J.*, vol. 77, no. 5, pp. 1461–1477, 2013, doi: 10.2136/sssaj2012.0435.
[112] J. Fu, H. R. Thomas, and C. Li, “Tortuosity of porous media: Image analysis and physical simulation,” *Earth-Science Rev.*, vol. 212, no. May 2020, p. 103439, 2021, doi: 10.1016/j.earscirev.2020.103439.
[113] S. Kolitcheff, E. Jolimaitre, A. Hugon, J. Verstraete, P. L. Carrette, and M. Tayakout-Fayolle, “Tortuosity of mesoporous alumina catalyst supports: Influence of the pore network organization,” *Microporous Mesoporous Mater.*, vol. 248, pp. 91–98, 2017, doi: 10.1016/j.micromeso.2017.04.010.

[114] C. J. Bae, C. K. Erdonmez, J. W. Halloran, and Y. M. Chiang, “Design of battery electrodes with dual-scale porosity to minimize tortuosity and maximize performance,” *Adv. Mater.*, vol. 25, no. 9, pp. 1254–1258, 2013, doi: 10.1002/adma.201204055.
[115] A. Çeçen, E. A. Wargo, A. C. Hanna, D. M. Turner, S. R. Kalidindi, and E. C. Kumbur, “3-D Microstructure Analysis of Fuel Cell Materials: Spatial Distributions of Tortuosity, Void Size and Diffusivity,” *J. Electrochem. Soc.*, vol. 159, no. 3, pp. B299–B307, 2012, doi: 10.1149/2.068203jes.
[116] A. G. Hunt, R. P. Ewing, and B. Ghanbarian, *Percolation theory for flow in porous media*, no. 880. Springer, 2009.
[117] A. G. Hunt and M. Sahimi, “Flow, Transport, and Reaction in Porous Media: Percolation Scaling, Critical-Path Analysis, and Effective Medium Approximation,” *Rev. Geophys.*, vol. 55, no. 4, pp. 993–1078, 2017, doi: 10.1002/2017RG000558.
[118] P. Leung, X. Li, C. Ponce De León, L. Berlouis, C. T. J. Low, and F. C. Walsh, “Progress in redox flow batteries, remaining challenges and their applications in energy storage,” *RSC Adv.*, vol. 2, no. 27, pp. 10125–10156, 2012, doi: 10.1039/c2ra21342g.
[119] A. A. Wong, M. J. Aziz, and S. Rubinstein, “Direct Visualization of Electrochemical Reactions in Porous Electrodes By Fluorescence Microscopy Using a Quinone-Based Flow Battery,” *ECS Meet. Abstr.*, vol. MA2017-01, no. 2, pp. 164–164, 2017, doi: 10.1149/ma2017-01/2/164.
[120] D. S. Aaron *et al.*, “Dramatic performance gains in vanadium redox flow batteries through modified cell architecture,” *J. Power Sources*, vol. 206, pp. 450–453, 2012, doi: 10.1016/j.jpowsour.2011.12.026.
[121] M. C. Tucker, K. Taek, A. Z. Weber, G. Lin, and T. Van Nguyen, “Optimization of electrode characteristics for the Br 2 / H 2 redox flow cell,” pp. 11–19, 2015, doi: 10.1007/s10800-014-0772-1.
[122] A. A. Shah, H. Al-Fetlawi, and F. C. Walsh, “Dynamic modelling of hydrogen evolution effects in the all-vanadium redox flow battery,” *Electrochim. Acta*, vol. 55, pp. 1125–1139, 2010, doi: 10.1016/j.electacta.2009.10.022.
[123] Q. He *et al.*, “Modeling of vanadium redox flow battery and electrode optimization with different flow fields,” *e-Prime - Adv. Electr. Eng. Electron. Energy*, vol. 1, no. October, p. 100001, 2021, doi: 10.1016/j.prime.2021.100001.
[124] S. Wan, X. Liang, H. Jiang, J. Sun, N. Djilali, and T. Zhao, “A coupled machine learning and genetic algorithm approach to the design of porous electrodes for redox flow batteries,” *Appl. Energy*, vol. 298, no. May, p. 117177, 2021, doi: 10.1016/j.apenergy.2021.117177.
[125] R. Jervis, M. D. R. Kok, J. Montagut, J. T. Gostick, D. J. L. Brett, and P. R. Shearing, “X-ray Nano Computed Tomography of Electrospun Fibrous Mats as Flow Battery Electrodes,” *Energy Technol.*, vol. 6, no. 12, pp. 2488–2500, 2018, doi: 10.1002/ente.201800338.
[126] B. A. Simon *et al.*, “Combining electrochemical and imaging analyses to understand the effect of electrode microstructure and electrolyte properties on redox flow batteries,” *Appl. Energy*, vol. 306, no. August 2021, 2022, doi: 10.1016/j.apenergy.2021.117678.
[127] M. M. Daino and S. G. Kandlikar, “3D phase-differentiated GDL microstructure generation with binder and PTFE distributions,” *Int. J. Hydrogen Energy*, vol. 37, no. 6, pp. 5180–5189, 2011, doi: 10.1016/j.ijhydene.2011.12.050.
[128] S. Didari, A. Asadi, Y. Wang, and T. A. L. Harris, “Modeling of composite fibrous porous diffusion media,” *Int. J. Hydrogen Energy*, vol. 39, no. 17, pp. 9375–9386, 2014, doi: 10.1016/j.ijhydene.2014.04.011.
[129] H. Wang *et al.*, “Effect of Binder and Compression on the Transport Parameters of a Multilayer Gas Diffusion Layer,” *Energy fuels*, vol. 35, pp. 15058–15073, 2021, doi: 10.1021/acs.energyfuels.1c01598.
[130] M. Messaggi *et al.*, “Analysis of flow field design on vanadium redox flow battery performance : Development of 3D computational fluid dynamic model and experimental validation,” vol. 228, no. July, pp. 1057–1070, 2018, doi: 10.1016/j.apenergy.2018.06.148.

[131] C. Yin, Y. Gao, S. Guo, and H. Tang, “A coupled three dimensional model of vanadium redox fl ow battery for fl ow fi eld designs,” *Energy*, vol. 74, pp. 886–895, 2014, doi: 10.1016/j.energy.2014.07.066.
[132] J. Gostick *et al.*, “PoreSpy: A Python Toolkit for Quantitative Analysis of Porous Media Images,” *J. Open Source Softw.*, vol. 4, no. 37, p. 1296, 2019, doi: 10.21105/joss.01296.
[133] E. L. Cussler, *Diffusion: mass transfer in fluid systems*. Cambridge university press, 2009.
[134] T. Koch, K. Weishaupt, J. Müller, and B. Weigand, *A (Dual) Network Model for Heat Transfer in Porous Media*. Springer Netherlands, 2021.
[135] B. F. Esteves, P. L. C. Lage, P. Couto, and A. R. Kovscek, “Pore-merging methodology for reactive transport and mineral dissolution in pore-network models,” *Adv. Water Resour.*, vol. 155, no. March, p. 104014, 2021, doi: 10.1016/j.advwatres.2021.104014.
[136] M. R. Gerhardt, J. E. Soc, M. R. Gerhardt, A. A. Wong, and M. J. Aziz, “The Effect of Interdigitated Channel and Land Dimensions on Flow Cell Performance,” *J. Electrochem. Soc.*, 2018, doi: 10.1149/2.0471811jes.
[137] M. L. Perry, R. M. Darling, and M. L. Perry, “of Electrode and Channel Configurations on Flow Battery Performance,” *J. Electrochem. Soc.*, no. November, 2015, doi: 10.1149/2.0941409jes.
[138] B. Delanghe, S. Tellier, and M. Astruc, “Mass transfer to a carbon or graphite felt electrode,” *ectrochimica Acta*, vol. 35, no. 9, pp. 1369–1376, 1990.
[139] K. Kinoshita and S. C. Leach, “Mass-Transfer Study of Carbon Felt, Flow-Through Electrode,” *J. Electrochem. Soc.*, vol. 129, no. 9, 1993.
[140] D. Schmal, J. Van Erkel, and P. J. Van Duin, “Mass transfer at carbon fibre electrodes,” *J. Appl. Electrochem.*, vol. 16, no. 3, pp. 422–430, 1986, doi: 10.1007/BF01008853.
[141] X. You, Q. Ye, and P. Cheng, “The Dependence of Mass Transfer Coefficient on the Electrolyte Velocity in Carbon Felt Electrodes : Determination and Validation,” *J. Electrochem. Soc.*, vol. 164, no. 11, pp. E3386–E3394, 2017, doi: 10.1149/2.0401711jes.
[142] R. Dobry and R. K. Finn, “Mass Transfer to a Cylinder at Low Reynolds Numbers,” *Ind. Eng. Chem.*, vol. 48, no. 9, pp. 540–543, 1956.
[143] M. D. R. Kok *et al.*, “Mass Transfer in Fibrous Media with Varying Anisotropy for Flow Battery Electrodes : Direct Numerical Simulations with 3D X-ray Computed Tomography,” *Chem. Eng. Sci.*, 2018, doi: 10.1016/j.ces.2018.10.049.
[144] M. Jacob, *Heat transfer*. New York: John Wiley & Sons, 1959.
[145] V. A. Beck *et al.*, “Computational Design of Microarchitected Flow-Through Electrodes for Energy Storage,” *J. Power Sources*, vol. 512, 2021.
[146] A. A. Shah, M. J. Watt-Smith, and F. C. Walsh, “A dynamic performance model for redox-flow batteries involving soluble species,” *Electrochim. Acta*, vol. 53, pp. 8087–8100, 2008, doi: 10.1016/j.electacta.2008.05.067.
[147] J. E. Santos *et al.*, “MPLBM-UT: Multiphase LBM library for permeable media analysis,” *SoftwareX*, vol. 18, p. 101097, 2022, doi: 10.1016/j.softx.2022.101097.
[148] J. Latt, O. Malaspinas, and D. Kontaxakis, “Palabos : Parallel Lattice Boltzmann Solver,” *Comput. Math. with Appl.*, vol. 81, pp. 334–350, 2021, doi: 10.1016/j.camwa.2020.03.022.
[149] J. Soete *et al.*, “Lattice boltzmann simulations of fluid flow in continental carbonate reservoir rocks and in upscaled rock models generated with multiple-point geostatistics,” *Geofluids*, vol. 2017, 2017, doi: 10.1155/2017/7240524.
[150] E. Ali, H. Kwon, J. Choi, J. Lee, J. Kim, and H. Park, “A numerical study of electrode thickness and porosity effects in all vanadium redox flow batteries,” *J. Energy Storage*, vol. 28, no. October 2019, p. 101208, 2020, doi: 10.1016/j.est.2020.101208.
[151] K. ~A. Boult, M. ~M. Cowper, T. ~G. Heath, H. Sato, T. Shibutani, and M. Yui, “Towards an understanding of the sorption of U(VI) and Se(IV) on sodium bentonite,” *J. Contam. Hydrol.*, vol. 35, no. 1, pp. 141–150, 1998, doi: 10.1016/S0169-7722(98)00122-3.
[152] Q. Xiong and A. P. Jivkov, “Analysis of pore structure effects on diffusive transport in Opalinus clay via pore network models,” *Mineral. Mag.*, vol. 79, no. 6, pp. 1369–1377, 2015, doi:

10.1180/minmag.2015.079.6.12.
[153] G. Ye, H. Wang, X. Zhou, F. J. Keil, M. O. Coppens, and W. Yuan, “Optimizing catalyst pore network structure in the presence of deactivation by coking,” *AIChE J.*, vol. 65, no. 10, 2019, doi: 10.1002/aic.16687.
[154] P. P. Mukherjee, Q. Kang, and C. Y. Wang, “Pore-scale modeling of two-phase transport in polymer electrolyte fuel cells - Progress and perspective,” *Energy Environ. Sci.*, vol. 4, no. 2, pp. 346–369, 2011, doi: 10.1039/b926077c.
[155] D. Qu, “Fundamental principals of battery design: Porous electrodes,” *AIP Conf. Proc.*, vol. 1597, no. February, pp. 14–25, 2014, doi: 10.1063/1.4878477.
[156] K. Wang, P. Pei, Z. Ma, H. Xu, P. Li, and X. Wang, “Morphology control of zinc regeneration for zinc-air fuel cell and battery,” *J. Power Sources*, vol. 271, pp. 65–75, 2014, doi: 10.1016/j.jpowsour.2014.07.182.
[157] M. A. Sadeghi, M. Aghighi, J. Barralet, and J. T. Gostick, “Pore network modeling of reaction-diffusion in hierarchical porous particles: The effects of microstructure,” *Chem. Eng. J.*, vol. 330, no. July, pp. 1002–1011, 2017, doi: 10.1016/j.cej.2017.07.139.
[158] J. S. Andrade, D. A. Street, Y. Shibusa, S. Havlin, and H. E. Stanley, “Diffusion and reaction in percolating pore networks,” *Phys. Rev. E - Stat. Physics, Plasmas, Fluids, Relat. Interdiscip. Top.*, vol. 55, no. 1, pp. 772–777, 1997, doi: 10.1103/PhysRevE.55.772.
[159] A. T. Borujeni, N. M. Lane, K. Thompson, and M. Tyagi, “Effects of image resolution and numerical resolution on computed permeability of consolidated packing using LB and FEM pore-scale simulations,” *Comput. Fluids*, vol. 88, pp. 753–763, 2013, doi: 10.1016/j.compfluid.2013.05.019.
[160] M. R. Bonilla and S. K. Bhatia, “Multicomponent effective medium-correlated random walk theory for the diffusion of fluid mixtures through porous media,” *Langmuir*, vol. 28, no. 1, pp. 517–533, 2012, doi: 10.1021/la2040888.
[161] Q. Xiong and A. P. Jivkov, “Analysis of pore structure effects on diffusive transport in Opalinus clay via pore network models,” in *Mineralogical Magazine*, 2015, vol. 79, no. 6, pp. 1369–1377, doi: 10.1180/minmag.2015.079.6.12.
[162] M. Fazeli *et al.*, “Pore network modeling to explore the effects of compression on multiphase transport in polymer electrolyte membrane fuel cell gas diffusion layers,” *J. Power Sources*, vol. 335, pp. 162–171, 2016, doi: 10.1016/j.jpowsour.2016.10.039.
[163] J. O. Helland, A. V. Ryazanov, and M. I. J. van Dijke, “Characterization of Pore Shapes for Pore Network Models,” no. September, 2008, doi: 10.3997/2214-4609.20146420.
[164] T. W. Patzek and J. G. Kristensen, “Shape factor correlations of hydraulic conductance in noncircular capillaries: II. Two-phase creeping flow,” *J. Colloid Interface Sci.*, vol. 236, no. 2, pp. 305–317, 2001, doi: 10.1006/jcis.2000.7414.
[165] H. Dehghanpour, B. Aminzadeh, and D. A. Dicarlo, “Hydraulic conductance and viscous coupling of three-phase layers in angular capillaries,” *Phys. Rev. E - Stat. Nonlinear, Soft Matter Phys.*, vol. 83, no. 6, pp. 1–10, 2011, doi: 10.1103/PhysRevE.83.066320.
[166] T. W. Patzek and D. B. Silin, “Shape Factor and Hydraulic Conductance in Noncircular Capillaries,” vol. 304, pp. 295–304, 2001, doi: 10.1006/jcis.2000.7413.
[167] L. W. Rong, K. J. Dong, A. B. Yu, K. J. Dong, and A. B. Yu, “Lattice-Boltzmann Computation of Hydraulic Pore-to-pore Conductance in Packed Beds of Uniform Spheres,” 2020, doi: 10.1016/j.ces.2020.115798.
[168] M. Dadvar and M. Sahimi, “Pore network model of deactivation of immobilized glucose isomerase in packed-bed reactors. Part III: Multiscale modelling,” *Chem. Eng. Sci.*, vol. 58, no. 22, pp. 4935–4951, 2003, doi: 10.1016/j.ces.2003.07.006.
[169] T. W. Patzek, “Verification of a Complete Pore Network Simulator of Drainage and Imbibition,” *SPE J.*, vol. 6, no. 02, pp. 144–156, 2001.
[170] N. A. Mortensen, F. Okkels, and H. Bruus, “Reexamination of Hagen-Poiseuille flow: Shape dependence of the hydraulic resistance in microchannels,” *Phys. Rev. E - Stat. Nonlinear, Soft*

Matter Phys., vol. 71, no. 5, pp. 1–4, 2005, doi: 10.1103/PhysRevE.71.057301.
[171] X. Chen, J. Li, Y. Zhang, Y. Lu, and S. Liu, "Automatic feature extraction in X-ray image based on deep learning approach for determination of bone age," *Futur. Gener. Comput. Syst.*, vol. 110, pp. 795–801, 2020, doi: 10.1016/j.future.2019.10.032.
[172] N. Alqahtani, R. T. Armstrong, and P. Mostaghimi, "Deep Learning Convolutional Neural Networks to Predict Porous Media Properties," *SPE Asia Pacific Oil Gas Conf. Exhib.*, 2018, doi: 10.2118/191906-MS.
[173] Z. Yang *et al.*, "Deep learning approaches for mining structure-property linkages in high contrast composites from simulation datasets," *Comput. Mater. Sci.*, vol. 151, no. May, pp. 278–287, 2018, doi: 10.1016/j.commatsci.2018.05.014.
[174] R. Cang, H. Li, H. Yao, Y. Jiao, and Y. Ren, "Improving direct physical properties prediction of heterogeneous materials from imaging data via convolutional neural network and a morphology-aware generative model," *Comput. Mater. Sci.*, vol. 150, no. March, pp. 212–221, 2018, doi: 10.1016/j.commatsci.2018.03.074.
[175] J. Wu, X. Yin, and H. Xiao, "Seeing permeability from images: fast prediction with convolutional neural networks," *Sci. Bull.*, vol. 63, no. 18, pp. 1215–1222, 2018, doi: 10.1016/j.scib.2018.08.006.
[176] O. Sudakov, E. Burnaev, and D. Koroteev, "Driving digital rock towards machine learning: Predicting permeability with gradient boosting and deep neural networks," *Comput. Geosci.*, vol. 127, no. February, pp. 91–98, 2019, doi: 10.1016/j.cageo.2019.02.002.
[177] J. E. Santos, D. Xu, H. Jo, C. J. Landry, M. Prodanović, and M. J. Pyrcz, "PoreFlow-Net: A 3D convolutional neural network to predict fluid flow through porous media," *Adv. Water Resour.*, vol. 138, no. November 2019, p. 103539, 2020, doi: 10.1016/j.advwatres.2020.103539.
[178] J. E. Santos *et al.*, "Modeling nanoconfinement effects using active learning," *eprint arXiv:2005.02587*, pp. 1–23, 2020.
[179] N. Srisutthiyakorn*, "Deep-learning methods for predicting permeability from 2D/3D binary-segmented images," in *SEG Technical Program Expanded Abstracts 2016*, 2016, pp. 3042–3046.
[180] A. Rabbani and M. Babaei, "Hybrid pore-network and lattice-Boltzmann permeability modelling accelerated by machine learning," *Adv. Water Resour.*, vol. 126, no. December 2018, pp. 116–128, Feb. 2019, doi: 10.1016/j.advwatres.2019.02.012.
[181] X. Miao, K. M. Gerke, and T. O. Sizonenko, "A new way to parameterize hydraulic conductances of pore elements: A step towards creating pore-networks without pore shape simplifications," *Adv. Water Resour.*, vol. 105, pp. 162–172, 2017, doi: 10.1016/j.advwatres.2017.04.021.
[182] "Scipy." [Online]. Available: https://www.scipy.org/.
[183] L. N. Smith, "Super-Convergence : Very Fast Training of Neural Networks Using Large Learning Rates," pp. 1–18.
[184] R. Pascanu, T. Mikolov, and Y. Bengio, "On the difficulty of training recurrent neural networks," *30th Int. Conf. Mach. Learn. ICML 2013*, no. PART 3, pp. 2347–2355, 2013.
[185] "Python." [Online]. Available: www.python.org.
[186] "TensorFlow." [Online]. Available: www.tensorflow.org.
[187] "h5py." [Online]. Available: www.h5py.org.
[188] F. Chollet, *Deep learning with Python*, Second. Manning Publications, 2021.
[189] "Paraview." [Online]. Available: www.paraview.org.
[190] "PMEAL." [Online]. Available: github.com/PMEAL.
[191] J. Schindelin *et al.*, "Fiji: an open-source platform for biological-image analysis," *Nat. Methods*, vol. 9, no. 7, pp. 676–682, 2012, doi: 10.1038/nmeth.2019.
[192] T. Hildebrand and P. Rüegsegger, "A new method for the model-independent assessment of thickness in three-dimensional images," *J. Microsc.*, vol. 185, no. 1, pp. 67–75, 1997, doi: 10.1046/j.1365-2818.1997.1340694.x.

Appendices

Appendix A. Deriving Mass Partitioning Equation

In this section deriving the mass partitioning equation for pore network models is explained. For a conduit element shown in Figure 3-6, the assumptions for the derivation are: 1) pore i and pore j are occupied by phase α and β, respectively. 2) The interface of phases is in the middle of the conduit's throat. 3) The interface of phases is at thermodynamic equilibrium which can be described by Henry's law.

Assuming the diffusive conductance from pore i to the interface as K_i , and from pore j to the interface as K_j, the rate of diffusion can be described as follows:

Rate of diffusion from pore i to the center of throat ij:

$$m_{ij} = K_i(c_i - c_i^*) \tag{A- 1}$$

Rate of diffusion from pore j to the center of throat ij:

$$m_{ji} = K_j(c_j - c_j^*) \tag{A- 2}$$

where the interface concentrations are related with dimensionless Henry's constant: $H_{ij} = c_i^*/c_j^*$ or $H_{ji} = c_j^*/c_i^*$.

Applying a mass conservation at the interface of phases, the diffusive mass transport rate from pore i to the interface is equal to the rate of species from the interface to pore j. By equating Eq. (A- 1) and Eq. (A- 2), the concentration at the interface can be found:

$$c_j^* = \frac{(K_i/K_j)c_i + c_j}{(K_i/K_j)H_{ij} + 1} \tag{A- 3}$$

By substituting Eq. (A- 3)into Eq. (A- 1)and rearranging, the formula for m_{ij} can be as follows:

$$m_{ij} = \frac{1}{\frac{1}{K_i} + \frac{H_{ij}}{K_j}}(c_i - H_{ij}c_j) \tag{A- 4}$$

where the values of the diffusive conductance ($K_i$and K_j) can be calculated using a resistor-in-series model.

Diffusive conductance from pore i to the interface:

$$\frac{1}{K_i} = \frac{1}{g_i^p} + \frac{0.5}{g_{ij}^t} \tag{A- 5}$$

Diffusive conductance from pore j to the interface:

$$\frac{1}{K_j} = \frac{1}{g_j^p} + \frac{0.5}{g_{ij}^t} \quad \text{(A- 6)}$$

Substituting Eq. (A- 5)and Eq. (A- 6)into Eq. (A- 4) results in the main equation used in this study Eq. (3-4).

Appendix B. Estimating Pore Size Distribution from Micrographs

Given a 2D image of the CL as shown in Figure B- 1, the gray scale image was binarized to label the void and solid phase pixels (Figure B- 1b) using image-processing Fiji software [191]. Next, the local thickness of the void space was extracted (Figure B- 1c) using PoreSpy's *local_thickness* filter. The local thickness of an object is "the diameter of the largest sphere that fits inside the object and contains the point" [192]. Finally, the pore size distribution of the sample was extracted (Figure B- 1) using PoreSpy's *metrics* class and *pore_size_distribution* method. The CL's pore size distribution and range of diameters were then used as a realistic base distribution and customized for further studies in section 3.4.4.

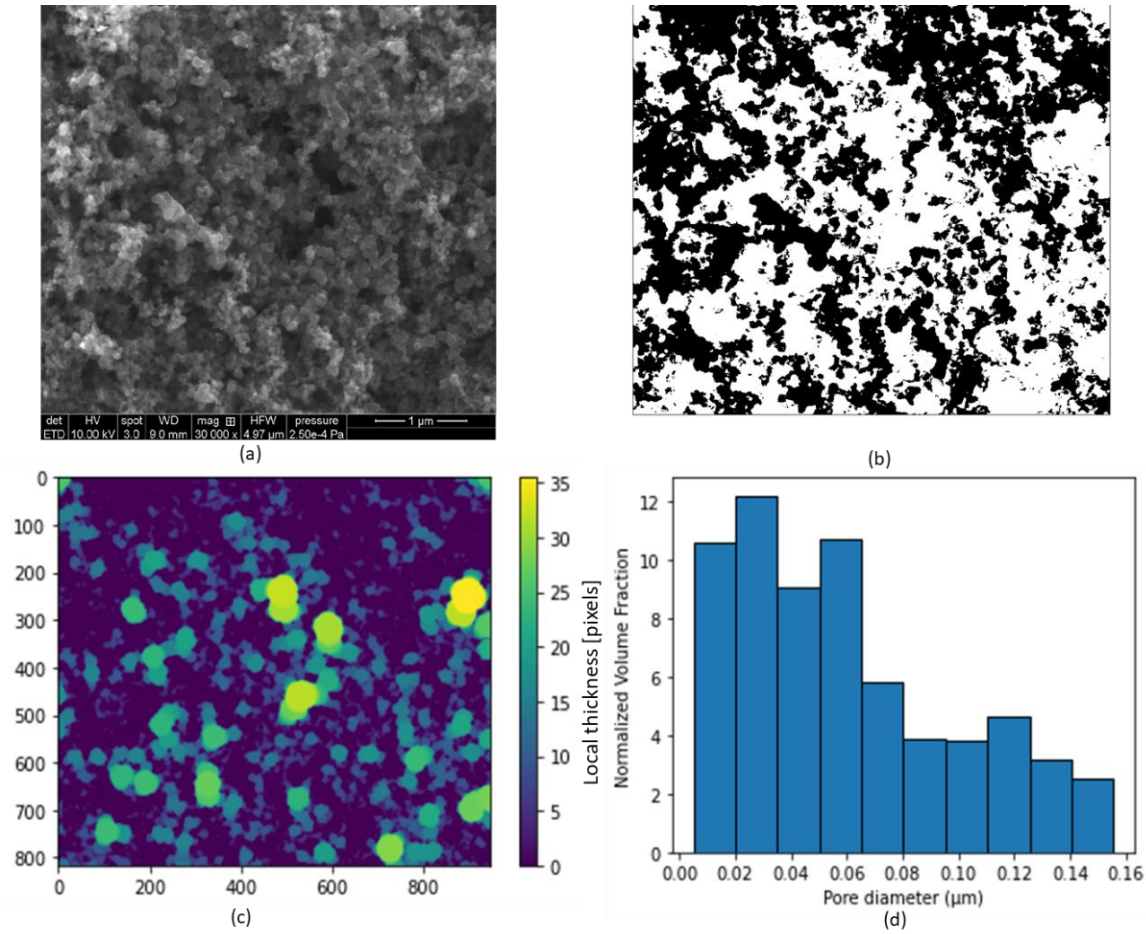

Figure B- 1 Extracting pore sizes from a CL sample. a) SEM image of a sample Zn-air CL. b) 2D Binarized image of the CL sample. Void phase and solid phase are white and black, respectively. c) Local thickness in the void space of the binarized image. d) Pore sizes distribution extracted from the local thickness image.

Appendix C. Generated layers

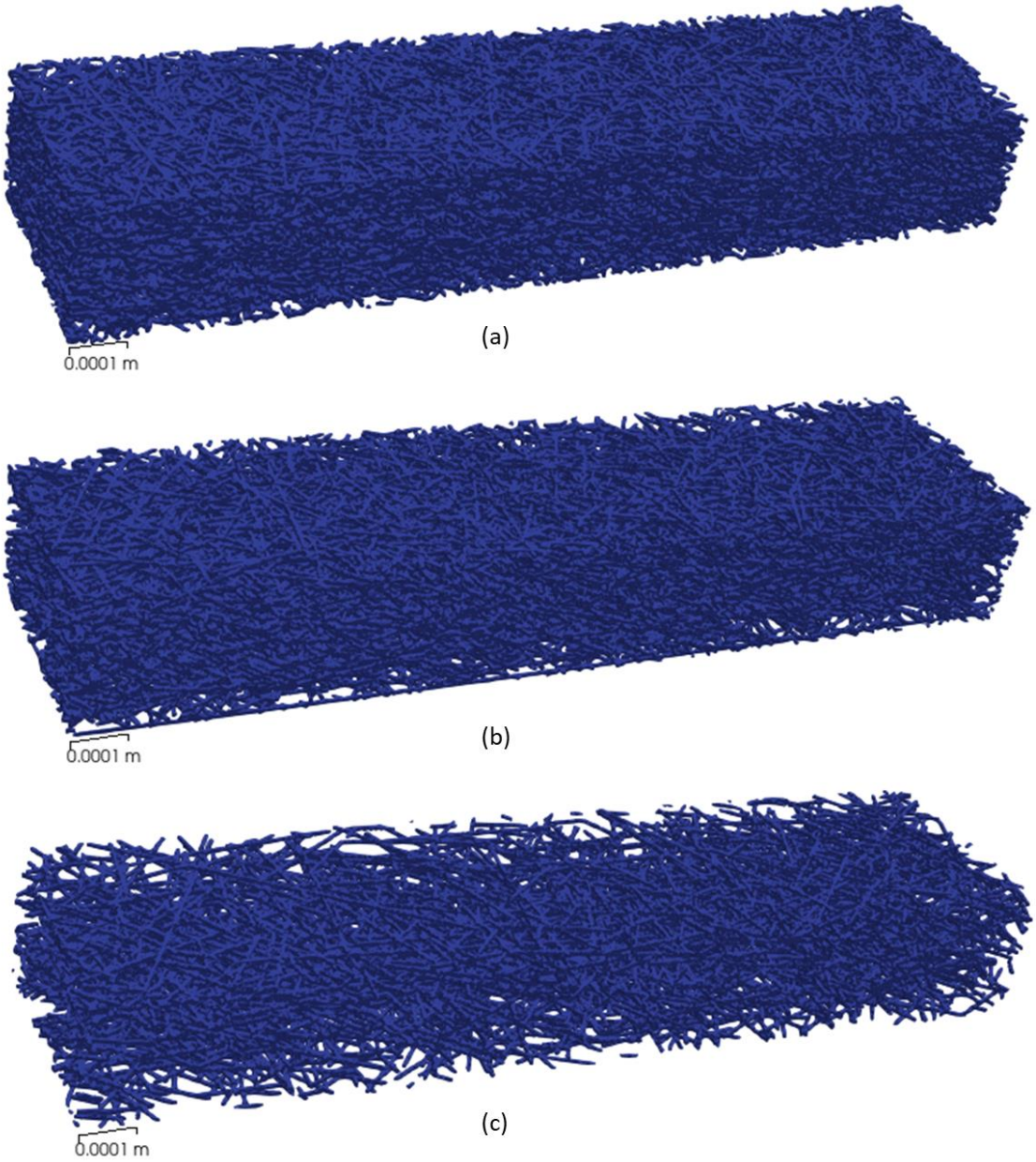

Figure C- 1 3D images of the generated fibrous materials as building blocks of multi-layer structures. a) layer with porosity = 0.7 b) layer with porosity = 0.8 c) layer with porosity = 0.9.